Structure-Property Relationships in Oxide-Ion Conductors

TATE, MATTHEW,LIAM

Abstract

"Structure-property relationships in oxide-ion conductors"

Ph.D. Thesis Matthew L. Tate March 2017

Literature review: Details the structure-property relationships of a selection of oxide-ion conductors and their potential use as solid electrolytes.

Experimental methods: Describes the synthesis methods and analytical techniques used during this project.

Structural characterisation and properties of the $Bi_{1-x}Nb_xO_{1.5+x}$ materials (x = 0.0625, 0.11, and 0.12): The characterisation of tetragonal $Bi_{0.9375}Nb_{0.0625}O_{1.5625}$ is reported for the first time. Thermal annealing of $Bi_{0.89}Nb_{0.11}O_{1.61}$ and $Bi_{0.88}Nb_{0.12}O_{1.62}$ resulted in decreases in oxide-ion conductivity due to partial cubic-to-tetragonal phase transitions.

The structure-property relationships of Bi(III)-containing apatite-type oxide-ion conductors: The first Bi(III)-containing triclinic apatite, $Bi_2La_8[(GeO_4)_6]O_3$, was characterised, with annular bright-field scanning-transmission electron microscopy directly imaging small concentrations of interstitial oxygen. Bond valence energy landscape modelling probed the potential pathways for interstitial oxide-ion migration in apatites.

Understanding variable Re coordination environments in $Bi_{28}Re_2O_{49}$: Reverse Monte Carlo analyses of $Bi_{28}Re_2O_{49}$ using neutron total-scattering data found the local-scale structure to contain 4-, 5-, and 6-coordinate ReO_x polyhedra. At 700 °C, migration of oxygen atoms between the Bi-O and Re-O sublattices occurs.

Structure-property relationships of bismuth molybdate compositions, $Bi_{38-x}Mo_{7+x}O_{78+3x/2}$ (x = 0, 0.5): The fluorite-related superstructure of orthorhombic $Bi_{38}Mo_7O_{78}$ was characterised using synchrotron X-ray and neutron diffraction data, with distortion-mode analysis undertaken to attempt to characterise the room-temperature monoclinic phase.

Floating-zone-furnace crystal growth of fluorite- and apatite-type oxide-ion conductors: Crystals for a range of materials were grown using a floating-zone furnace, upon which single-crystal Laue neutron diffraction data were subsequently collected. Using this data, the complex rhombohedral superstructure of $Bi_{0.913}V_{0.087}O_{1.587}$ was characterised.

Synthesis, characterisation, and properties of the $La_xSr_{10-x}Ga_6O_{19+x/2}$ family (x = 0, 0.2, and 0.4): A range of lanthanum strontium gallates were synthesised to investigate the effect of interstitial oxygen content on the oxide-ion conductivity of these materials.

Conclusions and future work: A summary of the project, including suggestions for future work.

Structure-Property Relationships in Oxide-Ion Conductors

Matthew L. Tate, MChem. (Hons)

Durham University

Australian Nuclear Science and Technology Organisation

Supervisors: Dr. Ivana Radosavljevic Evans and Prof. Garry J. McIntyre

A thesis submitted in partial fulfilment of the requirements for the degree of

Doctor of Philosophy

Department of Chemistry

Durham University

2017

Acknowledgements

Ivana and Garry, your knowledge and guidance as my supervisors over the past several years have proved invaluable, helping me to not only grow as a scientist, but also as a person.

My thanks go to the various scientists I have worked with, without whom this project would not have been possible: Tom Vogt and Doug Blom for collaborating on the ABF STEM work; Ray Withers for electron diffraction; Matt Tucker and Helen Playford for assisting with POLARIS data collections and helping me understand RMCProfile; Leon Bowen for SEM EDX; Aziz Daoud-Aladine, Max Avdeev, and Helen Brand for assistance with data collections at ISIS, ANSTO, and the Australian Synchrotron; Ross Piltz for fixing problems with KOALA; Chris Ling for providing access to the floating-zone furnace and associated equipment for crystal growths; Gary Oswald for keeping the diffractometers going; and finally John Evans, for helpful insight at group meetings.

To the IRE and JSOE PhD students, postdocs, and fourth-year students: Luiza, Chris, James, Melissa, Huiyu, Chunhai, Rafael, Sayonara, Andrew, Chloe, Jack, Jamie, Jenny, Heather, Lorna, Sam, and Zara. Whether it was discussing ideas, attending conferences together, or just simply having a relaxing chat over a cup of tea, you made my time in Durham considerably more enjoyable. Over in Australia, thanks to Julia, Morgan, Paula, and Josie, for assisting me with the floating-zone furnace and providing welcome company on the trips to Wagga Wagga, and also to Jack, Jonathan, Grace, and Sara at ANSTO, where we all had a good time in spite of variable air-conditioning temperatures, power outages, and numerous meetings.

To my friends, both in Durham and Sydney. Thanks to Beth, Laurie, Becca, Flora, Ben, and Bex for helping me to maintain a healthy work/life balance during my first year, and welcome breaks when finishing the project. To the ‘Rat Pack’, Alex, Andrew, Caillin, Lachlan, and Rihanna, for “adopting the foreigner” the first time I met you. I cannot thank you enough for helping me to find my feet so quickly on arriving in a strange land.

The biggest thanks have to be given to my Mum, Dad, and brother Lewis for your love and unwavering support over the years, always lending an ear to listen no matter the time of day. I would not have made it through to the end of this project without you, so for that, I thank you.

Tho’ much is taken, much abides; and though
We are not now that strength which in old days
Moved earth and heaven; that which we are, we are;
One equal temper of heroic hearts,
Made weak by time and fate, but strong in will
To strive, to seek, to find, and not to yield.

from Ulysses
Lord Alfred Tennyson

Declaration

The work presented in this thesis is entirely the work of the author, except where help is acknowledged from a named person, or a reference provided to a published source.

The research presented within was performed in the Department of Chemistry, Durham University, and the Australian Centre for Neutron Scattering (formerly Bragg Institute), Australian Nuclear Science and Technology Organisation, between October 2013 and March 2017. The results of this research have not been submitted for a degree in this or any other university. This thesis conforms to the word limit detailed in the Degree Regulation of the university.

Table of contents

1 Literature review

1.1 Oxide-ion conductors and conductivity mechanisms

Oxide-ion conductors are materials in which oxide ions act as charge carriers, migrating through the crystal lattice via thermally-activated movement in the direction of the electric field. The oxide-ion conductivity of a material, σ, is given by:

$$\sigma = nZe\mu \qquad \text{Equation 1.1}$$

where *n* is the number of charge carriers per unit volume, *Ze* is the charge or multiple of the charge of one electron, and μ is the mobility of the ions. The oxide-ion conductivity of a material is temperature dependent, given by:

$$\sigma = \frac{\sigma_o}{T} e^{-\frac{E_a}{RT}} \qquad \text{Equation 1.2}$$

where $\sigma_o$is a pre-exponent, E_a is the activation energy for oxide-ion migration, *R* is the gas constant, and *T* is the temperature.

The mechanism by which oxide-ion migration occurs varies depending on the material studied, with a number of conductivity mechanisms existing. An oxide ion migrates from a lattice site to a neighbouring vacant lattice site by thermally-activated hopping in the vacancy mechanism.[1] For this to be effective, the lattice must contain a sufficiently large concentration of vacancies for the oxide ions to migrate between. Secondly, oxide ions can migrate using an interstitial mechanism, whereby an oxide ion migrates from an interstitial lattice site to a neighbouring interstitial site, with no displacement of ions on other lattice sites. In the related interstitialcy mechanism however, an oxide ion migrates from an interstitial to non-interstitial site, causing migration of an ion from that non-interstitial site to a neighbouring interstitial site.[2] Finally, materials containing cations with the ability to support variable coordination numbers can provide further low-energy pathways through the structure using these MO_x variable coordination polyhedra.[3-6] If these MO_x polyhedra are also rotationally flexible, this allows additional low-energy migration pathways to be created.[7]

1.2 Applications of oxide-ion conductors

1.2.1 Solid-oxide fuel cells (SOFCs)

Oxide-ion conductors are used for a wide range of applications, including oxygen-separation membranes, oxygen pumps, and sensors,[8] with a large area of scientific interest focussing on their use in solid-oxide fuel cells (SOFCs). A SOFC is a device which converts chemical energy directly into electrical energy, with oxide-ion conductors acting as the solid electrolyte (Figure 1.1).

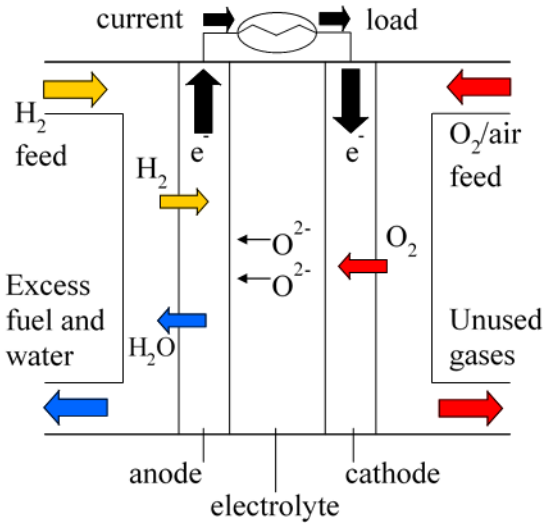

Figure 1.1: Schematic showing the operation of a solid-oxide fuel cell.

Within the SOFC, oxygen gas is reduced at the cathode (Equation 1.3), and the oxide ions produced are conducted through the electrolyte to the anode. At the anode, the oxide ions react with hydrogen (Equation 1.4) to create electrons which flow around the circuit (current) and provide the electrical energy. This use of hydrogen and oxygen (either purely or as a component of air) gases provides a clean method for generating electrical energy, as the sole by-product is water (Equation 1.5).

$$Cathode: \frac{1}{2}O_2 + 2e^- \rightarrow O^{2-} \qquad \text{Equation 1.3}$$

$$Anode: H_2 + O^{2-} \rightarrow H_2O + 2e^- \qquad \text{Equation 1.4}$$

$$Overall: H_2 + \frac{1}{2}O_2 \rightarrow H_2O \qquad \text{Equation 1.5}$$

For maximum efficiency, a SOFC electrolyte should have negligible electronic conductivity and an oxide-ion conductivity greater than 10^{-2} Scm^{-1} in the operating-temperature region.[9-11] Electronic conductivity allows electrons to permeate through the electrolyte without requiring oxide ions to act as charge carriers (leakage currents).[1]

There is an increasing drive to reduce SOFC operating temperatures, as expensive ceramics are required to manufacture the SOFC heat exchangers and interconnects for operating temperatures above 700 °C.[12, 13] Below 700 °C, stainless steel can instead be used for construction of these components, reducing manufacturing costs.[14] Additionally, unlike the ceramic components, stainless steel does not contain chromium, a metal which can poison the SOFC cathodes.[15]

To achieve the highest fuel-cell efficiency, a balance must be struck between the theoretical maximum efficiency of the fuel cell determined by thermodynamics, and the electrolyte oxide-ion conductivity. This is because the oxide-ion conductivity of the electrolyte has an Arrhenius relationship with temperature, whilst the thermodynamic fuel-cell efficiency is inversely proportional to the operating temperature.[16]

The SOFC anodes and cathodes must be compatible with the electrolyte used, to ensure mechanical stability of the SOFC as a whole. Mechanical stresses due to differing thermal-expansion coefficients of the individual SOFC components can lead to the SOFC fracturing. The cathodes and anodes need to be good ionic and electronic conductors, so oxide ions can migrate through the electrodes either following reduction at the cathode, or prior to oxidation at the anode, whilst also conducting current around the circuit.

Cathodes in SOFCs need to have good resistance to impurities such as CO_2 and Cr if air is used as the O_2 supply.[17, 18] This is because CO_2 and Cr (as Cr_2O_3) can form insulating layers on the cathode surface which decrease the rate of the oxygen-reducing reaction. The current commercially-used cathode for yttria-stabilised zirconia (YSZ) SOFCs is a Sr-doped $LaMnO_3$ (LSMO), $La_{1-x}Sr_xMnO_3$ (x = 0.1 to 0.2), and YSZ composite. This composite has an identical thermal-expansion coefficient to YSZ (α = 10.5 × 10^{-6} K^{-1}),[19] hence the mechanical stresses between the cathode and electrolyte due to thermal cycling are minimised. The composite also combines the electronic conductivity of LSMO with the oxide-ion conductivity of YSZ. However, YSZ only shows high levels of conductivity at elevated temperatures (*vide infra*), and so an alternative cathode material must be utilised in SOFCs with lower operating temperatures. Reports of using perovskite-based mixed ionic-electronic conductors (MIECs) as cathode materials have produced promising results, with $BaCo_{0.6}Fe_{0.3}Sn_{0.1}O_{3-\delta}$ reported by Qian *et al.* to have good ionic and electronic conductivities between 400 and 800 °C, and a thermal expansion coefficient of 15.8 × 10^{-6} K^{-1}.[20]

A Ni-containing composite is typically chosen for the anode material, as Ni has a high electronic conductivity and good electrocatalytic activity for electrochemical oxidation.[21] A composite is used instead of coating Ni onto an oxide-ion conductor to prevent Ni agglomerates forming, which would reduce the active surface area of the anode required for the oxidation process.[22] The use of Ni is also problematic if hydrocarbons are used as the H_2-containing fuel source, as cracking hydrocarbons on the anode directly can cause carbon build-up, leading to anode failure due to separation of Ni from the other composite components.[23]

The anode material used in YSZ-containing SOFCs is a Ni-YSZ composite, again due to similarities in thermal-expansion coefficient between the composite and electrolyte (α = 12 to 15 × 10^{-6} K^{-1} and 10.5 × 10^{-6} K^{-1} for Ni-YSZ and YSZ respectively).[19] However, use of a Ni and Gd-doped ceria (GDC) anode increases the number of available reaction sites,[24] as GDC is a MIEC in reducing atmospheres. GDC also has a higher oxide-ion conductivity than YSZ across the 300 to 700 °C temperature range, making it more suitable for use in low- and intermediate-temperature SOFCs. Whilst GDC can enhance the electrochemical activity of hydrocarbon oxidation within the SOFC (if hydrocarbons are used as the H_2 source) via the Ce^{4+}/Ce^{3+} redox reaction, the volume change associated with the reduction of Ce^{4+} to Ce^{3+} means that the anode has the potential to separate from the electrolyte.[25]

1.2.2 Oxygen-separation membranes

Oxide-ion conductors can be used to separate oxygen gas of high purity from an incoming air supply, without having to resort to costly techniques such as cryogenic air separation.[26] Oxygen-separation membranes operate using the differences in oxygen partial pressure between the high-pressure incoming gas supply and the low-pressure outflow stream to allow oxygen to migrate through the separation membrane as oxide ions, and then be oxidised into oxygen gas, which is then stored.

The oxide-ion conductors used in separation membranes are typically MIECs, operating between 800 and 900 °C.[27] MIECs are of interest for use in separation membranes as there is no need for an external circuit to provide a current for reduction and oxidation of the oxygen and oxide ions respectively, as the electronic conductivity acts as an internal short circuit (Figure 1.2).[28] Perovskite-based materials provide high levels of conductivity through the membrane. The recent work by Lu *et al.* into a group of Fe-based perovskites found that Gd-doping to produce materials with the formula $BiFe_{1-x}Gd_xO_{3-\delta}$ (x = 0.025 to 0.20) gave separation membranes with high structural and chemical stability, high oxygen permeability, and low permeation activation energies.[29]

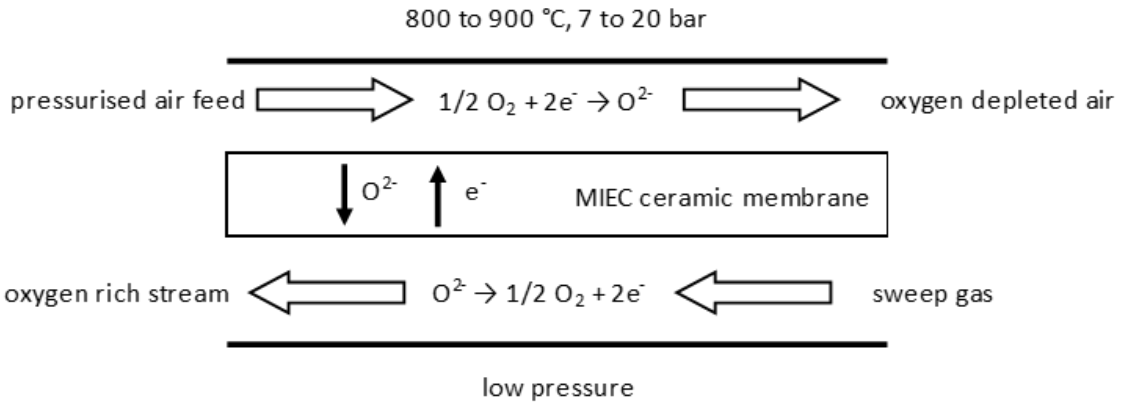

Figure 1.2: Schematic of oxygen transport through a MIEC ceramic oxygen separation membrane. Figure adapted from Hashim *et al.*[27]

1.2.3 Oxygen sensors

Solid-oxide oxygen sensors are useful in the automotive industry when placed into the exhaust system of a vehicle, as they help determine the fuel-to-air ratio supplied to the engine.[30] The sensor operates by generating a voltage due to the oxygen partial pressure difference between the incoming exhaust gas stream and that present in a reference cell. If the fuel-to-air ratio contains too little or too much oxygen compared to that in the reference cell, the voltage across the sensor increases or decreases respectively compared to an equilibrium voltage.[31] This information is then given to the fuel management system to alter the fuel-to-air ratio going into the engine. Zirconia-based materials such as YSZ are used in oxygen sensors, due to their high oxide-ion conductivities at elevated temperatures.[32]

1.3 Apatite-type oxide-ion conductors

1.3.1 Apatite structure

Apatite-type materials have the general formula $A_{10}(TO_4)_6X_{2\pm\delta}$ (A = large alkaline or rare earth metal, Pb, or Bi; T = Ge, P, Si, V; X = O, OH, halide). The alternative formula $[A^I]_4[A^{II}]_6[(TO_4)_6][X_2]$ distinguishes between the two distinct A sites in the lattice. With this formula, the apatite structure can be described as a three-dimensional $[A^I]_4[(TO_4)_6]$ framework, consisting of columns of A^IO_6 distorted trigonal prisms corner-connected to TO_4 tetrahedra (Figure 1.3). Cavities in this framework running along [001] accommodate $A^{II}{}_6X_2$ units.

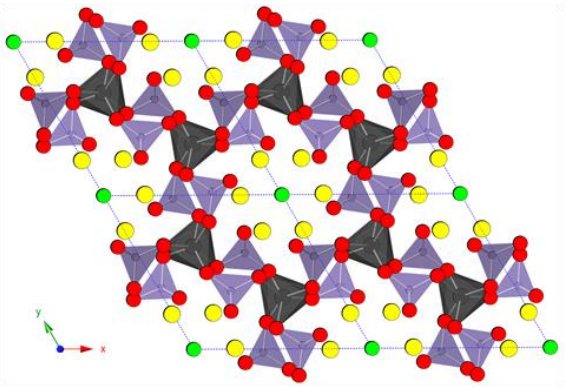

Figure 1.3: General $[A^I]_4[A^{II}]_6[(TO_4)_6][X_2]$ apatite structure viewed along the *z* axis. Black = A^I, yellow = A^{II}, red = O, green = X. Bonds to the A^{II} and X sites have been omitted for clarity.

1.3.2 Symmetry reduction in apatites

The vast majority of apatite-type materials are hexagonal, with space groups $P6_3/m$ or $P6_3$.[33] The remaining apatites crystallise with monoclinic or triclinic structures, with several triclinic materials reported in the past two decades.[34-38] Monoclinic structures form due to the X-site ions ordering above and below $z = 1/2$. The mirror plane in the hexagonal structure becomes a glide plane in the monoclinic structure, and one cell dimension (typically *b*) doubles in length. Examples of monoclinic apatites include the calcium phosphates $Ca_{10}[(PO_4)_6]Cl_2$ and $Ca_{10}[(PO_4)_6](OH)_2$.[39, 40]

The reduction of symmetry from hexagonal to triclinic is thought to arise from the flexible nature of the apatite framework. If the framework is too large compared to the size of the cavity unit, the A^{II}-O bonds undergo expansive stress, whilst the T–O bonds undergo compressive stress. To minimise these stresses, the TO_4 tetrahedra tilt and the apatite framework contracts, causing rotation of the triangular faces of the A^IO_6 trigonal prisms by a metaprism twist angle, ϕ. This metaprism twist angle is defined as the projected O1-A^I-O2 bond angle when viewed down the *z* axis. Metaprism twist angles usually range between 5 and 25 °, with larger values indicating a greater mismatch between the sizes of the framework and cavity units. Whilst metaprism twist angles up to 60 ° are theoretically possible,[33] meaning the A^IO_6 polyhedra would have octahedral coordination, there are no reported apatites containing A^IO_6 octahedra. A material with a large twist angle is more likely to adopt a structure with lower symmetry than hexagonal. This loss of symmetry is promoted by the presence of interstitial oxygen atoms, which are thought to cause further expansion of the apatite framework.[34, 38]

The size of the metaprism twist angle in apatite-type materials varies inversely with average crystal radii. A study by White and Dong into apatites with Ca, Cd, Pb, or Sr as the A-site cation found a virtually linear inverse relationship between the metaprism twist angle and average crystal radii when the T and X site ions are varied for a given A-site cation.[33] This is because apatites with smaller average crystal radii have to contract the framework more to satisfy the shorter-bond-length requirements of the smaller ions, leading to larger ϕ values.

1.3.3 Interstitial oxygen locations and conductivity mechanisms in apatite-type materials

The location of interstitial oxide ions within apatite-type materials and their associated conductivity pathways differ for Si- and Ge-containing apatites. In silicate apatites, interstitial oxygen atoms are reported within the framework cavities on either the rotation axis,[41] or near the cavity walls.[42-46] In germanium apatites, whilst interstitial oxygen atoms have also been reported near the walls of the framework cavities,[47-49] they are also reported within the apatite framework, between pairs of GeO_4 tetrahedra.[37, 38, 50] A range of conductivity mechanisms are reported for apatite-type materials. Some apatites are reported as conducting via vacancy hopping, whilst increasing numbers have been reported to conduct using an interstitial-oxide-ion mechanism.

Based on atomic-modelling techniques, in 2003 Tolchard *et al.*[51] reported a linear vacancy-hopping mechanism along the *z* axis down the centre of the apatite-framework cavities (Figure 1.4a), with saddle points midway between the channel O atoms in $La_8Sr_2[(SiO_4)_6]O_2$. Saddle points are locations along a given pathway with the highest activation energies. This linear pathway contrasts with the interstitial conductivity mechanism they reported for $La_{9.33}[(SiO_4)_6]O_2$, where the oxygen atoms migrate using a non-linear sinusoidal pathway across the face of SiO_4 tetrahedra at the channel walls, but still passing through the same saddle point as for $La_8Sr_2[(SiO_4)_6]O_2$ (Figure 1.4b). Oxide-ion migration along this pathway causes relaxation of the SiO_4 tetrahedra on a local scale, with displacements of up 0.2 Å for the Si atoms and 0.6 to 1.0 Å for the O atoms in the SiO_4 tetrahedra.

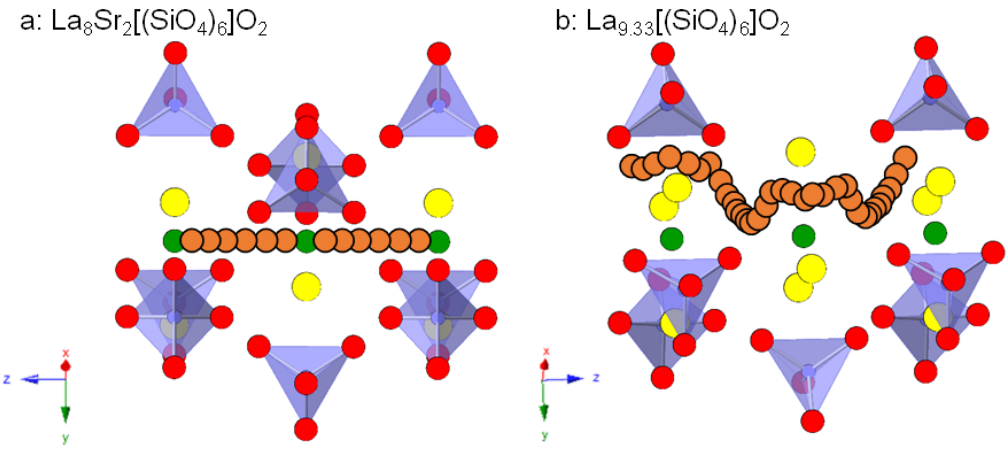

Figure 1.4: a) Linear vacancy-hopping migration pathway along the *z* axis in $La_8Sr_2[(SiO_4)_6]O_2$; b) Sinusoidal interstitial oxide-ion migration pathway in $La_{9.33}[(SiO_4)_6]O_2$. Figures adapted from report by Tolchard *et al.*[51] La/Sr = yellow, apatite framework O = red, apatite channel O = green, Si = purple. Oxide-ion migration pathway = orange.

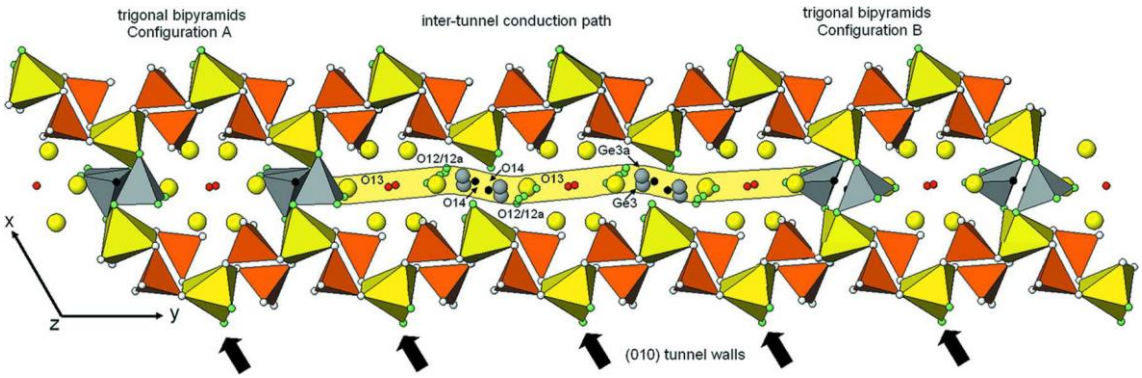

Figure 1.5: Proposed [010] oxide-ion migration pathway reported by Pramana *et al.*[38] Reproduced with permission of the International Union of Crystallography.

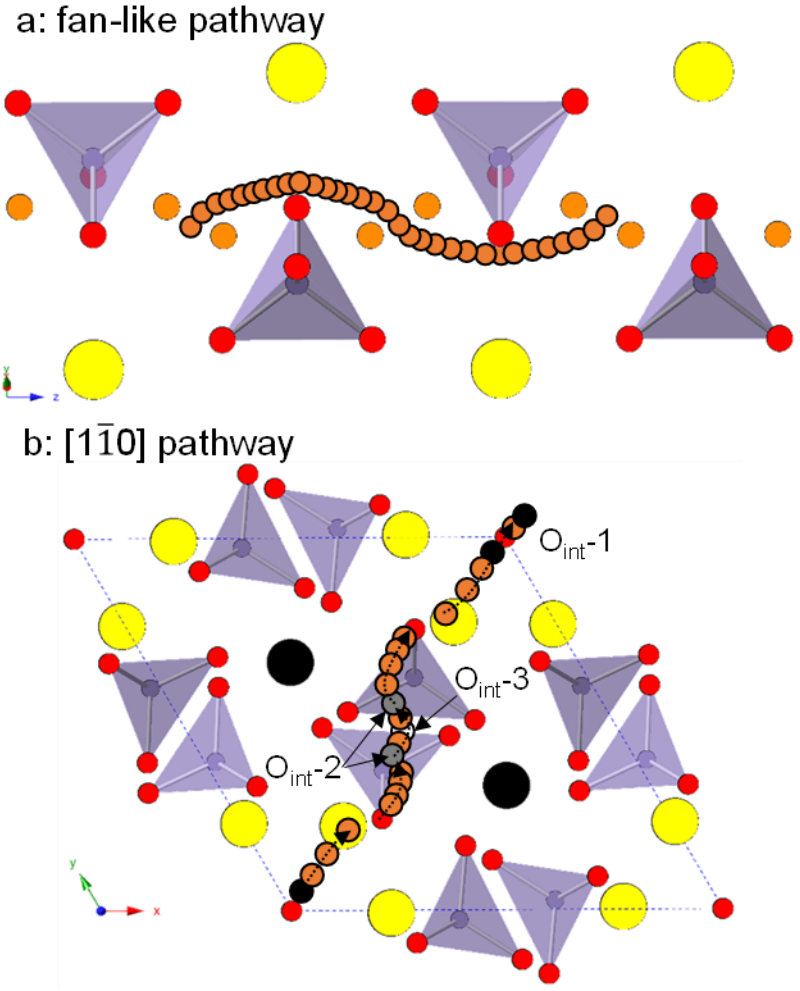

Figure 1.6: a) Fan-like migration pathway along the *z* axis for $La_8Y_2[(GeO_4)_6]O_3$ reported by Kendrick *et al.*[50] A^{II} = yellow, Ge = purple, O = red, interstitial O = orange, interstitial migration pathway = orange; b) *xy* plane interstitial oxide-ion migration pathway along [1 $\bar{1}$ 0] for $La_{10}[(SiO_4)_6]O_2$ reported by Imaizumi *et al.*[52] A^{I} = black, A^{II} = yellow, Si = purple, O = red, interstitial oxygen positions = black, grey, and white, interstitial migration pathway = orange.

In 2007, Pramana *et al*. located an interstitial oxygen atom at ~(0, 0.5, 0.5) in triclinic $La_{10}[(GeO_4)_6]O_3$,[38] which causes local distortion of the Ge(3)O_4 tetrahedra and the formation of a GeO_5 trigonal bipyramid. They proposed that interstitial oxygen atoms would migrate along the *y* axis using the O14 and O12/O12a oxygen sites, with a saddle point located at (0, 0, 0.5) (Figure 1.5). This is in contrast with Kendrick *et al.*,[50] who report a fan-like migration pathway of

interstitial oxygen atoms along the *z* axis between pairs of neighbouring GeO_4 tetrahedra in $La_8Y_2[(GeO_4)_6]O_3$ (Figure 1.6a). These interstitial oxygen atoms allow for the formation of GeO_5 trigonal bipyramids as the interstitial oxygen migrates between the GeO_4 tetrahedra. Computational modelling by Imaizumi *et al.* on $La_{10}[(GeO_4)_6]O_3$ supports this migration pathway,[53] as well as observing oxide-ion migration in the *xy* plane along $[1\ \bar{1}\ 0]$ for $La_{10}[(SiO_4)_6]O_2$ (Figure 1.6b).[52]

In 2009, Béchade *et al.* reported an interstitial-oxygen conductivity mechanism based on atomic modelling,[54] which is also proposed by Corrie *et al.*[55] Béchade *et al.* found that interstitial oxygen atoms in $La_{9.33}[(SiO_4)_6]O_2$ migrate along the *z* axis, with the conductivity occurring as a cooperative movement of a defect comprised of two interstitial oxygen atoms and one vacancy (Figure 1.7). As for the Tolchard *et al.* model discussed previously,[51] Béchade *et al.* report the rotation of the tetrahedral SiO_4 units due to the insertion of interstitial oxygen. However, they do not observe the same saddle point as Tolchard *et al.*, with the previously identified saddle point between the channel O atoms predicted not to be crossed by the migration pathway.

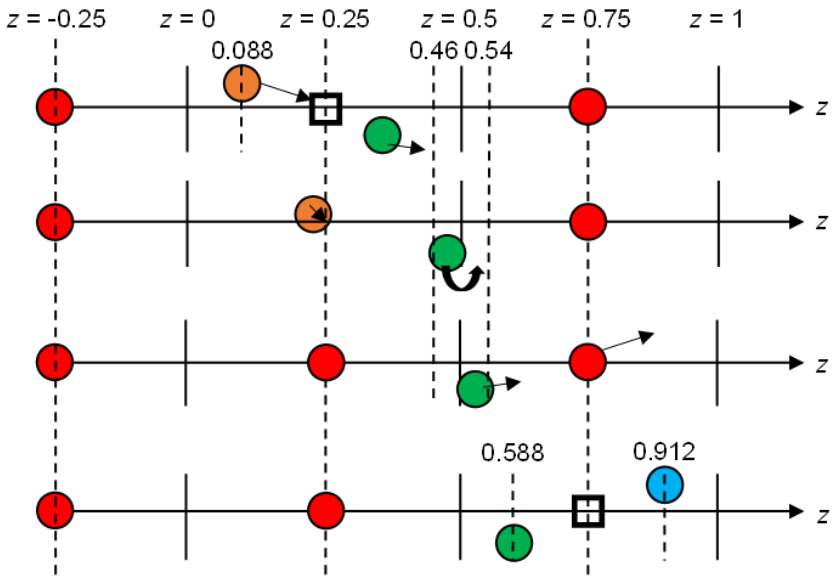

Figure 1.7: Oxide-ion migration mechanism involving concerted movement of a defect and two interstitial oxygen atoms along the *z* axis reported by Béchade *et al.*[54] Channel O atom = red, interstitial oxygen = orange, green, and blue, defect = black square.

Finally, An *et al.* reported interstitial oxygen positions along the centres of the framework cavities for $Nd_{(28+x)/3}[(SiO_4)_{6-x}(AlO_4)_x]O_2$ (x = 0.5, 1.0, and 1.5) at room temperature.[56] At elevated temperatures, these interstitial-oxygen atoms move up to 0.69 Å towards the cavity walls, with further interstitial positions found between SiO_4 tetrahedra at 500 °C. Oxide-ion conductivity is thought to occur in both the *xy* plane and along the *z* axis (Figure 1.8). For conductivity in the *xy* plane (Figure 1.8a), interstitial oxygen sites facilitate curved conductivity pathways between the O(3) oxygen sites and channel O(4) site across the face of the apatite cavity before conducting between cavities through the apatite framework. Along the *z* axis, oxide ions migrate between the two O(3) sites of an SiO_4 tetrahedron (Figure 1.8b), before crossing the framework cavity in a sinusoidal fashion using interstitial sites near the centre of the apatite cavity to interact with the channel O(4) site.

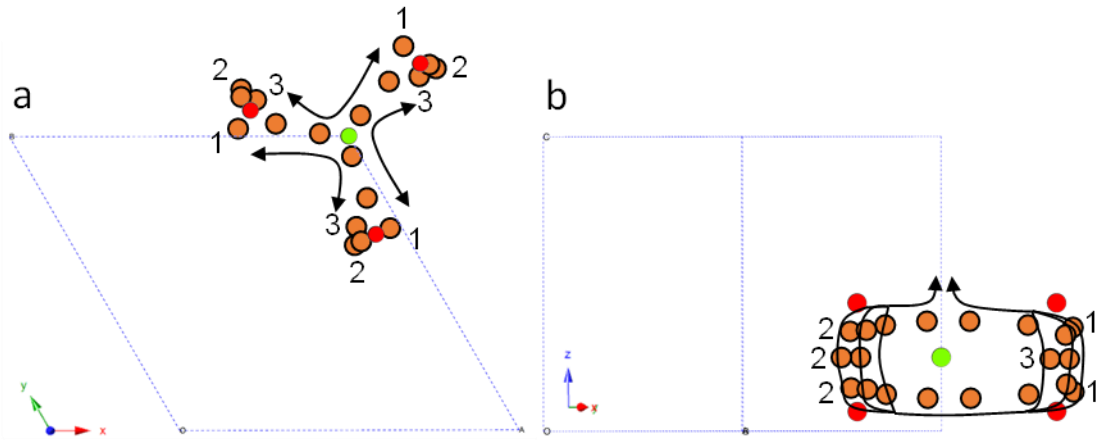

Figure 1.8: a) *xy* plane interstitial oxide-ion migration pathways; b) *z* axis interstitial oxide-ion migration pathways reported by An *et al.*[56] O4 = green, O3 = red, interstitial pathways = orange. Numbers 1 to 3 denote the three different potential migration pathways through the structure.

1.3.4 Effects of dopants and sintering temperatures on the oxide-ion conductivities of apatite-type materials

The oxide-ion conductivities reported for apatite-type materials are high in the intermediate-temperature SOFC region (500 to 650 °C), with the highest apatite conductivity values reported for $La_{9.5}[(GeO_4)_{5.5}(AlO_4)_{0.5}]O_2$, roughly an order of magnitude greater than yttria-stabilised zirconia at 500 °C (~6.3 × 10^{-3} Scm^{-1} and ~8.7 × 10^{-4} Scm^{-1} respectively).[47]

Apatites where A = La and T = Si or Ge are reported to have higher conductivity values than those using other cations, with $A_{10}[(SiO_4)_6]O_3$ (A = La, Nd, Sm) materials having conductivity values of 4.3 × 10^{-3} Scm^{-1}, 3.8 × 10^{-4} Scm^{-1}, and 4.7 × 10^{-5} Scm^{-1} at 500 °C respectively.[57] Higher oxide-ion conductivities are also observed for materials with either vacancies on the A sites (i.e. A < 10) or more than 26 oxygen atoms. This can be seen for $La_{9.33}[(SiO_4)_6]O_2$, which has A-site vacancies, 26 oxygen atoms, and σ = 2.5 × 10^{-4} Scm^{-1} at 800 °C,[58] roughly three orders of magnitude greater than the $La_8M_2[(SiO_4)_6]O_2$ (M = Sr, Ca, Ba) series which have 10 A-site cations and 26 oxygen atoms (σ = 5.4 × 10^{-7} Scm^{-1}, 9.9 × 10^{-7} Scm^{-1}, and 5.6 × 10^{-7} Scm^{-1} at 800 °C respectively).[59]

The conductivities of germanium apatites are higher at elevated temperatures compared to their silicate analogues. This can be seen for $La_{10}[(GeO_4)_6]O_3$ and $La_{10}[(SiO_4)_6]O_3$, with oxide-ion conductivities of ~8 × 10^{-2} Scm^{-1} and ~6 × 10^{-3} Scm^{-1} at 800 °C reported for the germanate and silicate apatites respectively.[60] The larger size of Ge^{4+} relative to Si^{4+} (0.39 Å and 0.26 Å, respectively)[61] causes the apatite framework to expand, increasing the diameter of the apatite cavities and allowing for improved mobility of the X-site channel oxygens. However, at lower temperatures silicate apatites have higher conductivities than germanium apatites, due to lower activation energies of oxygen migration. A range of mixed Si- and Ge-containing lanthanum apatites have been studied by a number of groups,[44, 62] with high levels of conductivity reported for $La_{9.33}[(SiO_4)_2(GeO_4)_4]O_2$ (σ = 1.2 × 10^{-2} Scm^{-1} at 800 °C),[44] three orders of magnitude greater than for $La_{9.33}[(SiO_4)_6]O_2$ (σ = 2.5 × 10^{-4} Scm^{-1} at 800 °C).[58]

In apatites containing 26 oxygen atoms and no interstitials, oxide-ion conduction occurs primarily along the *z* axis between the X sites down the centre of the apatite channels. Oxide-ion conductivity can occur in the *xy* plane, but measurements performed on a $La_{9.33}[(SiO_4)_6]O_2$ single crystal by Nakayama *et al.* found the conductivity to be approximately two orders of magnitude lower than along the *z* axis.[63] With the introduction of additional oxygen atoms on interstitial sites, elevated oxide-ion conductivity values are observed due to the extra migration pathways available. This is seen for $La_8Ca_2[(GeO_4)_6]O_2$ and $La_8Ca_2[(GeO_4)_{5.75}(VO_4)_{0.25}]O_{2.125}$, where V-doping on the T site necessitates the inclusion of additional oxygen content, leading to an increase in oxide-ion conductivity of roughly one order of magnitude (σ = 1.84 × 10^{-5} Scm^{-1} and 1.97 × 10^{-4} Scm^{-1} at 500 °C respectively).[64]

One method of improving the oxide-ion conductivities of apatite-type materials can be achieved through substitution of Si^{4+} or Ge^{4+} with M^{3+} cations on the T site. This is reported by Leon-Reina *et al.*, who show high conductivities for a range of Al-doped $La_{10-x}[(GeO_4)_{5.5}(AlO_4)_{0.5}]O_{2.75-3x/2}$ compositions (x = 0.25 to 0.50),[47] and Kioupis and Kakali, who report greater conductivities for $La_{9.38}Sr_{0.45}[(SiO_4)_{6-x}(AlO_4)_x]O_{2+\delta}$ (x = 0.30 to 0.50) compared to the x = 0 materials.[65] This improved conductivity is thought to be due to the weaker interactions between Al^{3+} and the migrating oxide ion compared to Si^{4+} or Ge^{4+}.[47] Elevated conductivities have also been reported for other M^{3+} cations such as in $La_{9.67}[(SiO_4)_5(FeO_4)]O_2$ (σ = 1.7 × 10^{-3} Scm^{-1}) and $La_{9.67}[(SiO_4)_5(CoO_4)]O_2$ (σ = 8.1 × 10^{-3} Scm^{-1}), both of which are roughly one order of magnitude more conductive than $La_{9.33}[(SiO_4)_6]O_2$ at 800 °C.[58] Apatites with fully-occupied A sites see the same effect but to a lesser degree, with In^{3+} doping in $La_{10}Si_{5.8}In_{0.2}O_{26.9}$ giving a higher conductivity than undoped $La_{10}Si_6O_{27}$ at 800 °C (σ = 3.14 × 10^{-2} Scm^{-1} and σ = 1.28 × 10^{-2} Scm^{-1} for the In-doped and undoped materials respectively).[66]

The choice of sintering temperature must be considered carefully when preparing Si- and Ge-containing apatites. A study by Marrero-López *et al.* found that the choice of sintering temperature plays an important role in the density of pellets produced for impedance spectroscopy, leading to significant changes in oxide-ion conductivity for silicate apatites, more so than for germanates.[67] Pellets of $La_{10}[(SiO_4)_{5.5}(AlO_4)_{0.5}]O_{2.75}$ were fired at temperatures ranging from 1400 °C to 1600 °C for 5 hours, producing pellets with densities 70 to 98 % of the theoretical values, and conductivities of 4.6 × 10^{-3} Scm^{-1} and 4.64 × 10^{-2} Scm^{-1} at 800 °C (for the 1400 °C and 1600 °C pellets respectively). For $La_{9.6}[(GeO_4)_{5.5}(AlO_4)_{0.5}]O_{2.15}$, whilst an increase in density was observed on using a higher sintering temperature (75 % density at 1000 °C and 98 % density at 1200 °C), the change in conductivity was smaller, with only a twofold increase in conductivity from 9.65 × 10^{-3} Scm^{-1} to 1.68 × 10^{-2} Scm^{-1} at 800 °C. Lower sintering temperatures must be used in the preparation of Ge-containing apatites as Ge volatilisation above 1300 °C[68] causes the formation of an La_2GeO_5 impurity due to the loss of Ge.[69]

1.4 Fluorite-type oxide-ion conductors

1.4.1 Fluorite structure description

Materials with a fluorite-type structure crystallise in space group $Fm\bar{3}m$. The metal atoms (M) occupy the lattice sites on the corners and centres of the unit-cell faces, whilst the oxygen atoms (O) occupy tetrahedral holes within the structure. This means that the fully-occupied structure has the formula M_2O_4, with two unique crystallographic sites. The metal atoms are eight-coordinate and form MO_8 cubic polyhedra, whilst the oxygen atoms form OM_4 tetrahedra (Figure 1.9).

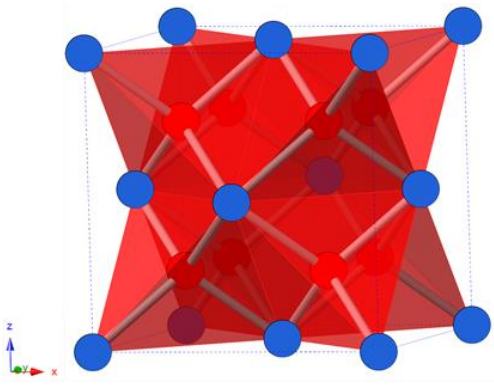

Figure 1.9: Fluorite-type structure of M_2O_4 showing the OM_4 tetrahedra. M sites = blue, O sites = red.

1.4.2 Zirconia- and ceria-based oxide-ion conductors

Three different structure types of zirconia (ZrO_2) exist at different temperatures: monoclinic α-ZrO_2 (space group $P2_1/c$) below 1170 °C, tetragonal β-ZrO_2 (space group $P4_2/nmc$) between 1170 °C and 2370 °C,[70] and fluorite-type cubic γ-ZrO_2 (space group $Fm\bar{3}m$) above 2370 °C.[71] Oxide-ion conduction occurs via the vacancy mechanism in cubic zirconia, but oxygen vacancies must be introduced for conductivity to occur, as the oxygen sites are fully occupied. This is achieved by substituting Zr^{4+} for aliovalent cations with a lower oxidation number, such as Ca^{2+}, Gd^{3+}, Sc^{3+}, or Y^{3+},[71] which also stabilise the fluorite-type phase at lower temperatures. These aliovalent cations are distributed statistically throughout the structure, with the metal site having mixed-occupancy between the Zr^{4+} and dopant cations. If the vacancies across the oxygen site are distributed randomly, then the cubic space group is retained.

The concentration of dopant cations introduced into the fluorite structure must be considered. If the dopant concentration is too low, then the highly-conductive cubic fluorite phase will not be stable in the temperature range required for SOFC operation. However, elevated concentrations of dopant introduce a large number of oxygen vacancies, leading to the formation of point defects which inhibit oxide-ion mobility and decrease the overall conductivity of the material.[72] These point defects migrate through the structure to form a larger defect cluster if:

$$BE_{cluster} = \left[\sum_{components} E_{defect}\right] - E_{cluster} \qquad \text{Equation 1.6}$$

is positive, where $BE_{cluster}$ is the binding energy of the defect cluster, E_{defect} is the enthalpy of defect formation, and $E_{cluster}$ is the enthalpy of defect-cluster formation.[73]

The highest oxide-ion conductivities for have been reported for Y- and Sc-doped zirconia (YSZ and ScSZ).[72] Of the $Zr_{1-x}Y_xO_{2-x}$ compositions, $Zr_{0.9}Y_{0.1}O_{1.9}$ (x = 0.1) has the most stable cubic phase.[10] However, $Zr_{0.92}Y_{0.08}O_{1.92}$ (x = 0.08) is the commercially-used material, due to it exhibiting the highest oxide-ion conductivity of the YSZ compounds (σ = 2.2 × 10^{-2} Scm^{-1} at 800 °C),[47] whilst also having sufficient stability to prevent defect-cluster formation.

$Zr_{0.92}Sc_{0.08}O_{1.92}$ forms a single-phase fluorite-type material. However, $Zr_{0.9}Sc_{0.1}O_{1.9}$ forms as a biphasic mixture of fluorite and rhombohedral ($R\bar{3}$) phases, whilst $Zr_{0.89}Sc_{0.11}O_{1.89}$ is comprised entirely of the rhombohedral phase.[74] As for the Y-doped analogue, the highest oxide-ion conductivity values are reported for cubic $Zr_{0.92}Sc_{0.08}O_{1.92}$ (σ = 8.5 × 10^{-2} Scm^{-1} at 800 °C),[74] approximately quadruple the conductivity of the Y-doped phase. This elevation in conductivity when using Sc^{3+} as a dopant is due to the smaller difference in ionic radii for Zr^{4+} and Sc^{3+} compared to Zr^{4+} and Y^{3+} (0.84, 0.87, and 1.02 Å for Zr^{4+}, Sc^{3+}, and Y^{3+} respectively).[61] This smaller difference means that ScSZ has a reduced defect association energy, thereby increasing oxide-ion mobility and promoting oxide-ion conduction.[72] Introducing dopant cations with different radii to those of the parent cation causes distortion of the crystal lattice, decreasing the ability of oxide ions to migrate through the structure by reducing the regularity of the conduction pathways, thereby lowering the oxide-ion conductivity of the material.

Both ScSZ and YSZ have similar thermal expansion coefficients, with α = 10.7 × 10^{-6} K^{-1} for $Zr_{0.92}Sc_{0.08}O_{1.92}$[54] and α = 10.5 × 10^{-6} K^{-1} for $Zr_{0.92}Y_{0.08}O_{1.92}$.[19] These are close to the values for the Ni-YSZ anodes and LSMO-YSZ cathodes used in current commercial SOFCs, hence these two electrolyte materials will both work with the anode and cathode composites. However, despite the similar thermal expansion coefficients of YSZ and ScSZ and the elevated conductivity values for ScSZ, YSZ is the commercially-used product, due to the considerably lower cost of Y_2O_3 relative to Sc_2O_3.[10]

Another advantage of using zirconia-based electrolytes in SOFCs is that they are chemically inert to the gas reactants used.[9] However, due to the low oxide-ion conductivity values at low temperatures, the minimum operating temperature for these zirconia-based electrolytes is ~700 °C. This limits their usage to high-temperature SOFCs (>700 °C), which require expensive components to produce. The lifespans of SOFCs containing YSZ and ScSZ as electrolytes are also limited due to sample aging, caused by the concentration of dopant cations needed to stabilise the highly-conductive fluorite phase to lower temperatures. Sample aging is a process where oxide-ion defect clusters begin to form over time, trapping oxide ions and decreasing the conductivity of the material. It has been reported that the conductivity of ScSZ halves after 5000 hrs of annealing,[75] with the fluorite phase undergoing a phase transition to a less-conductive tetragonal phase.[76]

Ceria (CeO_2) has a fluorite-type structure with the oxygen site fully occupied. Therefore, dopant cations with lower valence must substitute Ce^{4+} for oxygen vacancies to be incorporated

into the structure. Due to the greater ionic radius of Ce^{4+} relative to Zr^{4+} (0.97 Å and 0.84 Å respectively), rare-earth dopants such as Sm^{3+} (1.079 Å) and Gd^{3+} (1.053 Å) can be used.[61, 77] These are the primary dopants used in doped-ceria electrolytes due to their high oxide-ion conductivities: $Ce_{0.9}Gd_{0.1}O_{1.95}$ (σ = 9.5 × 10^{-3} Scm^{-1} at 500 °C); $Ce_{0.9}Sm_{0.1}O_{1.95}$ (σ = 3.3 × 10^{-3} Scm^{-1} at 500 °C).[78] $Ce_{0.9}La_{0.1}O_{1.9}$ contains the larger La^{3+} cation (1.16 Å)[61] and has a lower conductivity than the Sm- and Gd-doped materials (σ = 2.02 × 10^{-4} Scm^{-1} at 500 °C).[79] The use of Sm^{3+} and Gd^{3+} as dopants causes minimal lattice strain, thereby minimising decreases in conductivity due to irregularities in the oxide migration channels. Balancing the number of oxygen vacancies whilst avoiding defect-cluster formation leads to the highest conductivities observed for materials with ~10 % dopant.[80]

Further improvements to the oxide-ion conductivities of ceria are found when CeO_2 is co-doped. The introduction of a small percentage of Sr^{2+} as found in $Ce_{0.78}Sm_{0.2}Sr_{0.02}O_{1.88}$ improves the conductivity nearly two-fold compared to the singly-substituted material (σ = 6.1 × 10^{-2} Scm^{-1} and σ = 3.71 × 10^{-2} Scm^{-1} at 800 °C for $Ce_{0.78}Sm_{0.2}Sr_{0.02}O_{1.88}$ and $Ce_{0.8}Sm_{0.2}O_{1.9}$ respectively).[81] Comparable levels of improvement are found at lower temperatures when ceria is co-doped with Sm and Nd, with an oxide-ion conductivity for $Sm_{0.075}Nd_{0.075}Ce_{0.85}O_{1.925}$ of σ = 1.4 × 10^{-2} Scm^{-1} at 550 °C.[82]

A problem with ceria-based electrolytes is that at low oxygen partial pressures (such as found near the SOFC anode), the presence of H_2 causes the reduction of Ce^{4+} to Ce^{3+} and an increase in the electronic conductivity of the material.[83] This increase in electronic conductivity is also found in Pr-doped ceria, as Pr can exist as Pr^{3+} or Pr^{4+}, leading to the formation of a MIEC.[84] Reduction of Ce^{4+} to Ce^{3+} can be suppressed by coating the anode-facing surface of the ceria-based electrolyte with a fine layer of YSZ.[83, 85] However, this will impact the overall conductivity of the SOFC at temperatures below 700 °C, as the conductivity of YSZ at 500 °C (~8.4 × 10^{-4} Scm^{-1})[47] is one order of magnitude lower than that for $Ce_{0.9}Gd_{0.1}O_{1.95}$.

1.4.3 Bismuth-oxide-based oxide-ion conductors

1.4.3.1 Choosing the fluorite-type bismuth oxide polymorph

At room temperature, bismuth oxide (Bi_2O_3) exists as the monoclinic α-phase (space group $P2_1/c$), undergoing a phase transition to the fluorite-type δ-Bi_2O_3 phase (space group $Fm\bar{3}m$) above 729 °C, and remains stable to its melting point of 824 °C.[86, 87] On cooling, δ-Bi_2O_3 transforms to either the tetragonal β-Bi_2O_3 phase (space group $P\bar{4}2_1c$) at ~650 °C, or the body-centred-cubic γ-Bi_2O_3 phase (space group I23) at 639 °C.[86] The β-phase reverts to the monoclinic α-phase at ~330 °C, whilst the γ-phase can either transform to the α-phase or persist to room temperature if the rate of cooling is sufficiently slow.[87] A fifth polymorph, the metastable orthorhombic ϵ-Bi_2O_3 phase, has been identified following hydrothermal synthesis, undergoing a phase transition to the monoclinic α-phase above 400 °C.[88]

Of these five Bi_2O_3 polymorphs, δ-Bi_2O_3 is the most sought-after material for use as an electrolyte in SOFCs due to its excellent oxide-ion conductivity, reported as ~1 Scm^{-1} at 750 °C,[89] and rising to ~2.3 Scm^{-1} at 800 °C.[9] This high level of conductivity arises from the

presence of intrinsic oxygen vacancies, as only 75 % of the oxygen-containing tetrahedral holes in the fluorite-type structure are occupied. As δ-Bi_2O_3 is only thermally stable across a narrow high-temperature range, this fluorite phase must be stabilised to lower temperatures for use as an electrolyte between 300 and 700 °C. To achieve this, Bi^{3+} cations can be substituted with aliovalent or isovalent cations, thereby allowing for high oxide-ion conductivities at lower temperatures. For single-substituting dopants, the general formula can be written as $Bi_{1-x}M_xO_{1.5+((y-3)/2)x}$ for M^{y+} cations. A wide range of transition-metal and rare-earth dopants have been reported in the literature (e.g. Er, Gd, Ho, Mo, Nb, Ta, Te, V, W, Yb, and Zr).[90-101]

1.4.3.2 Doped bismuth oxide superstructures

The structure types which M^{y+}-doped $Bi_{1-x}M_xO_{1.5+((y-3)/2)x}$ (M = Mo, Nb, Ta, V, W) materials adopt differ greatly. Low-level dopant concentrations (x < ~0.07) typically result in the formation of sillenite-type phases,[102, 103] whilst higher concentrations (x > 0.2 to 0.3) usually leads to formation of materials with Aurivillius-type structures, such as $Bi_2VO_{5.5}$ and Bi_2WO_6,[104, 105] with $Bi_2VO_{5.5}$ forming the basis for the BIMEVOX compounds (*vide infra*). It is the bismuth oxide materials with M^{y+} concentrations between these two regions (~0.07 < x < ~0.25) which are of the most interest for use as electrolytes in SOFCs, as these form complex fluorite-type superstructures.

The fluorite-type structures with the smallest unit-cell parameters can be found for Nb- and Ta-dopant concentrations between 0.0625 < x < 0.234 and 0.1 < x < 0.25 respectively, where the M^{5+} cations are disordered over the metal site in fluorite-type δ -Bi_2O_3.[96] This ($1a_F \times 1a_F \times 1a_F$) structure (where a_F is the fluorite unit-cell parameter) is incommensurately modulated, first reported for the Nb-doped series by Miida and Tanaka,[106] then fully characterised by Ling *et al.* as a (3+3)-dimensional incommensurately modulated solid solution.[107] Alternatively, the introduction of M^{y+} cations can result in the formation of superstructures with considerably larger unit-cell volumes, with the phase at x = 0.254 for Nb-doped Bi_2O_3 forming as a tetragonal ($3a_F \times 3a_F \times 7a_F$) superstructure.[108]

If the concentration of dopant is low, the fluorite-type superstructures contain isolated MO_x polyhedra, such as for V (x < 0.1), where isolated VO_4 tetrahedra are found in the cubic ($3a_F \times 3a_F \times 3a_F$) superstructure,[109] or W (0.064 < x ≤ 0.143) where the tetragonal superstuctures contain isolated WO_6 octahedra.[96, 110] For $Bi_{1-x}W_xO_{1.5+3x/2}$, a ($\frac{\sqrt{10}}{2}a_F \times \frac{\sqrt{10}}{2}a_F \times 3a_F$) tetragonal superstructure was reported to exist between x = 0.064 and 0.134.[110] However, the x = 0.125 composition was found to have a tetragonal ($\sqrt{5}a_F \times \sqrt{5}a_F \times 2a_F$) superstructure.[96] The phase boundary between these two structure types was therefore shifted to a x ~0.108, as a number of compositional ranges were reported initially for the ($\sqrt{5}\,a_F \times \sqrt{5}\,a_F \times 2a_F$) superstructure,[110, 111] before being determined to be between x = 0.108 and 0.16 based on data collected using a number of analytical techniques.[96, 112]

Elevated concentrations of dopant result in the MO_x polyhedra needing to edge or corner share due to limited availability of non-neighbouring M^{y+}-containing sites in these

superstructures. For V-doped materials, a triclinic superstructure ($\frac{3\sqrt{2}}{2}a_F \times \frac{3\sqrt{2}}{2}a_F \times 3\sqrt{2}a_F$) is formed when $0.1 < x \leq 0.22$, containing clusters of VO_x polyhedra.[113] Likewise, for the $0.143 < x \leq 0.181$ W-doped compositions, the ($3a_F \times 3a_F \times 3a_F$) cubic superstructure contains W_4O_{18} units.[110]

However, this change in the MO_x polyhedra from isolated polyhedra to clustered units with increasing composition is not observed for the $Bi_{1-x}Mo_xO_{1.5+3x/2}$ materials, with isolated MoO_4 tetrahedra found when $0.0625 \leq x \leq 0.5$.[94, 114, 115] Within this composition range, a number of materials have been characterised containing groups of MoO_x polyhedra. These include $Bi_{26}Mo_{10}O_{69}$ (x = 0.256) a triclinic material with isolated MoO_4 tetrahedra and pairs of corner-sharing MoO_5 trigonal bipyramids which form Mo_2O_9 dimers,[5] and $Bi_{38}Mo_7O_{78}$ (x = 0.156), which has MoO_4 tetrahedra and chains of three corner-sharing MoO_6 octahedra forming Mo_3O_{16} structural units.[116]

1.4.3.3 Conductivities and thermal stability of doped bismuth oxides

Oxide-ion conductivity in fluorite-type bismuth oxide structures occurs primarily via the vacancy mechanism. As the concentration of M^{y+} dopant cations increases, the number of vacancies within the oxygen sublattice decreases if $y > 3$, due to the need to balance the charge in the material. Therefore, higher oxide-ion conductivities are expected for lower concentrations of dopant, and so a balance must be found between using sufficient concentration to stabilise these highly-conductive fluorite-type phases at lower temperatures, whilst also maintaining high levels of oxide-ion conductivity. The effect which the dopant concentration can have on the conductivity is reported for $Bi_{1-x}Nb_xO_{1.5+x}$ (x = 0.15 and 0.22), where the oxide-ion conductivities of $Bi_{0.85}Nb_{0.15}O_{1.65}$ and $Bi_{0.78}Nb_{0.22}O_{1.72}$ at 500 °C are 1.1×10^{-2} Scm^{-1} and 2.3×10^{-4} Scm^{-1} respectively, a difference of two orders of magnitude.[89] The bismuth niobate materials also have the issue that as the concentration of Nb-dopant increases, there are fewer polarisable Bi-O bonds due to the increased number of stronger Nb-O bonds, resulting in a reduction in oxide-ion conductivity as these bonds require more energy to break.[117]

If dopant cations with higher charge are used (e.g. W^{6+} compared to Nb^{5+}), this results in fewer oxygen vacancies in the fluorite-like structure for the same concentration of dopant. Therefore, the oxide-ion conductivity values obtained with the higher-charged dopant will be lower than their lower-charged counterpart for the same level of doping. This can be seen for $Bi_{0.85}W_{0.15}O_{1.725}$, which has an oxide-ion conductivity of ~1×10^{-3} Scm^{-1} at 500 °C,[118] one order of magnitude lower than for $Bi_{0.85}Nb_{0.15}O_{1.65}$ ($\sigma = 1.1 \times 10^{-2}$ Scm^{-1}).[89]

The highest oxide-ion conductivity for a singly-substituted bismuth oxide was originally found for metastable (*vide infra*) $Bi_{0.8}Er_{0.2}O_{1.5}$ (~2.6×10^{-2} Scm^{-1} at 500 °C),[119] but was surpassed by a more recent report on cubic $Bi_{0.913}V_{0.087}O_{1.587}$, which has a conductivity of 3.9×10^{-2} Scm^{-1} at 500 °C. The structure of this pseudo-cubic bismuth vanadate is comprised of a fluorite-like Bi-O sublattice containing isolated VO_4 tetrahedra. Studying this structure with molecular-dynamics simulations identified a number of oxide-ion conductivity pathways.[109] Over the course of the simulations, the average V coordination number was seen to increase from

4 to 4.33, due to the ability of V to support variable coordination environments. VO_5 and VO_6 polyhedra were formed, promoting oxide-ion conductivity by introducing additional oxygen vacancies into the Bi-O sublattice to regenerate some of the vacancies lost through doping V into Bi_2O_3. Variation in the coordination environments of cation dopants have also been reported for $Bi_{0.9375}Nb_{0.0625}O_{1.5625}$,[120] $Bi_{46}V_8O_{89}$,[4] $Bi_{26}Mo_{10}O_{69}$,[5] and $Bi_{28}Re_2O_{49}$.[6]

Co-doping bismuth oxide also results in increased oxide-ion conductivity. Punn *et al.* report high levels of conductivity in $Bi_{12.5}La_{1.5}ReO_{24.5}$, with $\sigma = 1.1 \times 10^{-3}$ Scm^{-1} at 300 °C.[121] However, it was found subsequently that prolonged annealing at 600 °C causes a cubic-to-tetragonal phase transition and a decrease in conductivity of three orders of magnitude ($\sigma = 4.8 \times 10^{-6}$ Scm^{-1} at 300 °C).[122] Similar effects are observed for $Bi_{0.85}Tb_{0.1}W_{0.05}O_{1.575}$ (TWSB) and $Bi_{0.75}Tb_{0.25}O_{1.5}$ (TSB), which show decreases in conductivity of up to one order of magnitude following prolonged annealing at 500 °C.[123] The conductivity lowering in TWSB is caused by loss of crystallinity and potential formation of an amorphous phase, whilst TSB undergoes a cubic-to-rhombohedral phase transition. The metastable nature of the fluorite-type phase is also reported for $Bi_{1-x}Y_xO_{1.5}$ ($x < 0.318$)[124] and $Bi_{1-x}Er_xO_{1.5}$ ($x < 0.275$),[125] with annealing at 650 °C resulting in the formation of hexagonal phases. Dordor *et al.* reported that the hexagonal polymorph of $Bi_{0.775}Y_{0.225}O_{1.5}$ has a lower conductivity than that of the cubic phase (σ ~5×10^{-4} Scm^{-1} and ~1×10^{-2} Scm^{-1} for the hexagonal and cubic phases respectively at 500 °C).[126]

1.4.3.4 Mitigating bismuth reduction in SOFC electrolytes

A problem with using δ-Bi_2O_3-based electrolytes is the reduction of Bi^{3+} to Bi^0 under low oxygen partial pressures. Wachsman and Duncan report that the oxygen partial pressure required to cause Bi^{3+} reduction increases with increasing temperature, with a pO_2 below 10^{-14} atm at 500 °C or 10^{-13} atm at 800 °C resulting in Bi^{3+} reduction.[127] This precludes the use of these electrolytes in SOFCs as the oxygen partial pressure near the anode is between 10^{-18} and 10^{-21} atm.[128] Therefore, these electrolytes have to be modified to prevent the reduction of Bi^{3+}, which can be achieved through the use of bilayer electrolytes or nanocomposite materials.

Bilayer electrolytes are formed by effectively sandwiching two materials together to prevent the negative effects of one from having a detrimental impact on the oxide-ion conductivity of the electrolyte as a whole. Reports show that YSZ can be used to coat the anode-facing surface of bismuth-oxide-based electrolytes, preventing the reduction of Bi^{3+}.[128, 129] However, as for the application of YSZ to ceria-based electrolytes (*vide supra*), YSZ shows low levels of oxide-ion conductivity below 700 °C, so cannot be used as a bilayer material for these low-temperature Bi_2O_3-based electrolytes.

Due to the excellent oxide-ion conductivity exhibited by both doped-Bi_2O_3 and ceria-based electrolytes, these have been the subject of much investigation into forming bilayer electrolytes.[130-132] Placing the ceria-based electrolyte on the anode-side of the bilayer will prevent the reduction of Bi^{3+}. Whilst this will mean that Ce^{4+} reduces to Ce^{3+} due to the low oxygen partial pressure, the Bi_2O_3-based layer will stop the electronic conductivity from the ceria

causing leakage currents within the SOFC. By altering the thicknesses of the bilayers, this will allow for the oxygen partial pressure gradient across the electrolyte to be tuned,[127] and the optimal bilayer thicknesses found to maximise conductivity and prevent unwanted reduction of Bi^{3+}.[133] Wachsman *et al.* report that a bilayer electrolyte containing $Bi_{0.8}Er_{0.2}O_{1.5}$ and $Ce_{0.9}Gd_{0.1}O_{1.95}$ has increased power density when compared to solely ceria-based electrolytes,[134] whilst Ruth *et al.* have found that replacing Er-doped Bi_2O_3 with Dy- and Gd-doped Bi_2O_3 leads to improved power densities over the Er-doped case, due to the increased oxide-ion conductivity of the co-doped material.[135] However, these Dy- and Gd-doped bismuth oxides were found to be unstable over extended periods of time, with loss of conductivity either through ordering of the oxide ions or undergoing phase transformations to a less-conductive phase.[136]

A different technique to prevent the reduction of Bi^{3+} in Bi_2O_3-based electrolytes is through the formation of a nanocomposite material. This has been reported recently by Joh *et al.*,[137] who show that isolating grains of Er-doped Bi_2O_3 within YSZ prevents leakage currents from flowing as the current cannot pass through the YSZ to reach other Bi-containing grains.

1.5 Additional oxide-ion-conductor families

1.5.1 Lanthanum molybdate, $La_2Mo_2O_9$

$La_2Mo_2O_9$ has two polymorphs, a monoclinic α-phase, and a cubic β-phase which forms following a reversible phase transition at ~580 °C.[3, 138] The β-phase (space group $P2_13$) contains three distinct oxygen sites, O1, O2, and O3, and it was found that the O2 and O3 sites are only partially occupied, with large anisotropic displacement parameters.[139] In the monoclinic α-form (space group $P2_1$), Mo exists in three coordination environments, due to the ability of Mo to support variable coordination: MoO_4 tetrahedra, MoO_5 trigonal bipyramids, and MoO_6 octahedra. The oxygen atoms in α-$La_2Mo_2O_9$ are statically distributed, but are disordered dynamically in the β-phase.[3] By grouping the oxygen atoms in the α-phase according to their relationship with the O1, O2, and O3 sites in the β-phase, it was found that the site occupancies obtained fitted closely with the occupancies of the experimentally determined oxygen sites. Work from Malavasi *et al.* supports this finding,[140] with the analysis of neutron total-scattering data collected for the α- and β-phases showing that on passing through the phase transition, the oxygen defects go from being static to dynamically distributed whilst maintaining an identical local-scale structure.

The oxide-ion conductivity in $La_2Mo_2O_9$ is three dimensional, with the partially occupied oxygen positions residing in three-dimensional channels.[141] The β-phase has increased oxide-ion conductivity compared to the α-phase by roughly two orders of magnitude, giving a conductivity of $\sigma = 6 \times 10^{-2}$ Scm^{-1} at 800 °C,[138] comparable to that of YSZ ($\sigma = 2.2 \times 10^{-2}$ Scm^{-1} at 800 °C).[47] Due to the significant decrease in conductivity below the phase transition, the usage of $La_2Mo_2O_9$ as an electrolyte in SOFCs is limited to operating temperatures in excess of 580 °C. However, the reversible phase transition leads to an abrupt change in $La_2Mo_2O_9$ unit-cell volume of 0.5 %, which could cause fractures between the electrolyte and electrodes on

thermal cycling, compromising the mechanical stability of the SOFC.[142] Therefore, substitution of La^{3+} with a number of cations has been investigated,[143-146] to attempt to stabilise the cubic β-phase down to room temperature.

These room-temperature doped-β-$La_2Mo_2O_9$ materials show evidence of deviation from linear Arrhenius behaviour at ~400 °C. A study by Corbel *et al.* on $La_{1.7}Bi_{0.3}Mo_2O_9$ found this non-linearity to arise from migration of oxide ions from the O1 site to nearest-neighbour vacancies on the O2 and O3 sites through distortion of the O1$(La/Bi)_3$Mo tetrahedra.[145] These distortions are caused by elongation of the metal-oxygen bonds, which expand the triangular faces of the tetrahedra, allowing oxygen atoms on the O1 sites to migrate between the metal atoms, creating additional migration pathways. However, despite these pathways involving the O1 sites, the conductivities of these doped materials are only marginally greater than that of α-$La_2Mo_2O_9$ between 300 and 580 °C, or greater than that of YSZ above ~500 °C, with conductivities of ~8 × 10^{-3} Scm^{-1} and ~3 × 10^{-3} Scm^{-1} reported for $La_{1.7}Bi_{0.3}Mo_2O_9$ and YSZ, respectively, at 600 °C.[146]

$La_2Mo_2O_9$ also has stability problems in H_2-containing atmospheres (such as near the anode of a SOFC). Cracks form in test samples annealed at 900 °C,[147] due to reduction of Mo^{6+} to lower-valency states and the formation of $La_{12}Mo_8O_{40}$ and $La_7Mo_7O_{30}$ impurities. $La_2Mo_2O_9$ can be recovered when placed under oxidising conditions, but running the material through these redox cycles leads to systematic failure. This reduction of Mo^{6+} has led to $La_2Mo_2O_9$ undergoing studies for use as an anode in SOFCs. When $La_2Mo_2O_9$ is annealed in a H_2-containing environment with low oxygen partial pressure (pO_2 < 10^{-23} atm), this leads to the formation of $La_2Mo_2O_{7-\delta}$. The oxygen stoichiometry in this material is not fixed, and decreasing the oxygen partial pressure further results in additional loss of oxygen content.[148] $La_2Mo_2O_{7-\delta}$ is useful as an anode material as it is a MIEC. However, care must be taken when designing the SOFC, to prevent chemical reactivity between the $La_2Mo_2O_{7-\delta}$ anode and electrolyte.[149]

Whilst $La_2Mo_2O_9$ is not viable for use as an electrolyte in SOFCs due to the stability issues described. However, by synthesising electrolyte materials containing cations able to display variable coordination, these can provide elevated levels of conductivity.

1.5.2 Melilite-type materials

Compounds with a melilite-type structure have the general formula $[A_2][B^I][B^{II}_2O_7]$, where A are large divalent or trivalent cations and B^I and B^{II} are small cations.[150] Melilites have tetragonal structures (space group $P\bar{4}2_1m$), comprised of two-dimensional alternating layers of corner-connected BO_4 tetrahedra and A cations. A number of melilites have been studied for their use as electrolytes, particularly the $La_{1+x}Sr_{1-x}Ga_3O_{7+x/2}$ (x > 0) series, as additional oxygen atoms are required to maintain charge balance caused by the substitution of Sr^{2+} by La^{3+}.[12] $La_{1+x}Sr_{1-x}Ga_3O_{7+x/2}$ has alternating layers of $[(La/Sr)_2]^{(5+x)+}$ cations and $[Ga_3O_{7+x}]^{(5+x)-}$ corner-sharing GaO_4 tetrahedra (Figure 1.10),[7, 151] with chains of eight-coordinate La/Sr cations running through pentagonal channels along [001].[152]

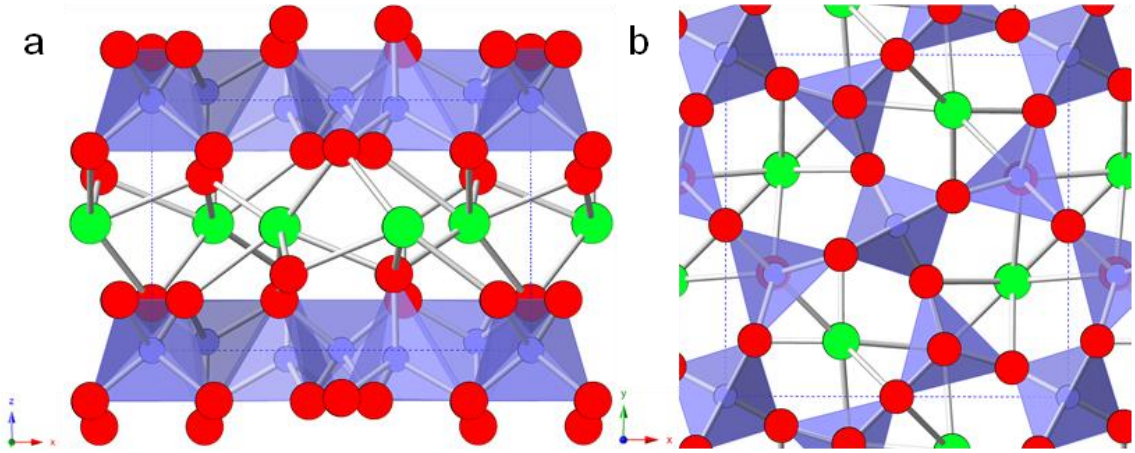

Figure 1.10: Projection of $LaSrGa_3O_7$ melilite-type structure along: a) [010], showing the La/Sr layers and GaO_4 corner-sharing tetrahedra; b) [001], showing the pentagonal channels containing the La/Sr atoms. La/Sr = green, Ga = purple, O = red.

The interstitial oxygen atoms occupy positions within the pentagonal channels in the same plane as the Ga atoms, causing one of the neighbouring GaO_4 tetrahedra to become a GaO_5 trigonal bipyramid.[12] This is possible as Ga can display variable coordination environments. To accommodate the insertion of these interstitial oxygen atoms into the Ga-O layers, the atoms within this layer move by up to 0.45 Å, whilst maintaining structural stability.[7] Synchrotron XRD data collected between 25 and 800 °C shows no evidence of phase transitions in these melilites, hence they would not undergo significant volume changes which could cause fracturing of SOFC components. Interstitial oxide-ion conductivity occurs through a cooperative mechanism with rotation of the GaO_4 tetrahedra.[7] This causes deformation of the melilite framework, enlarging the triangular O-O-O windows between neighbouring corner-sharing GaO_4 tetrahedra. This increases the distances between the O atoms forming the triangular windows and the O4 atoms, thereby minimising the bottlenecks preventing the O4 atoms from migrating to adjacent pentagonal channels, and promoting oxide-ion conductivity.

To highlight that the variable coordination of Ga cations plays a role in improving the oxide-ion conductivity of melilite-type materials, Park *et al.* studied a number of $Sr_2Mg_{1-x}Ga_xGe_2O_{7+0.5x}$ materials.[153] They found that the x = 0.2, 0.3, and 0.5 compositions showed an increase in conductivity of up to one order of magnitude compared to the x = 0.1 composition, with x = 0.2 having a conductivity of $\sigma = 1 \times 10^{-4}$ Scm^{-1} at 800 °C. As the concentration of Ga-dopant increased, more strontium-germanate-based impurities were found within the samples, which could account for the conductivity plateauing at x = 0.2.

Due to their layered nature, melilites have anisotropic oxide-ion conductivities. Wei *et al.* report that the conductivity of a $La_{1.5}Ca_{0.5}Ga_3O_{7.25}$ single crystal at 850 °C is 3.6×10^{-2} Scm^{-1} in the *xy* plane (intralayer), compared to 8×10^{-3} Scm^{-1} along the *z* axis (interlayer).[150] Introducing interstitial oxygen by increasing the La:Sr ratio in $La_{1+x}Sr_{1-x}Ga_3O_{7+x/2}$ elevates the observed oxide-ion-conductivity values, with $La_{1.54}Sr_{0.46}Ga_3O_{7.255}$ having the highest conductivity of this series of melilites (σ = 0.02 Scm^{-1} and 0.1 Scm^{-1} at 600 °C and 950 °C respectively),[152, 154] This is roughly four orders of magnitude greater than that of $LaSrGa_3O_7$ ($\sigma = 4 \times 10^{-5}$ Scm^{-1} at

950 °C).[7] Powdered samples of the Ca-containing analogue, $La_{1.5}Ca_{0.5}Ga_3O_{7.25}$, also show high levels of conductivity, with σ = 1 × 10^{-2} Scm^{-1} at 700 °C.[150]

The purity of synthesised melilites and their associated oxide ion conductivities in the $Ln_{1+x}Sr_{1-x}Ga_3O_{7+x/2}$ series (Ln = La, Ce, Pr, Nd, Sm, Eu, Gd, Dy, Y, and Yb) depends on the ionic radii of the A site cations. Liu *et al.* report that samples with no impurities were formed for the x = 0.2 melilites where Ln = La and Pr, whilst Ln = Nd, Sm, and Yb showed presence of impurity phases. Decreasing x to 0.1 allowed single-phase Ln = La, Pr, Nd, and Sm melilites to be synthesised, whilst Ln = Eu, Gd, Dy, and Yb samples contained impurities.[152] Eight-coordinate La^{3+} has the largest ionic radius of the cations studied in this melilite series (1.16 Å, decreasing to 0.985 Å for Yb^{3+}).[61] It therefore holds that the lanthanoids with ionic radii closest to that of La^{3+} would still be able to form single-phase materials.

Liu *et al.* also report that using a Ln^{3+} cation with a smaller ionic radius causes the oxide-ion conductivity of the melilite to decrease, with the conductivity of $Sm_{1.1}Sr_{0.9}Ga_3O_{7.05}$ (σ ~3 × 10^{-6} Scm^{-1}) nearly two orders of magnitude lower than for $La_{1.1}Sr_{0.9}Ga_3O_{7.05}$ (σ ~1 × 10^{-4} Scm^{-1}) at 800 °C. However, the conductivity was seen to increase for Ln = Pr compared to Ln = La (σ ~ 1 × 10^{-3} Scm^{-1} at 800 °C), which they attributed to Pr^{3+} oxidising to Pr^{4+}, causing the number of interstitial oxygen atoms in the structure to increase.[152] A similar phenomenon was seen by Xu *et al.* when studying $La_{1-x}Ce_xSrGa_3O_{7+\delta}$ (x = 0 to 1), with elevated conductivities reported with increasing x, though this was attributed to increased electronic conduction from the 4*f* electrons in Ce^{3+}, and not oxidation of Ce^{3+} to Ce^{4+}.[155]

Ultimately, the oxide-ion conductivities for $La_{1.54}Sr_{0.46}Ga_3O_{7.255}$ between 300 and 500 °C are insufficient for this material to be used as an electrolyte in the operation range (3 × 10^{-5} Scm^{-1} and 8 × 10^{-3} Scm^{-1} at 300 °C and 500 °C respectively),[7] relegating melilites to high-temperature applications (above 600 °C).

1.5.3 Aurivillius-type BIMEVOX

Aurivillius-type phases have the formula $M_2A_{x-1}B_xO_{3x+3}$, made up of layers of fluorite-like $[M_2O_2]^{2+}$ sandwiched between perovskite slabs of $[A_{x-1}B_xO_{3x+1}]^{2-}$. The value for x determines the number of layers of BO_6 octahedra within the slab.[156] Whilst γ-Bi_2WO_6 (M = Bi, B = W, x = 1 in the general Aurivillius formula) adopts this structure type with a single $[WO_4]^{2-}$ layer in the perovskite slab,[157] significant study has been undertaken in the literature centred around doping the $Bi_2VO_{5.5}$ Aurivillius-type phase.

$Bi_2VO_{5.5}$ has three polymorphs, with the room-temperature orthorhombic α -phase undergoing a phase transition at ~440 °C into the orthorhombic β-phase, then at ~560 °C into the tetragonal γ-phase (space group = I4/mmm).[158] The γ-phase has the highest conductivity of the three polymorphs, as the structure contains fully-occupied bismuth oxide layers $(Bi_2O_2)^{2+}$ alternating with oxygen-vacancy-containing vanadate layers $(VO_{3.5-\delta}Va_{0.5+\delta})^{2-}$ (Va = vacancy). It is these vanadate layers which are responsible for oxide-ion conductivity through the structure, with oxide ions migrating using the vacancy mechanism.[159]

As for the melilite-type materials, the conductivity in $Bi_2VO_{5.5}$ is anisotropic, with data collected on single crystals showing that the conductivity parallel to the *xy* plane (intralayer) is two orders of magnitude greater than along the *z* axis (interlayer) at 600 °C. The Arrhenius curves show clear changes in activation energies at the phase-transition temperature, along with jumps in conductivity.[160] By substituting V^{5+} with M^{y+} in $Bi_2V_{1-x}M_xO_{5.5-(2.5-y/2)x}$, a series of materials known as BIMEVOX are produced. These BIMEVOX materials stabilise the highly-conductive γ-phase to lower temperatures, making them potentially useful as electrolyte materials in low-temperature (300 to 500 °C) SOFCs.

The choice of M^{y+} dopant and level of V^{5+} substitution affects which phase is stable at room temperature, α, β, or γ. Al-Alas *et al.* report that the γ-phase for $Bi_2V_{1-x/2}Cd_{x/2}O_{5.5-(3x)/4}$ (x = 0 to 0.25) is only stable at room temperature when $x \geq 0.175$, with compositions with lower levels of substitution showing evidence of $\alpha \leftrightarrow \beta \leftrightarrow \gamma$ phase transitions on heating.[159] In the $Bi_2Cu_{0.1-x}Mg_xV_{0.9}O_{5.35}$ (x = 0 to 0.1) series, Beg *et al.* found that the γ-phase is only stable at room temperature when x ≥ 0.06.[158] Both groups found that these room-temperature tetragonal structures are actually incommensurate γ'-phases, with the materials undergoing order-disorder phase transitions of the oxygen vacancies at ~450 °C to the commensurate γ-phase.[159, 161] This order-disorder transition can also be found in $Bi_2V_{0.9}Nb_{0.1}O_{5.5}$, where a γ'-to-γ phase transition is observed at 445 °C, whereas $Bi_2V_{0.8}Nb_{0.2}O_{5.5}$ exists as the γ-phase at room temperature.[162]

High levels of oxide-ion conductivity are reported for a wide range of M^{y+} dopants in BIMEVOX materials. For $Bi_2V_{0.7}Sb_{0.3}O_{5.5}$[163] and $Bi_2V_{0.7}Nb_{0.3}O_{5.5}$,[162] conductivities of 1×10^{-1} Scm^{-1} and ~4.4×10^{-3} Scm^{-1} are reported at 500 °C respectively. However, the highest conductivity was found for $Bi_2V_{0.8}Nb_{0.2}O_{5.5}$, with a conductivity of ~1.7×10^{-2} Scm^{-1} at 500 °C.[162] The decrease in conductivity with elevated levels of cation substitution is due to the formation of defect clusters.[164]

If M^{y+} (y < 5) cations are used, additional oxygen vacancies are introduced into the vanadate layers. High levels of conductivity are reported for $Bi_2V_{0.9}Fe_{0.1}O_{5.4}$ ($\sigma = 6.7 \times 10^{-2}$ Scm^{-1} at 650 °C),[165] $Bi_2V_{0.93}Ni_{0.07}O_{5.395}$ ($\sigma = 1 \times 10^{-1}$ Scm^{-1} at 500 °C),[166] and $Bi_2Cu_{0.1}V_{0.9}O_{5.35}$ (σ ~5.5×10^{-2} Scm^{-1} at 500 °C).[167] Under SOFC operating conditions, reduction of Cu-doped BIMEVOX occurs, with oxygen concentrations below 4×10^{-4} mol/dm^3 causing n-type electronic conduction.[9] Therefore, additional steps must be taken when designing BIMEVOX-based electrolytes for use in SOFCs, with techniques similar to those used to mitigate Bi^{3+} reduction in Bi_2O_3-based oxide-ion conductors being potentially applicable.

1.6 Overview of oxide-ion conductivity

Presented in Figure 1.11 is a selection of the different types of materials discussed in this review. A number of the materials do exhibit oxide ion conductivities in excess of the desired $\sigma = 1 \times 10^{-2}$ Scm^{-1} threshold value (dashed line in Figure 1.11) below 700 °C. However, these materials all have flaws associated with them which need to be addressed in the design of new electrolytes for the production of efficient and stable SOFCs. The potential electrolytes studied

in this thesis will be compared to the σ = 1 × 10^{-2} Scm^{-1} conductivity value, to assess their viability for use as electrolytes in SOFCs.

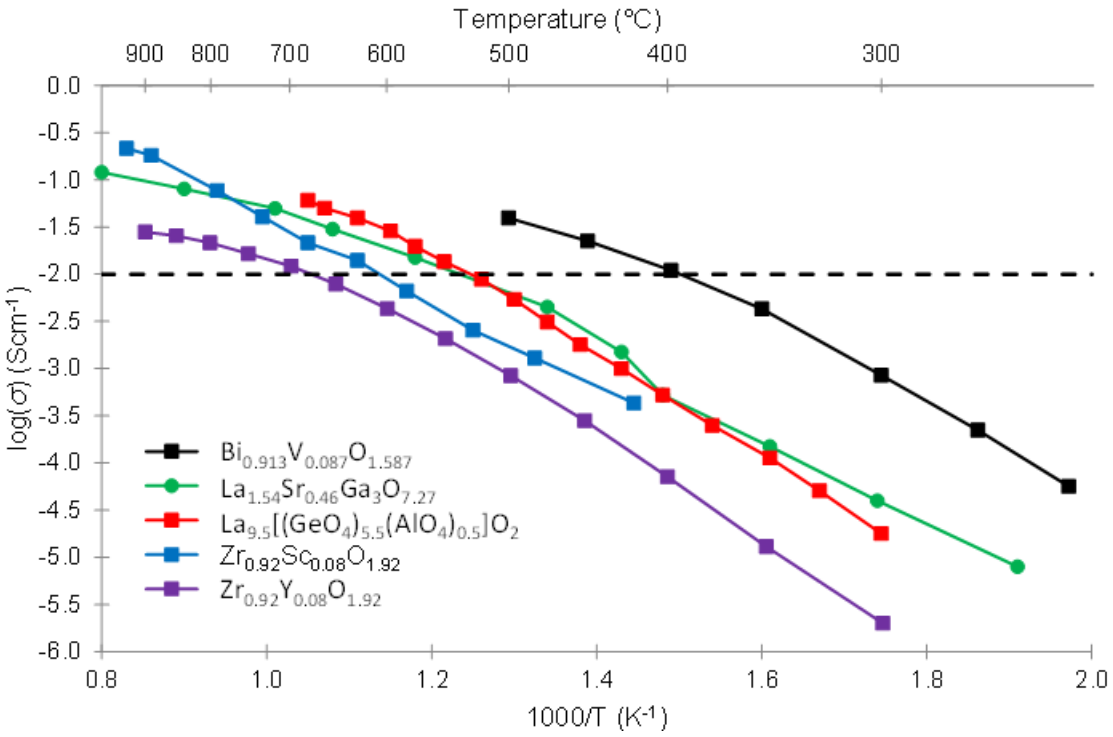

Figure 1.11: Oxide-ion conductivities as a function of temperature for a number of potential SOFC electrolyte materials: $Bi_{0.913}V_{0.087}O_{1.587}$,[109] melilite $La_{1.54}Sr_{0.46}Ga_3O_{7.27}$,[7] apatite $La_{9.5}[(GeO_4)_{5.5}(AlO_4)_{0.5}]O_2$,[47] scandia-stabilised zirconia $Zr_{0.92}Sc_{0.08}O_{1.92}$,[74] and yttria-stabilised zirconia $Zr_{0.92}Y_{0.08}O_{1.92}$.[44] The dashed line at log(σ) = –2 signifies the desired 1 × 10^{-2} Scm^{-1} conductivity threshold.

1.7 References

1. S. J. Skinner and J. A. Kilner, *Materials Today*, 2003, **6**, 30-37.
2. A. Chroneos, R. V. Vovk and I. L. Goulatis, *Monatshefte Fur Chemie*, 2012, **143**, 345-353.
3. I. R. Evans, J. A. K. Howard and J. S. O. Evans, *Chemistry of Materials*, 2005, **17**, 4074-4077.
4. X. Kuang, J. L. Payne, J. D. Farrell, M. R. Johnson and I. R. Evans, *Chemistry of Materials*, 2012, **24**, 2162-2167.
5. C. D. Ling, W. Miiller, M. R. Johnson, D. Richard, S. Rols, J. Madge and I. R. Evans, *Chemistry of Materials*, 2012, **24**, 4607-4614.
6. J. L. Payne, J. D. Farrell, A. M. Linsell, M. R. Johnson and I. R. Evans, *Solid State Ionics*, 2013, **244**, 35-39.
7. X. Kuang, M. A. Green, H. Niu, P. Zajdel, C. Dickinson, J. B. Claridge, L. Jantsky and M. J. Rosseinsky, *Nature Materials*, 2008, **7**, 498-504.
8. J. B. Goodenough, A. Manthiram, M. Paranthaman and Y. S. Zhen, *Materials Science and Engineering: B*, 1992, **12**, 357-364.
9. J. B. Goodenough, *Annual Review of Materials Research*, 2003, **33**, 91-128.
10. D. J. L. Brett, A. Atkinson, N. P. Brandon and S. J. Skinner, *Chemical Society Reviews*, 2008, **37**, 1568-1578.
11. F. Wei, T. Baikie, T. An, C. Kloc, J. Wei and T. White, *Inorganic Chemistry*, 2012, **51**, 5941-5949.

12. L. Malavasi, C. A. J. Fisher and M. S. Islam, *Chemical Society Reviews*, 2010, **39**, 4370-4387.

13. C. R. Xia and M. L. Liu, *Advanced Materials*, 2002, **14**, 521-523.

14. K. Kuroda, I. Hashimoto, K. Adachi, J. Akikusa, Y. Tamou, N. Komada, T. Ishihara and Y. Takita, *Solid State Ionics*, 2000, **132**, 199-208.

15. S. T. Norberg, S. Hull, I. Ahmed, S. G. Eriksson, D. Marrocchelli, P. A. Madden, P. Li and J. T. S. Irvine, *Chemistry of Materials*, 2011, **23**, 1356-1364.

16. J. Larminie, A. Dicks, J. Larminie and A. Dicks, in *Fuel Cell Systems Explained*, John Wiley & Sons, Ltd,. 2013, DOI: 10.1002/9781118878330.ch2, pp. 25-43.

17. T. Horita, D.-H. Cho, F. Wang, T. Shimonosono, H. Kishimoto, K. Yamaji, M. E. Brito and H. Yokokawa, *Solid State Ionics*, 2012, **225**, 151-156.

18. Y. Chen, W. Zhou, D. Ding, M. Liu, F. Ciucci, M. Tade and Z. Shao, *Advanced Energy Materials*, 2015, **5**, 1500537.

19. I. Yasuda and M. Hishinuma, *Electrochemistry*, 2000, **68**, 526-530.

20. B. Qian, Y. Chen, M. O. Tade and Z. Shao, *Journal of Materials Chemistry A*, 2014, **2**, 15078-15086.

21. T. Setoguchi, K. Okamoto, K. Eguchi and H. Arai, *Journal of the Electrochemical Society*, 1992, **139**, 2875-2880.

22. A. Orera and P. R. Slater, *Chemistry of Materials*, 2010, **22**, 675-690.

23. B. Novosel, M. Marinšek and J. Maček, *Journal of Fuel Cell Science and Technology*, 2012, **9**, 061003.

24. Z. Jamil, E. Ruiz-Trejo, P. Boldrin and N. P. Brandon, *International Journal of Hydrogen Energy*, 2016, **41**, 9627-9637.

25. M. Mogensen and K. Kammer, *Annual Review of Materials Research*, 2003, **33**, 321-331.

26. K. Zhang, J. Sunarso, Z. Shao, W. Zhou, C. Sun, S. Wang and S. Liu, *RSC Advances*, 2011, **1**, 1661-1676.

27. S. S. Hashim, A. R. Mohamed and S. Bhatia, *Renewable and Sustainable Energy Reviews*, 2011, **15**, 1284-1293.

28. Q. A. Islam, M. W. Raja and R. N. Basu, *International Journal of Hydrogen Energy*, 2016, **41**, 4682-4689.

29. Y. Lu, H. Zhao, X. Chang, X. Du, K. Li, Y. Ma, S. Yi, Z. Du, K. Zheng and K. Swierczek, *Journal of Materials Chemistry A*, 2016, **4**, 10454-10466.

30. A. Irimescu, G. Vasiu and G. T. Tordai, *Applied Energy*, 2014, **121**, 196-206.

31. M. M. Moser, C. H. Onder and L. Guzzella, *Sensors and Actuators B: Chemical*, 2014, **191**, 384-395.

32. J. A. Harris and N. Collings, *Sensors and Actuators B: Chemical*, 2015, **221**, 81-87.

33. T. J. White and Z. L. Dong, *Acta Crystallographica Section B*, 2003, **59**, 1-16.

34. L. Leon-Reina, M. C. Martin-Sedeno, E. R. Losilla, A. Cabeza, M. Martinez-Lara, S. Bruque, F. M. B. Marques, D. V. Sheptyakov and M. A. G. Aranda, *Chemistry of Materials*, 2003, **15**, 2099-2108.

35. P. Alberius-Henning, E. Adolfsson, J. Grins and A. Fitch, *Journal of Materials Science*, 2001, **36**, 663-668.

36. T. Baikie, P. H. J. Mercier, M. M. Elcombe, J. Y. Kim, Y. Le Page, L. D. Mitchell, T. J. White and P. S. Whitfield, *Acta Crystallographica Section B*, 2007, **63**, 251-256.

37. E. Kendrick and P. R. Slater, *Materials Research Bulletin*, 2008, **43**, 2509-2513.

38. S. S. Pramana, W. T. Klooster and T. J. White, *Acta Crystallographica Section B*, 2007, **63**, 597-602.

39. P. E. Mackie, J. C. Elliot and R. A. Young, *Acta Crystallographica Section B*, 1972, **28**, 1840-1848.

40. Y. Suetsugu and J. Tanaka, *Journal of Materials Science: Materials in Medicine*, 2002, **13**, 767-772.

41. J. E. H. Sansom, D. Richings and P. R. Slater, *Solid State Ionics*, 2001, **139**, 205-210.

42. M. S. Islam, J. R. Tolchard and P. R. Slater, *Chemical Communications*, 2003, 1486-1487.

43. L. Leon-Reina, E. R. Losilla, M. Martinez-Lara, S. Bruque and M. A. G. Aranda, *Journal of Materials Chemistry*, 2004, **14**, 1142-1149.

44. L. Leon-Reina, E. R. Losilla, M. Martinez-Lara, S. Bruque, A. Llobet, D. V. Sheptyakov and M. A. G. Aranda, *Journal of Materials Chemistry*, 2005, **15**, 2489-2498.

45. R. Ali, M. Yashima, Y. Matsushita, H. Yoshioka, K. Ohoyama and F. Izumi, *Chemistry of Materials*, 2008, **20**, 5203-5208.

46. J. R. Tolchard and P. R. Slater, *Journal of Physics and Chemistry of Solids*, 2008, **69**, 2433-2439.

47. L. Leon-Reina, E. R. Losilla, M. Martinez-Lara, M. C. Martin-Sedeno, S. Bruque, P. Nunez, D. V. Sheptyakov and M. A. G. Aranda, *Chemistry of Materials*, 2005, **17**, 596-600.

48. L. Leon-Reina, J. M. Porras-Vazquez, E. R. Losilla and M. A. G. Aranda, *Solid State Ionics*, 2006, **177**, 1307-1315.

49. L. Leon-Reina, J. M. Porras-Vazquez, E. R. Losilla and M. A. G. Aranda, *Journal of Solid State Chemistry*, 2007, **180**, 1250-1258.

50. E. Kendrick, A. Orera and P. R. Slater, *Journal of Materials Chemistry*, 2009, **19**, 7955-7958.

51. J. R. Tolchard, M. S. Islam and P. R. Slater, *Journal of Materials Chemistry*, 2003, **13**, 1956-1961.

52. K. Imaizumi, K. Toyoura, A. Nakamura and K. Matsunaga, *Journal of Physics: Condensed Matter*, 2015, **27**, 365601.

53. K. Imaizumi, K. Toyoura, A. Nakamura and K. Matsunaga, *Solid State Ionics*, 2014, **262**, 512-516.

54. E. Béchade, O. Masson, T. Iwata, I. Julien, K. Fukuda, P. Thomas and E. Champion, *Chemistry of Materials*, 2009, **21**, 2508-2517.

55. B. J. Corrie, J. F. Shin, S. Hull, K. S. Knight, M. C. Vlachou, J. V. Hanna and P. R. Slater, *Dalton Transactions*, 2016, **45**, 121-133.

56. T. An, T. Baikie, A. Orera, R. O. Piltz, M. Meven, P. R. Slater, J. Wei, M. L. Sanjuán and T. J. White, *Journal of the American Chemical Society*, 2016, **138**, 4468-4483.

57. E. Kendrick, M. S. Islam and P. R. Slater, *Journal of Materials Chemistry*, 2007, **17**, 3104-3111.

58. J. McFarlane, S. Barth, M. Swaffer, J. E. H. Sansom and P. R. Slater, *Ionics*, 2002, **8**, 149-154.

59. P. R. Slater and J. E. H. Sansom, *Solid State Phenomena*, 2003, **90-91**, 195-200.

60. H. Arikawa, H. Nishiguchi, T. Ishihara and Y. Takita, *Solid State Ionics*, 2000, **136**, 31-37.

61. R. D. Shannon, *Acta Crystallographica Section A*, 1976, **32**, 751-767.

62. H. Li, T. Baikie, S. S. Pramana, J. F. Shin, P. J. Keenan, P. R. Slater, F. Brink, J. Hester, T. An and T. J. White, *Inorganic Chemistry*, 2014, **53**, 4803-4812.

63. S. Nakayama, A. Ikesue, Y. Higuchi, M. Sugawara and M. Sakamoto, *Journal of the European Ceramic Society*, 2013, **33**, 207-210.

64. H. Li, T. Baikie, S. S. Pramana, J. F. Shin, P. R. Slater, F. Brink, J. Hester, K. Wallwork and T. J. White, *Journal of Materials Chemistry*, 2012, **22**, 2658-2669.

65. D. Kioupis and G. Kakali, *Ceramics International*, 2016, **42**, 9640-9647.

66. J. Xiang, Z.-G. Liu, J.-H. Ouyang and F.-Y. Yan, *Journal of Power Sources*, 2014, **251**, 305-310.

67. D. Marrero-Lopez, L. dos Santos-Gomez, L. Leon-Reina, J. Canales-Vazquez and E. R. Losilla, *J. Power Sources*, 2014, **245**, 107-118.

68. D. Marrero-Lopez, M. C. Martin-Sedeno, J. C. Ruiz-Morales, P. Nunez and J. R. Ramos-Barrado, *Materials Research Bulletin*, 2010, **45**, 409-415.

69. J. E. H. Sansom and P. R. Slater, *Solid State Ionics*, 2004, **167**, 23-27.

70. D. K. Smith and H. W. Newkirk, *Acta Crystallographica*, 1965, **18**, 983-991.

71. H. A. Abbas, F. F. Hamad, A. K. Mohamad, Z. M. Hanafi and M. Kilo, *Diffusion Fundamentals*, 2007, **8**, 7.1-7.8.

72. J. W. Fergus, *Journal of Power Sources*, 2006, **162**, 30-40.

73. L. Minervini, M. O. Zacate and R. W. Grimes, *Solid State Ionics*, 1999, **116**, 339-349.

74. O. Yamamoto, Y. Arati, Y. Takeda, N. Imanishi, Y. Mizutani, M. Kawai and Y. Nakamura, *Solid State Ionics*, 1995, **79**, 137-142.

75. K. Nomura, Y. Mizutani, M. Kawai, Y. Nakamura and O. Yamamoto, *Solid State Ionics*, 2000, **132**, 235-239.

76. A. C. Muller, A. Weber, D. Herbstritt and E. Ivers-Tiffee, *Long term stability of yttria and scandia doped zirconia electrolytes*, Electrochemical Society Inc., Pennington, 2003.

77. S. Dikmen, P. Shuk, M. Greenblatt and H. Gocmez, *Solid State Sciences*, 2002, **4**, 585-590.

78. B. C. H. Steele, *Solid State Ionics*, 2000, **129**, 95-110.

79. N. Jaiswal, S. Upadhyay, D. Kumar and O. Parkash, *Journal of Power Sources*, 2013, **222**, 230-236.

80. H. Inaba and H. Tagawa, *Solid State Ionics*, 1996, **83**, 1-16.

81. Y. Tsung-Her and C. Chen-Chia, *Physica Scripta*, 2007, **2007**, 303.

82. S. Omar, E. D. Wachsman and J. C. Nino, *Applied Physics Letters*, 2007, **91**, 144106.

83. K. Eguchi, T. Setoguchi, T. Inoue and H. Arai, *Solid State Ionics*, 1992, **52**, 165-172.

84. V. V. Kharton, A. P. Viskup, F. M. Figueiredo, E. N. Naumovich, A. L. Shaulo and F. M. B. Marques, *Materials Letters*, 2002, **53**, 160-164.

85. J. Qian, Z. Tao, J. Xiao, G. Jiang and W. Liu, *International Journal of Hydrogen Energy*, 2013, **38**, 2407-2412.

86. H. A. Harwig, *Zeitschrift Fur Anorganische Und Allgemeine Chemie*, 1978, **444**, 151-166.

87. H. A. Harwig and A. G. Gerards, *Thermochimica Acta*, 1979, **28**, 121-131.

88. N. Cornei, N. Tancret, F. Abraham and O. Mentré, *Inorganic Chemistry*, 2006, **45**, 4886-4888.

89. T. Takahashi and H. Iwahara, *Materials Research Bulletin*, 1978, **13**, 1447-1453.

90. N. A. S. Webster, C. D. Ling, C. L. Raston and F. J. Lincoln, *Solid State Ionics*, 2007, **178**, 1451-1457.

91. K. Koto, H. Mori and Y. Ito, *Solid State Ionics*, 1986, **18–19, Part 2**, 720-724.

92. Y. Ito, T. Mukoyama, H. Mori and K. Koto, *Solid State Ionics*, 1995, **79**, 81-83.

93. K. Sooryanarayana, R. Somashekar and T. N. Guru Row, *Solid State Ionics*, 1997, **104**, 319-324.

94. H.-Y. Chen and A. W. Sleight, *Journal of Solid State Chemistry*, 1986, **63**, 70-75.

95. W. Zhou, D. A. Jefferson and J. M. Thomas, *Proceedings of the Royal Society of London Series a-Mathematical Physical and Engineering Sciences*, 1986, **406**, 173-182.

96. C. D. Ling, R. L. Withers, S. Schmid and J. G. Thompson, *Journal of Solid State Chemistry*, 1998, **137**, 42-61.

97. G. A. Lovas, I. Dódony, L. Pöppl and Z. Szaller, *Journal of Solid State Chemistry*, 1998, **135**, 175-181.

98. T. Takahashi, H. Iwahara and T. Esaka, *Journal of the Electrochemical Society*, 1977, **124**, 1563-1569.

99. M. Takahashi and H. Iwahara, *Journal of Applied Electrochemistry*, 1973, **3**, 65-72.

100. X. L. Chen, F. F. Zhang, Y. M. Shen, J. K. Liang, W. H. Tang and Q. Y. Tu, *Journal of Solid State Chemistry*, 1998, **139**, 398-403.

101. I. Abrahams, A. J. Bush, S. C. M. Chan, F. Krok and W. Wrobel, *Journal of Materials Chemistry*, 2001, **11**, 1715-1721.

102. M. Valant and D. Suvorov, *Journal of the American Ceramic Society*, 2001, **84**, 2900-2904.

103. F. E. N. Ramirez, E. E. Espinosa, L. S. Pedroza and J. A. Souza, *Journal of Materials Science*, 2016, **51**, 10982-10989.

104. R. W. Wolfe, R. E. Newnahm and M. I. Kay, *Solid State Communications*, 1969, **7**, 1797-1801.

105. K. Sooryanarayana, T. N. G. Row and K. B. R. Varma, *Materials Research Bulletin*, 1997, **32**, 1651-1656.

106. R. Miida and M. Tanaka, *Japanese Journal of Applied Physics Part 1*, 1990, **29**, 1132-1138.

107. C. D. Ling, S. Schmid, P. E. R. Blanchard, V. Petricek, G. J. McIntyre, N. Sharma, A. Maljuk, A. A. Yaremchenko, V. V. Kharton, M. Gutmann and R. L. Withers, *Journal of the American Chemical Society*, 2013, **135**, 6477-6484.

108. C. D. Ling and M. R. Johnson, *Journal of Solid State Chemistry*, 2004, **177**, 1838-1846.

109. X. Kuang, J. L. Payne, M. R. Johnson and I. R. Evans, *Angewandte Chemie-International Edition*, 2012, **51**, 690-694.

110. W. Zhou, *Journal of Solid State Chemistry*, 1994, **108**, 381-394.

111. A. Watanabe, N. Ishizawa and M. Kato, *Journal of Solid State Chemistry*, 1985, **60**, 252-257.

112. N. Sharma, R. B. Macquart, M. Avdeev, M. Christensen, G. J. McIntyre, Y. S. Chen and C. D. Ling, *Acta Crystallographica Section B*, 2010, **66**, 165-172.

113. W. Zhou, *Journal of Solid State Chemistry*, 1988, **76**, 290-300.

114. T. E. Crumpton, M. G. Francesconi and C. Greaves, *Journal of Solid State Chemistry*, 2003, **175**, 197-206.

115. P. J. Bereciartua, F. J. Zuniga, J. M. Perez-Mato, V. Petricek, E. Vila, A. Castro, J. Rodriguez-Carvajal and S. Doyle, *Acta Crystallographica Section B*, 2012, **68**, 323-340.

116. N. Sharma, R. B. Macquart, M. Christensen, M. Avdeev, Y.-S. Chen and C. D. Ling, *Journal of Solid State Chemistry*, 2009, **182**, 1312-1318.

117. A. A. Yaremchenko, V. V. Kharton, E. N. Naumovich and A. A. Vecher, *Journal of Solid State Electrochemistry*, 1998, **2**, 146-149.

118. C.-Y. Hsieh and K.-Z. Fung, *Journal of Solid State Electrochemistry*, 2009, **13**, 951-957.

119. N. M. Sammes, G. A. Tompsett, H. Nafe and F. Aldinger, *Journal of the European Ceramic Society*, 1999, **19**, 1801-1826.

120. M. L. Tate, J. Hack, X. Kuang, G. J. McIntyre, R. L. Withers, M. R. Johnson and I. Radosavljevic Evans, *Journal of Solid State Chemistry*, 2015, **225**, 383-390.

121. R. Punn, A. M. Feteira, D. C. Sinclair and C. Greaves, *Journal of the American Chemical Society*, 2006, **128**, 15386-15387.

122. C. H. Hervoches and C. Greaves, *Journal of Materials Chemistry*, 2010, **20**, 6759-6763.

123. D. W. Jung, K. T. Lee and E. D. Wachsman, *Journal of the Korean Ceramic Society*, 2014, **51**, 260-260.

124. H. Kruidhof, K. J. De Vries and A. J. Burggraaf, *Solid State Ionics*, 1990, **37**, 213-215.

125. H. Kruidhof, H. J. M. Bouwmeester, K. J. de Vries, P. J. Gellings and A. J. Burggraaf, *Solid State Ionics*, 1992, **50**, 181-186.

126. P. J. Dordor, J. Tanaka and A. Watanabe, *Solid State Ionics*, 1987, **25**, 177-181.

127. E. D. Wachsman and K. L. Duncan, *Ceria/bismuth oxide bilayered electrolytes for low temperature solid oxide fuel cells*, Electrochemical Society Inc, Pennington, 1999.

128. S. H. Chan, X. J. Chen and K. A. Khor, *Solid State Ionics*, 2003, **158**, 29-43.

129. Y.-C. Tu, C.-Y. Chang, M.-C. Wu, J.-J. Shyue and W.-F. Su, *RSC Advances*, 2014, **4**, 19925-19931.

130. J. S. Ahn, M. A. Camaratta, D. Pergolesi, K. T. Lee, H. Yoon, B. W. Lee, D. W. Jung, E. Traversa and E. D. Wachsman, *Journal of the Electrochemical Society*, 2010, **157**, B376-B382.

131. J. Y. Park, H. Yoon and E. D. Wachsman, *Journal of the American Ceramic Society*, 2005, **88**, 2402-2408.

132. J. Hou, L. Bi, J. Qian, Z. Zhu, J. Zhang and W. Liu, *Journal of Materials Chemistry A*, 2015, **3**, 10219-10224.

133. K. T. Lee and E. D. Wachsman, *Science*, 2011, **334**, 935-939.

134. E. D. Wachsman, P. Jayaweera, N. Jiang, D. M. Lowe and B. G. Pound, *Journal of the Electrochemical Society*, 1997, **144**, 233-236.

135. A. L. Ruth, K. T. Lee, M. Clites and E. D. Wachsman, *ECS Transactions*, 2014, **64**, 135-141.

136. D. W. Jung, K. T. Lee and E. D. Wachsman, *Journal of the Electrochemical Society*, 2016, **163**, F411-F415.

137. D. W. Joh, J. H. Park, D. Y. Kim, B.-H. Yun and K. T. Lee, *Journal of Power Sources*, 2016, **320**, 267-273.

138. P. Lacorre, F. Goutenoire, O. Bohnke, R. Retoux and Y. Laligant, *Nature*, 2000, **404**, 856-858.

139. F. Goutenoire, O. Isnard, R. Retoux and P. Lacorre, *Chemistry of Materials*, 2000, **12**, 2575-2580.

140. L. Malavasi, H. Kim, S. J. L. Billinge, T. Proffen, C. Tealdi and G. Flor, *Journal of the American Chemical Society*, 2007, **129**, 6903-6907.

141. O. A. Alekseeva, I. A. Verin, N. I. Sorokina, N. E. Novikova, D. S. Kolesnikova and V. I. Voronkova, *Crystallography Reports*, 2010, **55**, 199-205.

142. G. Corbel, P. Durand and P. Lacorre, *Journal of Solid State Chemistry*, 2009, **182**, 1009-1016.

143. T. Paul and A. Ghosh, *Journal of Applied Physics*, 2016, **119**, 065104.

144. T. Paul and A. Ghosh, *Journal of Applied Physics*, 2013, **114**, 164101.

145. G. Corbel, E. Suard and P. Lacorre, *Chemistry of Materials*, 2011, **23**, 1288-1298.

146. G. Corbel, A. Selmi, E. Suard and P. Lacorre, *Chemistry of Materials*, 2014, **26**, 6838-6851.

147. D. Marrero-López, J. C. Ruiz-Morales, D. Pérez-Coll, P. Núñez, J. C. C. Abrantes and J. R. Frade, *Journal of Solid State Electrochemistry*, 2004, **8**, 638-643.

148. J. E. Vega-Castillo, U. K. Ravella, G. Corbel, P. Lacorre and A. Caneiro, *Dalton Transactions*, 2012, **41**, 7266-7271.

149. G. Buvat, E. Quarez and O. Joubert, *Journal of Power Sources*, 2016, **302**, 107-113.

150. F. Wei, H. Gasparyan, P. J. Keenan, M. Gutmann, Y. Fang, T. Baikie, J. B. Claridge, P. R. Slater, C. L. Kloc and T. J. White, *Journal of Materials Chemistry A*, 2015, **3**, 3091-3096.

151. A. Mancini, C. Tealdi and L. Malavasi, *International Journal of Hydrogen Energy*, 2012, **37**, 8073-8080.

152. B. Liu, D. Ding, Z. Liu, F. Chen and C. Xia, *Solid State Ionics*, 2011, **191**, 68-72.

153. H. J. Park, T.-G. Kim, C. Kwak, D. W. Jung, S. Lee and K. H. Lee, *Journal of Power Sources*, 2015, **275**, 884-887.

154. C. Tealdi, P. Mustarelli and M. S. Islam, *Advanced Functional Materials*, 2010, **20**, 3874-3880.

155. J. Xu, X. Kuang, E. Véron, M. Allix, M. R. Suchomel, F. Porcher, C. Liang, F. Pan and M. Wu, *Inorganic Chemistry*, 2014, **53**, 11589-11597.

156. R. N. Vannier, G. Mairesse, F. Abraham, G. Nowogrocki, E. Pernot, M. Anne, M. Bacmann, P. Strobel and J. Fouletier, *Solid State Ionics*, 1995, **78**, 183-189.

157. A. D. Rae, J. G. Thompson and R. L. Withers, *Acta Crystallographica Section B*, 1991, **47**, 870-881.

158. S. Beg, S. Hafeez and N. A. S. Al-Areqi, *Solid State Ionics*, 2014, **261**, 125-130.

159. A. Al-Alas, S. Beg and N. A. S. Al-Areqi, *Materials Chemistry and Physics*, 2012, **136**, 15-20.

160. S.-K. Kim and M. Miyayama, *Solid State Ionics*, 1997, **104**, 295-302.

161. S. Beg, A. Al-Alas and N. A. S. Al-Areqi, *Mater. Chem. Phys.*, 2010, **124**, 305-311.

162. D. S. Khaerudini, G. Guan, P. Zhang and A. Abudula, *Ionics*, 2016, **22**, 93-97.

163. O. Joubert, A. Jouanneaux, M. Ganne, R. N. Vannier and G. Mairesse, *Solid State Ionics*, 1994, **73**, 309-318.

164. R. Kant, K. Singh and O. P. Pandey, *International Journal of Hydrogen Energy*, 2008, **33**, 455-462.

165. A. Cherrak, R. Hubaut, Y. Barbaux and G. Mairesse, *Catalysis Letters*, 1992, **15**, 377-383.

166. E. Pernot, M. Anne, M. Bacmann, P. Strobel, J. Fouletier, R. N. Vannier, G. Mairesse, F. Abraham and G. Nowogrocki, *Solid State Ionics*, 1994, **70–71, Part 1**, 259-263.

167. S. P. Simner, D. SuarezSandoval, J. D. Mackenzie and B. Dunn, *Journal of the American Ceramic Society*, 1997, **80**, 2563-2568.

2 Experimental methods

2.1 Synthetic methods

2.1.1 Fundamentals of solid-state synthesis

Solid-state synthesis occurs via chemical diffusion of the reagent atoms, with ions substituting across a compositional gradient using vacant lattice and interstitial sites, whilst maintaining overall charge neutrality. Factors aiding the transfer of reagents through the reagent mixture include: large areas of reagent particulate contact, small diffusion path lengths, and minimum pore volume.[1] It is therefore helpful to use powdered reagents, which are finely ground together, and then pressed into pellets. Whilst this will increase the areas of particulate contact, cold pressing will still leave pellets porous.[2]

To illustrate the primary pathway involved in a solid state reaction, consider the following reaction:

$$AO_{(s)} + B_2O_{3(s)} \rightarrow AB_2O_{4(s)} \qquad \text{Equation 2.1}$$

In this reaction, the A^{2+} and B^{3+} cations will be responsible for the transfer of mass to form the final compound, with O^{2-} acting as a fixed reference. Initially, nucleation will occur between the AO and B_2O_3 reagents, forming the AB_2O_4 compound. This nucleation point will then act as a boundary between the two reagent sites, resulting in the A^{2+} and B^{3+} cations needing to diffuse across the phase boundaries into the compound phase, in addition to diffusing through the product phase. Difficulties in nucleation can occur if the reactant and product phases possess different structure types, due to the large amount of atomic reorganisation required to form the products. Due to the slow rate of solid state diffusion, high temperatures are employed to provide sufficient thermal energy to the chemical ions to travel from the lattice sites in the reagents and diffuse through the reactant and product phases to form crystalline products.

2.1.2 Solid-state synthesis

In this work, stoichiometric quantities of the required reagents were weighed to within ± 0.0001 g, then ground together in an agate mortar and pestle. If hygroscopic reagents were used, they were heated initially at a high temperature to ensure that no water was present. The homogeneous precursor powders were then either loaded into alumina or platinum crucibles, or pressed into pellets prior to loading. The filled crucibles were then heated in a furnace for the length of time given for each system in the relevant chapter.

If water-quenching was required to cool the product, the crucible was removed from the furnace with a pair of tongs and then immersed in water. When quenching the samples, welding goggles were worn when operating at furnace temperatures in excess of 800 °C, to prevent damage to the eyes due to ultraviolet radiation emission by the heating elements of the furnace.

2.1.3 Single-crystal growth

Growth of single-crystal samples has been carried out using a floating-zone furnace (FZF) at the University of Sydney. This piece of equipment houses a series of four mirrored lamps surrounding a central zone (hot zone) onto which focussed heating is applied. High density rods of powdered sample are passed through this zone to form a single crystal rod. For this synthetic technique, large quantities (~8 cm^3) of powdered sample are synthesised initially via the solid-state synthetic method described in Section 2.1.2. The product is then divided equally into two cylindrical balloons (to form the feed and seed rods) and a vacuum applied to remove any air, before pressing in a hydrostatic press. The rods are then extracted from the balloons, and sintered in alumina crucibles, creating rods of high density.

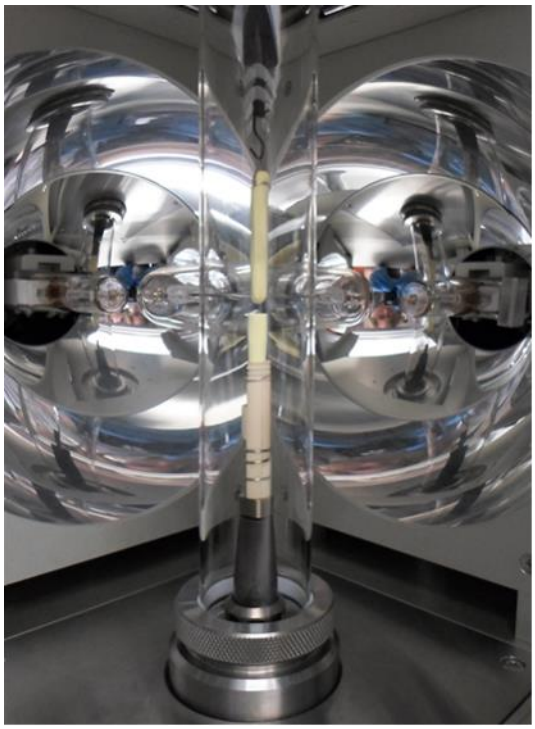

Figure 2.1: The feed and seed rods mounted within the furnace cavity along the vertical axis.

These rods are aligned along the central vertical axis of the furnace (Figure 2.1), so when they undergo rotation, there is a minimal risk of fracturing the newly formed single crystal due to misalignment. At the start of the experiment, both rods are counter-rotated and the tips of the lower (seed) rod and upper (feed) rod positioned to be in the hot zone of the furnace. During heating, once the tips of the rods begin to melt, the feed rod is lowered so the two molten regions touch.

Both rods are then programmed to lower through the hot zone of the furnace at a specified rate (up to several mm/hr depending on the material), allowing a single crystal to grow potentially onto the seed rod. The experiment is stopped once the majority of the feed rod has been depleted. The crystal grown is cut free from the remnants of the feed and seed rods once the rod has cooled.

2.2 Characterisation methods

2.2.1 Diffraction

Crystalline materials can be thought of as based on a regular repeating array of lattice points, all with identical environments. To build the entire crystal structure, motifs (atoms, ions or molecules) are associated with each lattice point. The smallest volume from which the crystal structure can be created through purely translational movements is called the unit cell.

A crystalline sample diffracts when the wavelength of the incoming radiation is of comparable size to the interatomic distances present within the sample, resulting in interference between electromagnetic waves scattered by individual atoms. This interference can be either constructive or destructive, with the constructively interfering waves creating the observable peaks in the diffraction pattern.

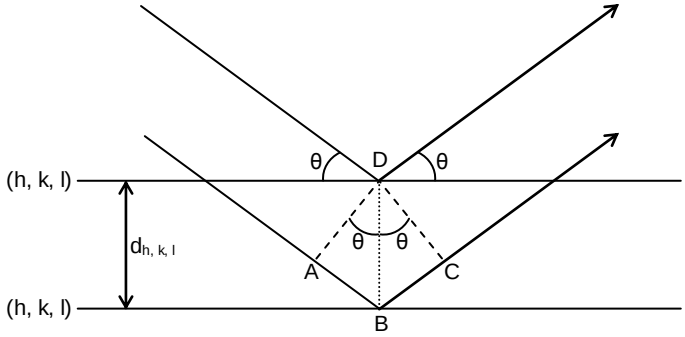

Figure 2.2: Visual representation of Bragg's Law. The length ABC is equal to 2*d*sin*θ*, and *h*, *k*, and *l* correspond to the Miller indices of the lattice plane.

The position of each (*hkl)* reflection can be expressed in terms of the *2θ* angle using Bragg's Law (see Equation 2.2 and Figure 2.2):

$$2d_{hkl}\sin\theta = \lambda \qquad \text{Equation 2.2}$$

where d_{hkl} is the interplanar spacing of lattice planes with identical (*hkl*) values, θ is the diffraction angle, and λ is the wavelength of radiation used during the diffraction experiment. If the angles of the unit cell (α, β, and γ) are all equal to 90 ° (for orthorhombic, tetragonal, and cubic systems), then the *d*-spacing can be found by the following equation:

$$\frac{1}{d_{hkl}} = \sqrt{\frac{h^2}{a^2} + \frac{k^2}{b^2} + \frac{l^2}{c^2}} \qquad \text{Equation 2.3}$$

where *a*, *b*, and *c* are the unit cell dimensions.

2.2.1.1 Powder X-ray diffraction

X-rays are electromagnetic waves with wavelengths in the region of 10 pm to 10 nm. This makes them ideal for use in diffraction experiments, as this wavelength range is comparable to interatomic separations. Powder X-ray diffraction involves the study of an essentially infinite number of crystallites, which all possess random orientations. Unlike in single crystal X-ray diffraction, powder diffraction produces cones of diffracted X-rays. A detector scans through an

arc, which intersects each cone at a single point, producing a one-dimensional diffraction pattern. This diffraction pattern contains peaks which overlap due to reflections from similar (or exactly equal) lattice plane *d*-spacings, and the intensities of the peaks are measured relative to the angle of diffraction (as 2θ).

For any crystal structure, the structure factor, F_{hkl}, can be written as:

$$F_{hkl} = \sum_{1}^{n} f_n e^{2\pi i(hx_n + ky_n + lz_n)} \qquad \text{Equation 2.4}$$

where the $e^{2\pi i(hx_n+ky_n+lz_n)}$ exponent contains the atomic fractional coordinates for an individual atom, *n*, within the sample, and f_n is the atomic scattering factor of atom *n*. The scattering factor of an atom, *f*, decreases with increasing scattering angle,[1] and, due to the X-rays being scattered by electrons, is also related to the number of electrons which the atom possesses.[2] The applied summation is over all atoms in the unit cell. The structure factor is related to the observed intensities, I_{hkl}, by the relationship:

$$I_{hkl} \propto |F_{hkl}|^2. \qquad \text{Equation 2.5}$$

To obtain a direct relationship corrections must be applied, including the scale, Lorentz polarisation factors, and the Debye-Waller factor.[1] A powder diffraction pattern is a superposition of these individual (*hkl*) peaks across a specific 2θ range, with each reflection having a separate peak position and width, and the integrated area under the peak equal to I_{hkl}.

2.2.1.2 Powder neutron diffraction

Tuning the energy which a neutron possesses will alter its wavelength, allowing it to have wavelengths similar to the interatomic distances in crystalline materials. Whilst the scattering of an X-ray beam depends on the atomic number, this is not the case with neutron scattering, due to the neutrons being scattered by the nucleus, and not the electrons. The result of this is that lighter elements can make a significant contribution to the neutron diffraction pattern, making neutron diffraction a viable technique for the accurate determination of, for example, oxygen atom positions in compounds containing heavy metals. Also, as the scattering lengths of adjacent elements in the Periodic Table can differ dramatically, this allows the atomic positions and other parameters of elements with similar X-ray atomic scattering factors to be determined more accurately.

2.2.1.3 Single-crystal Laue neutron diffraction

Single-crystal Laue neutron diffraction uses a polychromatic neutron beam – with a wavelength range of λ_{min} to λ_{max} and a wavelength-dependent intensity – to illuminate a fixed single-crystal sample. Data are recorded in two dimensions, allowing for symmetry-equivalent reflections to contribute to separate spot intensities, unlike for powder diffraction where there is overlap of symmetry-equivalent reflections as the data are recorded in a single dimension.

The use of a polychromatic beam, and a large solid angle of detection possible with high-efficiency image plate detectors gives gains in data collection efficiencies of several orders

of magnitude compared with conventional monochromatic single-crystal neutron diffraction.[3] Use of the reciprocal lattice is particularly useful in Laue diffraction. The reciprocal lattice vector, $\vec{g}$, is normal to a series of lattice planes (represented by the Miller indices, *hkl*, and shown in Figure 2.3), with the length of the vector described by the inverse of the distance between identical (*hkl*) lattice planes:

$$|\vec{g}| = \frac{1}{d_{hkl}} \qquad \text{Equation 2.6}$$

where:

$$\vec{g} = h\overrightarrow{a^*} + k\overrightarrow{b^*} + l\overrightarrow{c^*} \qquad \text{Equation 2.7}$$

and $\overrightarrow{a^*}, \overrightarrow{b^*}, \overrightarrow{c^*}$ are the three vectors in the reciprocal lattice: $\overrightarrow{a^*} = 2\pi\frac{\vec{b}\times\vec{c}}{V}$, $\overrightarrow{b^*} = 2\pi\frac{\vec{c}\times\vec{a}}{V}$, $\overrightarrow{c^*} = 2\pi\frac{\vec{a}\times\vec{b}}{V}$.

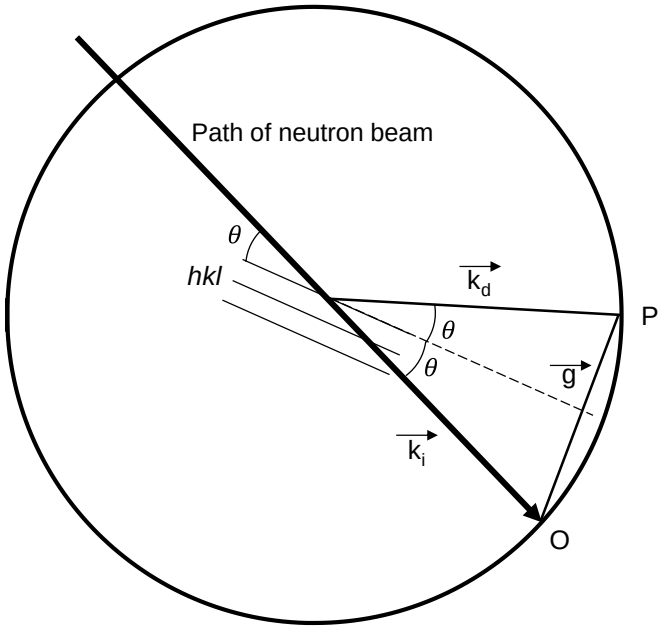

Figure 2.3: Graphical representation of the geometry of Bragg's Law upon an Ewald sphere. k_i is the direct beam vector, k_d is the diffracted beam vector, and *g* is the reciprocal lattice vector.

Diffraction occurs when one of the wavelengths of incoming radiation satisfies Bragg's Law for a lattice plane with Miller indices (*hkl*). The diffraction spot corresponding to that set of lattice planes is recorded on the Laue pattern at an angle where the Ewald sphere intersects the reciprocal lattice vector (P in Figure 2.3). Due to the polychromatic beam having a specific wavelength range, diffraction spots will be observed only on the collected pattern for reflections in the reciprocal lattice which are intersected between the Ewald spheres corresponding to λ_{min} and λ_{max} and contained within the limiting sphere of diffraction (denoted with 'X' marks in Figure 2.4). To provide as complete a sphere of data as possible, the sample is rotated around one axis between the collection of each Laue diffraction pattern.

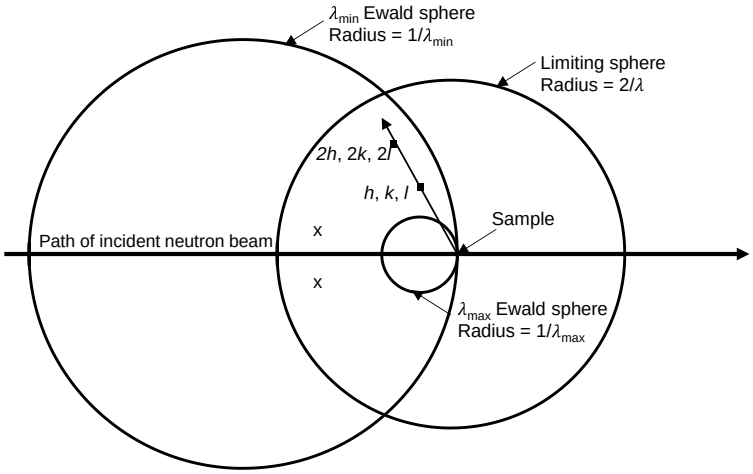

Figure 2.4: Diagram illustrating the area of the reciprocal lattice for which data can be collected, as denoted by the X symbols.

A problem with Laue diffraction is that a single Laue diffraction spot has the potential to contain information on a series of overlapping reflections, with between 10 to 20 % of data affected.[4] This can arise due to either harmonic overlap (Miller indices n*h*, n*k*, n*l*, where n is an integer) or spatial overlap of neighbouring reflections due to the size of the reflection spots on the image plates.

The observed diffraction spots are arranged along the circumference of ellipses, parabolas, and hyperbolae, where all spots on a single conic section correspond to reflections of planes which all possess the same zone axis. Neutron Laue diffractometers are located generally on neutron guides which give incident beams of low divergence. This, combined with the excellent resolution of charge-coupled devices (CCD) or image plate detectors, allows for separate integration of each spot. As not all diffraction spots are multiples, and spots are produced for lattice planes with the same (*hkl*) indices diffracting at different wavelengths in successive Laue patterns, a wavelength intensity profile can be refined, allowing the entire data set to be normalised to a common wavelength.

2.2.2 Neutron total-scattering analysis

Conventional diffraction methods are related to the study of the average structure of a crystalline material, which is contained within the Bragg peaks of a diffraction pattern. For total-scattering analysis, the information within the region between the Bragg peaks (diffuse scattering) is also included, therefore local-scale ordering can be studied by considering the pair-distribution functions.[5] Therefore, complete analysis of a disordered crystalline material can be achieved on both the local and average scales. Whilst there are different formalisms reported in the field of total scattering, the formalism presented by Keen in their review will be used here.[6]

In order for the details of the diffuse scattering to be accurate, the background being analysed must be corrected to include only information from the sample, and not from the sample environment. Therefore, prior to data collection on the sample, data must be collected

for an empty instrument (including a furnace if variable-temperature data are to be collected), a V rod, and an empty V sample can of the same dimensions as that used to contain the samples.

A total-scattering experiment measures all the scattering intensity of the analysed sample, allowing for *F(Q)*, the total scattering structure factor, to be obtained, where:

$$Q = \frac{4\pi sin\theta}{\lambda}$$ Equation 2.8

and:

$$F(Q) = \sum_{i,j=1}^{n} c_i c_j \bar{b_i} \bar{b_j} [A_{ij}(Q) - 1]$$ Equation 2.9

c_i and c_j represent the concentrations of atoms of type *i* and *j*, $\bar{b_i}$ and $\bar{b_j}$ are the coherent neutron scattering lengths of atoms *i* and *j*, and $A_{ij}(Q)$ are the Faber-Ziman partial structure factors.[7] By performing a Fourier transformation, *F(Q)* can be related to *G(r)*, the total radial distribution function (Equation 2.11).[5]

$$F(Q) = \rho_o \int_0^{\infty} 4\pi r^2 G(r) \frac{\sin(Qr)}{Qr} dr$$ Equation 2.10

$$G(r) = \frac{1}{(2\pi)^3 \rho_o} \int_0^{\infty} 4\pi Q^2 F(Q) \frac{\sin(Qr)}{Qr} dQ$$ Equation 2.11

ρ_o is the average atom number density, where $\rho_o = N/V$ (atoms Å^{-3}), *Q* represents the magnitude of the diffraction vector, and *r* is the interatomic distance for a specific pair of atoms. *G(r)* can also be defined in terms of the partial radial distribution functions, $g_{ij}(r)$:

$$G(r) = \sum_{i,j=1}^{n} c_i c_j \bar{b_i} \bar{b_j} (g_{ij}(r) - 1)$$ Equation 2.12

where $g_{ij}(r)$ is defined as:

$$g_{ij}(r) = \frac{n_{ij}(r)}{4\pi r^2 dr \rho_j}.$$ Equation 2.13

$g_{ij}(r)$ describes the probability of locating an atom with an interatomic distance *r* to *r*+d*r* to another atom, $n_{ij}(r)$ are the number of particles of type *j* between the distances *r* and *r*+d*r* from a particle of type *i*, and $\rho_j = c_j \rho_o$.[5]

A relationship can be drawn between *T(r)*, the total correlation function, and *G(r)*:

$$T(r) = 4\pi r \rho_o \left[G(r) + \left(\sum_{i=1}^{n} c_i \bar{b_i} \right)^2 \right]$$ Equation 2.14

A final relationship which can be drawn is between *F(Q)* and the normalised total scattering structure function, *S(Q)*:

$$S(Q) - 1 = \frac{F(Q)}{\sum_{i=1}^{n} \left(c_i \bar{b_i} \right)^2}$$ Equation 2.15

where the total-scattering cross section of the compound studied equals $4\pi \sum_{i=1}^{n} \left(c_i \bar{b_i} \right)^2$.[6]

For total-scattering analysis, experimental data sets of both *F(Q)* and *G(r)* are required, and the difference between these and the calculated *F(Q)* and *G(r)* data sets from the structural model are minimised through the use of Reverse Monte Carlo computer modelling techniques.[8]

2.2.3 Impedance spectroscopy

Impedance spectroscopy is used to measure the dielectric properties of a material as a function of the applied frequency. A variable single-frequency alternating voltage is applied to the sample, and the impedance measured as it passes through. As an alternating voltage is applied, an alternating response is expected from the sample, with an identical frequency to that of the initial frequency, but shifted in phase.

The initial voltage signal has the profile given by Equation 2.16, where V_o is the amplitude of the initial signal, V_t is the potential at time *t*, and ω is the angular frequency ($\omega = 2\pi f$).

$$V_t = V_o \sin(\omega t) \qquad \text{Equation 2.16}$$

Therefore the system will produce a current response in the following form, with ϕ representing the value of the phase shift:

$$I_t = I_o \sin(\omega t + \phi) \qquad \text{Equation 2.17}$$

By Ohm's Law, the magnitude of the impedance, *Z*, can be expressed as:

$$Z = \frac{V_t}{I_t} = \frac{V_o \sin(\omega t)}{I_o \sin(\omega t + \phi)} = Z_o \frac{\sin(\omega t)}{\sin(\omega t + \phi)} \qquad \text{Equation 2.18}$$

Using Euler's relationship, the impedance can be expressed as a complex function which can therefore be plotted:

$$Z(\omega) = Z_o(cos\phi + isin\phi) \qquad \text{Equation 2.19}$$

where $i = \sqrt{-1}$. The real and imaginary parts can be plotted on the *x* and *y* axes respectively in a Nyquist plot. The shape of the graph forms semicircles corresponding to different regions of the pelletised sample (see Figure 2.5).

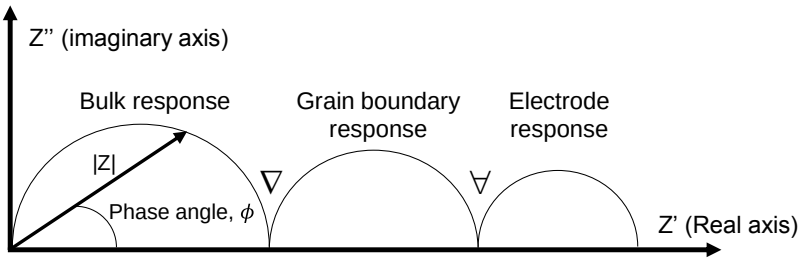

Figure 2.5: Nyquist plot illustrating the three different responses exhibited by a sample in impedance spectroscopy. The value of |*Z*| corresponds to Z_o in Equation 2.19.

Each point on the plotted curves corresponds to the impedance of the material at a given frequency. The conductivity of a compound at a given temperature is related to the low-frequency intercept of the semi-circle to the real (Z') axis corresponding to the bulk or grain-boundary resistance (∇ and $\forall$ respectively in Figure 2.5) by the following equation:

$$\sigma = \frac{1}{\rho} = \frac{l}{RA}$$ Equation 2.20

where ρ is the resistivity of the sample, R is the resistance obtained from the Nyquist plot, l is the thickness of the pellet, and A is the area of one circular face of the pellet.

2.3 Instrumentation

2.3.1 Laboratory diffractometers

2.3.1.1 Bruker AXS D8 Advance Diffractometers

Three Bruker D8 Advance diffractometers, known in Durham as the 'd7', 'd8', and 'd9', were used for collection of laboratory X-ray diffraction patterns throughout this work. All three diffractometers typically operate at 40 kV and 40 mA, and are controlled by the Bruker Diffrac+ XRD Commander software.[9]

The 'd7' and 'd9' diffractometers operate with identical setups, using a Cu tube to provide Cu $K_{\alpha 1,2}$ radiation (λ = 1.5406 Å and 1.5444 Å for $K_{\alpha 1}$ and $K_{\alpha 2}$ respectively), with a Ni filter to exclude K_β radiation. The X-rays emitted from the Cu tube pass through a series of Soller and variable divergence slits before reaching the sample. Variable divergence slits allow a constant area of sample to be illuminated by X-ray radiation during the data collection. The diffracted beam then reaches the Lynx Eye semiconductor strip detector (SSD), which detects X-rays as a function of 2θ.

Sample preparation for the 'd7' and 'd9' diffractometers involves grinding the sample to be analysed using an agate mortar and pestle. The ground powder is sieved onto a zero-background silicon slide covered in Vaseline®. The silicon slides are either placed into an aluminium holder in the case of the 'd9' diffractometer, or for the 'd7' diffractometer preloaded into circular plastic holders before the sample is applied.

The 'd8' diffractometer uses Cu K_α radiation, and is equipped with a Ni filter to remove Cu K_β radiation, and fixed Soller (2 °) and divergence slits (0.6 mm) to minimise beam divergence, before the diffracted X-ray beam reaches a Vantec linear position-sensitive detector (PSD), which can operate with a minimum step size of 0.0085 °. For *in situ* variable-temperature diffraction studies, an Anton Paar HTK1200 furnace was attached to the 'd8' diffractometer for all the studies contained within this report. A range of atmospheric conditions can be used with this furnace, but all studies in this report were performed in air. The operating temperature range of the furnace is between room temperature and 1100 °C. To obtain accurate values for the temperature of the furnace, a correction function was applied to all obtained temperature readings. This correction function was calculated by studying the thermal expansion of Al_2O_3,[10] and is given in Equation 2.21 below. T_{set} represents the furnace set temperature, whilst T_{corr} represents the corrected temperature applied to the sample.

$$T_{corr} = T_{set} + (aT_{set}^3 + bT_{set}^2 + cT_{set} + d)$$ Equation 2.21

The values of the coefficients in the polynomial are: a = 1.61 x 10^{-7} K^{-2}, b = –5.86 x 10^{-4} K^{-1}, c = 0.565, and d = –134 K.

Preparation of samples for use inside the furnace on the 'd8' diffractometer required two different methods, depending upon whether pelletised or sieved samples were being studied. For the sieved samples, the sample was ground in an agate mortar and pestle, sieved onto Vaseline® coated amorphous fused silica glass slides, and then mounted into an alumina sample holder. For the pelletised samples, the powdered sample was pressed in a 13 mm diameter press, then mounted directly onto the alumina sample holder. To ensure that the pellets and silica slides remained stationary throughout the diffraction experiments, vacuum grease was applied to the underside of the pellets and slides, to fix them to the alumina sample holder.

2.3.1.2 Measurement parameters

For characterisation of the samples presented in this report, the measurement parameters are given in Table 2.1. For routinely determining the purity of synthesised samples, ~30 minute scans from either the d7 or d9 diffractometers were used. For full structural characterisation work, long 11 hour scans from the d7 diffractometer were used. The d8 scans were used for *in situ* variable-temperature diffraction experiments.

Table 2.1: Powder X-ray diffraction parameters used for collecting room- and variable-temperature data. The XXXXX in the scan code is the identifying number for that particular data collection.

Instrument	Scan code	2θ range (°)	Step size (°)	No. of steps	Time/step (s)	Scan length
d7	d7_XXXXX	10–90	0.02049	3905	0.45	29 mins
d7	d7_XXXXX	10–120	0.02049	5370	7.25	11 hours
d8	d8_XXXXX	10–70	0.02077	2889	0.50	26 mins
d9	d9_XXXXX	10–90	0.02055	3894	0.45	29 mins

2.3.2 Time-of-flight neutron diffraction, ISIS spallation source

The High Resolution Powder Diffractometer (HRPD) and Polaris diffractometer described below are both neutron diffraction instruments at the ISIS spallation source of the Rutherford Appleton Laboratory. An ion source produces H^- ions, which are then accelerated by a linear accelerator towards the synchrotron ring. Before the H^- ions enter the ring, gold foil removes the electrons from the ions, leaving protons which then undergo further acceleration within the ring until they possess energies of ~800 MeV. The accelerated protons are then ejected from the synchrotron ring at a frequency of 50 Hz, where they collide with a tungsten target and produce neutrons via the spallation process through the interaction of tungsten nuclei and the incoming protons.

The neutron pulse is polychromatic, and is slowed to speeds where the wavelengths of the produced neutrons are useful for the study of crystalline solids by using moderators containing hydrogen atoms (e.g. H_2O or CH_4). The detectors of the various instruments at ISIS are arranged to cover fixed 2θ ranges, with different detector banks allowing for a wide 2θ range to be probed simultaneously.

The relationship between the wavelengths of the incoming neutrons and their time-of-flight can be calculated by rearranging the de Broglie relationship (see Equation 2.22):

$$\lambda = \frac{h}{p} = \frac{ht}{mL} \qquad \text{Equation 2.22}$$

where λ = neutron wavelength, h = Planck's constant, p = neutron momentum, t = neutron time-of-flight, m = neutron mass, and L = diffractometer path length.

2.3.2.1 High Resolution Powder Diffractometer (HRPD)

The High Resolution Powder Diffractometer (HRPD) at ISIS uses a 110 K CH_4 moderator to cool the fast spallation neutrons. Due to the depth of the moderator used to slow the neutrons, a 100 m long guide is required to reduce the ratio of the path length uncertainty relative to the overall path length for the diffractometer.[11] A result of the long neutron flight path is that 'frame overlap' occurs due to the 50 Hz frequency of the neutron pulses. Therefore, two disk choppers are situated between the CH_4 moderator and the sample to allow for operation at 5 or 10 Hz and negate the overlap effect.

HRPD contains three different detector banks: back-scattering (2θ = 160 to 176 °), 90 ° (2θ = 87 to 93 °), and low-angle scattering (2θ = 28 to 32 °).[11] Both the back-scattering and 90 ° banks use ZnS scintillator detectors, whilst the low angle bank contains ^{3}He detector tubes. The bank with highest resolution is the back-scattering bank, with a resolution of $\frac{\Delta d}{d}$ of 4 × 10^{-4} to 5 × 10^{-4}, an order of magnitude greater than the 90 ° bank, and two orders of magnitude greater than the low angle bank. The accessible range of d-spacing is 0.3 to 16.5 Å when analysing data from all three detector banks.[11]

For variable-temperature powder neutron diffraction data, a furnace with V windows was inserted into HRPD, into which samples could be placed. For the variable-temperature experiments, data collections with a total of 190 μAh (~5 hours) were carried out in the time-of-flight range from 30 to 130 ms. No sample environment was used for the room-temperature scans, and data for accurate structural characterisation were collected for ~15 hours in the 30 to 130 ms time-of-flight range. Samples were prepared for HRPD by grinding and loading into 8 or 11 mm diameter V cans to a depth of ~2 to 2.5 cm. V cans are used as sample containers for neutron diffraction experiments because V exhibits a low coherent neutron scattering length (–0.3824 fm).[12] In the data collected on the back-scattering detector bank, a small peak corresponding to the V can is observed primarily at a time of flight of ~104 ms.

2.3.2.2 Polaris diffractometer

The Polaris diffractometer was used for collecting total-scattering data. The moderator used for the slowing of fast neutrons is an ambient temperature water moderator, unlike the CH_4 moderator on HRPD. Also, as the entire diffraction pattern will be analysed during total-scattering studies and not just the Bragg peaks, the background needs to be minimised as much as possible. A nimonic (Ni, Cr, and additives) alloy chopper helps to stop fast neutrons and reduce the background by blocking the beamline as the protons hit the W target. The

inclusion of a radial collimator inside the sample chamber helps to reduce the background caused by the sample environment equipment.

The neutron flight path for Polaris is 14 m, resulting in a reduction in the resolution of the data compared with HRPD, due to the greater $\frac{\Delta t}{t}$ ratio. The detector banks on Polaris are comprised of ZnS scintillator strips, arranged from 2θ = 6 to 168 °. Whilst the resolution may not be as good as that for HRPD, the high neutron flux and access to short wavelengths (minimum wavelength of 0.3 Å) allow for a large value for Q_{max}, the scattering vector (Equation 2.8), to be obtained. It is this Q range which allows the Polaris diffractometer to produce high-quality outputs of Bragg and diffuse scattering, making it ideal for total-scattering diffraction studies. The total-scattering data collected for $Bi_{28}Re_2O_{49}$ were obtained for 150 μAh per run (~1 hour), with 12 runs performed at 14 °C, and 9 runs at 700 °C. The diffraction patterns collected on POLARIS follow the naming convention POLXXXXX_bY, where XXXXX is the identifying number for a particular data collection, and Y is the number of the detector bank.

2.3.3 Neutron diffraction, ACNS (formerly Bragg Institute), ANSTO

Both the ECHIDNA powder diffractometer and KOALA single-crystal diffractometer described below are located at the Australian Centre for Neutron Scattering (ACNS, formerly Bragg Institute) of the Australian Nuclear Science and Technology Organisation (ANSTO), Australia, receiving neutrons from the Open Pool Australian Lightwater (OPAL) reactor.

The 20 MW reactor operates through the fission of ^{235}U, and the reactor pool contains a zirconium alloy 'reflector' vessel filled with D_2O, which sits beneath the fuel assembly and maintains the fission reactions by reflecting neutrons back towards the fuel assemblies. So that neutrons reach the instruments in the reactor guide hall, thermal neutron guides extend outwards from the reactor core.

2.3.3.1 ECHIDNA high resolution neutron powder diffractometer

The ECHIDNA neutron powder diffractometer is situated at the end of a 58 m neutron guide. The incoming polychromatic neutron beam reaches initially a rotatable Ge monochromator, allowing a specific neutron wavelength to be selected using either the (331) [2.44 Å], (335) [1.62 Å], or (337) [1.30 Å] Ge reflection. The monochromatic neutron beam then reaches the sample, interacts with the atomic nuclei, and is scattered subsequently towards the detector bank.

The detector bank for ECHIDNA is comprised of 128 detector units, each consisting of a 5' collimator in front of a vertically-arranged linear position-sensitive ^3He detector tube, with the detector bank covering a 158.75 ° arc around the sample position.[13] The data collection process is stepped, with the detector undergoing rotation so the pattern can overlap in one or two detectors, to produce a more accurate intensity profile.

For variable-temperature powder neutron diffraction experiments, a vacuum furnace replaces the conventional sample stage in the path of the incoming monochromated neutron beam. Collected diffraction patterns contain a number of small peaks due to a contribution from

Nb present in the heating elements of the furnace, and so were included in any refinements performed using this data. Data collections were carried out for 1 to 8 hrs (depending on the material and whether the sample was being heated or cooled) across a 2θ range of 6.5 to 164 °. Samples were prepared for the ECHIDNA experiments by grinding and then placing in 6 or 9 mm diameter V cans to a depth of ~3 to 4 cm. The diffraction patterns collected on ECHIDNA follow the naming convention ECH00XXXXX, where XXXXX is the identifying number for a particular pattern.

2.3.3.2 KOALA single-crystal diffractometer

KOALA has a neutron-sensitive cylindrical image-plate detector, with the single crystal held stationary on the cylindrical axis whilst undergoing irradiation by the neutron beam. Unlike on ECHIDNA, the neutron beam used for KOALA experiments is polychromatic, which reduces both the time required for data collection and crystal size needed compared to monochromatic single-crystal neutron experiments.[14] Following each data collection, the detector is rotated on its axis and the collected diffraction information read by a translating laser and photomultiplier tube. The detector is vertical so a range of sample environments can be applied easily to the sample (e.g. cryostats, furnaces).

For the data collection on KOALA, single crystals are first screened, whereby diffraction patterns are collected for short periods of time (~5 to 10 minutes) for a range of different crystals (typically between 0.5 and 1.0 mm^3 in size) , before the highest-quality candidate is selected for a complete data collection cycle. During this screening, the most-intense peak is used to help calculate the collection times of the final patterns, as a compromise has to be made between obtaining data with peaks of high intensity whilst avoiding exceeding the 16-bit limit of the read-out electronics, which can cause inaccurate intensity information to be obtained. The sample rotation angle between pattern collections can be adjusted to suit the total collection time available, but is usually kept to between 10 and 20 °. As an example, a data collection was carried out on a bismuth vanadate single crystal; 8 samples were screened before one was selected, 22 patterns were collected with a crystal rotation of 9 ° between each collection, with a collection time of 40 mins per pattern.

2.3.4 Synchrotron X-ray diffraction, Australian Synchrotron

Synchrotrons are useful for diffraction experiments owing to the combination of tuneable wavelengths, high resolution, and high intensities. These factors combine to provide increased peak resolution compared to laboratory X-ray experiments, whilst also allowing detection of weak diffraction peaks. The synchrotron PXRD data presented within this work was collected at the Powder Diffraction beamline of the Australian Synchrotron.

A 500 MHz voltage is applied to an electron gun with a tungsten cathode which undergoes thermionic emission, generating bunches of electrons separated by 2 ns. These bunches are guided into a linear accelerator and accelerated to energies of 100 MeV over a distance of 10 m, then inserted into the booster ring to increase the energy to 3 GeV. Following this acceleration, the electrons are transferred to the storage ring, comprised of 14 identical sectors,

each formed from a combination of straight and curved sections containing bending magnets to keep the beam travelling around the ring. When the electron beam travels past a bending magnet the beam is deviated, causing synchrotron light to leave at a tangent to the beam path. Synchrotron light spans an energy range from the infrared to X-ray regions of the electromagnetic spectrum. This synchrotron light is then guided via a series of beamline optics (including focussing mirrors, monochromators, and horizontal and vertical slits) which select the specific energy of X-rays required, before they reach the end stations containing the experimental equipment.

2.3.4.1 Powder Diffraction beamline

The Powder Diffraction sample stage is located 24.4 m from a bending magnet within the synchrotron storage ring. A silicon monochromator is used to select X-rays of specific energies, thereby avoiding the fluorescence edges from elements present within the sample. The incoming X-rays are scattered by the sample and reach a Mythen microstrip detector, which covers an arc of 2θ = 80 °, separated into individual modules spanning approximately 2θ = 5 °. Owing to the design of the detector bank, data cannot be collected in the entire 2θ range, so a second pattern is collected with a 2θ = 0.5 ° offset. Once the experiment has ended, the two data files are combined using the PDViPer software,[15] producing a complete diffraction pattern.

For variable-temperature experiments, a hot air blower is mounted beneath the capillary to heat the sample region which is probed by the incoming X-rays. To prevent the rising heat from the hot air blower producing a higher background on the Mythen detector, a cold air stream is placed between the sample and detector to dissipate the hot air.

Experimental data were collected in capillary mode, with data collection times varying from 5 to 30 minutes depending upon the structural complexity of the sample, and the relative intensities of the structural features being probed (attempts to collect information on low-intensity diffraction peaks necessitated longer collection times). For room-temperature measurements, 0.2 mm diameter borosilicate capillaries were used, whilst 0.2 mm quartz capillaries were used for variable-temperature measurements, as the lower softening temperature of the borosilicate capillaries (820 °C versus 1730 °C for quartz) would have hindered data collection. The capillaries were filled to depths in excess of 1 cm, and aligned upon the instrument prior to data collection, so that the incoming X-ray beam came into contact with the sample.

2.3.5 Solartron 1260A impedance analyser

To obtain a pellet for impedance measurements, a quantity of the compound to be studied is pressed, then fired at the synthesis temperature of the compound for a length of time given in the relevant sections of this thesis. The sintered pellet is weighed, the dimensions measured with Vernier callipers, and then fixed to two platinum electrodes with a metallic paste suitable for the highest temperature being studied (gold or platinum paste for T < 500 °C or T < 800 °C respectively). The pellet is then fired in a furnace at either 500 °C or 800 °C (for gold and

platinum pastes respectively) for 30 minutes, to remove the organic components from the paste and provide a metallic attachment of the electrodes to the pellet.

To perform the impedance measurements, a Solartron 1260A impedance analyser was used, which measured the resistance of the compound as a function of temperature to five significant figures. To measure the temperature inside the furnace, an S-type thermocouple was positioned next to the pellet, to minimise errors in the temperature values obtained. The error of the recorded temperatures was taken to be ± 0.1 °C. To obtain the impedance of the sample at a given temperature, the intercept of the semicircle to the real (Z') axis corresponding to the bulk or grain boundary resistance was determined and recorded for each temperature measured.

2.4 Data analysis

2.4.1 Pawley fitting

Pawley fitting is a procedure in which the provision of the space group and approximate unit-cell parameters allow for the unit-cell parameters to be refined from powder data, without the need for structural information (atom types and positions).[16] From the supplied information, the *d*-spacings for allowed *hkl* reflections are calculated, and through refinement of the unit-cell parameters and intensities, seeks to minimise the difference between the observed and calculated diffraction patterns. Peak intensity is assigned solely on the basis of attempting to minimise the difference between the patterns, as there is no structural information to calculate the intensity. *TOPAS Academic* (henceforth called *Topas*) was used for all Pawley fits presented in this thesis,[17] with the *jEdit* software package utilised for editing the input files.[18]

2.4.2 Rietveld refinement

A Rietveld refinement is a procedure in which the difference between a calculated diffraction pattern (based on a structural model with refinable parameters) and an experimentally obtained diffraction pattern is minimised, through the use of a non-linear least squares minimisation routine.[19] A good starting model is required for the refinement to be successful, including information about the space group, lattice parameters, atom types, atomic coordinates, fractional occupancies, and a description of the peak shape for the sample being analysed. By refining this model, the disagreement between the observed and calculated diffraction patterns is minimised. The Rietveld refinement seeks to minimise the residual, S_y, given by the following equation:

$$S_y = \sum_i w_i \left(y_i(obs) - y_i(calc)\right)^2 \qquad \text{Equation 2.23}$$

where the weighting factor, $w_i = 1/y_i(obs)$, and $y_i(obs)$ and $y_i(calc)$ are the observed and calculated intensities at point *i*.

The refined parameters of a Rietveld refinement fall into two categories, global variables and sample-dependent variables. Global variables include: Chebyshev background parameters (based on Chebyshev polynomials),[20] Thompson-Cox-Hastings pseudo-Voigt peak-shape

function parameters,[21] and a zero-point error correction parameter. Refineable sample-dependent variables include: unit cell dimensions, scale factor, atomic displacement parameters, fractional occupancies, particle size and strain, and fractional coordinates of the atoms in the structural model.

The quality of a Rietveld refinement is expressed via the weighted profile residual, R_{wp}:

$$R_{wp} = \left[\frac{S_y}{\sum_{i=1}^{n} w_i y_i (obs)^2}\right]^{0.5} \times 100\ \% \qquad \text{Equation 2.24}$$

If the experimental pattern possesses a high background, then the R_{wp} can incorrectly suggest a good fit, as the background is included in the calculation of the y_i values. Therefore, care must be exercised when choosing the conditions for the diffraction experiment, to ensure that the obtained peak intensities are orders of magnitude greater than the background intensities.

R_{exp} can be defined as the best expected value from the statistics of the data, and is denoted by:

$$R_{exp} = \left[\frac{N - P}{\sum w_i y_i (obs)^2}\right]^{0.5} \qquad \text{Equation 2.25}$$

where N is the number of observations and P is the number of refinable parameters. The goodness of fit, *GOF*, is also an indicator of how closely the calculated structural model fits that of the diffraction data:

$$GOF = \frac{R_{wp}}{R_{exp}} = [\chi^2]^{0.5}. \qquad \text{Equation 2.26}$$

The Rietveld refinements performed on the diffraction patterns presented in this report were carried out using a combination of the *Topas* and *jEdit* software packages,[17, 18] or the GSAS (General Structure Analysis System) package.[22]

2.4.3 Variable-temperature powder X-ray diffraction data analysis

A variable-temperature powder X-ray diffraction experiment produces a number of data sets according to the temperature range and temperature step size studied. Multiple refinements can be performed consecutively using the local *multitopas* routine.[23] Sequential Pawley fits or Rietveld refinements can be done with *multitopas* using a single input file for the analysis of all the data sets studied. An initial refinement using the input file is performed in *Topas*, before a batch file including the filename for the data set and the temperature range the data were recorded over is produced. The batch file can be programmed to allow a given data set to be refined using either the output of the preceding data set, or that of the initial refinement. The outputs of the refinements are stored in a text document, and can be read into other pieces of software for subsequent data analysis.

2.4.4 Total-scattering Reverse Monte Carlo (RMC) analysis

Prior to performing total-scattering analyses using the software package RMCProfile v6,[5] the data collected on the Polaris diffractometer were processed with Gudrun.[24] The RMCProfile package allows the Bragg data, the total correlation function, *T(r)*, and the normalised total-scattering function, *S(Q)*, to be fitted simultaneously. Fitting the Bragg data in addition to the diffuse-scattering data prevents atomic configurations inconsistent with the average structure from being generated within the structural model. To model atomic disorder over a specific atomic site, atom swapping can be performed between two different atom types.

In order for any distortions from the local structure to be observed, a supercell must be specified. During the refinement, random atomic movements are applied to the atoms within the supercell model, and the level of agreement observed. The calculated and experimental total-scattering structure factors, *F(Q)*, and total radial distribution functions, *G(r)*, are also compared. If the agreement factor improves, the atomic movement is accepted, but if the agreement factor worsens, the move can be accepted within a certain probability, *P*:[25]

$$P = e^{\left(\frac{-\Delta\chi^2_{RMC}}{2}\right)} \qquad \text{Equation 2.27}$$

where χ^2_{RMC} is the RMC agreement factor.

For the Bragg data, Bank 3 (52.4 °) of the Polaris diffractometer was chosen, as this contains data from a wide *Q* range. For the total-scattering analyses, a range of restraints and constraints were applied[5] to maintain the atomic connectivity and not explore unfeasible models. For the refinements presented in this report, bond-valence sum (BVS)[26] and distance window restraints were applied. The individual atomic bond-valence sums, s_{ij}, are calculated using the following equation:

$$s_{ij} = e^{\left(\frac{R_o - r_{ij}}{b}\right)} \qquad \text{Equation 2.28}$$

where r_{ij} corresponds to the bond length between atoms *i* and *j*, and R_o and *b* are empirically determined parameters for each bond type.[27, 28] By summing together all the individual s_{ij} values, the atomic valence of each atom type, *j*, can be determined.[28]

2.4.5 Impedance spectroscopy analysis

To calculate the conductivity, σ, exhibited by a sample, the value of the resistance obtained from the Nyquist plot can be placed into Equation 2.20 along with the dimensions of the pellet. The Nyquist plots may deviate from the image shown in Figure 2.5, with a 45 ° slope corresponding to a Warburg-type impedance response, which is impedance brought about by diffusion from the electrolyte to the electrodes (Figure 2.6).

To calculate the capacitance, the frequency of the maximum of the arc is used to calculate ω, and then used in Equation 2.29 along with the resistance *R*, to obtain the capacitance, *C*.

$$C = \frac{1}{\omega R} \qquad \text{Equation 2.29}$$

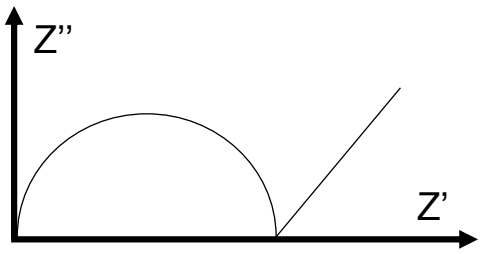

Figure 2.6: Nyquist plot illustrating a Warburg-type impedance response.

Once the conductivity values for the sample have been calculated, a graph illustrating the conductivity of a sample as a function of temperature can be plotted, with the axes corresponding to log(σ) and 1000/T (for the *y* and *x* axes respectively). The conductivity typically follows the Arrhenius relationship:

$$\sigma = \frac{\sigma_o}{T} e^{-\frac{E_a}{RT}} \qquad \text{Equation 2.30}$$

where σ_o is a pre-exponential factor, *R* is the gas constant, *T* is the temperature, and E_a is the activation energy of conductivity. The activation energy can be calculated from a plot of ln(σT) as a function of $\frac{1}{T}$, with the gradient representing $-\frac{E_a}{R}$, with the units of kJmol^{-1}.

2.5 Additional characterisation methods

2.5.1 Scanning electron microscopy - energy dispersive X-ray analysis

An electron gun bombards the sample with electrons, causing ionisation of the sample. Following ionisation, an electron relaxes from a higher-energy orbital, resulting in the emission of X-rays with energies (and therefore wavelengths) characteristic to specific atoms. This therefore allows for the exact composition of the sample being analysed to be attained.

To prepare the samples for analysis, pellets are pressed and mounted onto carbon sheets affixed to glass slides. To prevent charge build-up, carbon is coated across the surface of the pellet and slide to act as a conductive layer. The energy dispersive X-ray (EDX) data were collected by Mr. Leon Bowen (Durham Physics) on a Hitachi SU-70 Field Emission Gun Scanning Electron Microscope (FEG SEM), with an operating voltage of 15 keV.

2.5.2 Electron diffraction

Electron diffraction is performed in conjunction with transmission electron microscopy, analysing extremely thin samples. The transmission electron microscope produces electrons with short de Broglie wavelengths, and so only small Bragg angles are required to obtain data on the *d*-spacing scale comparable to those found inside crystalline materials.

Samples were prepared for electron diffraction by placing a small quantity of the sample in a volatile solvent, before placing a drop of the solution onto a holey carbon grid, and allowing the solvent to evaporate. The electron diffraction patterns contained in this report were collected by Prof. Ray Withers (Australian National University, Canberra) using a JEOL 2100-F TEM.

2.6 References

1. A. K. Cheetham and P. Day, *Solid State Chemistry Techniques*, Oxford University Press, New York, 1987.
2. A. R. West, *Solid State Chemistry and its Applications*, John Wiley & Sons Ltd., Chichester, 1984.
3. G. J. McIntyre, M.-H. Lemée-Cailleau and C. Wilkinson, *Physica B: Condensed Matter*, 2006, **385–386, Part 2**, 1055-1058.
4. J. W. Campbell and Q. Hao, *Acta Crystallographica Section A*, 1993, **49**, 889-893.
5. M. G. Tucker, D. A. Keen, M. T. Dove, A. L. Goodwin and Q. Hui, *Journal of Physics-Condensed Matter*, 2007, **19**, 1-16.
6. D. A. Keen, *Journal of Applied Crystallography*, 2001, **34**, 172-177.
7. T. E. Faber and J. M. Ziman, *Philosophical Magazine*, 1965, **11**, 153-173.
8. R. L. McGreevy and L. Pusztai, *Molecular Simulation*, 1988, **1**, 359-367.
9. Bruker AXS, Diffrac+ XRD Commander v2.3, Kahlsruhe, 2000.
10. S. Allen, *PhD. Thesis*, University of Durham, 2003.
11. R. M. Ibberson, W. I. F. David and K. S. Knight, *The High Resolution Neutron Powder Diffractometer (HRPD) at ISIS - A User Guide*, ISIS Crystallography, Didcot, 1992
12. V. F. Sears, *Neutron News*, 1992, **3**, 29-37.
13. K.-D. Liss, B. Hunter, M. Hagen, T. Noakes and S. Kennedy, *Physica B: Condensed Matter*, 2006, **385–386, Part 2**, 1010-1012.
14. A. J. Edwards, *Australian Journal of Chemistry*, 2011, **64**, 869-872.
15. C. D. Ling, *Journal of Solid State Chemistry*, 1999, **148**, 380-405.
16. G. S. Pawley, *Journal of Applied Crystallography*, 1981, **14**, 357-361.
17. A. A. Coelho, J. Evans, I. Evans, A. Kern and S. Parsons, *Powder Diffraction*, 2011, **26**, S22-S25.
18. http://www.jedit.org.
19. H. M. Rietveld, *Journal of Applied Crystallography*, 1969, **2**, 65-71.
20. P. L. Chebyshev, *Mémoires des Savants étrangers présentés á l'Académie de Saint-Pétersbourg*, 1854, **7**, 539-586.
21. P. Thompson, D. E. Cox and J. M. Hastings, *Journal of Applied Crystallography*, 1987, **20**, 79-83.
22. A. C. Larson and R. B. Von Dreele, *The General Structure Analysis System (GSAS)*, Los Alamos National Laboratory: Los Alamos, 2004.
23. J. S. O. Evans, *multitopas, FORTRAN 77 routine*, University of Durham, 1999.
24. A. C. Hannon, W. S. Howells and A. K. Soper, *Institute of Physics Conference Series*, 1990, **107**, 193-211.
25. T. Egami and S. J. L. Billinge, *Underneath the Bragg Peaks: Structural Analysis of Complex Materials*, Pergamon, Amsterdam, 2003.
26. S. T. Norberg, M. G. Tucker and S. Hull, *Journal of Applied Crystallography*, 2009, **42**, 179-184.
27. N. E. Brese and M. O'Keeffe, *Acta Crystallographica Section B*, 1991, **47**, 192-197.
28. I. D. Brown and D. Altermatt, *Acta Crystallographica Section B*, 1985, **41**, 244-247.

3 Structural characterisation and properties of the $Bi_{1-x}Nb_xO_{1.5+x}$ materials (x = 0.0625, 0.11, and 0.12)

3.1 Background

Fluorite-type Bi_2O_3 (δ-Bi_2O_3) has one of the highest oxide-ion conductivities known ($\sigma_{750\,°C}$ ~1 Scm^{-1}),[1] but is only stable between 730 and 824 °C.[2] The aim of a wealth of work reported in the literature has been to stabilise the highly conductive phase to room temperature through substitution of Bi^{3+} with aliovalent or isovalent cations.[3] However, cation doping can lead to superstructures forming with lower conductivities, necessitating a balance between stabilising the fluorite structure to lower temperatures and keeping the oxide-ion-conductivity levels high.

Ionic conductivity through the structure can be improved by doping in cations which can support variable coordination numbers, as seen for $La_2Mo_2O_9$,[4] where flexible Mo coordination (4-, 5-, and 6-fold coordination) provides a pathway for oxide-ion migration, allowing for fast ion conduction. Doping Bi_2O_3 with variable coordination cations has been demonstrated with great success for $Bi_{1-x}V_xO_{1.5+x}$ (x = 0.087, 0.095) compositions, which show high conductivities at low temperatures ($\sigma_{500\,°C}$ ~3.9 × 10^{-2} Scm^{-1} when x = 0.087),[5] and also for other bismuth rhenates and molybdates.[6, 7] As for Mo and V, Nb cations can support variable coordination numbers allowing NbO_x polyhedra to provide a low-energy pathway for oxide ions through the structure.[8] As the oxide ions migrate through the structure, they are incorporated into the NbO_x polyhedra, forming transient NbO_{x+1} species.

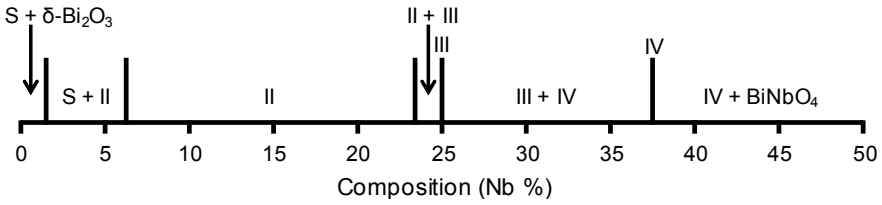

Figure 3.1: Partial phase diagram illustrating the Bi-rich end of the Bi_2O_3-Nb_2O_5 system. 'S' is the sillenite-type phase, and 'II', 'III', and 'IV' relate to the various 'Types' of structure for bismuth niobate materials.

Several structure types have been reported for compositions at the Bi-rich end of the Bi_2O_3-Nb_2O_5 phase diagram, $Bi_{1-x}Nb_xO_{1.5+x}$ ($0 \leq x \leq 0.5$) (Figure 3.1).[9] When $x < 0.0625$, the sillenite-type phase, $Bi_{12}Nb_{0.29}O_{18.7+x}$, is present, whilst materials with Type II superstructures – a complex cubic fluorite-based superstructure – form as single phases in the compositional range x = 0.0625 to 0.234. The Type II superstructure was reported to be incommensurately modulated by Miida and Tanaka, based on high-resolution electron microscopy and electron-diffraction studies for seven compositions in the range x = 0.112 to 0.266.[10] A complete characterisation of the Type II incommensurately-modulated bismuth niobate superstructure was reported subsequently by Ling *et al.*, who described the material with the nominal composition $Bi_{0.76}Nb_{0.24}O_{1.74}$ as having a (3+3)-dimensional incommensurately-modulated hypercubic structure.[11] As the Nb content is increased, there are two phases at: x = 0.25

corresponding to Bi_3NbO_7, a tetragonal 3 × 3 × 7 fluorite-based superstructure denoted as Type III, and $x = 0.375$ for $Bi_5Nb_3O_{15}$, the Type IV Aurivillius-type phase. Either side of these two line phases are mixtures of the various phases: Type II + Type III; Type III + Type IV; or Type IV + $BiNbO_4$, depending on the Nb content (Figure 3.1).

In this chapter, the findings of an experimental study of the Bi-rich end of the Bi_2O_3-Nb_2O_5 phase diagram are presented, focussing on the $Bi_{1-x}Nb_xO_{1.5+x}$ (x = 0.0625, 0.11, and 0.12) compositions and their conductivities. These compositions were chosen as the conductivity values are generally the highest in the Bi-rich end of the Type II superstructure region of the phase diagram,[12] but no conductivity data have yet been reported for these three compositions. The x = 0.0625 composition forms a cubic structure only if quenched from a high temperature, otherwise it forms a tetragonal ($\sqrt{2} \times \sqrt{2} \times 1$) fluorite-type superstructure. A crystallographic model for the tetragonal structure is proposed based on powder neutron diffraction data and details the thermal stability for this material. For all three compositions, the oxide-ion conductivities measured over a series of thermal cycles are presented, and show that the cubic x = 0.11 and 0.12 compositions undergo slow phase transformations to the tetragonal structure on extended heating, resulting in a decrease in conductivity.

3.2 Synthesis of $Bi_{1-x}Nb_xO_{1.5+x}$ materials (x = 0.0625, 0.11, and 0.12)

Solid-state synthesis was carried out to prepare samples of the $Bi_{1-x}Nb_xO_{1.5+x}$ (x = 0.0625, 0.11, and 0.12) compositions. For x = 0.0625, Bi_2O_3 (7.7069 g, 16.56 mmol, Sigma-Aldrich, 99.9 %) and Nb_2O_5 (0.2931 g, 1.12 mmol, Sigma-Aldrich, 99.99 %) were combined together then fired for 48 hours at 825 °C in an alumina crucible, with a heating and cooling rate of 5 °C/min, yielding a yellow powder. A further sample of this composition was prepared consisting of 1.9267 g of Bi_2O_3 (4.14 mmol) and 0.0733 g of Nb_2O_5 (0.28 mmol), which was pelletised prior to firing at 825 °C for 36 hours. Instead of cooling gradually in a controlled fashion, the pellet was quenched from 825 °C to room temperature by placing it into water. For $Bi_{0.89}Nb_{0.11}O_{1.61}$, 1.8683 g of Bi_2O_3 (4.01 mmol) and 0.1317 g of Nb_2O_5 (0.49 mmol) were ground together with a pestle in a mortar, whilst 1.8557 g of Bi_2O_3 (3.98 mmol) and 0.1444 g of Nb_2O_5 (0.54 mmol) were ground together for $Bi_{0.88}Nb_{0.12}O_{1.62}$, then both powdered mixtures were fired at 825 °C for 36 hours each, yielding yellow powders.

3.3 Characterisation of $Bi_{1-x}Nb_xO_{1.5+x}$ materials (x = 0.0625, 0.11, and 0.12)

3.3.1 Laboratory powder X-ray diffraction

Laboratory powder X-ray diffraction (PXRD) data were collected for all four synthesised samples, to ascertain their phase purity (Figure 3.2). For the x = 0.0625 (quenched), 0.11, and 0.12 compositions, the face-centred cubic unit cell reported by Gattow and Schroeder for δ-Bi_2O_3 was used as a starting model for phase identification,[13] with the stoichiometry modified to include Nb and the additional oxygen content (Table 3.1). 10 background parameters, 1 lattice parameter, 1 isotropic displacement parameter, 4 peak-shape terms, zero-point error, and a scale factor were refined for these three compositions, producing good fits to the collected data (Figure 3.2a-c).

Table 3.1: Starting cubic structural model for the *x* = 0.0625 (quenched), 0.11, and 0.12 compositions. Space group = Fm$\bar{3}$m, *a* ~5.6 Å.

Atom	Site	x	y	z	Occupancy
Bi	4a	0	0	0	1–*x*
Nb	4a	0	0	0	*x*
O	8c	0.25	0.25	0.25	0.75+*x*/2

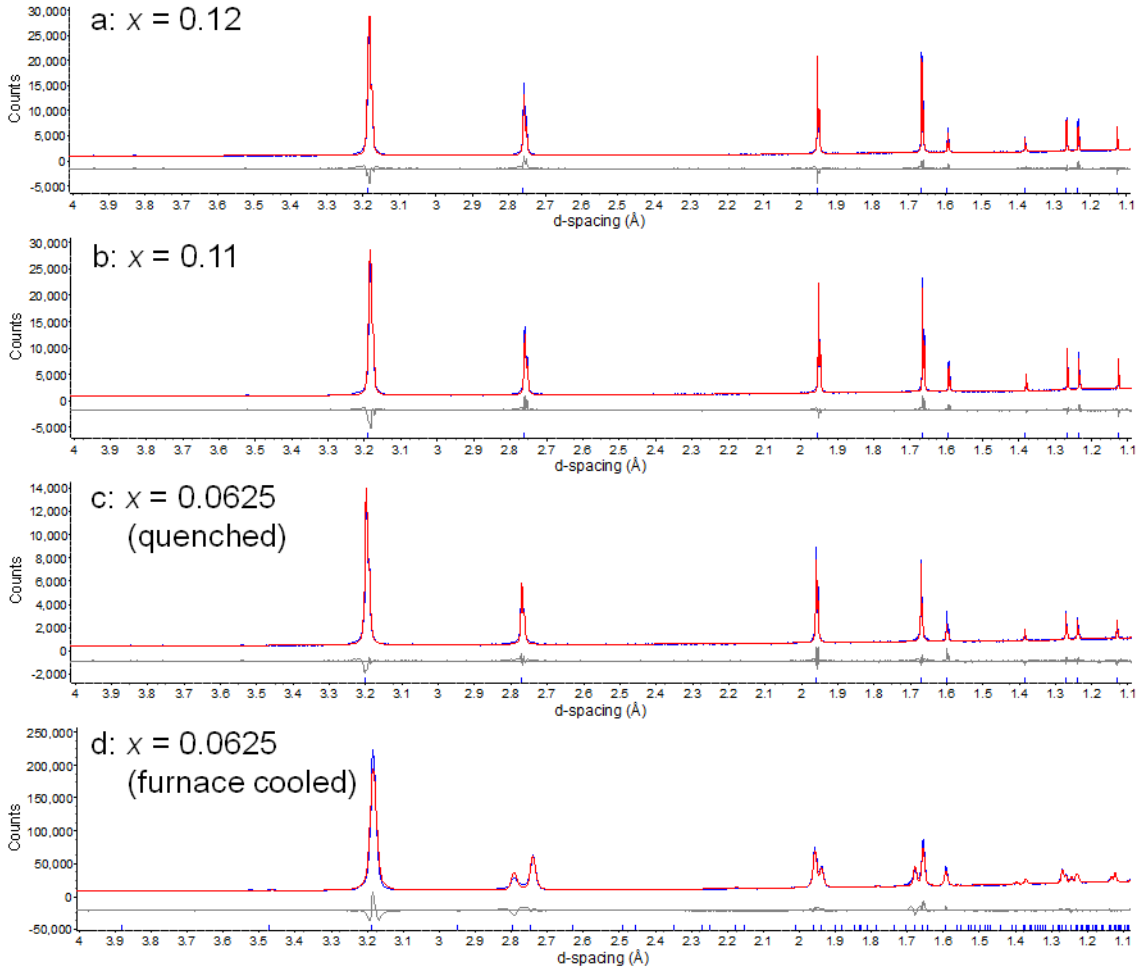

Figure 3.2: Rietveld[14] refinements of: a) $Bi_{0.88}Nb_{0.12}O_{1.62}$, d7_07023, *a* = 5.5221(1) Å, R_{wp} = 5.649 %, b) $Bi_{0.89}Nb_{0.11}O_{1.61}$, d7_03046, *a* = 5.5274(1) Å, R_{wp} = 5.574 %, c) $Bi_{0.9375}Nb_{0.0625}O_{1.5625}$ (quenched), d7_04564, *a* = 5.5438(1) Å, R_{wp} = 6.566 %, all using the fluorite-type Fm$\bar{3}$m structural model. d) $Bi_{0.9375}Nb_{0.0625}O_{1.5625}$, d7_05842, *a* = 7.7616(2) Å, *c* = 5.5919 Å, R_{wp} = 4.582 %, using the tetragonal structural model.

For the furnace-cooled sample of $Bi_{0.9375}Nb_{0.0625}O_{1.5625}$, splitting of a number of the diffraction peaks was observed (Figure 3.2d), indicating the structure possesses symmetry lower than cubic. The starting model for the refinement was that of tetragonal β-Bi_2O_3 reported by Blower and Greaves,[15] with the metal site occupancy altered to include Nb in the structure (i.e. $Bi_{0.9375}Nb_{0.0625}O_{1.5}$, Table 3.2). This tetragonal structure is a ($\sqrt{2} \times \sqrt{2} \times 1$) superstructure of the fluorite subcell (a_F ~5.5 Å). The additional oxygen content was not included when refining against the PXRD data for phase identification purposes, as both oxygen sites are fully occupied (Table 3.2), and neutron diffraction data would be required to locate the additional oxygen positions. This is because the neutron scattering length for O is comparable to those for Bi and Nb (5.803 fm, 8.532 fm, and 7.054 fm for O, Bi, and Nb, respectively), whilst the

contribution from O is overshadowed by those from Nb and Bi when using X-rays. 10 background parameters, 2 lattice parameters, 1 isotropic displacement parameter, peak-shape terms, zero-point error, and a scale factor were refined. Good fits to the data were achieved for all four samples (Figure 3.2a-d).

Table 3.2: Starting tetragonal structural model for the *x* = 0.0625 composition based on the model reported by Blower and Greaves.[15] Space group = $P\bar{4}2_1c$, *a* = 7.741(3) Å, *c* = 5.634(2) Å.

Atom	Site	x	y	z	Occupancy
Bi	8e	0.0178(8)	0.2539(7)	0.2532(10)	0.9375
Nb	8e	0.0178(8)	0.2539(7)	0.2532(10)	0.0625
O1	8e	0.295(1)	0.3074(7)	0.027(2)	1
O2	4d	0	0.5	0.101(2)	1

3.3.2 Powder neutron diffraction and refined structure of $Bi_{0.9375}Nb_{0.0625}O_{1.5625}$

High-quality powder neutron diffraction data were collected at room temperature using the HRPD diffractometer at ISIS for $Bi_{0.9375}Nb_{0.0625}O_{1.5625}$, to allow the interstitial oxygen atom positions to be located and the structural model completed. The data used for the subsequent refinements were collected on the backscattering detector bank for 562 μAh (~15 hours) between 30 and 130 ms, corresponding to a *d*-spacing range of 0.62 to 2.69 Å.

The initial refinement using the model reported by Blower and Greaves (Table 3.2)[15] did not produce a good fit to the data (Figure 3.3). Whilst accurate peak positions indicate that the correct space group and lattice parameters were used, the peak intensities fit poorly to the collected data. The refined parameters include: 10 background terms, 2 lattice parameters, all atomic coordinates, 3 isotropic displacement parameters (one metal and two oxygen), peak-shape terms, and a scale factor.

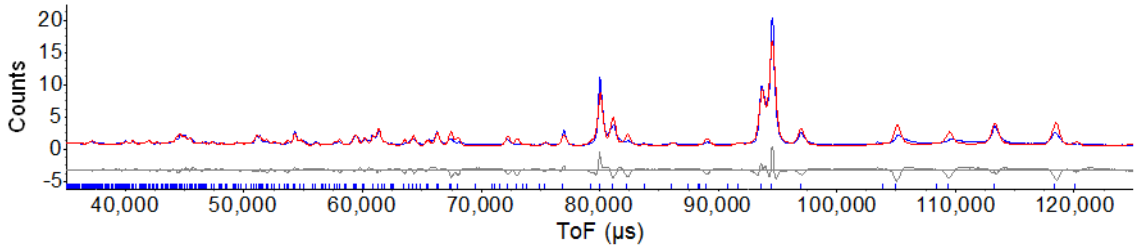

Figure 3.3: Rietveld refinement to PND data using the initial tetragonal structural model for $Bi_{0.9375}Nb_{0.0625}O_{1.5625}$: hrp58775_b1, *a* = 7.769(9) Å, *c* = 5.596(6) Å, R_{wp} = 16.878 %.

As with the laboratory PXRD analysis, the structural model used for the initial PND refinement only possessed 1.5 oxygen atoms per formula unit, instead of the stoichiometric 1.5625, and so difference Fourier maps were generated to locate the interstitial oxygen positions. Two peaks of residual nuclear density were identified as the new oxygen sites O3 and O4 (Table 3.3). Oxygen atoms placed on these sites have sensible *M*-O bond lengths (*M* = Bi, Nb, 2.399(4) to 2.410(4) Å), and form OM_4 (*M* = Bi/Nb) tetrahedra. Subsequently, the isotropic displacement parameters and site occupancies for the O3 and O4 sites were refined in addition to the parameters previously stated, whilst restraining the total oxygen content to maintain the correct stoichiometry. The site occupancies for O3 and O4 refined to 0.14(4) and

0.11(4) respectively, corresponding to the composition $Bi_{0.9375}Nb_{0.0625}O_{1.56(5)}$, in agreement with the nominal O content. As the O3 and O4 occupancies were very similar, they were subsequently fixed to 0.125, generating the expected stoichiometry of $Bi_{0.9375}Nb_{0.0625}O_{1.5625}$.

Throughout the refinement process for this tetragonal structure, the calculated peak shapes were fitting poorly to the observed PND pattern, and so a *hkl*-dependent peak-shape function was introduced to attempt to improve the overall quality of fit to the data.[16] This peak-shape function did marginally improve the fit (Figure 3.4), but poorly fitted asymmetric tails are still observed across a range of Bragg peaks, suggesting a degree of local-scale ordering of the Bi and Nb atoms (*vide infra*).

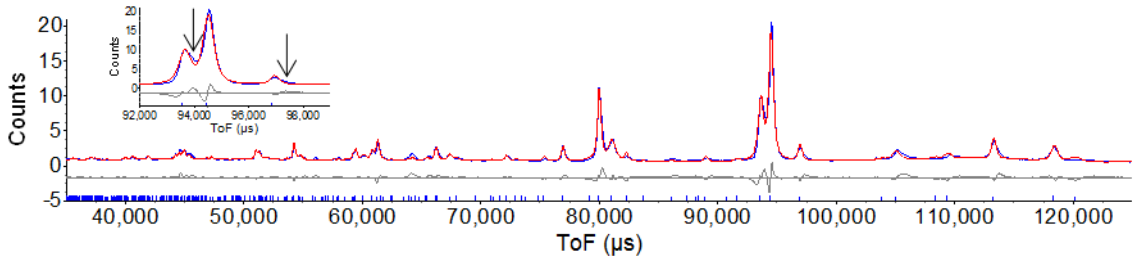

Figure 3.4: Rietveld refinement to PND data using the tetragonal structural model for $Bi_{0.9375}Nb_{0.0625}O_{1.5625}$, hrp58775_b1, *a* = 7.7638(1) Å, *c* = 5.5923(1) Å, R_{wp} = 8.779 %. Arrows in the inset image denote asymmetric tails seen on some Bragg peaks.

Table 3.3: Final crystallographic data for tetragonal $Bi_{0.9375}Nb_{0.0625}O_{1.5625}$. Space group = $P\bar{4}2_1c$, *a* = 7.7638(1) Å, *c* = 5.5923(1) Å, *V* = 337.08(1) Å^3.

Atom	Site	x	y	z	Occupancy	B_{iso} (Å^2)
Bi	8e	0.5025(8)	0.7520(7)	0.7517(5)	0.9375	1.94(4)
Nb	8e	0.5025(8)	0.7520(7)	0.7517(5)	0.0625	1.94(4)
O1	8e	0.7822(8)	0.8065(8)	0.535(1)	1	5.9(1)
O2	4d	0	0.5	-0.091(1)	1	4.9(1)
O3	2a	0	0	0	0.125	5(2)
O4	2b	0	0	0.5	0.125	5(2)

The final structural model for tetragonal $Bi_{0.9375}Nb_{0.0625}O_{1.5625}$ is presented in Table 3.3 and shown in Figure 3.5. This structural model is consistent with the stoichiometry, comprised of a mixed Bi/Nb site (occupancy ratio of 0.9375:0.0625) with two fully and two partially occupied O sites. The tetragonal structure is comprised of a continuous three-dimensional network of O1- and O2-centred OM_4 tetrahedra (*M* = Bi, Nb) containing tetrahedral and octahedral holes. O3 and O4 partially occupy the tetrahedral holes which are vacant normally in the β-Bi_2O_3 structure, forming chains of edge-sharing OM_4 polyhedra running parallel to the *z* axis (Figure 3.5). At room temperature the octahedral holes at (0.5, 0.25, 0.25) are unoccupied, but are observed in *ab initio* molecular dynamics simulations to provide oxide-ion migration pathways at higher temperatures via ionic hopping.[17] The Bi and Nb atoms occupy distorted cubic environments with *M*-O bond lengths of 2.124(5) to 2.896(9) Å and statistical variation of the metal coordination numbers due to the fractional occupancies of the O3 and O4 sites.

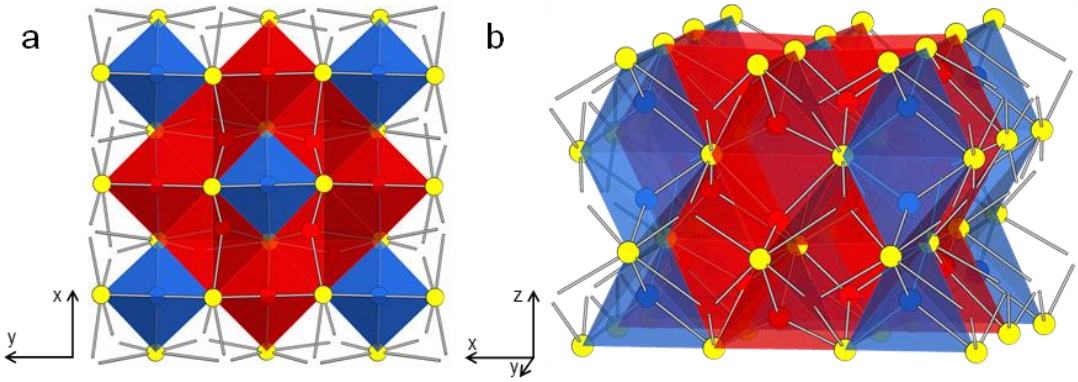

Figure 3.5: Room-temperature tetragonal structure of $Bi_{0.9375}Nb_{0.0625}O_{1.5625}$ viewed along the: a) *z* axis; b) *y* axis (approximately). These images show the three-dimensional network of OM_4 tetrahedra (O1 and O2 sites), and one-dimensional chains of OM_4 tetrahedra running parallel to the *z* axis. Bi/Nb = yellow, O1/O2 = red, interstitial O3/O4 = blue.

The relationship between the room-temperature tetragonal and high-temperature cubic structures is due to the arrangement of the oxygen sublattice. In the high-temperature cubic structure, the oxide ions are disordered, whilst in the tetragonal structure they are largely ordered, with only a small fraction of the oxide ions (~4 %) residing on the two partially-occupied sites. In the average structures obtained by diffraction for both forms, Bi and Nb cations are disordered on the same crystallographic site.

3.3.3 Electron diffraction of $Bi_{0.9375}Nb_{0.0625}O_{1.5625}$

Electron diffraction patterns for $Bi_{0.9375}Nb_{0.0625}O_{1.5625}$ obtained and indexed by Prof. Ray Withers (Research School of Chemistry, Australian National University (ANU), Canberra, Australia) confirm the $P\bar{4}2_1c$ space group and tetragonal unit cell obtained from analysis of PXRD and neutron diffraction data (Figure 3.6). In Figure 3.6a and Figure 3.6b, the indexing denoted demonstrates the relationship between the underlying δ-Bi_2O_3 fluorite-type subcell and the tetragonal superstructure where $a = a_F + b_F$, $b = -a_F + b_F$, and $c = c_F$.

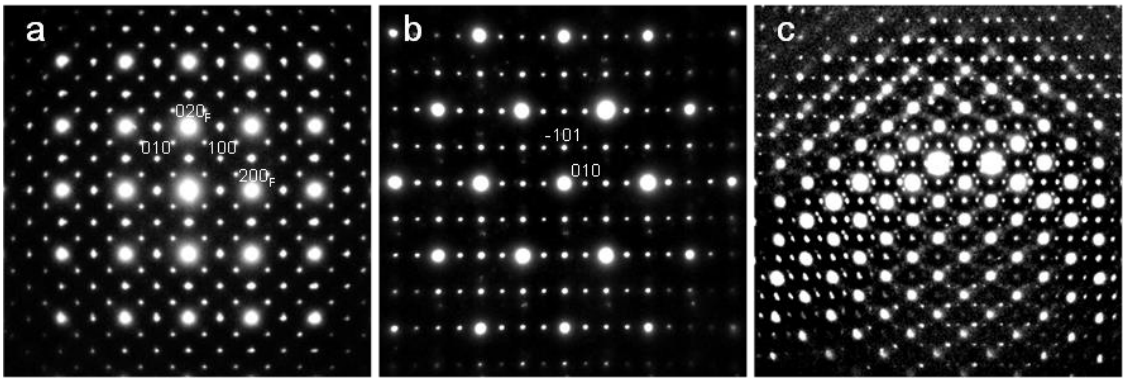

Figure 3.6: Electron diffraction patterns of tetragonal $Bi_{0.9375}Nb_{0.0625}O_{1.5625}$ ($\sqrt{2} \times \sqrt{2} \times 1$ fluorite superstructure), with a) and b) showing two views demonstrating the $a = a_F + b_F$, $b = -a_F + b_F$, and $c = c_F$ relationship between the fluorite subcell and tetragonal superstructure. The 020_F and 200_F spots in Figure 3.6a are indexed relative to the fluorite subcell. c) Streaks in the electron diffraction pattern when viewed off-axis indicate structured diffuse scattering. These electron diffraction patterns were collected and indexed by Prof. Ray Withers (ANU, Canberra).

When viewed off-axis, the electron diffraction pattern reveals weak lines connecting the bright diffraction spots together, a feature indicative of structured diffuse scattering

(Figure 3.6c). Diffuse scattering is reported for a wide range of materials in the literature, including $Ni_{0.7}Mg_{0.3}PS_3$ and $PbZn_{1/3}Nb_{2/3}O_3$,[18, 19] caused by clustering of Mg atoms in the former case, and partial ordering of Zn and Nb in the latter case. These effects occur due to the differing bonding requirements for the Ni/Mg and Zn/Nb cations, and are also reported for the pyrochlores $Bi_{1.499}Zn_{0.805}Nb_{1.5}O_{6.805}$ and $Ho_{2.67}Ti_{1.33}O_{6.67}$.[20, 21] The diffuse streaks in the electron diffraction patterns are consistent with the observed asymmetry in the tails of a number of Bragg peaks in the neutron diffraction data (inset of Figure 3.4), which is tentatively attributed to local-scale ordering of the Bi and Nb atoms. Local-scale ordering due to mismatch in ionic radii can also induce lattice microstrain,[22] leading to slight broadening of the diffraction peaks.[23] This phenomenon can be seen for $La_{2-x}Sr_xNiO_{4-\delta}$ (x = 0.15 to 0.50), where partial ordering of the oxygen vacancies causes local-scale fluctuations of the oxygen content, giving rise to microstrains and anisotropic broadening of diffraction peaks.[24]

Owing to the diffuse scattering observed via electron diffraction, and the anisotropic broadening of a number of peaks in the powder neutron diffraction data, the obtained structural model for tetragonal $Bi_{0.9375}Nb_{0.0625}O_{1.5625}$ (Table 3.3) should be treated as an approximate, average-structure description.

3.3.4 Phase transitions in $Bi_{0.9375}Nb_{0.0625}O_{1.5625}$

A variable-temperature (VT) PXRD experiment on $Bi_{0.9375}Nb_{0.0625}O_{1.5625}$ was carried out to investigate the temperature at which this material exhibits a tetragonal-to-cubic phase transition, in addition to whether thermal instability seen by Kuang *et al*. for $Bi_{1-x}V_xO_{1.5+x}$ (x = 0.087, 0.095) is also observed for $Bi_{0.9375}Nb_{0.0625}O_{1.5625}$.[5] Data were collected on a pelletised sample of $Bi_{0.9375}Nb_{0.0625}O_{1.5625}$ between 40 and 800 °C on heating and 790 and 30 °C on cooling in 20 °C steps, with the resulting line surface plot showing five distinct regions with different sample structures owing to phase transformations (colour coded in Figure 3.7).

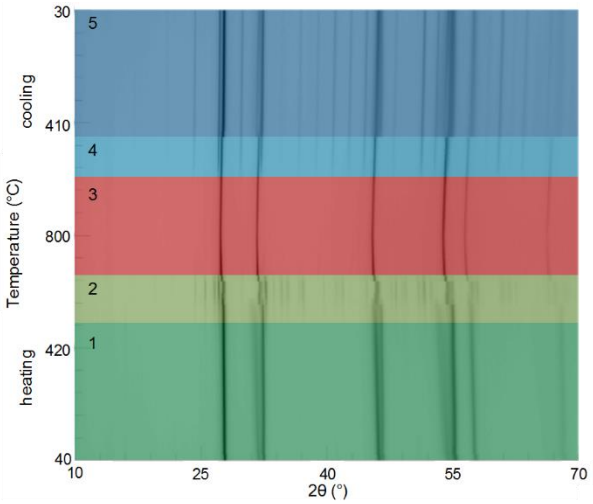

Figure 3.7: Line surface plot using *in situ* variable-temperature PXRD data collected for tetragonal $Bi_{0.9375}Nb_{0.0625}O_{1.5625}$ between 40 and 800 °C on heating and 790 and 30 °C on cooling. The regions are numbered and colour coded based on the structure types present in the sample. Region 1 (dark green) contains only the tetragonal phase. Region 2 (light green) contains a mixture of tetragonal, monoclinic, and fluorite-type cubic phases. Region 3 (red) contains only the fluorite-type cubic phase. Region 4 (light blue) contains a mixture of fluorite-type cubic and body-centered cubic phases. Regions 5 (dark blue) contains a mixture of tetragonal and body-centered-cubic phases.

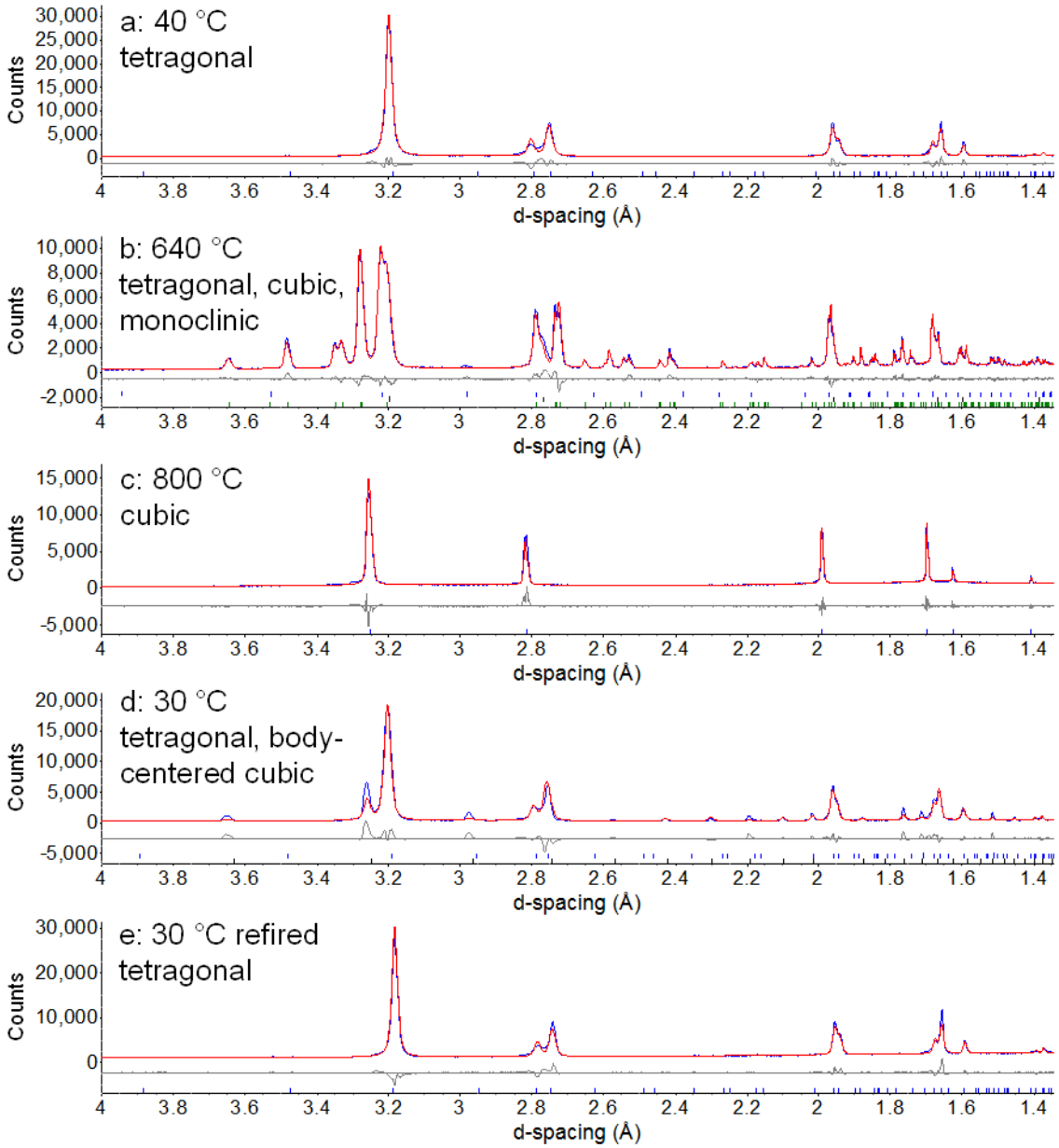

Figure 3.8: Rietveld fits to the PXRD patterns of $Bi_{0.9375}Nb_{0.0625}O_{1.5625}$ at: a) 40 °C, single-phase tetragonal material, d9_07269 range 1; b) 640 °C, a mixture of tetragonal, cubic, and monoclinic phases (blue, black, and green tick marks respectively), d9_07269 range 31; c) 800 °C, single-phase face-centred cubic material, d9_07269 range 39; d) 30 °C following cooling, a mixture of tetragonal and body-centred cubic phases (blue and black tick marks respectively), d9_07269 range 78; e) 30 °C following the sample being re-fired *ex situ* at 825 °C for 12 hours, single-phase tetragonal material, d7_05161.

Initially, the sample is a single-phase tetragonal material (Figure 3.7 region 1 and Figure 3.8a), which undergoes phase segregation into a mixture of tetragonal, δ -Bi_2O_3-based fluorite-type cubic, and α-Bi_2O_3-based monoclinic phases between 450 and 660 °C (Figure 3.7 region 2 and Figure 3.8b). At 680 °C, the sample undergoes another phase transformation into a fluorite-type cubic phase, which remains on heating to 800 °C (Figure 3.7 region 3 and Figure 3.8c). This correlates with the observation that a sample synthesised at 825 °C and subsequently quenched to room temperature possesses a cubic fluorite-type structure. On cooling the sample from 800 °C to room temperature, the sample firstly undergoes a phase transformation into a mixture of the fluorite-type cubic phase and the γ -Bi_2O_3-based body-centred cubic phase at 660 °C (Figure 3.7 region 4), before transforming into a mixture of

the tetragonal phase with a small percentage of the body-centred cubic phase (Figure 3.7 region 5 and Figure 3.8d).

To investigate whether the formation of the body-centred cubic phase was solely due to the slow cooling rate used in the VT experiment, the VT-PXRD sample was re-fired for 12 hours at 825 °C with a heating and cooling rate of 5 °C per minute. The PXRD data in Figure 3.8e were collected after this heating regime, and show that the slow rate of cooling during the VT experiment allows the fluorite-type phase to transform partially into the metastable body-centred cubic phase instead of solely into the tetragonal phase. Based on the results of the VT experiment, it can be concluded that $Bi_{0.9375}Nb_{0.0625}O_{1.5625}$ is thermally stable below 450 °C as a tetragonal phase and above 680 °C as a cubic phase.

3.4 Ionic conductivities of $Bi_{1-x}Nb_xO_{1.5+x}$ (x = 0.0625, 0.11, and 0.12)

Pellets for impedance measurements on the three $Bi_{1-x}Nb_xO_{1.5+x}$ materials (x = 0.0625 (tetragonal), 0.11, and 0.12) were pressed with 250 MPa of pressure then fired at 825 °C for 6 hours, producing pellets with the dimensions given in Table 3.4. Conductivity data were collected between 200 °C and 500 °C in 50 °C increments on heating and cooling. The pellets were allowed to equilibrate for approximately 45 minutes at each temperature before data were collected. The temperature range chosen for the experiment did not exceed 500 °C, to prevent the x = 0.0625 sample from undergoing a partial tetragonal-to-monoclinic phase transition.

Table 3.4: Pellet dimensions for the bismuth niobate samples used for impedance spectroscopy.

Composition	Mass (g)	Diameter (cm)	Height (cm)	Density (%)
$Bi_{0.9375}Nb_{0.0625}O_{1.5625}$	0.7996 ± 0.0001	0.904 ± 0.001	0.149 ± 0.001	93.99 ± 0.01
$Bi_{0.89}Nb_{0.11}O_{1.61}$	0.7000 ± 0.0001	0.893 ± 0.001	0.140 ± 0.001	91.40 ± 0.01
$Bi_{0.88}Nb_{0.12}O_{1.62}$	0.5678 ± 0.0001	0.881 ± 0.001	0.117 ± 0.001	91.01 ± 0.01

At low temperatures, all of the collected complex impedance spectra display a large semi-circular arc attributed to the bulk response, in addition to a Warburg-type electrode response at low frequencies (Figure 3.9a). The grain boundary and bulk responses could not be separated in the semi-circular arc at high frequencies, and the bulk responses were treated using a parallel resistor-capacitor model. The low-frequency intercept of the semi-circular arc corresponds to the bulk resistivity of the sample. The capacitances at this intercept calculated using $\omega RC = 1$ ($\omega = 2\pi f_{max}$, where f_{max} is the frequency for the maximum imaginary impedance of the semi-circular arc, Z''_{max}) at 200 °C are 9.0, 9.0, and 9.7 pF cm^{-1} for $Bi_{0.9375}Nb_{0.0625}O_{1.5625}$, $Bi_{0.89}Nb_{0.11}O_{1.61}$, and $Bi_{0.88}Nb_{0.12}O_{1.62}$ respectively. These values are consistent with a bulk response for all three samples.[25] The capacitance for the Warburg-type electrode response at low frequencies (<10 Hz) ranges between 10^{-7} and 10^{-5} F cm^{-1}, indicative of ionic conduction.[26] The bulk response was no longer observed at high temperatures, with only a single arc seen (Figure 3.9b), and so the high-frequency intercept was estimated to be the total resistivity value for each sample.

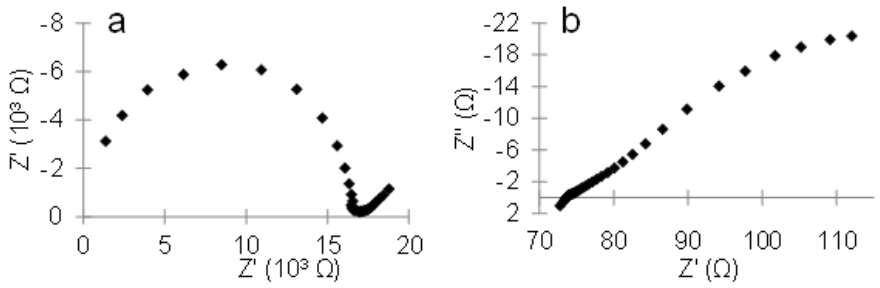

Figure 3.9: Complex impedance plots for $Bi_{0.88}Nb_{0.12}O_{1.62}$ at: a) 200 °C, showing the semi-circular bulk response arc and Warburg-type electrode response; b) 500 °C, showing the single impedance arc.

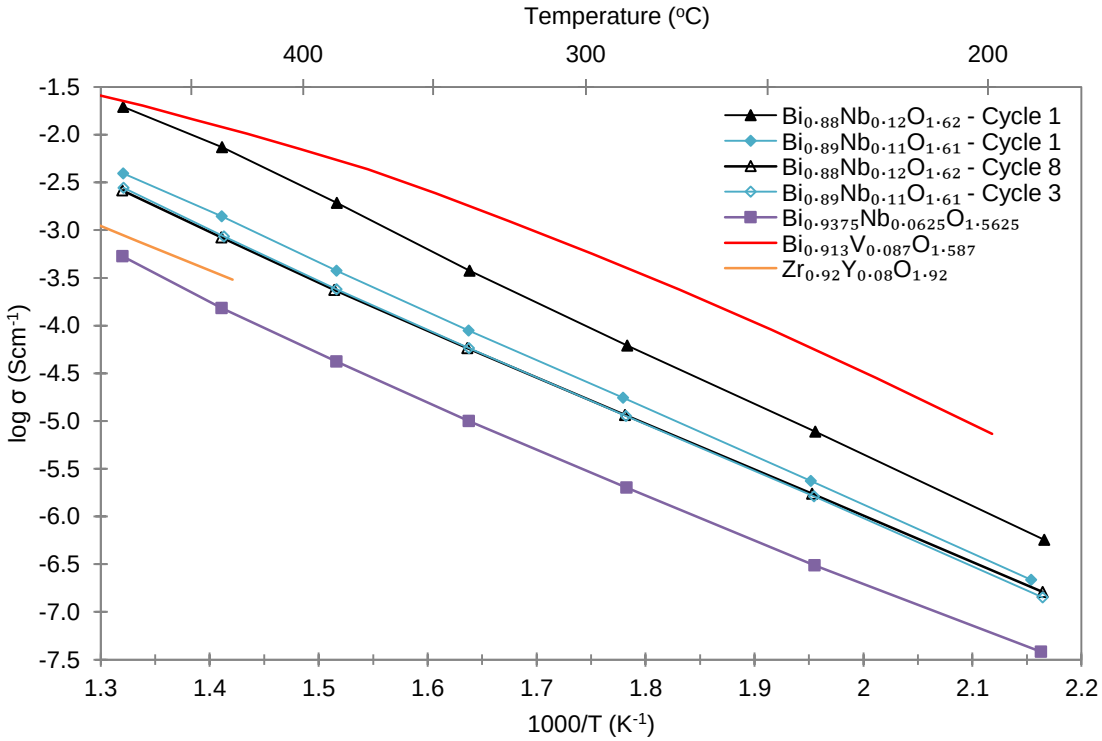

Figure 3.10: Arrhenius plot of log conductivity as a function of temperature for $Bi_{0.9375}Nb_{0.0625}O_{1.5625}$, in the initial and final thermal cycles of $Bi_{0.89}Nb_{0.11}O_{1.61}$ and $Bi_{0.88}Nb_{0.12}O_{1.62}$, and the phases $Bi_{0.913}V_{0.087}O_{1.587}$ and $Zr_{0.92}Y_{0.08}O_{1.92}$.[5, 27]

Additionally, to assess the thermal stabilities of these materials, the pellet for each composition was cycled through the temperature range multiple times, until the conductivity values recorded stabilised. The conductivity values obtained for tetragonal $Bi_{0.9375}Nb_{0.0625}O_{1.5625}$ did not change across three thermal cycles of heating and cooling (Figure 3.10, $\sigma_{450\ °C}$ ~2.1 × 10^{-4} Scm^{-1}), denoting that prolonged exposure to high temperatures does not cause a decrease in conductivity for the material. However, both of the cubic samples ($Bi_{0.89}Nb_{0.11}O_{1.61}$ and $Bi_{0.88}Nb_{0.12}O_{1.62}$) exhibited conductivity decreases over the course of the experiment (Figure 3.10), with $Bi_{0.89}Nb_{0.11}O_{1.61}$ showing a marginal decrease in conductivity over three cycles before stabilising ($\sigma_{450\ °C}$ ~1.9 × 10^{-3} and 1.2 × 10^{-3} Scm^{-1} for cycles 1 and 3), whilst the conductivity for $Bi_{0.88}Nb_{0.12}O_{1.62}$ decreased by ~1 order of magnitude over eight cycles ($\sigma_{450\ °C}$ ~9.7 × 10^{-3} and 1.2 × 10^{-3} Scm^{-1} for cycles 1 and 8 respectively).

Across the entire temperature range studied, the cubic samples possess conductivities between one and two orders of magnitude higher than the tetragonal sample. Above 450 °C, the total conductivity of $Bi_{0.88}Nb_{0.12}O_{1.62}$ is initially in excess of 0.01 Scm^{-1}, and despite the decreases in conductivity, both cubic samples maintain conductivities higher than that of yttria-stabilised zirconia ($Zr_{0.92}Y_{0.08}O_{1.92}$, $\sigma_{450\ °C}$ ~4.5 × 10^{-4} Scm^{-1}), with $Bi_{0.9375}Nb_{0.0625}O_{1.5625}$ being only marginally less conductive than the commercial electrolyte. The conductivities of the three bismuth niobate samples measured are similar to the those reported in the literature for other M^{5+}-doped bismuth oxide materials (M = V, Ta). The conductivity seen during the initial thermal cycle of $Bi_{0.88}Nb_{0.12}O_{1.62}$ is comparable to that of $Bi_{0.913}V_{0.095}O_{1.595}$ (σ ~6 × 10^{-3} Scm^{-1} at 400 °C),[5] whilst tetragonal $Bi_{0.9375}Nb_{0.0625}O_{1.5625}$ has a similar conductivity to that of $Bi_{0.9}Ta_{0.1}O_{1.6}$ (~2 × 10^{-4} Scm^{-1} at 400 °C).[12]

3.5 Metastable nature of the cubic fluorite-based structures (*x* = 0.11, 0.12)

To investigate the cause of the conductivity decreases for the cubic materials, the pellets of $Bi_{0.89}Nb_{0.11}O_{1.61}$ and $Bi_{0.88}Nb_{0.12}O_{1.62}$ used for the impedance measurements were analysed by PXRD, revealing partial conversion of the cubic phase to the tetragonal ($\sqrt{2} \times \sqrt{2} \times 1$) phase (blue and black tick marks for cubic and tetragonal phases in Figure 3.11a and Figure 3.11c for $Bi_{0.89}Nb_{0.11}O_{1.61}$ and $Bi_{0.88}Nb_{0.12}O_{1.62}$ respectively). Samples of these two compositions were heated for extended periods, and it was observed that the originally single-phase cubic materials decrease in phase purity to ~77 % after 15 hours heating for $Bi_{0.89}Nb_{0.11}O_{1.61}$ (Figure 3.11b), whilst $Bi_{0.88}Nb_{0.12}O_{1.62}$ displays ~85 % and 78 % phase purity after 48 and 120 hours of heating (Figure 3.11d and Figure 3.11e respectively). After 120 hours of heating, $Bi_{0.88}Nb_{0.12}O_{1.62}$ also shows evidence of a small percentage (~4 %) of a body-centered-cubic γ-Bi_2O_3-based phase (Figure 3.11e).

The metastable nature of the cubic (*a* ~5.5 Å) doped δ-Bi_2O_3 materials and the issues with their associated aging are reported for a range of compositions. For a range of Bi_3MO_6 materials (*M* = Dy, Er, Ho, Y, Yb), Boyapati *et al.* reported that annealing the samples resulted in decreased conductivity values due to ordering of the oxygen sublattice along the <111> direction. This ordering was coupled with displacement of almost all the oxide ions from tetrahedral 8c positions to interstitial 32f positions, resulting in the formation of a 2 × 2 × 2 superstructure.[28, 29] Leszczynska *et al.* report that the occupancy of the 32f interstitial site increases with temperature between 400 and 600 °C for $Bi_{0.8}Yb_{0.2}O_{1.5}$ based on neutron diffraction data, with annealing at 600 °C causing an increase in weight fraction of the orthorhombic $Bi_{17}Yb_7O_{36}$ phase.[30] Ordering of the oxygen sublattice in $Dy_{0.08}W_{0.04}Bi_{0.88}O_{1.56}$ also causes a decrease in conductivity of nearly two orders of magnitude when annealed at 500 °C.[31]

In addition, it was reported that $Bi_{25}Ln_3Re_2O_{49}$ (*Ln* = La, Pr) compounds display a decrease in conductivity of approximately two orders of magnitude on a second heating cycle ($\sigma_{500\ °C}$ ~10^{-2} Scm^{-1} in cycle 1 to 2.8 × 10^{-4} Scm^{-1} and 2.1 × 10^{-4} Scm^{-1} in cycle 2 for *Ln* = La,

Pr, respectively). The reason for this conductivity decrease is due to the materials undergoing cubic-to-tetragonal phase transitions, with the resulting structures similar to that reported for $Bi_{28}Re_2O_{49}$, with space group I4/m and cell parameters of *a* ~8.7 Å and *c* ~17.4 Å.[32, 33]

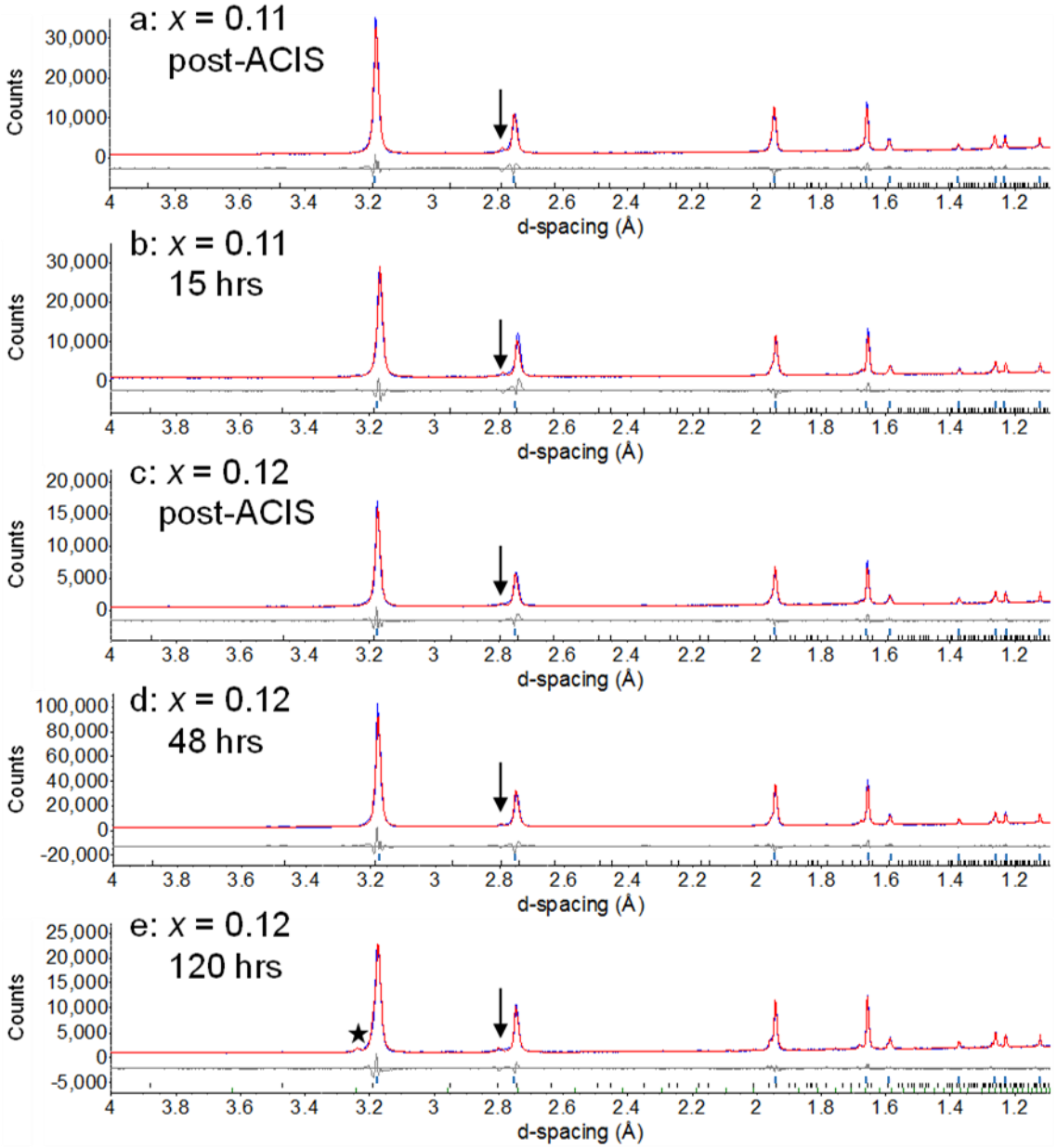

Figure 3.11: Rietveld fits to the PXRD patterns for $Bi_{.89}Nb_{0.11}O_{1.61}$ following: a) three cycles of heating during the impedance experiment, d7_02954; b) 15 hours heating at 825 °C, d7_03073. Rietveld fits to PXRD patterns for $Bi_{0.88}Nb_{0.12}O_{1.62}$ following: c) eight cycles of heating during impedance experiments, d7_06416; d) 48 hours at 825 °C, d7_04511; e) 120 hours at 825 °C, d7_07036. The blue and black tick marks correspond to the cubic and ($\sqrt{2} \times \sqrt{2} \times 1$) tetragonal phases respectively, and the arrows denote the key peaks arising from the tetragonal phase. The black star and green tick marks in Figure 3.11e denote the body-centered-cubic γ-Bi_2O_3-based phase.

3.6 Conclusions

$Bi_{0.9375}Nb_{0.0625}O_{1.5625}$ – previously reported as the Bi-rich end member of the Type II fluorite superstructure compositional range – forms two different polymorphs depending on the synthetic route taken: a tetragonal phase if furnace-cooled to room temperature, or a cubic phase if quenched. The tetragonal material adopts a $\sqrt{2} \times \sqrt{2} \times 1$ superstructure of the

δ-Bi_2O_3-based fluorite subcell, akin to β-Bi_2O_3. This material is stable as a tetragonal phase below 450 °C, and above 680 °C as a cubic phase, with the intermediate temperature region allowing for formation of a monoclinic phase.

The primary difference between the cubic and tetragonal materials is the atomic arrangement in the oxygen sublattices, which is mostly ordered in the tetragonal phase, but disordered in the cubic phase, consistent with the measured oxide-ion conductivities. In both forms, Bi and Nb remain disordered over the same crystallographic sites in the average structures, with evidence of structured diffuse scattering in electron and neutron diffraction patterns suggesting that a degree of short-range ordering is present.

The cubic forms of $Bi_{0.89}Nb_{0.11}O_{1.61}$ and $Bi_{0.88}Nb_{0.12}O_{1.62}$ are metastable, with both materials exhibiting conductivity decreases on extended heating of up to an order of magnitude due to partial transformation to the tetragonal phase. Despite this, the conductivities of the cubic materials remain slightly higher than that for yttria-stabilised zirconia, whilst the novel tetragonal phase is roughly an order of magnitude less conductive than the cubic phases, but still similar to the conductivities reported for other M^{5+}-doped bismuth oxide materials.

3.7 References

1. T. Takahashi and H. Iwahara, *Materials Research Bulletin*, 1978, **13**, 1447-1453.
2. H. A. Harwig, *Zeitschrift Fur Anorganische Und Allgemeine Chemie*, 1978, **444**, 151-166.
3. N. M. Sammes, G. A. Tompsett, H. Nafe and F. Aldinger, *Journal of the European Ceramic Society*, 1999, **19**, 1801-1826.
4. I. R. Evans, J. A. K. Howard and J. S. O. Evans, *Chemistry of Materials*, 2005, **17**, 4074-4077.
5. X. Kuang, J. L. Payne, M. R. Johnson and I. R. Evans, *Angewandte Chemie-International Edition*, 2012, **51**, 690-694.
6. C. D. Ling, W. Miiller, M. R. Johnson, D. Richard, S. Rols, J. Madge and I. R. Evans, *Chemistry of Materials*, 2012, **24**, 4607-4614.
7. J. L. Payne, J. D. Farrell, A. M. Linsell, M. R. Johnson and I. R. Evans, *Solid State Ionics*, 2013, **244**, 35-39.
8. M. T. Dunstan, F. Blanc, M. Avdeev, G. J. McIntyre, C. P. Grey and C. D. Ling, *Chemistry of Materials*, 2013, **25**, 3154-3161.
9. C. D. Ling, R. L. Withers, S. Schmid and J. G. Thompson, *Journal of Solid State Chemistry*, 1998, **137**, 42-61.
10. R. Miida and M. Tanaka, *Japanese Journal of Applied Physics Part 1*, 1990, **29**, 1132-1138.
11. C. D. Ling, S. Schmid, P. E. R. Blanchard, V. Petricek, G. J. McIntyre, N. Sharma, A. Maljuk, A. A. Yaremchenko, V. V. Kharton, M. Gutmann and R. L. Withers, *Journal of the American Chemical Society*, 2013, **135**, 6477-6484.
12. T. Takahashi, H. Iwahara and T. Esaka, *Journal of the Electrochemical Society*, 1977, **124**, 1563-1569.
13. G. Gattow and H. Schroeder, *Zeitschrift Fur Anorganische Und Allgemeine Chemie*, 1962, **318**, 176-189.
14. H. M. Rietveld, *Journal of Applied Crystallography*, 1969, **2**, 65-71.
15. S. K. Blower and C. Greaves, *Acta Crystallographica Section C*, 1988, **44**, 587-589.

16. P. Stephens, *Journal of Applied Crystallography*, 1999, **32**, 281-289.

17. M. L. Tate, J. Hack, X. Kuang, G. J. McIntyre, R. L. Withers, M. R. Johnson and I. Radosavljevic Evans, *Journal of Solid State Chemistry*, 2015, **225**, 383-390.

18. T. R. Welberry, M. J. Gutmann, H. Woo, D. J. Goossens, G. Xu, C. Stock, W. Chen and Z.-G. Ye, *Journal of Applied Crystallography*, 2005, **38**, 639-647.

19. D. J. Goossens, D. James, J. Dong, R. E. Whitfield, L. Norén and R. L. Withers, *Journal of Physics: Condensed Matter*, 2011, **23**, 065401.

20. R. L. Withers, T. R. Welberry, A. K. Larsson, Y. Liu, L. Norén, H. Rundlöf and F. J. Brink, *Journal of Solid State Chemistry*, 2004, **177**, 231-244.

21. G. C. Lau, T. M. McQueen, Q. Huang, H. W. Zandbergen and R. J. Cava, *Journal of Solid State Chemistry*, 2008, **181**, 45-50.

22. A. Martinelli, A. Palenzona, I. Pallecchi, C. Ferdeghini, M. Putti, S. Sanna, C. Curfs and C. Ritter, *Journal of Physics: Condensed Matter*, 2013, **25**, 395701.

23. C. Muller, F. Jacob, Y. Gagou and E. Elkaim, *Journal of Applied Crystallography*, 2003, **36**, 880-889.

24. M. Medarde and J. Rodríguez-Carvajal, *Zeitschrift für Physik B Condensed Matter*, 1997, **102**, 307-315.

25. J. T. S. Irvine, D. C. Sinclair and A. R. West, *Advanced Materials*, 1990, **2**, 132-138.

26. D. C. Sinclair, *Boletín de la Sociedad Española de Cerámica y Vidrio*, 1995, **34**, 55-65.

27. V. V. Kharton, F. M. B. Marques and A. Atkinson, *Solid State Ionics*, 2004, **174**, 135-149.

28. S. Boyapati, E. D. Wachsman and B. C. Chakoumakos, *Solid State Ionics*, 2001, **138**, 293-304.

29. E. D. Wachsman, S. Boyapati, M. J. Kaufman and N. Jiang, *Journal of the American Ceramic Society*, 2000, **83**, 1964-1968.

30. M. Leszczynska, X. Liu, W. Wrobel, M. Malys, M. Krynski, S. T. Norberg, S. Hull, F. Krok and I. Abrahams, *Chemistry of Materials*, 2013, **25**, 326-336.

31. D. W. Jung, K. L. Duncan, M. A. Camaratta, K. T. Lee, J. C. Nino and E. D. Wachsman, *Journal of the American Ceramic Society*, 2010, **93**, 1384-1391.

32. C. H. Hervoches and C. Greaves, *Journal of Materials Chemistry*, 2010, **20**, 6759-6763.

33. R. Punn, A. M. Feteira, D. C. Sinclair and C. Greaves, *Journal of the American Chemical Society*, 2006, **128**, 15386-15387.

4 The structure-property relationships of Bi(III)-containing apatite-type oxide-ion conductors

4.1 Background

Apatite-type materials are useful potentially as electrolyte materials in solid-oxide fuel cells (SOFCs) due to their high conductivities between 500 and 650 °C.[1-8] In recent years, increasing numbers of apatites have been reported as containing interstitial oxide ions, but debates on the precise locations of the interstitial oxygen atoms and conduction pathways are still ongoing.[3, 9-18]

In the literature, only a small number of Bi-containing apatites have been reported,[19-22] including the $Bi_2Ca_{8-2x}La_{2x}[(VO_4)_{6-2x}(GeO_4)_{2x}]O_2$ (x = 1, 2, 3) series by Zhuravlev *et al.*,[23] and $Bi_4Ca_2La_4[(SiO_4)_6]O_2$ by Lakshminarasimhan and Varadaraju.[24] In the latter case, the research focussed on the applications of a Eu^{3+}-doped form of this compound for luminescence, but the similarity of this compound with those reported by Zhuravlev *et al.* means that a family of compounds based on the general formula of $Bi_4Ca_{6-2x}La_{2+2x}[(VO_4)_{4-2x}(GeO_4)_{2+2x}]O_2$ (x = 0, 1, 2) could potentially be synthesised. No oxide-ion-conductivity measurements have been reported for these two sets of materials, and so this work investigates the effect of doping various concentrations of aliovalent cations onto the A and T metal sites (Figure 1.3) to promote the inclusion of interstitial oxide ions, and to investigate the effect this has on the oxide-ion conductivities of the materials.

From the range of materials synthesised, $Bi_2La_8[(GeO_4)_6]O_3$ is the first example of a triclinic Bi(III)-containing apatite. The structures of its triclinic and hexagonal forms at 30 °C and 830 °C respectively were determined using combined Rietveld refinements against synchrotron powder X-ray diffraction (PXRD) and powder neutron diffraction (PND) data. Variable-temperature (VT) synchrotron PXRD is also used to describe the reversible phase transition between the triclinic and hexagonal forms. The triclinic-structure determination is supported by annular bright-field scanning-transmission electron microscopy (ABF STEM) – which has imaged directly low concentrations of interstitial oxide ions for the first time – and second-harmonic-generation (SHG) analyses. The ABF STEM work was carried out in collaboration with Prof. Thomas Vogt (Department of Chemistry and Biochemistry and NanoCenter, University of South Carolina, USA) and Dr. Douglas Blom (Department of Chemical Engineering and NanoCenter, University of South Carolina, USA), whilst Prof. Shiv Halasyamani (Department of Chemistry, University of Houston, USA) collaborated on the SHG analysis.

Additionally, descriptions of the room-temperature hexagonal structures of two other novel compounds, $Bi_4Ca_2La_4[(GeO_4)_6]O_2$ and $Bi_4Ca_4La_2[(VO_4)_2(GeO_4)_4]O_2$, are presented. For these and $Bi_2La_8[(GeO_4)_6]O_3$, difference bond-valence-sum (BVS) maps and bond-valence energy landscapes (BVEL) reveal a link between bond-valence deviations from the ideal values for oxygen, and the oxide-ion migration pathways. For these three compounds and the related $Bi_2Ca_{8-2x}La_{2x}[(VO_4)_{6-2x}(GeO_4)_{2x}]O_2$ (x = 1, 2, 3) materials, conductivity data are presented

demonstrating the increased conductivity of the triclinic Bi(III)-containing apatite compared to those with hexagonal structures.

4.2 Synthesis of Bi(III)-containing apatite-type materials

Solid-state synthesis was used in an attempt to introduce additional oxygen content into the $Bi_2Ca_{8-2x}La_{2x}[(VO_4)_{6-2x}(GeO_4)_{2x}]O_2$ (x = 1, 2, 3) and $Bi_4Ca_{6-2x}La_{2x}[(VO_4)_{4-2x}(GeO_4)_{2+2x}]O_2$ (x = 0, 1, 2) families. Samples were synthesised for these six compositions (Parent in Table 4.2), in addition to others for which systematic A- and T-site doping was attempted (A-doped, T-doped, and A+T-doped), to increase the oxygen content and vary the A and T species. A total of 20 compositions were attempted (Table 4.2), with pure or almost pure samples obtained for eight of these compositions (highlighted in green in Table 4.2). The samples for the other 12 compositions were found to contain high percentages of a number of impurity phases, including GeO_2, $LaVO_3$, $LaVO_4$, and $Bi_4V_2O_{11}$. The large (25 and 30 g) samples of compositions 9 and 20 were prepared for use in floating-zone-furnace (FZF) crystal-growth experiments, the details of which are described in Section 7.6 of this thesis.

The reagents used for the syntheses are specified in Table 4.1, and the synthesis temperatures and heating durations given in Table 4.2, where heating and cooling rates of 5 °C per minute were used. Prior to use as a reagent, La_2O_3 was pre-calcined at 1000 °C for 2 hours.

Table 4.1: Manufacturer and purity of the reagents used for synthesis of the powdered samples.

	3 g samples		8 g and FZF samples	
Reagent	Manufacturer	Purity (%)	Manufacturer	Purity (%)
Al_2O_3	Sigma-Aldrich	99.00	Sigma-Aldrich	99.00
Bi_2O_3	Sigma-Aldrich	99.90	Sigma-Aldrich	99.90
$CaCO_3$	BDH	99.50	Sigma-Aldrich	99.00
GeO_2	Sigma-Aldrich	99.99	Sigma-Aldrich	99.99
La_2O_3	Sigma-Aldrich	99.99	Sigma-Aldrich	99.90
V_2O_5	Sigma-Aldrich	99.99	Sigma-Aldrich	99.60

Table 4.2: Reagent masses, structure types, and sample purities for the apatite-type compounds synthesised. The green highlighting shows samples which contain little to no impurities, with Y* denoting small percentages of impurity phases (from 0.7(1) % to 6.1(4) %), but which are still of sufficient purity for subsequent analysis. Compositions 9, 15, 16, and 19 have multiple samples of different masses, as they were used in a variety of analytical techniques.

$Bi_2Ca_{6-2x}La_{2x}[(VO_4)_{6-2x}(GeO_4)_{2x}]O_2$ Family																
			Bi_2O_3		$CaCO_3$		La_2O_3		V_2O_5		GeO_2					
Series	Type	Composition	Mass (g)	mmol	Mass (g)	mmol	Mass (g)	mmol	Mass (g)	mmol	Mass (g)	mmol	Structure	T (°C)	Time (hrs)	Serial Number	Pure?
x=1	Parent	$Bi_2Ca_4La_2[(VO_4)_4(GeO_4)_2]O_2$	0.8217	176	1059	10.58	0.5745	176	0.6415	3.53	0.3689	3.53	Hexagonal	1100	18	1	Y
	A-dope	$Bi_2Ca_4La_2[(VO_4)_4(GeO_4)_2]O_3$	0.73	157	0.6272	6.27	1.0209	3.13	0.5699	3.13	0.3278	3.13	Hexagonal	1100	54	2	N
	T-dope	$Bi_2Ca_4La_2[(VO_4)_4]O_3$	0.8351	179	1.0763	10.75	0.5839	179	0.9779	5.38	-	-	Hexagonal	1100	42	3	N
	A+T-dope	$Bi_2Ca_4La_2[(VO_4)_4(GeO_4)]O_3$	0.779	167	0.8367	8.36	0.8171	2.51	0.7602	4.18	0.1749	1.67	Hexagonal	1100	30	4	N
x=2	Parent	$Bi_2Ca_2La_4[(VO_4)_2(GeO_4)_4]O_2$	0.7197	154	0.6184	6.18	1.0065	3.09	0.2809	1.54	0.6463	6.18	Hexagonal	1100	30	5	Y
	A-dope	$Bi_2Ca_2La_4[(VO_4)_2(GeO_4)_4]O_3$	0.6484	139	0.2786	2.78	1.3601	4.17	0.2531	1.39	0.5823	5.57	Hexagonal	1100	18	6	N
	A+T-dope	$Bi_2Ca_2La_4[(VO_4)_2(GeO_4)_4]O_3$	0.6868	147	0.4426	4.42	1.2005	3.68	0.4021	2.21	0.4626	4.42	Hexagonal	1100	18	7	N
x=3	Parent	$Bi_2Ca_2La_4[(GeO_4)_6]O_2$	0.6403	137	0.2751	2.75	1.3431	4.12	-	-	0.8625	8.24	Hexagonal	1100	30	8	Y
	A-dope	$Bi_2La_4[(GeO_4)_6]O_3$	0.5832	125	-	-	1.6312	5.01	-	-	0.7856	7.51	Triclinic	1100	30	9	Y
	A-dope	$Bi_2La_4[(GeO_4)_6]O_3$	1.5552	3.34	-	-	4.3498	13.36	-	-	2.0949	20.03	Triclinic	1100	42	9	Y
	A-dope	$Bi_2La_4[(GeO_4)_6]O_3$	4.86	10.43	-	-	13.593	41.72	-	-	6.5466	62.58	Triclinic	1050	30	9	Y
	A+T-dope	$Bi_2CaLa_3[(VO_4)(GeO_4)_5]O_3$	0.6141	132	0.1319	1.32	1.5028	4.61	0.1198	0.66	0.6893	6.59	Hexagonal	1100	42	10	N

$Bi_4Ca_{4-2x}La_{2+2x}[(VO_4)_{4-2x}(GeO_4)_{2+2x}]O_2$ Family																	
			Bi_2O_3		$CaCO_3$		La_2O_3		V_2O_5		GeO_2						
Series	Type	Composition	Mass (g)	mmol	Mass (g)	mmol	Mass (g)	mmol	Mass (g)	mmol	Mass (g)	mmol	Structure	T (°C)	Time (hrs)	Serial Number	Pure?
x=0	Parent	$Bi_4Ca_4[(VO_4)_4(GeO_4)_2]O_2$	1.5183	3.26	0.9784	9.78	-	-	0.5927	3.26	0.3409	3.26	Hexagonal	1000	42	11	N
	A-dope	$Bi_4Ca_4La_2[(VO_4)_4(GeO_4)_2]O_3$	1.3604	2.92	0.5844	5.84	0.4756	1.46	0.531	2.92	0.3054	2.92	Hexagonal	1000	30	12	N
	T-dope	$Bi_4Ca_4[(VO_4)_4]O_3$	1.5412	3.31	0.9931	9.92	-	-	0.9024	4.96	-	-	Hexagonal	850	24	13	N
	A+T-dope	$Bi_4Ca_4La[(VO_4)_4(GeO_4)]O_3$	1.4452	3.1	0.7761	7.75	0.2526	0.78	0.7051	3.88	0.1622	1.55	Hexagonal	900	30	14	N
x=1	Parent	$Bi_4Ca_2La_4[(VO_4)_2(GeO_4)_4]O_2$	1.3426	2.88	0.5768	5.76	0.4694	1.44	0.262	1.44	0.6028	5.76	Hexagonal	1000	54	15	Y
	Parent	$Bi_4Ca_2La_4[(VO_4)_2(GeO_4)_4]O_2$	3.5802	7.68	1.5381	15.37	1.2517	3.84	0.6987	3.84	1.6076	15.37	Hexagonal	1000	42	15	Y*
x=2	Parent	$Bi_4Ca_2La_4[(GeO_4)_6]O_2$	1.2033	2.58	0.2585	2.58	0.8414	2.58	-	-	0.8104	7.75	Hexagonal	1100	54	16	Y
	Parent	$Bi_4Ca_2La_4[(GeO_4)_6]O_2$	3.2089	6.89	0.6893	6.89	2.2437	6.89	-	-	2.1612	20.66	Hexagonal	1050	30	16	Y*
	A-dope	$Bi_4La_4[(GeO_4)_6]O_3$	1.102	2.36	-	-	1.1558	3.55	-	-	0.7422	7.09	Hexagonal	1000	30	17	N

Additional Bi-containing Apatites																
			Bi_2O_3		$CaCO_3$		La_2O_3		GeO_2		Al_2O_3						
		Composition	Mass (g)	mmol	Mass (g)	mmol	Mass (g)	mmol	Mass (g)	mmol	Mass (g)	mmol	Structure	T (°C)	Time (hrs)	Serial Number	Pure?
		$Bi_6Ca_4La_2[(GeO_4)_6]O_2$	1.7023	3.65	0.2438	2.44	0.3968	1.22	0.7643	7.31	-	-	Hexagonal	900	42	18	N
		$Bi_6La_{3.6}[(GeO_4)_6]_{0.6}(AlO_4)_{0.4}]O_2$	0.6108	1.31	-	-	1.6014	4.92	0.7541	7.21	0.0334	0.33	Triclinic	1100	66	19	Y
		$Bi_6La_{3.6}[(GeO_4)_{5.6}(AlO_4)_{0.4}]O_2$	1.6287	3.5	-	-	4.2705	13.11	2.011	19.22	0.0891	0.87	Triclinic	1100	24	19	Y*
		$La_{9.4}[(GeO_4)_{5.4}(AlO_4)_{0.6}]O_2$	-	-	-	-	2.1608 6	66.32	8.0355	76.79	0.3559	3.49	Triclinic	1250	18	20	Y

4.3 Characterisation of the Bi(III)-containing apatite-type materials

4.3.1 Structural analysis of $Bi_2La_8[(GeO_4)_6]O_3$

For $Bi_2La_8[(GeO_4)_6]O_3$ (composition 9), a Rietveld refinement was performed using laboratory PXRD data and the hexagonal model reported by León-Reina *et al.* for $La_{9.5}[(GeO_4)_{5.5}(AlO_4)_{0.5}]O_2$ (space group $P6_3/m$) as a starting model.[25] The stoichiometry of the model was modified to reflect the cation composition, with the occupancies of the cation sites split according to the nominal composition, the O4 channel site occupancy altered to be fully occupied, and the interstitial O5 site removed, giving a structural formula of $Bi_2La_8[(GeO_4)_6]O_2$. The following parameters were refined: ten background parameters, one equated isotropic displacement parameter for all sites, peak-shape and scale-factor terms, zero-point error, and two lattice parameters.

From this refinement, it was found that the hexagonal structure produces a poor fit to the data (Figure 4.1a), with additional peaks observed (inset of Figure 4.1a). However, the fit improved greatly when a modified form of the triclinic structural model reported by León-Reina *et al.* for $La_{9.75}[(GeO_4)_6]O_{2.62}$ (space group $P\bar{1}$) was used (Figure 4.1b).[26] The choice of triclinic space group $P\bar{1}$ as opposed to P1 was confirmed by SHG measurements,[27] which when using 1064 nm light showed no response at 532 nm. This indicates that the material does not show evidence of second-harmonic generation, hence it is centrosymmetric, and that the choice of triclinic space group is correct. As for the hexagonal case, the triclinic model was altered to have the correct metal stoichiometry (with the Bi content split equally across all La sites), and the interstitial oxygen site identified in the León-Reina *et al.* model removed. For the triclinic phase, the same parameters were refined as the hexagonal phase, except six lattice parameters were refined instead of two. This is the first reported instance of a Bi(III)-containing apatite-type material with a triclinic structure.

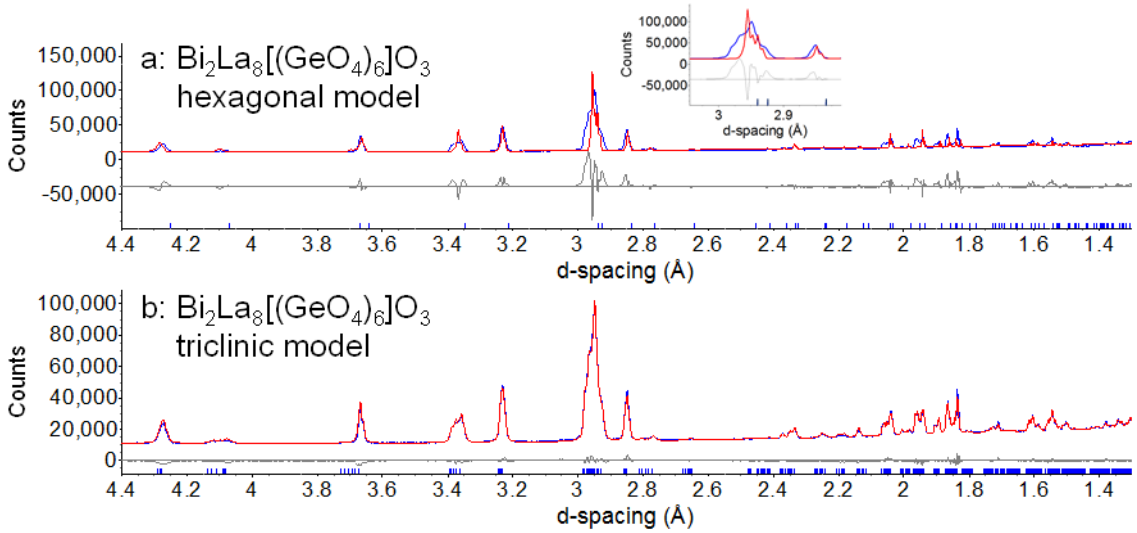

Figure 4.1: Rietveld refinements of: a) $Bi_2La_8[(GeO_4)_6]O_3$ (hexagonal structure), d7_05579, *a* = 9.8182(8) Å, *c* = 7.2825(6) Å, R_{wp} = 10.575 %; b) $Bi_2La_8[(GeO_4)_6]O_3$ (triclinic structure), d7_05579, *a* = 9.9067(2) Å, *b* = 9.8977(3) Å, *c* = 7.3496(1) Å, α = 90.580(2) °, β = 89.167(2) °, γ = 120.158(2) °, R_{wp} = 1.886 %.

In light of the analysis using laboratory PXRD data, synchrotron PXRD and PND data were collected to allow an accurate and complete triclinic structural model to be obtained, including refinement of the Bi occupancies across the A sites and the identification of the interstitial oxygen sites. In the literature, apatites with triclinic structures are reported to undergo phase transitions to hexagonal structures at high temperatures,[28, 29] and so VT synchrotron PXRD measurements were collected to investigate whether $Bi_2La_8[(GeO_4)_6]O_3$ undergoes the same triclinic-to-hexagonal phase transition (*vide infra*).

VT PND data were collected on heating and cooling between 30 and 830 °C in 100 °C steps, with collection times of 8 hours at 30 and 830 °C, and 2 hours for the intermediate temperatures. The temperature was equilibrated for 5 minutes upon reaching the set point prior to data collection. For the synchrotron PXRD data collections, 50 °C increments were used on heating and cooling between 30 and 930 °C, with 30 minutes for data collection at each of the two detector positions per temperature, with an equilibration time of 2 minutes per temperature.

Rietveld refinements using the 30 °C synchrotron PXRD data were performed initially, to refine the metal positions and A-site occupancies in the triclinic structure. The Bi content was refined across all the A^I (A1) and A^{II} (A2) sites (Table 4.3) where it was found to occupy only the three channel sites (A2), in an approximately 2:1 ratio of La:Bi.

For the 830 °C synchrotron PXRD data set, it was found that the data could be modelled with a hexagonal structure, and so the starting model used was a modified version of the hexagonal structural model for $La_{9.5}[(GeO_4)_{5.5}(AlO_4)_{0.5}]O_2$ reported by León-Reina *et al*.[25] As for the 30 °C data, the metal atomic coordinates and site occupancies were refined, with all of the Bi content found to occupy the A2 site.

Following the refinements using synchrotron PXRD data solely, neutron diffraction data were used to refine the oxygen atomic coordinates and locate the positions of the additional interstitial oxygen content using difference Fourier maps for both the triclinic and hexagonal structures (Figure 4.2). In the literature, there are two main areas suggested for the location of interstitial oxygen, either residing close to or just inside the wall of the framework cavity,[3, 9, 14, 25, 28, 30] or between pairs of neighbouring GeO_4 tetrahedra.[11, 12, 31]

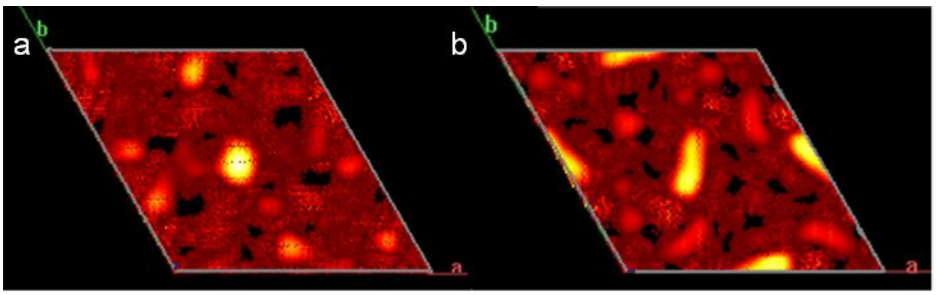

Figure 4.2: Difference Fourier maps for $Bi_2La_8[(GeO_4)_6]O_3$, viewed down the *z* axis showing the oxygen interstitial position, O5 (bright yellow) at: a) room temperature; b) 830 °C.

From the difference Fourier map for the triclinic structure at 30 °C (Figure 4.2a), one position at (0.5, 0.5, 0) was suggested with strong intensity, and reasonable distances and angles to

existing crystallographic sites. A better fit to the data and a more sensible structural model was obtained when the oxygen content was placed onto a general 2*i* position close to the 1*e* (0.5, 0.5, 0) special position. This 2*i* position means the oxygen atoms reside on either side of the inversion centre at the middle of the *xy* face, and was assumed in all further refinements. For the hexagonal structure at 830 °C (Figure 4.2b), one position of strong nuclear density was identified on the general 12*i* position at (0.45, 0.46, 0.03).

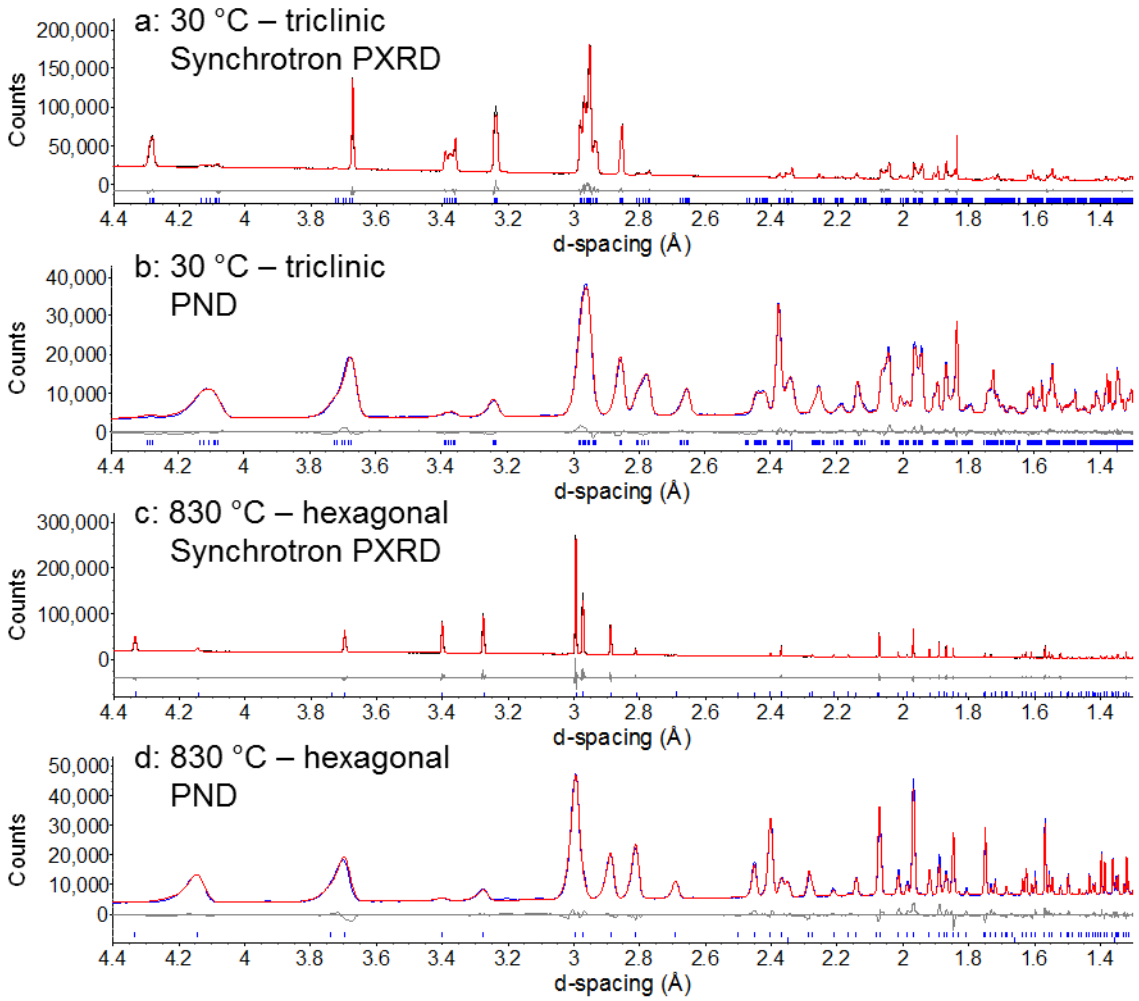

Figure 4.3: Rietveld fits for $Bi_2La_8[(GeO_4)_6]O_3$ at room temperature using: a) synchrotron PXRD data, MLT068_p12_ns_00 (filename), R_{wp} = 2.940 %; b) PND data, ECH0013068_Bi2La8Ge6O27_, R_{wp} = 4.346 %, (*a* = 9.9038(1) Å, *b* = 8.9959(1) Å, *c* = 7.15231(4) Å, *α* = 90.565(1) °, *β* = 89.199(1) °, *γ* = 120.140(1) °, space group $P\bar{1}$), and at 830 °C using: c) synchrotron PXRD data, MLT068_p12_ns_16 (filename), R_{wp} = 3.999 %; d) PND data, ECH0013076_Bi2La8Ge6O27_, R_{wp} = 4.904 %, (*a* = 10.00481(4) Å, *c* = 7.39163(4) Å, space group $P6_3/m$). The PND patterns contain a small contribution from the Nb in the furnace heating elements, shown by the lower set of blue tick marks in b) and d).

Following the identification of the O5 interstitial oxygen positions, combined refinements were performed using both synchrotron PXRD and PND data sets simultaneously to finalise the structural models at 30 °C (Figure 4.3a and Figure 4.3b) and 830 °C (Figure 4.3c and Figure 4.3d). For these refinements, the following parameters were refined: 10 or 20 (PND and synchrotron PXRD respectively) background terms and scale factors for each data set, peak-shape terms (PND) and size-strain terms (synchrotron PXRD), independent isotropic displacement parameters for each crystallographic site, six or two lattice parameters (for triclinic or hexagonal structures respectively), all atomic coordinates, spherical-harmonics parameters to

account for preferred orientation, and one lattice parameter for Nb modelled using Pawley[32] fitting (PND data only). Anti-bump restraints of 2.4 Å were used initially for the O5-O* distances (O* is any fully-occupied oxygen site), to prevent the interstitial oxygen positions from refining to unfeasibly short distances with neighbouring oxygen atoms, before being removed for the final refinement cycles.

To attempt to observe directly the interstitial oxygen atoms in triclinic $Bi_2La_8[(GeO_4)_6]O_3$ as opposed to just from difference Fourier maps, collaborative experiments were undertaken with Prof. Thomas Vogt and Dr. Douglas Blom (University of South Carolina, USA) using annular bright-field (ABF) imaging and frozen-phonon multi-slice image simulations. Dark shadows in the collected images denote the locations of atoms, including those with low atomic numbers (Z). Frozen-phonon multi-slice image simulations were also used to guide the experimental observations, as the simple Z-contrast approximations used in HAADF imaging are insufficient for the atomic columns observed via ABF imaging.

Frozen-phonon multi-slice image simulations were performed for the [001] orientation of $Bi_2La_8[(GeO_4)_6]O_3$ over a thickness of 30 cations, using the structure obtained via analysis of the room-temperature PND and synchrotron PXRD data as a starting model. This orientation provides maximum separation between the projected columns of interstitial oxygen atoms and neighbouring atomic sites. However, the separation of the A^I framework sites is below the resolution of the scanning-transmission electron microscope (STEM), meaning the A^I(a) and A^I(b) cations appear as one column in the simulated and experimental STEM images. For the three A^{II} sites, 10 Bi and 20 La atoms were arranged randomly along [001], as the Bi content on each A^{II} site varies by less than 3.3 atomic % (1 atom in 30). The interstitial O5 oxygen site is 50 % occupied, and so 15 oxygen atoms were distributed randomly across the 30 potential sites in both O5 projected columns in the unit cell.

An ABF simulation is shown in Figure 4.4a, with the unit cell denoted as a blue parallelogram, and the *x* axis horizontal. Figure 4.4b shows the assignment of the various columns of projected sites in the ABF simulation, including those for oxygen (black text) and cation sites (white text). Distinct projected columns are observed for the O1_1, O2_1, and O4 oxygen sites, whilst the columns of O1_2 and O2_2, and O1_3 and O2_3 overlap in this orientation, so cannot be resolved. Sites O3_1 and O3_4 overlap with the A2b site. The projected interstitial oxygen site O5 is at the approximate centre of the unit cell, and contrasts weakly. To test the intensity of the O5 site, two additional oxygen locations corresponding to the symmetry-equivalent *6g* sites in the hexagonal aristotype were tested, denoted as projected-sites X and Y in Figure 4.4b. The projected X site corresponds to the second-strongest feature in the difference Fourier map from neutron diffraction (Figure 4.2a), and is defined as halfway between the Ge T1_3 sites along the *x* axis. Likewise, projected-site Y lies halfway between the Ge T1_2 sites at $z = 0$ and 0.5. The local environments for sites O5, X, and Y are all similar. The integrated intensities for the different projected sites were extracted from the ABF simulation image and plotted (Figure 4.4c). In this plot, the site with highest contrast has the lowest integrated intensity (average ABF sum).

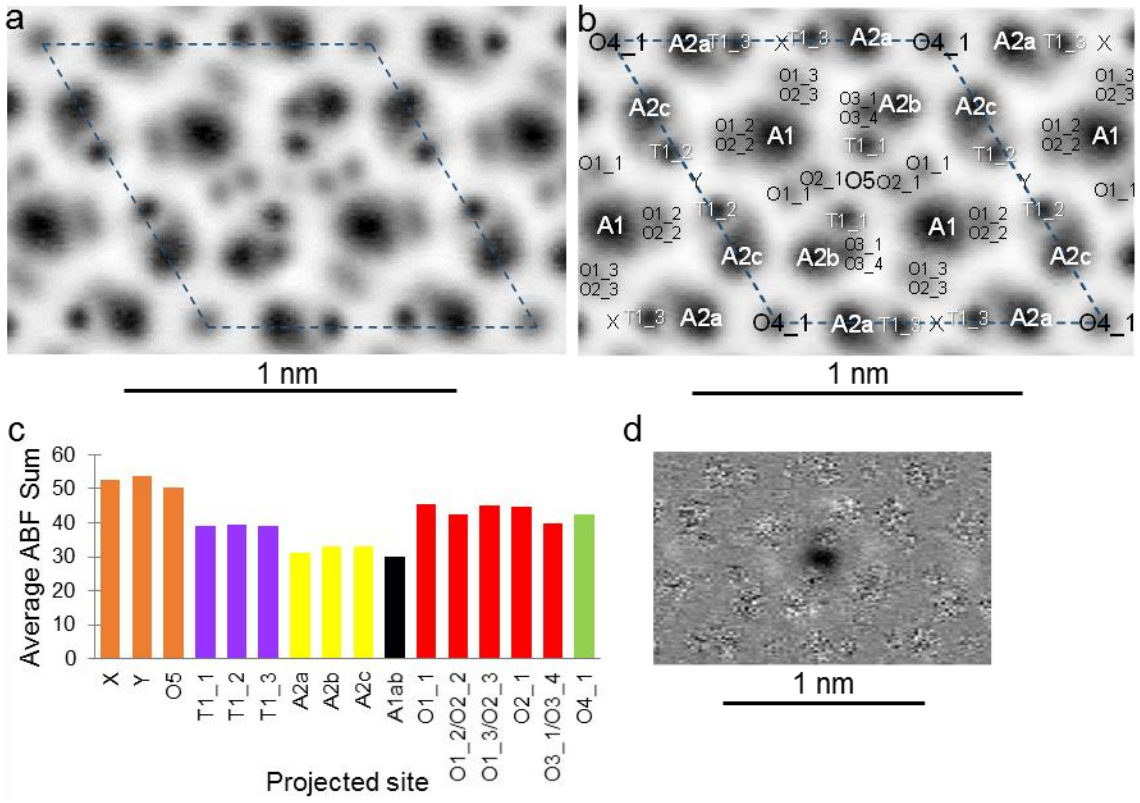

Figure 4.4: a) ABF image simulation for $Bi_2La_8[(GeO_4)_6]O_3$ viewed along [001]; b) The assignments of sites to the projected columns; c) Integrated intensities for the projected cation and oxygen sites. The graph is colour coded corresponding to the representation of the structure shown in Figure 4.7a; d) Difference ABF image between simulations including and excluding interstitial oxygen on the O5 site.

The columns of A^I framework cations (A1ab) have the highest image intensity, with the second-highest intensities found for the three A^{II} cation sites (A2a-c). The T sites contain lighter Ge atoms, and so are the next-most intense, followed by those for the various oxygen sites. The simulation suggests that placing interstitial oxygen content onto the O5 site does provide measurable contrast, shown by the lower average ABF sum compared to projected sites X and Y. An additional simulation was performed using an identical structural model, but no oxygen content was placed onto the O5 site. The difference image between these two simulations (Figure 4.4d), shows contrast localised to the projected location of the O5 site, suggesting that ABF STEM imaging is sensitive sufficiently to detect the 50 % occupancy of the O5 site.

The experimental ABF image collected for $Bi_2La_8[(GeO_4)_6]O_3$ along [001] (Figure 4.5a) shows all of the projected atomic columns that are observed in the ABF simulation image. For each column type across the experimental image, the signal intensities varied. If the intensity variations between different columns of the same type are due to random measurement errors, these intensities will follow a normal distribution. Deviations from normal distribution were observed for Ge T1_1, La/Bi A2b, and Ge T1_3, and to identify their cause, an analysis was performed for a non-centrosymmetric case with space group P1. Using this P1 model, the distributions of intensity for projected cation sites Ge T1_1 and A2b, and projected oxygen sites O3_1/O3_4 and O1_2/O2_2 show two distinct subsets, each of which is distributed normally. This suggests that the average structure of $Bi_2La_8[(GeO_4)_6]O_3$ is centrosymmetric, but that there

are local-scale deviations from centrosymmetry on a length scale too short for observation by SHG measurements.

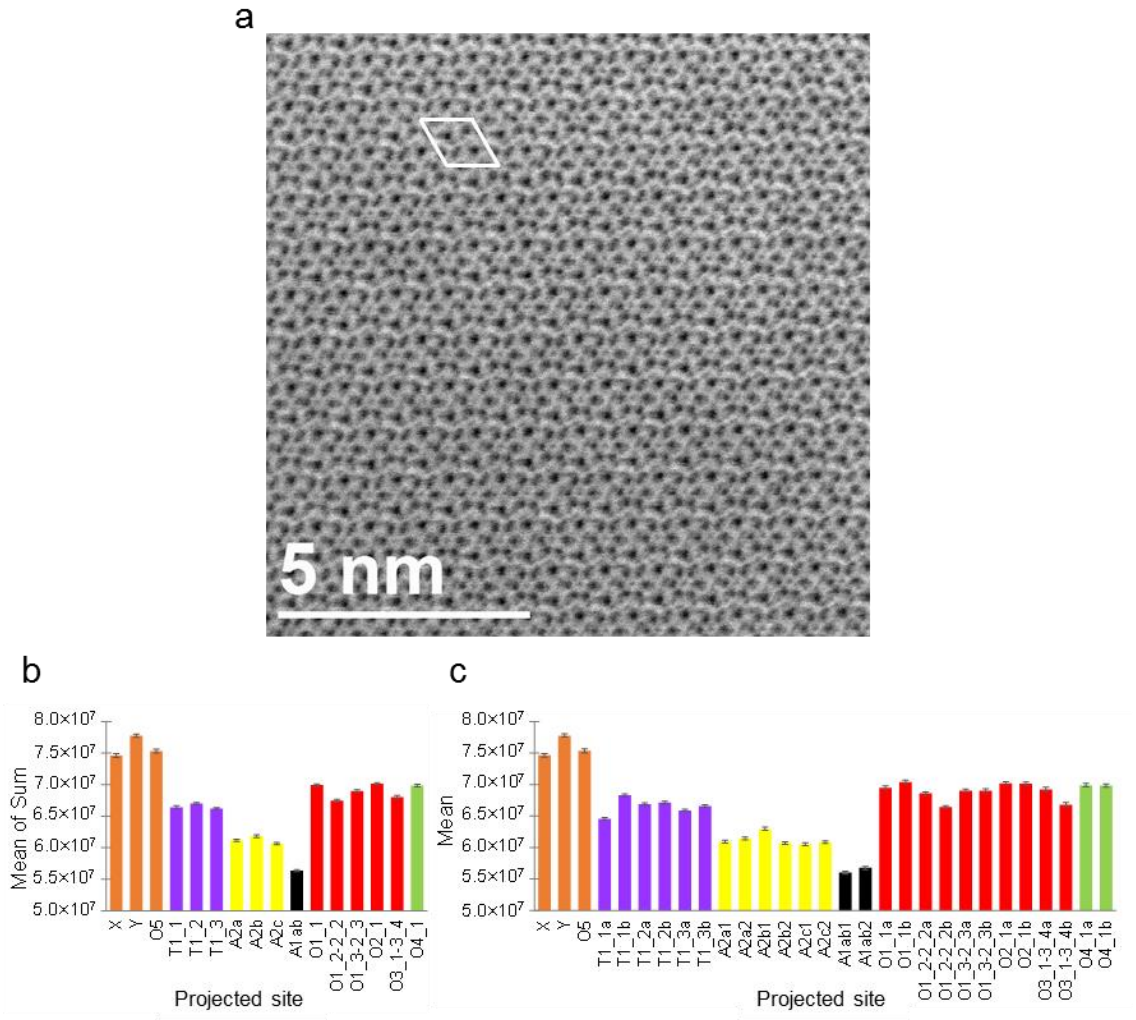

Figure 4.5: a) Experimental ABF image for the [001] orientation of $Bi_2La_8[(GeO_4)_6]O_3$; b) Integrated intensities for the cation and oxygen atom columns in space group $P\bar{1}$; c) Integrated intensities for different cation and oxygen atom columns without the inversion-centre symmetry constraint. b) and c) are colour coded corresponding to the representation of the structure shown in Figure 4.7a.

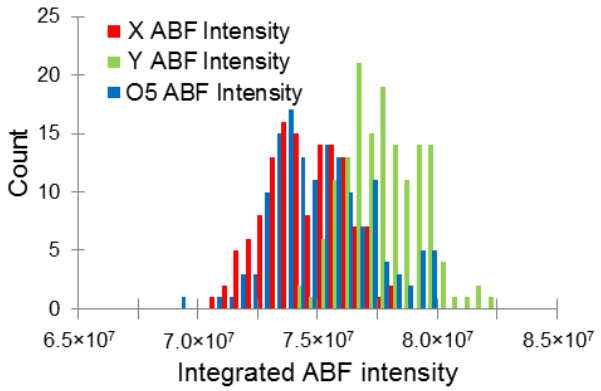

Figure 4.6: Integrated ABF intensities for projected sites O5, X, and Y. A darker contrast results in a lower integrated ABF intensity.

Virtually identical levels of electron scatter are observed for projected-sites O5 and X based on the integrated column intensities from the experimental image, both of which are more

intense than that observed for projected-site Y (Figure 4.5b and Figure 4.5c). Projected-sites X and Y should have identical intensities and be brighter than site O5 based on the results of the frozen-phonon multi-slice simulations. However, histograms of the column intensities for these three projected sites (Figure 4.6) show that there is more electron scattering density on sites O5 and X than on Y. Therefore, it can be concluded that low-level interstitial oxygen content can be imaged successfully in $Bi_2La_8[(GeO_4)_6]O_3$ in two locations, with a combined occupancy of one oxygen atom per formula unit. In the literature previously, dark spots distributed randomly through high-resolution transmission electron microscopy images were observed in apatite and perovskite materials,[33, 34] with these dark spots thought to arise from local-scale lattice distortion caused by interstitial oxygen. However, the interstitial oxygen was not imaged directly in these cases, making this ABF STEM analysis the first to image directly interstitial oxygen content.

In light of the ABF STEM work identifying multiple locations for interstitial oxygen content, oxygen atoms were placed onto the second-strongest residual peak ~(0.50826, 0.89497, 0.93865) from the 30 °C difference Fourier map, along with the four similar sites which are independent in the triclinic structure, but with the O5 site, comprise the six *6g* symmetry-equivalent sites in the hexagonal apatite aristotype. A systematic analysis was undertaken with various parameters refined: performing Rietveld refinements using both combined data sets (synchrotron PXRD and PND data) or PND data solely; testing the six interstitial sites occupied either one at a time, or simultaneously; either using or omitting restraints for the total O content; using equated or independent atomic displacement parameters. This series of analyses shows that whilst some information is contained in the powder diffraction data with regards to the excess oxygen content, the data are not sensitive enough to determine reliably the distribution of oxygen across all possible interstitial sites. A decrease in R_{wp} is observed when oxygen content is placed onto any one of the six symmetry-equivalent interstitial sites (PND R_{wp} = 5.083 to 5.276 %) compared to no presence of additional oxygen (PND R_{wp} = 5.357 %). However, whilst a further decrease in R_{wp} occurs when oxygen content is placed onto multiple symmetry-equivalent interstitial sites simultaneously, issues arise relating to isotropic displacement values or bond distances. When refining the oxygen content across all six symmetry-equivalent sites together, this results in a PND R_{wp} of 4.140 %, but the isotropic displacement parameters are all negative, and short O-O distances of 1.28(3) and 1.32(6) Å are found. Likewise, attempts to refine oxygen content on the O5 and X (from ABF study) sites gives a PND R_{wp} of 4.482 %, with positive isotropic displacement parameters of B_{iso} = 4(2) and 6(2) $Å^2$ for the O5 and X sites respectively, but the X-O1_3 distance is 1.34(6) Å, which is unrealistically short.

In light of this, Figure 4.7a and Table 4.3 show currently the best possible triclinic structural model for $Bi_2La_8[(GeO_4)_6]O_3$. Several sites in this model have very small isotropic displacement parameters (O2_1 and O3_4 B_{iso} = 0.2(2) $Å^2$, and O1_1 B_{iso} = 0.3(2) $Å^2$). These oxygen atoms are within the T1_1O_x coordination sphere, the same T site to which the interstitial O5 is bonded. An alternative approximate structural model was generated which equates the isotropic displacement parameters of the fully-occupied O1 to O3 sites according to the T site to which they are bonded. The fits to the data using a structural model with equated isotropic

displacement parameters give R_{wp} values similar to those found for the model with independent isotropic displacement parameters (Figure 4.3a and Figure 4.3b), where the synchrotron PXRD R_{wp} = 2.740 % and 2.940 % and the PND R_{wp} = 3.988 % and 4.346 % for the equated and independent cases respectively.

Table 4.3: Crystallographic data for triclinic $Bi_2La_8[(GeO_4)_6O_3$ at 30 °C. Space group $P\bar{1}$, a = 9.9038(1) Å, b = 9.8959(1) Å, c = 7.3462(1) Å, α = 90.565(1) °, β = 89.199(1) °, γ = 120.140(1) °, V = 622.57(1) Å^3. The A^I sites are denoted as A1a and A1b, A^{II} sites are A2a, A2b and A2c, whilst the T sites are T1_1, T1_2, and T1_3.

Site	Atom	x	y	z	occ	B_{iso} (Å^2)
A1a	La	0.3220(6)	0.6705(6)	0.4943(5)	1	2.01(9)
A1b	La	0.6579(6)	0.3471(6)	0.0012(5)	1	1.61(9)
A2a	La	0.2255(4)	–0.0062(4)	0.2578(4)	0.66(2)	2.01(8)
A2a	Bi	0.2255(4)	–0.0062(4)	0.2578(1)	0.34(2)	2.01(8)
A2b	La	0.2341(4)	0.2281(4)	0.7579(5)	0.68(2)	2.30(9)
A2b	Bi	0.2341(4)	0.2281(4)	0.7579(5)	0.32(2)	2.30(9)
A2c	La	0.0037(4)	0.2360(5)	0.2573(5)	0.66(2)	2.8(1)
A2c	Bi	0.0037(4)	0.2360(5)	0.2573(5)	0.34(2)	2.8(1)
T1_1	Ge	0.4081(6)	0.3754(5)	0.2575(6)	1	1.8(1)
T1_2	Ge	0.0218(5)	0.3959(6)	0.7540(6)	1	0.8(1)
T1_3	Ge	0.6230(6)	0.0138(5)	0.2380(6)	1	0.8(1)
O1_1	O	0.2747(7)	0.4544(7)	0.2549(9)	1	0.3(2)
O1_2	O	0.8232(10)	0.3327(9)	0.7754(11)	1	1.3(2)
O1_3	O	0.5024(11)	0.8268(11)	0.2452(13)	1	3.1(2)
O2_1	O	0.6158(9)	0.4928(7)	0.2831(10)	1	0.2(2)
O2_2	O	0.1532(9)	0.6034(10)	0.7542(11)	1	1.9(2)
O2_3	O	0.5298(12)	0.1284(9)	0.2230(11)	1	2.2(3)
O3_1	O	0.3175(10)	0.2299(11)	0.0738(11)	1	2.4(2)
O3_2	O	0.0560(13)	0.2827(12)	0.6037(14)	1	5.1(3)
O3_3	O	0.7738(12)	0.0676(11)	0.0683(12)	1	3.2(3)
O3_4	O	0.6469(8)	0.7503(8)	0.5615(10)	1	0.2(2)
O3_5	O	0.9091(11)	0.6567(12)	0.0562(15)	1	3.5(3)
O3_6	O	0.2539(13)	0.8918(12)	0.5484(14)	1	4.4(3)
O4	O	0.0145(11)	0.0100(13)	0.3105(8)	1	2.9(2)
O5	O	0.475(4)	0.510(4)	0.024(4)	1/2	6.1(7)

Table 4.4: Crystallographic data for hexagonal $Bi_2La_8[(GeO_4)_6O_3$ at 830 °C. Space group $P6_3/m$, a = 10.00489(4) Å, c = 7.39165(4) Å, V = 640.762(6) Å^3. The A^I site is denoted A1, the A^{II} site is A2, and the T site is T1.

Site	Atom	x	y	z	occ	B_{iso} (Å^2)
A1	La	1/3	2/3	0.4998(3)	1	2.93(4)
A2	La	0.2271(1)	–0.0070(2)	1/4	2/3	3.93(3)
A2	Bi	0.2271(1)	–0.0070(2)	1/4	1/3	3.93(3)
T1	Ge	0.4015(2)	0.3757(1)	1/4	1	2.31(4)
O1	O	0.3180(3)	0.4902(3)	1/4	1	4.27(7)
O2	O	0.6011(3)	0.4674(3)	1/4	1	3.79(7)
O3	O	0.3341(2)	0.2461(2)	0.0657(2)	1	5.77(5)
O4	O	0	0	1/4	1	6.3(1)
O5	O	0.506(2)	0.542(2)	–0.070(2)	1/12	0.1(4)

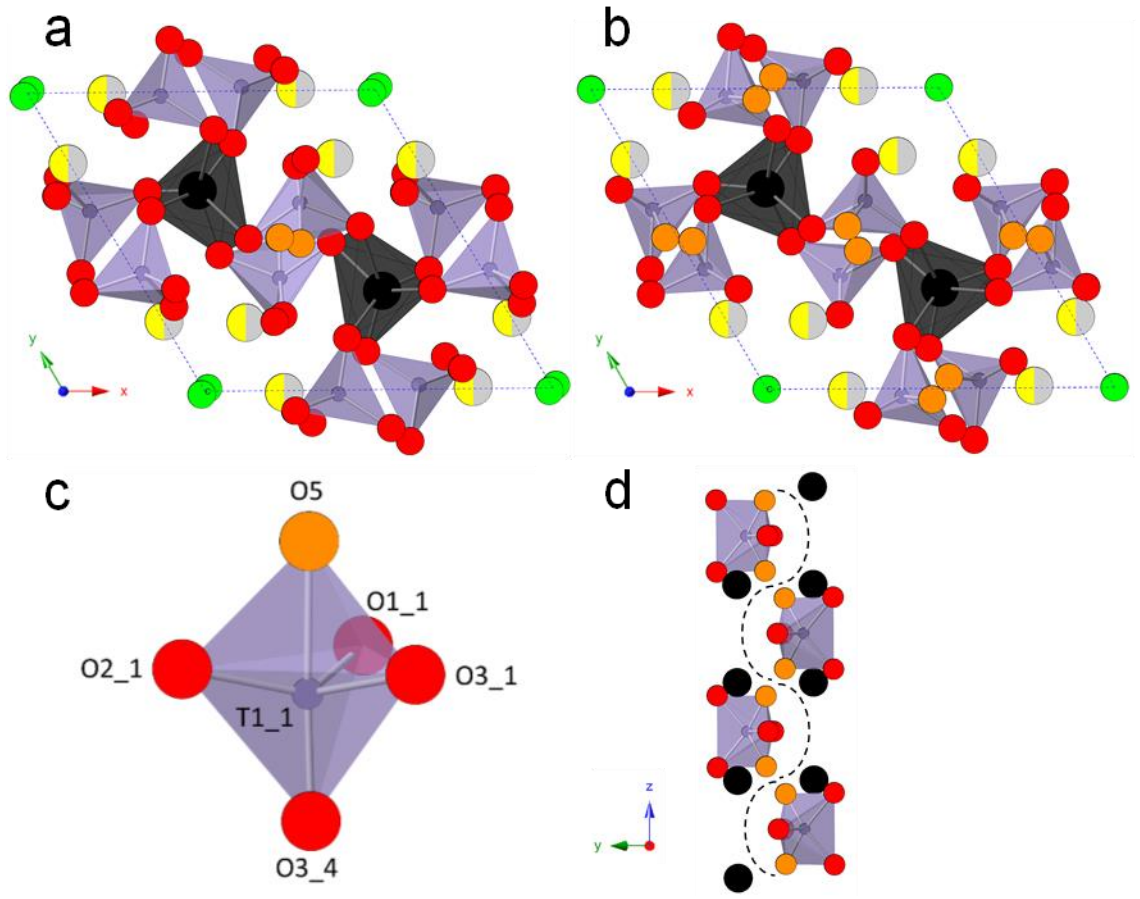

Figure 4.7: a) Room temperature triclinic structure of $Bi_2La_8[(GeO_4)_6]O_3$ viewed down the *z* axis. b) 830 °C hexagonal structure for $Bi_2La_8[(GeO_4)_6]O_3$ viewed down the *z* axis. c) The Ge T1_1O_5 trigonal bipyramid in triclinic $Bi_2La_8[(GeO_4)_6]O_3$. d) View down the *x* axis of a GeO_x polyhedral chain, showing a potential interstitial oxide-ion migration pathway (dotted line). [A^I] (La) = black, [A^{II}] (La/Bi) = grey/yellow, T (Ge) = purple, O1-O3 = red, O4 = green, and interstitial O5 = orange. The mixed occupancy sites are denoted by their split colouration, and the bonds to the A^{II} and O4 sites have been omitted for clarity.

Figure 4.7b and Table 4.4 show the hexagonal structural model for $Bi_2La_8[(GeO_4)_6]O_3$ at 830 °C, using independent isotropic displacement parameters for the atomic sites. If a similar approach is taken as for the triclinic case, and the isotropic displacement parameters for the fully-occupied oxygen sites are equated, the R_{wp} values are virtually identical. The independent model has R_{wp} values of 4.904 % (PND) and 3.999 % (synchrotron PXRD), whilst the equated case has R_{wp} values of 5.044 % (PND) and 3.976 % (synchrotron PXRD).

Both the triclinic and hexagonal structures can be described as $La_4[(GeO_4)_6O]$ apatite frameworks containing $(La_4Bi_2)O_2$ units in the framework cavities, with differences between the two structural models arising due to the location of the interstitial oxygen atoms within the apatite framework. The interstitial oxygen atoms, O5, occupy positions close to the centre of the pairs of neighbouring GeO_4 tetrahedra, forming GeO_5 trigonal bipyramids (Figure 4.7c). In the triclinic structure, the O5 position lies between the GeO_4 tetrahedra near the centre of the *xy* face (0.475(4), 0.520(4), 0.024(4)).

In the literature, Pramana *et al.* report that the interstitial oxygen content is located near the centre of the *yz* face at (0.028(4), 0.477(4), 0.511(5)) for triclinic $La_{10}[(GeO_4)_6]O_3$, similar to the

interstitial position for triclinic $Bi_2La_8[(GeO_4)_6]O_3$, but on a different face.[11] However, the PND data used for their Rietveld analysis are of poor quality relatively, with collected intensities roughly two orders of magnitude lower than those used in this report, hence the peaks with weak intensities will be much harder to discern from the background in their data. For hexagonal $Bi_2La_8[(GeO_4)_6]O_3$, the O5 atoms occupy positions between all pairs of neighbouring GeO_4 tetrahedra in the hexagonal structure (0.506(2), 0.542(2), –0.070(2)), meaning the interstitial oxygen content can potentially be found near any of the face centres, the body centre, or centres of the cell edges (bar ~(0, 0, 0.5)) of the unit cell. These positions are similar to those reported by Kendrick *et al.* for $La_8Y_2[(GeO_4)_6]O_3$ (0.070(2), 0.473(2), –0.043(3)).[12] Due to the occupancy of the O5 site, statistically there will be one GeO_5 trigonal bipyramid per unit cell, and so the alternative structural formula of $Bi_2La_8[(GeO_4)_5(GeO_5)]O_2$ can be used.

Formation of a GeO_5 trigonal bipyramid occurs through introduction of an interstitial oxygen atom coupled with distortion of the GeO_4 tetrahedron, where the interstitial oxygen position occupies an axial site on the polyhedron (Figure 4.7c). Distortion of the polyhedra is evidenced by the O-Ge-O bond angles ranging from 76.6(9) to 124.1(4) ° and 60.7(6) to 117.5(1) ° in the triclinic and hexagonal structures respectively. These wide bond-angle ranges are similar to those reported by Pramana *et al.* for the GeO_5 polyhedra in $La_{10}[(GeO_4)_6]O_3$ of 83(3) to 105(3) °,[11] and by Kendrick *et al.* for $La_8Y_2[(GeO_4)_6]O_3$ of 66.7(8) to 126.8(6) °.[12] The wider bond-angle range given by Kendrick is due to increased distortion of the polyhedra in the hexagonal structure to allow for potential inclusion of two interstitial oxygen atoms (i.e. forming a GeO_6 polyhedron) due to the 1/12 multiplicity of the interstitial oxygen site. A similar level of distortion is seen for hexagonal $Bi_2La_8[(GeO_4)_6]O_3$ (again due to the 1/12 multiplicity of the O5 site), as shown by the O-Ge-O bond-angle range of 56.8(6) ° compared to 60.1(8) ° given by Kendrick.

The interstitial oxide-ion migration pathway was reported previously by Kendrick *et al.* as occurring in a ‘fan-like’ motion parallel to the *z* axis between the GeO_4 tetrahedra (Figure 4.7d).[12] This motion is also reported for $La_{10}[(GeO_4)_6]O_3$ by Imaizumi *et al.*, who through computational modelling techniques observed the same migration pathway, in addition to migration between channels perpendicular to the *z* axis.[15] This conductivity mechanism has also been reported by Pramana *et al.* for $La_{10}[(GeO_4)_6]O_3$, who propose an intra-tunnel migration pathway utilising oxygen atoms on the O3 and O5 sites (O12 and O14 in their description) which move along [010] through a saddle point located between the O4 channel oxygen atoms at (0, 0, 0.5).[11] The saddle point denotes the position along the migration pathway with the highest energy. However, this proposed pathway is just hypothetical, with Pramana *et al.* providing no simulations or experimental results to support their claim. Conductivity in the *xy* plane is not limited to lanthanum germanates, with reports detailing an oxide-ion migration pathway using the O3 and O4 atoms and either vacancies in the framework lattice[17] or rotation of SiO_4 tetrahedra to give Si_2O_9 dimers.[35] Overall, the additional oxygen content in $Bi_2La_8[(GeO_4)_6]O_3$ lies along these same migration pathways, supporting the findings for the interstitial oxygen positions.

4.3.2 Structural phase transition in $Bi_2La_8[(GeO_4)_6]O_3$

From the 30 °C and 830 °C data sets, it is shown that $Bi_2La_8[(GeO_4)_6]O_3$ undergoes a triclinic-to-hexagonal phase transition. To investigate the temperature at which this transition occurs, sequential Rietveld refinements were performed to observe the change in the lattice parameters as a function of temperature from the *in situ* VT synchrotron PXRD data between 30 and 930 °C on heating and cooling in 50 °C increments.[36]

For each temperature range, the following parameters were refined: zero-point error, ten background terms, six lattice parameters, two isotropic displacement parameters (one for the metal sites and one for the oxygen sites), scale factor, and size-strain terms to model sample contributions to the peak shape. Plots showing the variation of the lattice parameters and cell volume with temperature are given in Figure 4.8.

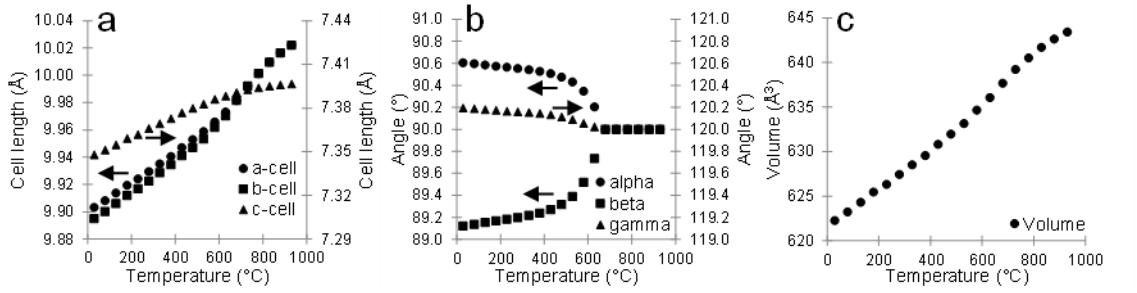

Figure 4.8: Change in the lattice parameters with temperature for $Bi_2La_8[(GeO_4)_6]O_3$ between 30 and 930 °C, demonstrating the reversible triclinic-to-hexagonal phase transition. a) *a*, *b*, and *c* cell lengths; b) α, β, and γ angles; c) unit-cell volume. The error bars are smaller than the data points.

On increasing the temperature from 30 to 930 °C, there is a gradual transition from the triclinic to hexagonal structure between 480 and 680 °C, with the hexagonal phase present above 680 °C. This can be seen clearly in Figure 4.8b, where the α and β angles decrease and increase with temperature respectively to 90 °, whilst the γ angle decreases to 120 ° as the temperature is increased up to 680 °C, denoting the change to the hexagonal structure. This is also seen in Figure 4.8a, where the *a* and *b* cell-length parameters are identical above the phase-transition temperature. On cooling, the phase transition was found to be reversible, with the hexagonal-to-triclinic phase transition occurring at 680 °C. This phase transition occurs at a similar temperature to that reported for the triclinic apatites, $La_{9.75}[(GeO_4)_6]O_{2.625}$ and $La_{10}[(GeO_4)_6]O_3$, which undergo triclinic-to-hexagonal phase transformations at ~750 °C and 850 °C respectively.[28, 29]

For $La_{10}[(GeO_4)_6]O_3$, Abram *et al.* only report that they indexed the pattern using a hexagonal cell above 850 °C, but do not present a structural model for this hexagonal phase.[29] Whilst León-Reina *et al.* do present a hexagonal structural model for $La_{9.75}[(GeO_4)_6]O_{2.625}$,[28] the interstitial oxygen content is found ~1.1 Å from the fully-occupied O3 site based on analysis of their difference Fourier maps generated from PND data at 800 °C. They suggest that local relaxation will occur following the introduction of oxygen on this interstitial site to increase the O-O distance, though no results were presented to support this. Additionally, the triclinic structural model used to describe the low-temperature structure was obtained in a previous

work and is incomplete, having a structural formula of $La_{9.75}[(GeO_4)_6]O_2$.[26] Therefore, the work presented here for $Bi_2La_8[(GeO_4)_6]O_3$ is the first to characterise fully the triclinic-to-hexagonal phase transition, and give complete structural models for both phases.

4.3.3 Structural analysis of novel hexagonal apatite-type materials

Analysis of laboratory PXRD data collected for $Bi_4Ca_4La_2[(VO_4)_2(GeO_4)_4]O_2$ and $Bi_4Ca_2La_4[(GeO_4)_6]O_2$ (compositions 15 and 16) using modified versions of the hexagonal structural model reported by León-Reina *et al.* for $La_{9.5}[(GeO_4)_{5.5}(AlO_4)_{0.5}]O_2$ (space group $P6_3/m$)[25] as starting models produced good fits to the data (Figure 4.9).

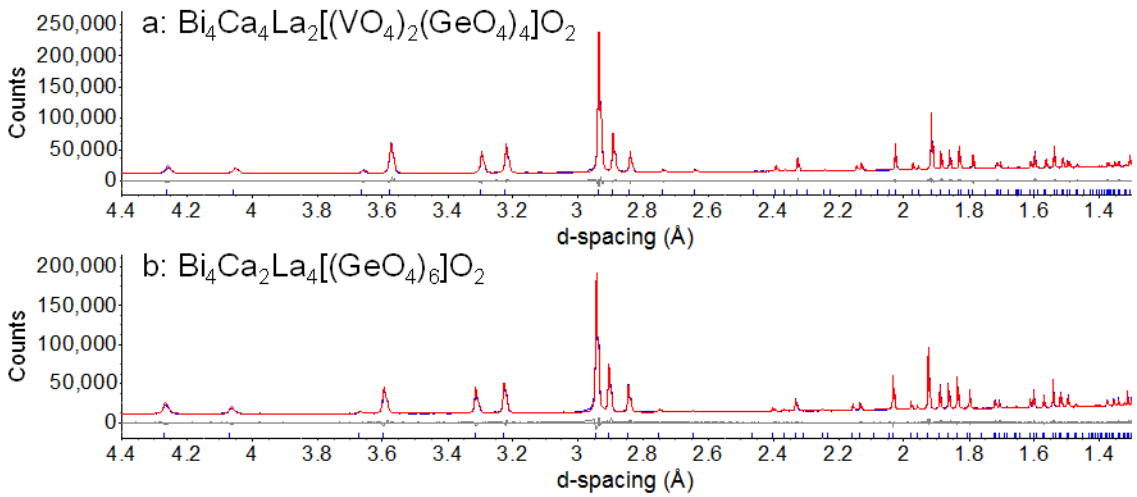

Figure 4.9: Rietveld refinements of: a) $Bi_4Ca_4La_2[(VO_4)_2(GeO_4)_4]O_2$, d7_05704, *a* = 9.8469(1) Å, *c* = 7.1548(1) Å, R_{wp} = 2.055 %; b) $Bi_4Ca_2La_4[(GeO_4)_6]O_2$, d7_05703, *a* = 9.8642(1) Å, *c* = 7.1979(1) Å, R_{wp} = 2.324 %.

For the starting structural models in both refinements, the occupancies of the A sites were split according to the nominal compositions, the O4 channel site occupancies were changed to be fully occupied, and the interstitial O5 sites were removed. Ten background parameters, one isotropic displacement parameter for all sites, peak-shape and scale-factor terms, zero-point error, and two lattice parameters were refined for both samples.

Following the analysis of the laboratory PXRD data, room-temperature synchrotron PXRD and PND data were collected for $Bi_4Ca_4La_2[(VO_4)_2(GeO_4)_4]O_2$ and $Bi_4Ca_2La_4[(GeO_4)_6]O_2$, so that complete structural models of these new materials could be obtained. The starting model for the refinements was the hexagonal structural model of $Bi_2La_8[(GeO_4)_6]O_3$ (Table 4.4), albeit with the interstitial oxygen content removed and the metal content split equally across all relevant sites according to the stoichiometry of the material. For each composition, a combined refinement of the synchrotron PXRD and PND data sets was undertaken with the following parameters refined: 10 or 20 background parameters (PND and synchrotron PXRD), two lattice parameters, independent isotropic displacement parameters for each crystallographic site, all atomic coordinates, metal-site occupancies, scale factors, peak-shape terms (PND) and size-strain terms (synchrotron PXRD). The metal-site occupancies were restrained to maintain the correct overall stoichiometry, but were allowed to refine freely across the A1 and A2 sites. For

$Bi_4Ca_4La_2[(VO_4)_2(GeO_4)_4]O_2$, the La occupancy on the A^I site refined to zero, so all of the La atoms were placed onto the A^{II} site. Likewise, for $Bi_4Ca_2La_4[(GeO_4)_6]O_2$, the Ca occupancy on the A^{II} site refined to zero, so all of the Ca atoms were placed onto the A^I site. The $Bi_4Ca_4La_2[(VO_4)_2(GeO_4)_4]O_2$ sample contains a small percentage of $Bi_4V_2O_{11}$, and so two lattice parameters and one isotropic displacement parameter were refined for this impurity phase, whilst $Bi_4Ca_2La_4[(GeO_4)_6]O_2$ contains a small amount of Bi_2GeO_5, so three lattice parameters and one isotropic displacement parameter were refined for this phase. The final fits to the data sets are presented in Figure 4.10.

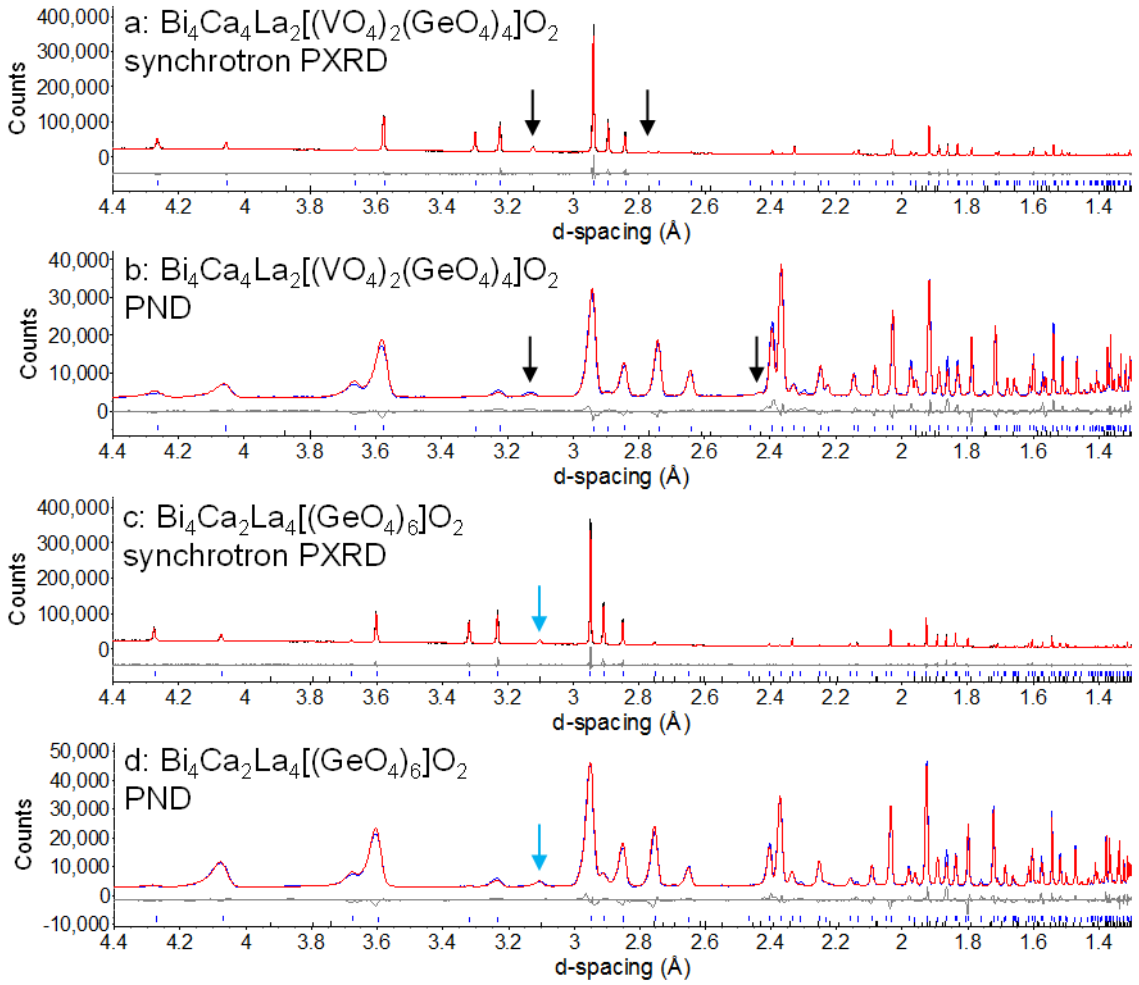

Figure 4.10: Rietveld fits for $Bi_4Ca_4La_2[(VO_4)_2(GeO_4)_4]O_2$ (*a* = 9.84710(5) Å, *c* = 7.15231(4) Å, space group $P6_3/m$) at room temperature to: a) synchrotron PXRD data, MLT069_p12_ns_0, R_{wp} = 4.642 %; b) PND data, ECH0013084_Bi4Ca4La2V2Ge4O26_, R_{wp} = 5.755 %. The peak positions for the $Bi_4V_2O_{11}$ impurity phase are denoted with black tick marks and the $Bi_4V_2O_{11}$ impurity peaks with black arrows. Rietveld fits for $Bi_4Ca_2La_4[(GeO_4)_6]O_2$ (*a* = 9.86970(4) Å, *c* = 7.19700(4) Å, space group $P6_3/m$) at room temperature to: c) synchrotron PXRD data, MLT070_p12_ns_0, R_{wp} = 4.804 %; d) PND data, ECH0013085_Bi4Ca2La4Ge6O26_, R_{wp} = 7.490 %. The peak positions for the Bi_2GeO_5 impurity phase are denoted with black tick marks and the Bi_2GeO_5 impurity peaks with blue arrows.

The general structure for these two materials is the same as for hexagonal $Bi_2La_8[(GeO_4)_6]O_3$: a framework of $[A^I_4][(TO_4)_6]$ surrounding $A^{II}_6O_2$ units (A = Bi/Ca/La, T = V/Ge), with the Bi atoms favouring the channel site (A2) predominantly, whilst the Ca atoms prefer the framework site (A1). The same site preferences were observed in the structure of $Bi_2Ca_8[(VO_4)_6]O_2$, determined from single-crystal data, which shows Bi favouring the channel site whilst the Ca atoms occupy primarily the framework sites.[19] For both hexagonal materials,

the isotropic displacement parameter is highest for O4 (as these oxygens are involved in oxide-ion migration along the *z* axis, and so are likely to be the most mobile).

Table 4.5: Crystallographic data for hexagonal $Bi_4Ca_4La_2[(VO_4)_2(GeO_4)_4]O_2$ at room temperature. Space group $P6_3/m$, a = 9.84710(5) Å, c = 7.15231(4) Å, V = 600.612(7) Å^3. The A^I site is denoted A1, the A^{II} site is A2, and the T site is T1.

Site	Atom	x	y	z	occ	B_{iso} (Å^2)
A1	Ca	1/3	2/3	0.4889(3)	0.81(1)	1.19(6)
A1	Bi	1/3	2/3	0.4889(3)	0.204(4)	1.19(6)
A2	La	0.2354(1)	0.0060(2)	1/4	1/3	2.04(3)
A2	Ca	0.2354(1)	0.0060(2)	1/4	0.13(1)	2.04(3)
A2	Bi	0.2354(1)	0.0060(2)	1/4	0.533(6)	2.04(3)
T1	Ge	0.4002(2)	0.3779(2)	1/4	2/3	0.48(3)
T1	V	0.4002(2)	0.3779(2)	1/4	1/3	0.48(3)
O1	O	0.3241(2)	0.4966(2)	1/4	1	0.79(5)
O2	O	0.6034(2)	0.4687(2)	1/4	1	1.50(5)
O3	O	0.3329(2)	0.2442(2)	0.0678(2)	1	2.11(4)
O4	O	0	0	1/4	1	5.1(1)

Table 4.6: Crystallographic data for hexagonal $Bi_4Ca_2La_4[(GeO_4)_6]O_2$ at room temperature. Space group $P6_3/m$, a = 9.86970(4) Å, c = 7.19700(4) Å, V = 607.142(6) Å^3. The A^I site is denoted A1, the A^{II} site is A2, and the T site is T1.

Site	Atom	x	y	z	Occ	B_{iso} (Å^2)
A1	La	1/3	2/3	0.4917(3)	0.31(1)	1.46(6)
A1	Ca	1/3	2/3	0.4917(3)	1/2	1.46(6)
A1	Bi	1/3	2/3	0.4917(3)	0.20(1)	1.46(6)
A2	La	0.2349(1)	0.0019(2)	1/4	0.46(1)	1.61(4)
A2	Bi	0.2349(1)	0.0019(2)	1/4	0.54(1)	1.61(4)
T1	Ge	0.4022(2)	0.3773(1)	1/4	1	0.45(3)
O1	O	0.3224(2)	0.4968(2)	1/4	1	0.85(5)
O2	O	0.6043(2)	0.4709(2)	1/4	1	2.08(6)
O3	O	0.3350(2)	0.2440(2)	0.0663(2)	1	2.60(4)
O4	O	0	0	1/4	1	5.4(1)

4.3.4 Effects of doping on unit-cell volume for $Bi_2Ca_{8-2x}La_{2x}[(VO_4)_{6-2x}(GeO_4)_{2x}]O_2$ (x = 1, 2, and 3) hexagonal apatite materials

Good fits to laboratory PXRD data were found for $Bi_2Ca_6La_2[(VO_4)_4(GeO_4)_2]O_2$, $Bi_2Ca_4La_4[(VO_4)_2(GeO_4)_4]O_2$, and $Bi_2Ca_2La_6[(GeO_4)_6]O_2$ (compositions 1, 5, and 8 respectively) when using hexagonal structures (Figure 4.11). As for $Bi_4Ca_4La_2[(VO_4)_2(GeO_4)_4]O_2$ and $Bi_4Ca_2La_4[(GeO_4)_6]O_2$, the structural models used were modified versions of that reported for $La_{9.5}[(GeO_4)_{5.5}(AlO_4)_{0.5}]O_2$ (*vide supra*).[25] The following parameters were refined for all three samples: ten background parameters, one isotropic displacement parameter for all sites, peak-shape and scale-factor terms, zero-point error, and two lattice parameters. The cations were distributed across the A and T sites according to the nominal compositions of the materials. Given the lack of visible impurity peaks in the data, these samples were used subsequently for ionic conductivity characterisation experiments (*vide infra*). For these three

$Bi_2Ca_{8-2x}La_{2x}[(VO_4)_{6-2x}(GeO_4)_{2x}]O_2$ (x = 1, 2, and 3) compositions, the a cell and c cell lengths (Figure 4.12a) and unit-cell volumes (Figure 4.12b) increase with larger values of x. As x increases, Ca^{2+} A-site cations are substituted with La^{3+} (ionic radii of 1.18 Å and 1.216 Å respectively) and V^{5+} T-site cations are substituted with Ge^{4+} (ionic radii of 0.355 Å and 0.39 Å respectively), with substitution for these larger cations causing the unit cell to expand.

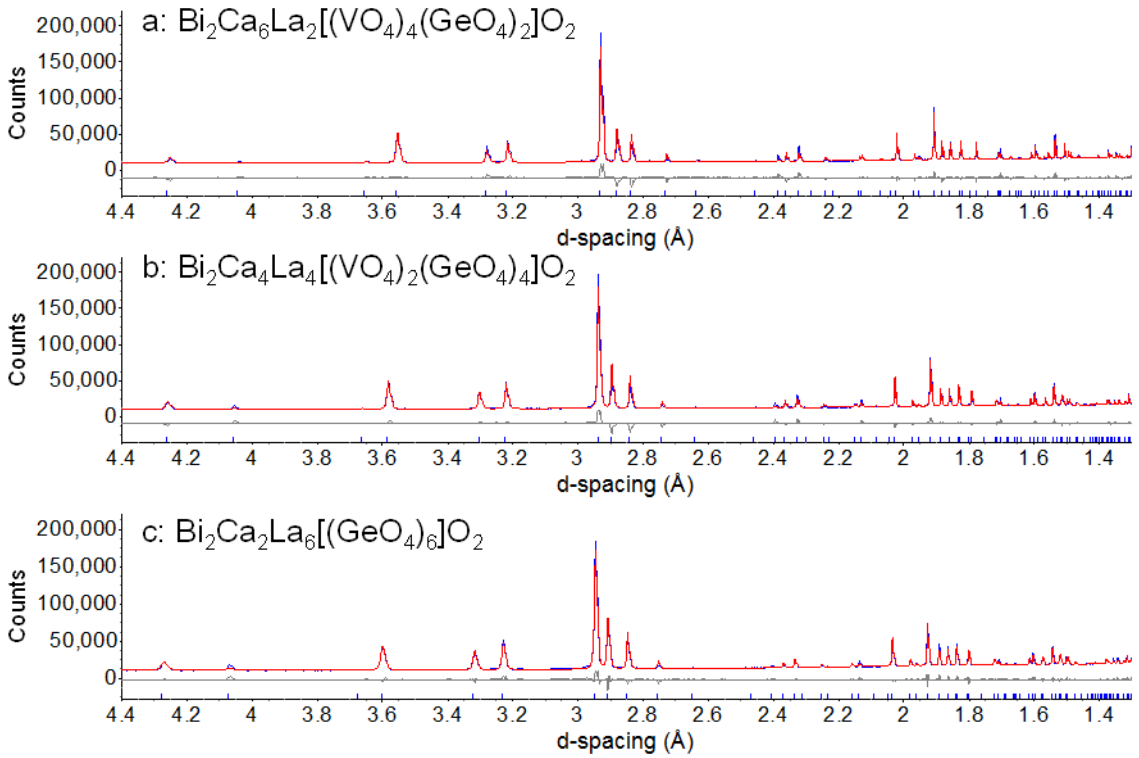

Figure 4.11: Rietveld refinements of: a) $Bi_2Ca_6La_2[(VO_4)_4(GeO_4)_2]O_2$, d7_06413, a = 9.8378(1) Å, c = 7.1196(1) Å, R_{wp} = 4.128 %; b) $Bi_2Ca_4La_4[(VO_4)_2(GeO_4)_4]O_2$, d7_06414, a = 9.8473(1) Å, c = 7.1709(1) Å, R_{wp} = 3.671 %; c) $Bi_2Ca_2La_6[(GeO_4)_6]O_2$, d7_06415, a = 9.8758(1) Å, c = 7.2084(1) Å, R_{wp} = 2.867 %.

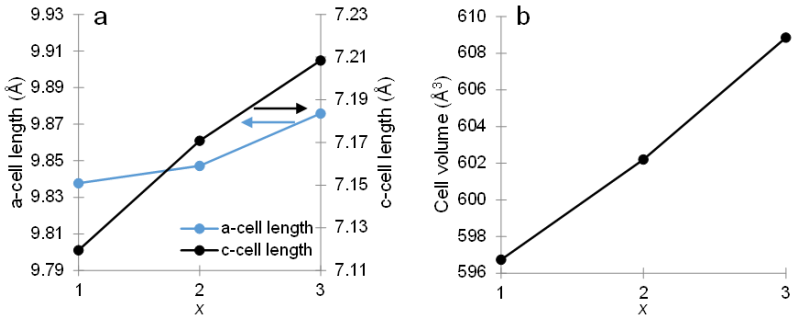

Figure 4.12: Plots showing the: a) increase in a and c cell lengths; b) increase in unit-cell volume for increasing values of x in the $Bi_2Ca_{8-2x}La_{2x}[(VO_4)_{6-2x}(GeO_4)_{2x}]O_2$ (x = 1, 2, and 3) series.

4.3.5 Structural analysis of Al-containing apatite-type materials

$La_{9.5}[(GeO_4)_{5.5}(AlO_4)_{0.5}]O_2$ (composition 20) was reported previously as having a hexagonal structure.[25] A Rietveld refinement using laboratory PXRD data and refining ten background parameters, one isotropic displacement parameter, peak-shape and scale-factor terms, zero-point error, and two lattice parameters for the hexagonal phase, along with two lattice parameters and one isotropic displacement parameter corresponding to the $LaAlO_3$ impurity

resulted in a poor fit to the data (Figure 4.13), with a number of additional peaks observed (inset of Figure 4.13a).

However, when a triclinic structural model was used instead (modified from the triclinic structural model reported by León-Reina *et al.* for $La_{9.75}[(GeO_4)_6]O_{2.62}$ (space group $P\bar{1}$),[26] this produced an improved fit to the data (Figure 4.13b), with a decrease in R_{wp} from 6.135 % to 3.246 %. For this refinement, the same parameters were refined as for the hexagonal case, but six lattice parameters were refined for $La_{9.5}[(GeO_4)_{5.5}(AlO_4)_{0.5}]O_2$ instead of two. Further work will need to be undertaken to characterise fully the triclinic structural model, with VT PND and synchrotron PXRD data needing to be collected.

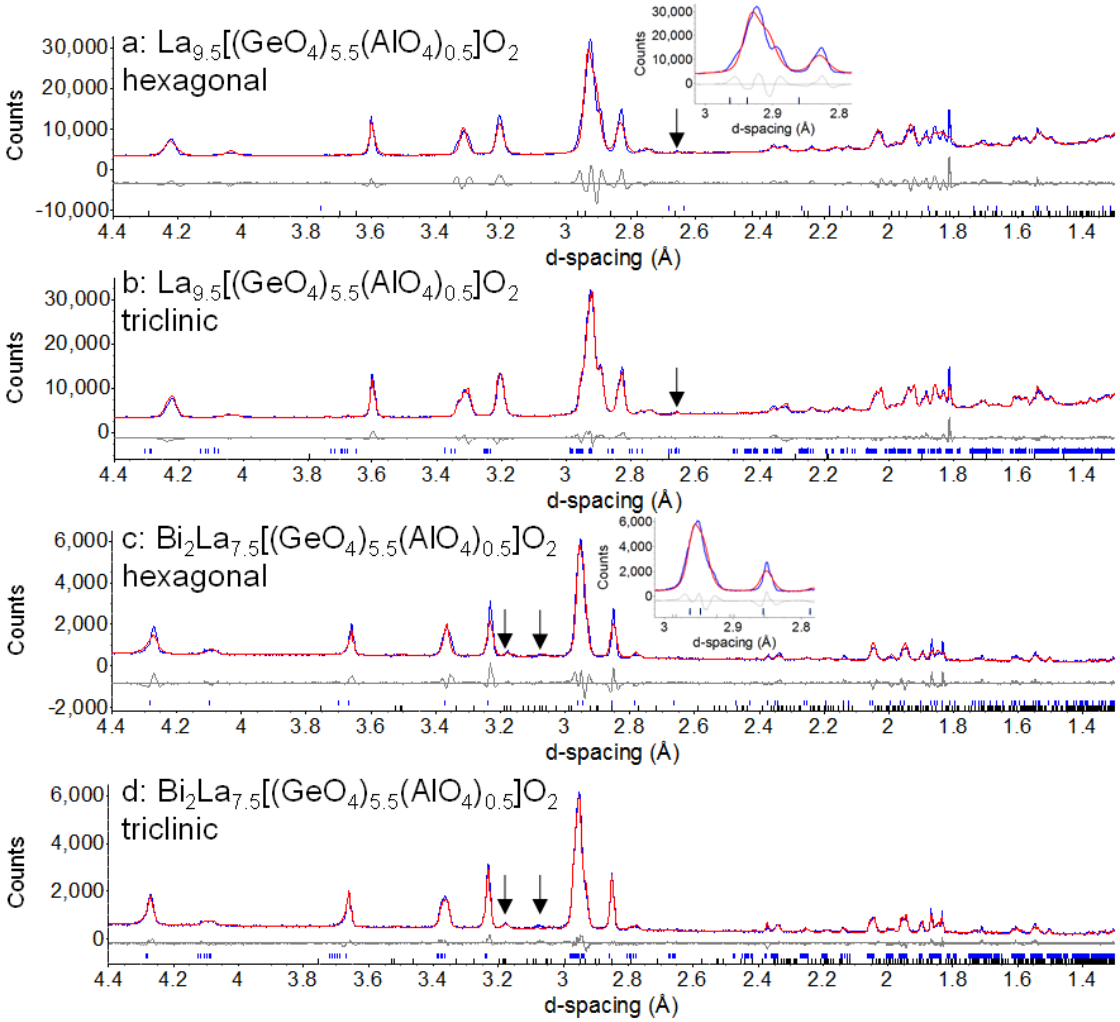

Figure 4.13: Rietveld refinements of: a) $La_{9.5}[(GeO_4)_{5.5}(AlO_4)_{0.5}]O_2$ (hexagonal structure), d7_09918, *a* = 9.906(2) Å, *c* = 7.297(2) Å, R_{wp} = 6.135 %; b) $La_{9.5}[(GeO_4)_{5.5}(AlO_4)_{0.5}]O_2$ (triclinic structure), d7_09918, *a* = 9.9295(5) Å, *b* = 9.9215(6) Å, *c* = 7.3013(3) Å, α = 90.424(6) °, β = 89.147(3) °, γ = 120.287(3) °, R_{wp} = 3.246 %. The black tick marks and arrows correspond to a $LaAlO_3$ impurity phase (0.7(1) %); c) $Bi_2La_{7.5}[(GeO_4)_{5.5}(AlO_4)_{0.5}]O_2$ (hexagonal structure), MLT071_01, *a* = 9.8930(9) Å, *c* = 7.3406(8) Å, R_{wp} = 10.364 %; d) $Bi_2La_{7.5}[(GeO_4)_{5.5}(AlO_4)_{0.5}]O_2$ (triclinic structure), MLT071_01, *a* = 9.9005(5) Å, *b* = 9.8968(7) Å, *c* = 7.3434(2) Å, α = 90.424(5) °, β = 89.420(3) °, γ = 120.048(4) °, R_{wp} = 6.847 %. The black tick marks and arrows correspond to the $La_2Ge_2O_7$ impurity phase (3.5(2) %).

Likewise, an attempt to fit a hexagonal structure to the laboratory PXRD data collected for $Bi_2La_{7.5}[(GeO_4)_{5.5}(AlO_4)_{0.5}]O_2$ (composition 19) proved unsuccessful. A Rietveld refinement using the same refined parameters as for hexagonal $La_{9.5}[(GeO_4)_{5.5}(AlO_4)_{0.5}]O_2$, but with the A sites

modified to have mixed occupancies corresponding to the nominal composition produced a poor fit to the data (Figure 4.13c). Replacing the hexagonal structure with a triclinic structure (Figure 4.13d) improved the fit to the data, and the R_{wp} decreased from 5.428 % to 1.981 %. This sample was found to contain a small percentage of a $La_2Ge_2O_7$ impurity (3.5(2) % by weight).

For $Bi_2La_{7.5}[(GeO_4)_{5.5}(AlO_4)_{0.5}]O_2$, combined refinements using room-temperature synchrotron PXRD and PND data were undertaken, and the following parameters refined: 10 or 20 background parameters (PND and synchrotron PXRD), four isotropic displacement parameters (for the A^I, A^{II}, T, and O sites), scale factors, peak-shape terms (PND) and size-strain terms (synchrotron PXRD), site occupancies for the A and T sites (using restraints to maintain correct overall stoichiometry), and six lattice parameters. Additionally, six lattice parameters, one isotropic displacement parameter, scale factors, and peak-shape terms were also refined for the $La_2Ge_2O_7$ impurity (~6 to 7 % by weight). Whilst good fits to the data were obtained (Figure 4.14), analysis of the T-site occupancies found the Al content to be 0.09(6). The large standard uncertainties associated with these occupancies place into question whether Al is incorporated into the structure of the material, or if it is present in a secondary phase.

Substituting Ge^{4+} with Al^{3+} cations in $Bi_2La_{7.5}[(GeO_4)_{5.5}(AlO_4)_{0.5}]O_2$ causes the removal of La^{3+}, and a loss of one oxygen atom relative to $Bi_2La_8[(GeO_4)_6]O_3$. This would be thought to affect the overall cell volume, because whilst Ge^{4+} and Al^{3+} have identical ionic radii (coordination number = 4, 0.39 Å),[37] the removal of 0.5 La and 1 O atom would result in a decrease in the unit-cell volume of ~14 $Å^3$ for the Al-doped apatite. However, the unit-cell volume for $Bi_2La_{7.5}[(GeO_4)_{5.5}(AlO_4)_{0.5}]O_2$ is very similar to that for $Bi_2La_8[(GeO_4)_6]O_3$ (621.48(2) $Å^3$ and 622.57(1) $Å^3$, respectively), suggesting that the primary phase in the nominal $Bi_2La_{7.5}[(GeO_4)_{5.5}(AlO_4)_{0.5}]O_2$ sample is $Bi_2La_8[(GeO_4)_6]O_3$. In light of these findings, no complete structural model was obtained for this composition, and no conductivity measurements were performed on this sample.

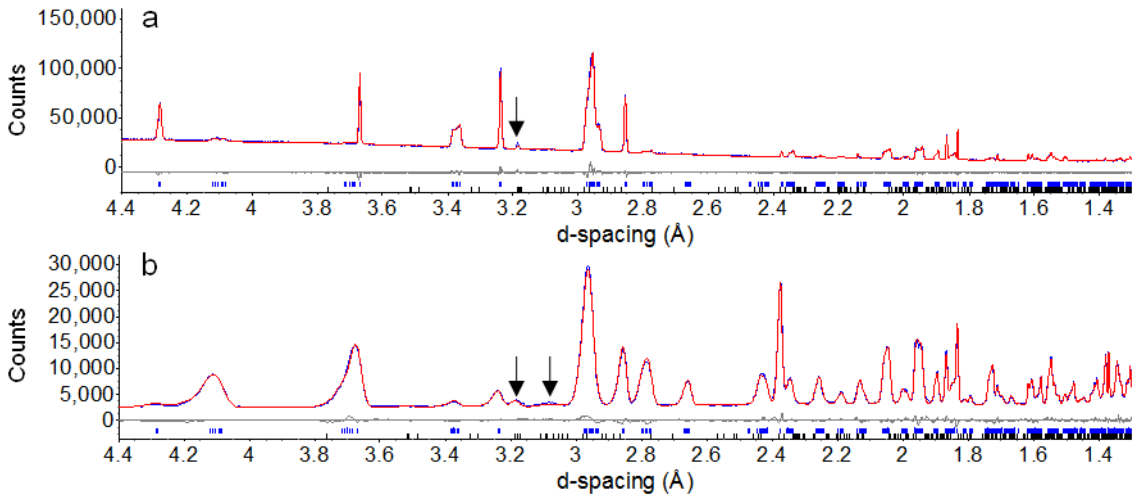

Figure 4.14: Rietveld fits for $Bi_2La_{7.5}[(GeO_4)_{5.5}(AlO_4)_{0.5}]O_2$ at room temperature using: a) synchrotron PXRD data, MLT071_p12_ns_00 (filename), R_{wp} = 3.900 %, b) PND data, ECH0013086_Bi2La7p5Ge5p5Al0p5O26_, R_{wp} = 3.552 %, *a* = 9.8956(2) Å, *b* = 9.8904(3) Å, *c* = 7.3385(1) Å, α = 90.394(5) °, β = 89.442(2) °, γ = 120.061(2) °, space group $P\bar{1}$. Black tick marks and arrows denote the $La_2Ge_2O_7$ impurity phase.

4.3.6 Identifying cause of symmetry reduction in $Bi_2La_8[(GeO_4)_6]O_3$

It was reported by Baikie *et al.* that the reason for the reduction in symmetry of an apatite-type material from a hexagonal to triclinic structure is to reduce underbonding on the A^I site and overbonding on the T site (bond-valence sums less than or greater than those expected, respectively), caused by differences in the sizes of the $A^I_4(TO_4)_6$ framework and $A^{II}_6X_2$ cavity units.[38] To investigate whether this is the case for $Bi_2La_8[(GeO_4)_6]O_3$, BVS values were calculated (Table 4.7) for the triclinic and hexagonal structural forms of this material (Table 4.3 and Table 4.4) and for the two hexagonal compositions, $Bi_4Ca_4La_2[(VO_4)_2(GeO_4)_4]O_2$ and $Bi_4Ca_2La_4[(GeO_4)_6]O_2$ (Table 4.5 and Table 4.6). The cut-off values used for the MO_x coordination spheres to determine the BVS values were 3.1 Å and 2.1 Å for the A and T sites, respectively. For sites containing mixed occupancies of cations, the BVS values were calculated individually for each cation species and then averaged according to the relative occupancies of the species on that site.

Table 4.7: Bond valence sums for the novel Bi(III)-containing apatite-type materials. Cut-off values of 3.1 Å (A sites) and 2.1 Å (T sites) for the coordination spheres were used. The values enclosed in square brackets are those expected for the site based on the ratio of M^{2+} and M^{3+} cations. The BVS values were calculated manually using values for the bond-valence parameters reported by Brese and O'Keeffe.[39]

$Bi_2La_8[(GeO_4)_6]O_3$ (triclinic)		$Bi_2La_8[(GeO_4)_6]O_3$ (hexagonal)		$Bi_4Ca_2La_4[(GeO_4)_6]O_2$		$Bi_4Ca_4La_2[(VO_4)_2(GeO_4)_4]O_2$	
Site	Valence	Site	Valence	Site	Valence	Site	Valence
A1a	2.73(3)	A1	2.65(5)	A1	2.36(1) [2.53]	A1	2.03(1) [2.25]
A1b	3.15(10)	A2	2.41(1)	A2	2.68(1) [3.00]	A2	2.62(1) [2.87]
A1 (average)	2.9(1)	T1	4.27(5)	T1	4.16(1) [4.00]	T1	4.57(2) [4.33]
A2a	2.99(5)						
A2b	2.61(4)						
A2c	2.62(4)						
A2 (average)	2.74(7)						
T1_1	3.73(8)						
T1_2	3.96(5)						
T1_3	3.79(5)						
T (average)	3.8(1)						

The results of the four materials studied show that underbonding on the A^I sites and overbonding on the T sites does not necessarily force a reduction in symmetry from a hexagonal structure to a triclinic one, as the sites in all three hexagonal structures show evidence of underbonding and overbonding (Table 4.7). Similarly, hexagonal apatites with underbonded A sites and overbonded T sites are reported in the literature for a range of silicates and germanates, with $La_{7.8}Ca_2[(GeO_4)_6]O_2$ having BVS values of 2.31(2), 2.72(1), and 4.20(2) for the A^I, A^{II}, and T sites, respectively, compared to the expected values of 2.47, 2.92, and 4.00 based on the site occupancies.[40] Likewise, $Nd_{9.464}[(SiO_4)_6]O_{2.2}$ has BVS values reported for Nd(1), Nd(2), and Si of 2.85(1), 2.91(1), and 4.20(3), respectively.[41] However, lowering the symmetry of $Bi_2La_8[(GeO_4)_6]O_3$ does reduce these effects, with the BVS value for the A1 site increasing from 2.65(5) in the hexagonal structure to within error of the expected

value in the triclinic structure, with an average value of 2.9(1). Likewise, the valence of the overbonded T site in the hexagonal structure (4.27(5)) decreases to within two standard uncertainties of the expected value (an average of 3.8(1)) in the triclinic structure, demonstrating the removal of T-site overbonding on symmetry reduction. Whilst the underbonding on the A2 site is not removed completely, the reduction in symmetry does cause the valence to increase (valence of 2.41(1) and average valence of 2.74(7) in the hexagonal and triclinic structures, respectively). A similar effect is reported for $La_{9.75}[(GeO_4)_6]O_{2.62}$, where average values for the sites in the triclinic structure of 2.96(9) (A1), 2.78(8) (A2), and 3.90(9) (T) are given,[26, 28] which are close to those for $Bi_2La_8[(GeO_4)_6]O_3$, showing the reduction in symmetry from hexagonal to triclinic results in the A1 and T sites having average BVS values within error of the expected values, whilst the A2 sites show signs of underbonding.

It is also reported that increasing the A^IO_x metaprism twist angle, ϕ, reduces underbonding and overbonding of the metal sites in the structure, and results in lower-symmetry phases.[38] The method for calculating the metaprism twist angle is given by White and Dong, as measurement of the O1-A1-O2 bond angle of the A^IO_x metaprisms viewed as a projection along [001].[42] For $Bi_2La_8[(GeO_4)_6]O_3$, metaprism twist angles of 23.7(4) ° and 23.29(3) ° are observed for the triclinic and hexagonal structures, respectively, whilst $Bi_4Ca_2La_4[(GeO_4)_6]O_2$ and $Bi_4Ca_4La_2[(VO_4)_2(GeO_4)_4]O_2$ possess twist angles of 21.20(3) ° and 20.94(3) °. These values are similar to those reported in the literature, with hexagonal $La_8Y_2[(GeO_4)_6]O_3$ exhibiting a twist angle of 21.17(3) °,[12] whilst triclinic $La_{10}[(GeO_4)_6]O_3$ has a twist angle of 22.5(11) °.[11]

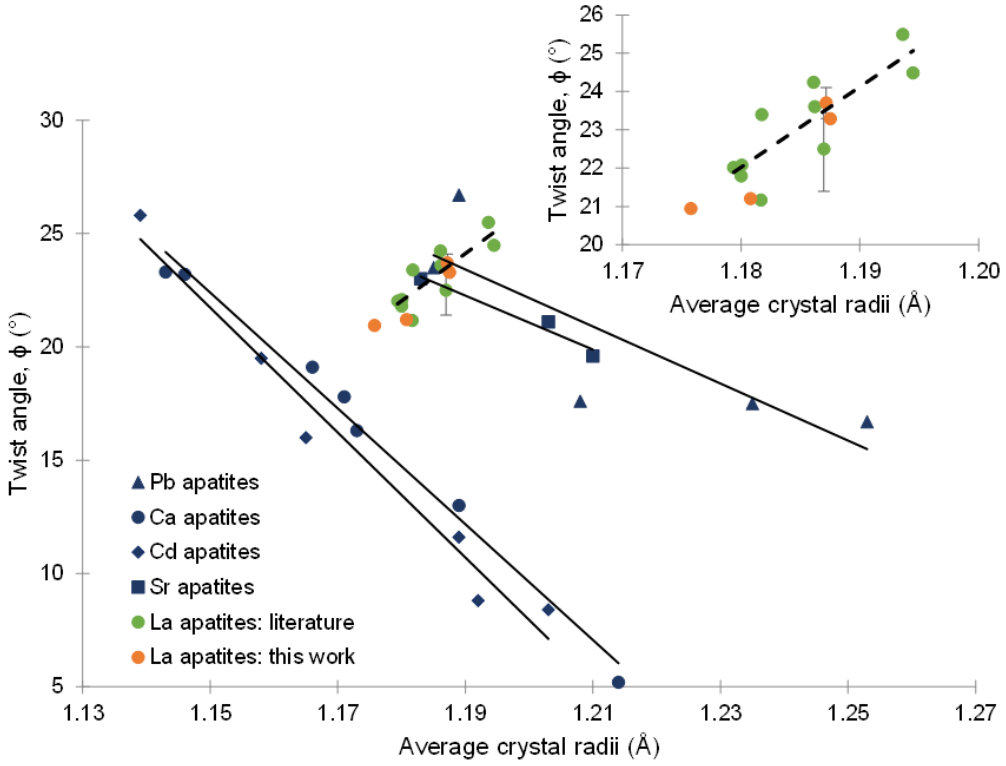

Figure 4.15: Variation of metaprism twist angle with average crystal radii for a number of different $A_{10}(TO_4)_6X_2$ apatite series. The values for the Pb, Ca, Cd, and Sr apatites were reported by White and Dong, and are shown in dark blue.[42] The values for a number of La-containing apatites calculated from reported structural models are shown in green.[11, 12, 25, 40] The orange points correspond to the four Bi-containing lanthanum apatite materials studied in this work. Inset showing only the points for the lanthanum apatite materials.

Additionally, White and Dong plotted the variation in metaprism twist angle with average crystal radii (calculated over the entire content of the unit cell)[42] for a range of $A_{10}(TO_4)_6X_2$ (A = Ca, Cd, Pb, and Sr) apatite series in which the ions on the T and X sites were varied, whilst keeping the A-site cation content constant (dark-blue points in Figure 4.15). From their findings, they show an inverse relationship between the average crystal radii and metaprism twist angles. This is because larger anions on the X site decrease the difference in size between the framework and cavity units of the apatite, resulting in an overall decrease in the twist angle.

This is in contrast to the findings for the new apatite-type materials studied in this chapter (orange circles in Figure 4.15) and other reported La-containing apatites (green circles),[11, 12, 25, 40] which show an increase in metaprism twist angle with increasing average crystal radii. The primary reason for this difference in observed trend can be attributed to the fact that for the La apatites, the contents of the A site are being varied, not the contents of the X site. This means that as the average crystal radius for a material increase, this causes an expansion of the apatite framework with respect to the cavity units, thereby increasing the metaprism twist angle. Whilst there is variation in the T-site content through V doping onto these sites, this was reported by Li *et al.* not to make a difference to the results for Ca-containing apatites, whereas Sr- and Ba-containing apatites show an increase in metaprism twist angle on V doping.[40]

In conclusion, distortion of the GeO_4 polyhedra results in a decrease in the underbonding of the A sites in apatite materials, but deviation from the expected bond-valence values does not correlate necessarily with a reduction in the symmetry. Additionally, there is not a simple relationship between the metaprism twist angle and symmetry of the lanthanum apatites, with hexagonal apatites $Bi_2La_8[(GeO_4)_6]O_3$, $La_{7.88}Ba_2[(GeO_4)_6]O_2$, $La_{7.67}Ba_2[(GeO_4)_{5.29}(VO_4)_{0.71}]O_2$, and $La_{7.99}Sr_2[(GeO_4)_{5.58}(VO_4)_{0.42}]O_2$ exhibiting larger twist angles than other reported triclinic materials.

4.3.7 Bond-valence-sum maps and energy landscapes for Bi(III)-containing apatite-type materials

In crystallography, the bond-valence model is primarily used to assess the validity of crystal structures,[43] based on the relationships between observed bond lengths and valence. It has also been shown that there is good agreement between the shape of ion-migration pathways and cation displacements determined from molecular dynamics simulations and maps of low mismatch in bond valence for a number of alkali metal (Li^+ and Na^+) conductors.[43-52]

The 3DBVSMapper software,[44] (a plug-in for the Accelrys Materials Studio software package)[53] generates a spatial distribution of calculated bond-valence values for a given test species placed at all points on a three-dimensional grid of specified resolution covering the entire unit cell. The distribution of bond-valence values can be calculated in two ways using 3DBVSMapper, both based on the bond-valence sum (BVS) method.[44] The first is a three-dimensional BVS map where the individual BVS value for an imaginary ion of the test species is calculated at each point on the grid, accounting for the interatomic distances between the test

ion and those with opposite charges, within a cut-off radius (8 Å). The second method is based on the work by Adams *et al*. and calculates the bond-valence energy landscape (BVEL),[51] a variation of the BVS map where a scaling term is introduced to convert the mismatch in oxidation state to energy. For the BVEL analyses, three energy values can be presented: E_{min}, the minimum energy of the material; E, a specified energy of the isosurface; Δisovalue, $E - E_{min}$, the use of which allows for direct comparison between materials with differing values of E_{min}.

All atoms of the same species as the selected test atom are deleted from the crystal structure, so the software can calculate the conduction pathways for the test species without having to implement either blocking spheres (BVS method) or local repulsive energy fields (BVEL method) which could potentially block the migration pathways. This also means that an interstitial oxide ion conductor, for example, can be studied without knowledge of the exact interstitial oxygen positions. The results of the analyses can be loaded into a visualisation package (VESTA)[54] so the generated isosurfaces can be overlaid on the crystal structure. The threshold Δisovalue energy at which the isosurface forms a continuous pathway provides an estimate of the activation energy for oxide-ion migration along that pathway using the BVEL method. The activation energy determined from the Δisovalue energy does not compare directly to the activation energy obtained from impedance spectroscopy, but qualitative relationships are expected.

Previous literature reports on apatites studied using BVS mapping methods are limited, whilst no reports are given which utilise BVEL mapping. Adams *et al.* only reported conduction pathways for $La_8Sr_2[(SiO_4)_6]O_2$ within the framework cavities, choosing not to study the pathways within the apatite framework and instead treating the framework oxygens as different anion types.[55] Yashima *et al.* did study the conductivity pathways throughout the whole structure for $Ca_{10}[(PO_4)_6](OH)_2$ using BVS mapping, though they focussed on proton conductivity. They found proton conduction to occur both along the framework cavities and in the *xy* plane at $z = 0$ and 0.5, though no energy values for these conductivity pathways were provided.[56] Therefore, the following work presents the first complete quantitative study of oxide-ion conduction pathways in apatite-type materials using BVEL and BVS methods.

Analysis using the 3DBVSMapper software was performed on: triclinic and hexagonal $Bi_2La_8[(GeO_4)_6]O_3$ (Table 4.3 and Table 4.4, respectively), hexagonal $Bi_4Ca_4La_2[(VO_4)_2(GeO_4)_4]O_2$ (Table 4.5), and hexagonal $Bi_4Ca_2La_4[(GeO_4)_6]O_2$ (Table 4.6) using grid resolutions of 0.1 Å, and the literature apatites $La_8Y_2[(GeO_4)_6]O_3$,[12] $La_{10}[(GeO_4)_6]O_3$,[11] and $La_8Sr_2[(SiO_4)_6]O_2$,[13] with grid resolutions of 0.2 Å. For these seven apatite-type materials, both BVEL and BVS map analyses were performed, with the oxygen atoms removed from the structures during the calculations, and an imaginary O^{2-} anion used as the test species.

For the seven apatite-type materials, the oxygen BVEL isosurfaces show that the oxygen atoms are confined to their respective TO_x polyhedra at low energies (example shown for $Bi_2La_8[(GeO_4)_6]O_3$ in Figure 4.16a). When the oxide ions have increased energies, the isosurfaces extend between all TO_x polyhedra in the framework (Figure 4.16b) both along the *z* axis and in the *xy* plane, whilst higher energies are required to connect the isosurface to the O4

oxygen atoms in the framework cavity (Figure 4.16c). This can also be shown in Table 4.8, where the approximate Δisovalue energies for connecting the isosurfaces between TO_x polyhedra parallel to the *z* axis (TO_x intra-column) and in the *xy* plane (TO_x inter-column) are lower than those required to connect the isosurfaces parallel to the *z* axis down the centre of the framework cavity (channel) for all seven apatite-type materials studied.

BVEL mapping suggests that oxide-ion conductivity in the seven apatites studied is favoured within the framework as opposed to along the *z* axis of the cavity. Therefore, if interstitial oxygen atoms are located within the framework, they should promote oxide-ion conductivity in these materials, as the apatites can utilise the lower activation-energy framework pathways and not have to rely on the O4 channel oxygen atoms conducting via the higher-energy channel pathways.

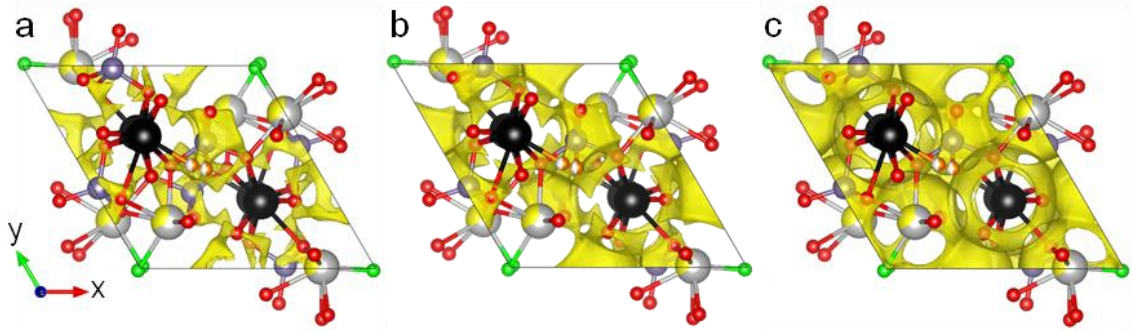

Figure 4.16: BVEL isosurfaces for triclinic $Bi_2La_8[(GeO_4)_6]O_3$ showing: a) isolated GeO_x polyhedra, Δisovalue = 1 eV; b) three-dimensional isosurface connecting the framework GeO_x polyhedra, Δisovalue = 1.5 eV; c) three-dimensional isosurface connecting the framework GeO_x polyhedra and the O4 channel oxygen atoms, Δisovalue = 2.6 eV. The oxygen BVEL isosurface is shown in yellow, and the atom sites are coloured according to the representation of the structure in Figure 4.7a.

Table 4.8: Approximate Δisovalue energies for connectivity of the isosurfaces: between TO_x polyhedra parallel to the *z* axis (TO_x intra-column), between neighbouring TO_x columns (TO_x inter-column), and parallel to the *z* axis along the centre of the apatite cavity (channel) for the apatite-type materials studied.

	Δisovalue (eV)		
	TO_x intra-column	TO_x inter-column	Channel
$Bi_2La_8[(GeO_4)_6]O_3$ – triclinic	1.35	1.15	2.60
$Bi_2La_8[(GeO_4)_6]O_3$ – hexagonal	1.35	1.35	2.40
$Bi_4Ca_4La_2[(VO_4)_2(GeO_4)_4]O_2$	0.75	1.05	2.70
$Bi_4Ca_2La_4[(GeO_4)_6]O_2$	1.05	1.05	2.00
$La_8Y_2[(GeO_4)_6]O_3$	1.05	1.20	2.30
$La_{10}[(GeO_4)_6]O_3$	1.00	1.20	3.30
$La_8Sr_2[(SiO_4)_6]O_2$	1.35	2.00	3.20

Analysis of the BVEL can provide insight into the potential locations of interstitial oxygen atoms in the structure. For triclinic $Bi_2La_8[(GeO_4)_6]O_3$, slices of the isosurface along the *x* axis at *x* = 0.5 (Figure 4.17a) and *x* = 0 (Figure 4.17b) show the Δisovalue energies for the six symmetry-equivalent sites in the hexagonal aristotype. The lowest-energy site is at (0.5, 0.5, 0) (black circles in Figure 4.17a, 0.85 eV), whilst the remaining five have energies ranging from 1.08 to 1.45 eV. This agrees with the structural model in Table 4.3, where the interstitial O5 oxygen atoms are located close to the low-energy (0.5, 0.5, 0) site, with the energy at their

coordinates of ~0.9 eV. Interstitial oxygen positions residing in regions of low energy in the BVEL are also observed in triclinic $La_{10}[(GeO_4)_6]O_3$, where Pramana *et al.* located interstitial oxygen content close to the (0, 0.5, 0.5) site (orange atoms circled in Figure 4.17c),[11] a site of very low energy (Δisovalue ~0.15 eV) in the BVEL.

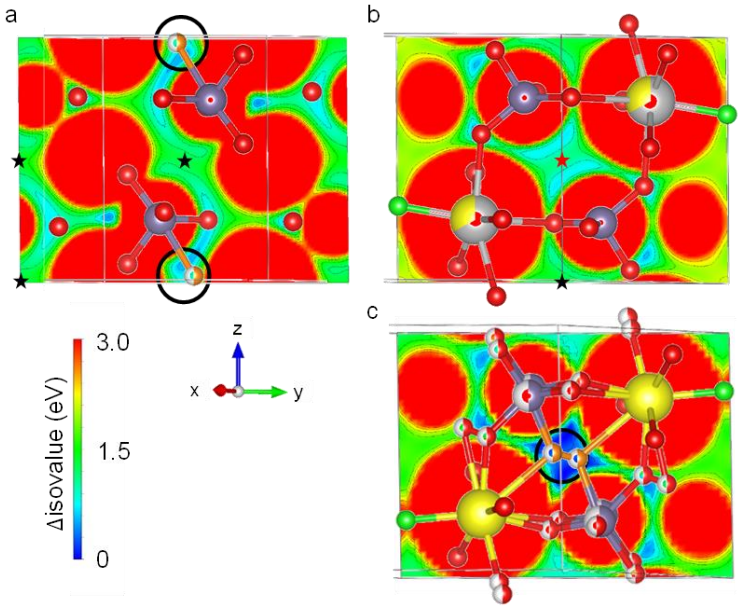

Figure 4.17: BVEL isosurface slices at: a) *x* = 0.5 for triclinic $Bi_2La_8[(GeO_4)_6]O_3$ with atoms shown from *x* = –0.1 to 0.1; b) *x* = 0 for triclinic $Bi_2La_8[(GeO_4)_6]O_3$ with atoms shown from *x* = 0.4 to 0.6; c) *x* = 0 for $La_{10}[(GeO_4)_6]O_3$ with atoms shown from *x* = –0.1 to 0.1. The black circle highlights the region of low energy, with the interstitial oxygen atoms coloured orange. In a) and b) the six symmetry-equivalent sites in the hexagonal aristotype are denoted by: black circles = (0.5, 0.5, 0); red star = (0, 0.5, 0.5); black stars = ((0.5, 0, 0), (0.5, 0, 0.5), (0, 0.5, 0), and (0.5, 0.5, 0.5). All slices are shown perpendicular to the *yz* face, and atoms coloured according to Figure 4.7a.

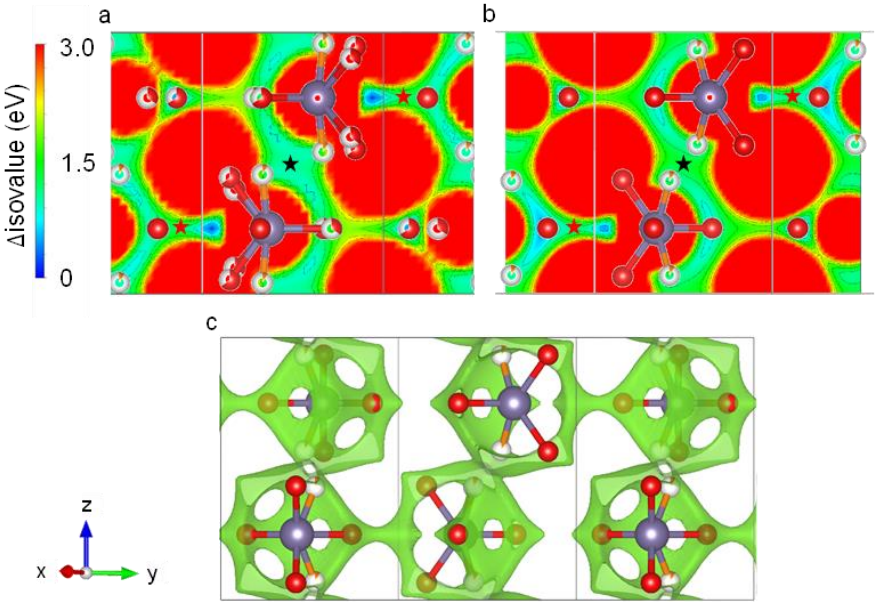

Figure 4.18: BVEL isosurface slices at *x* = 0.5 for: a) $La_8Y_2[(GeO_4)_6]O_3$; b) hexagonal $Bi_2La_8[(GeO_4)_6]O_3$. Both images show the sinusoidal migration pathway along the *z* axis. The black stars indicate the saddle points of the migration pathway for intra-channel migration, whilst red stars show saddle points for the inter-channel migration pathways. The saddle points are locations of highest energy along a given pathway; c) BVEL isosurface for hexagonal $Bi_2La_8[(GeO_4)_6]O_3$ from *x* = 0.4 to 0.6 with Δisovalue = 1.4 eV, showing the intra- and inter-channel migration pathways in green. All atoms are given from *x* = 0.4 to 0.6, and all images shown perpendicular to the *yz* face, with atomic sites coloured according to Figure 4.7b.

For hexagonal $Bi_2La_8[(GeO_4)_6]O_3$, sinusoidal pathways along the *z* axis within the apatite framework are observed which allow interstitial oxygen to migrate between GeO_x polyhedra, with the interstitial oxygen atoms residing on this pathway at a Δisovalue energy of 1.31 eV (Figure 4.18b), a low-energy region of the isosurface. In addition, the Δisovalue energies required for intra- and inter-column oxygen migration within the framework are very similar, with Δisovalue ~1.35 eV required to connect the oxygen isosurface within the framework in three dimensions (Figure 4.18b and Figure 4.18c) at the saddle points. The saddle points are the locations of highest energy along a given migration pathway. This suggests that oxygen migration within the framework of $Bi_2La_8[(GeO_4)_6]O_3$ is as likely to occur along the *z* axis as it is in the *xy* plane between columns of GeO_x polyhedra, and at lower energies compared to conductivity within the framework cavities parallel to the *z* axis.

This sinusoidal interstitial oxide-ion migration pathway parallel to the *z* axis within the apatite framework is reported by Kendrick *et al.*[12] From the BVEL isosurfaces, this pathway can be observed for $La_8Y_2[(GeO_4)_6]O_3$ at $x = 0.5$. A Δisovalue energy of ~1.05 eV is required to connect the isosurfaces of the corner-sharing GeO_x polyhedra together (black star in Figure 4.18a) along the *z* axis. However, for oxygen atoms to migrate between neighbouring GeO_x columns within the framework, an increased energy is required (Δisovalue ~1.2 eV, red stars in Figure 4.18a). This means that inter-column migration is less likely to occur than intra-column migration for the interstitial oxygen atoms within the framework. As for hexagonal $Bi_2La_8[(GeO_4)_6]O_3$, the energies required for oxide-ion conductivity within the $La_8Y_2[(GeO_4)_6]O_3$ framework are lower than those required for conductivity parallel to the *z* axis through the framework cavities.

Another interstitial oxide-ion-migration pathway reported in the literature is that from Pramana *et al*., who report that the interstitial oxygen migration in triclinic $La_{10}[(GeO_4)_6]O_3$ can occur along [010] following displacement of oxygen on the O12/O12a sites by the interstitial oxygen, O14, before migrating across the framework cavity through a saddle point at (0, 0, 0.5).[11] Whilst the oxygen BVEL shows that this pathway is possible, the energy required to migrate through the saddle point is ~1.7 eV (Figure 4.19a), higher than for inter-column connectivity of GeO_x polyhedra (1.2 eV). This means a more plausible method of conductivity for the oxygen interstitials is therefore either along the *z* axis (~1 eV) within the framework, or in the *xy* plane between neighbouring columns of GeO_x polyhedra, not across the cavity. The structure of triclinic $Bi_2La_8[(GeO_4)_6]O_3$ cannot facilitate this same migration pathway along the *y* axis, as the interstitial oxygen atoms are located at the centre of the *xy* face. This means a linear migration pathway parallel to the *y* axis (Figure 4.19c) would not pass through the apatite cavity at (0, 0, 0.5). The hexagonal phase can utilise this pathway (Figure 4.19b), but as the Δisovalue energy is ~0.75 eV greater than migration between neighbouring GeO_x columns (~2.1 eV and ~1.35 eV respectively), this is not likely to be the principal migration pathway in the *xy* plane.

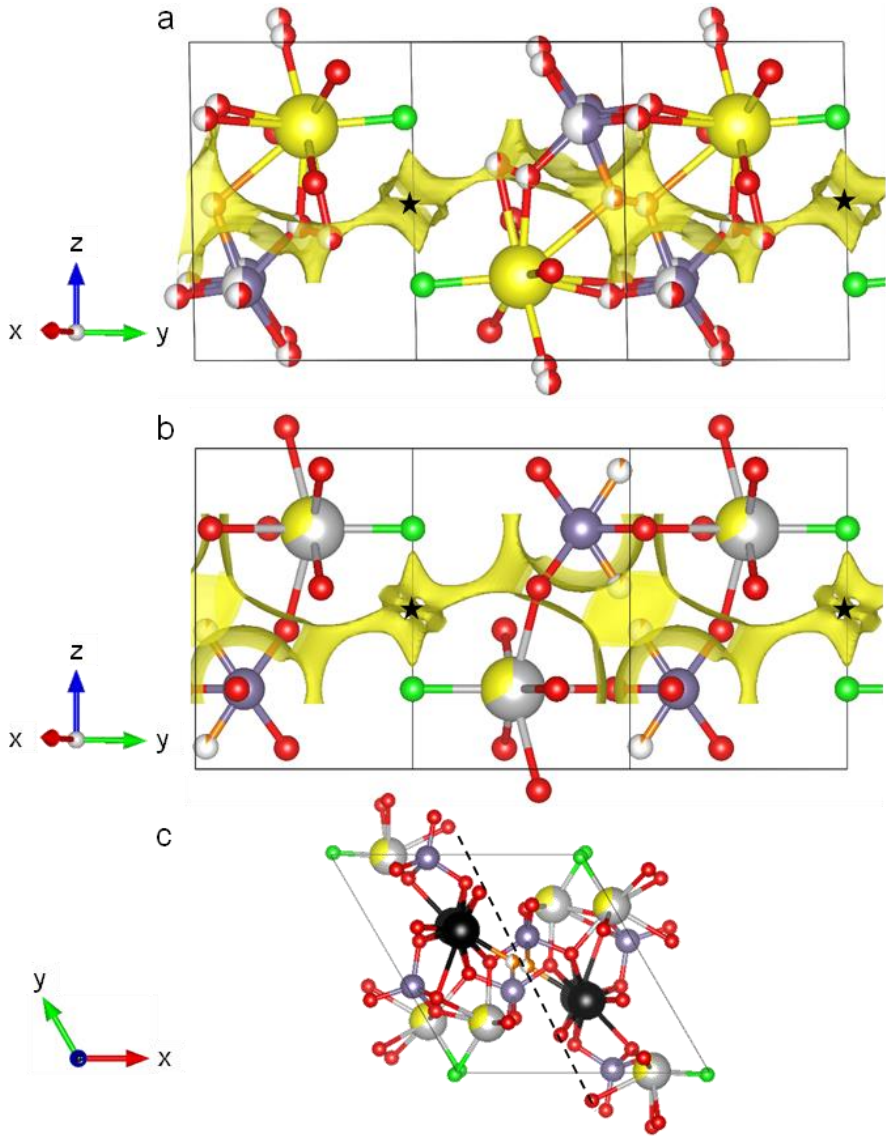

Figure 4.19: BVEL isosurfaces in yellow showing the potential linear oxygen migration pathways along [010] for: a) $La_{10}[(GeO_4)_6]O_3$, Δ isovalue = 1.8 eV; b) hexagonal $Bi_2La_8[(GeO_4)_6]O_3$, Δisovalue = 2.1 eV. c) projection of triclinic $Bi_2La_8[(GeO_4)_6]O_3$ along the *z* axis with the dashed line showing the linear pathway for the interstitial O5 oxygen atoms parallel to the *y* axis does not cross through (0, 0, 0.5). The atomic sites are colour coded according to Figure 4.7a.

Understanding potential pathways for oxygen migration is not just relevant for interstitial oxygen content, but also for the channel oxygen atoms. Tolchard *et al.* report a linear conductivity pathway for the channel oxygen atoms along the *z* axis through a saddle point at (0, 0, 0.5) for stoichiometric $La_8Sr_2[(SiO_4)_6]O_2$ based on MD simulations.[57] From BVEL isosurface slices taken at *x* = 0 perpendicular to the *yz* face, the same linear pathway crossing through (0, 0, 0.5) is observed, with a direct connection between the O4 oxygen atoms seen for the four Bi(III)-containing apatite phases studied and $La_8Sr_2[(SiO_4)_6]O_2$ (Figure 4.20a-e). From slices taken from BVS map isosurfaces at identical *x* values, similarities are seen for the isosurfaces within the apatite frameworks. However, differences are observed within the apatite cavities, where a non-linear sinusoidal pathway between the channel oxygen atoms (black stars in Figure 4.20) is found to be more likely (Figure 4.20f-j). In light of these results, the oxygen-migration pathway for the channel oxygen atoms from bond-valence analysis cannot be shown conclusively.

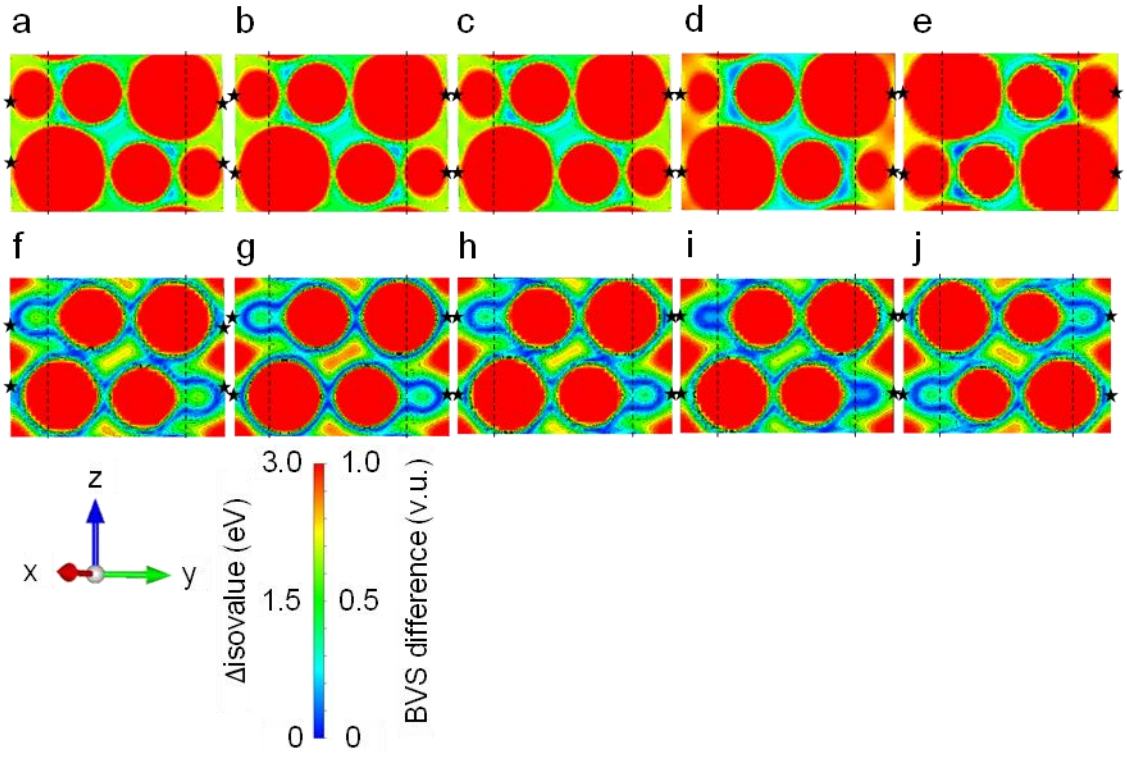

Figure 4.20: BVEL and BVS isosurface slices at *x* = 0 respectively for: a) and f) triclinic $Bi_2La_8[(GeO_4)_6]O_3$; b) and g) hexagonal $Bi_2La_8[(GeO_4)_6]O_3$; c) and h) $Bi_4Ca_2La_4[(GeO_4)_6]O_2$; d) and i) $Bi_4Ca_4La_2[(VO_4)_2(GeO_4)_4]O_2$; e) and j) $La_8Sr_2[(SiO_4)_6]O_2$.[13] The channel oxygen sites are denoted by black stars, whilst the dotted lines signify approximately the boundaries between the apatite framework (within the lines) and cavity (outside the lines).

Overall, bond-valence analysis of the three novel apatite-type materials has corroborated the findings from PND as to the locations of the interstitial oxygen atoms, and identified a number of potential oxide-ion migration pathways within the frameworks of these apatite-type materials. The migration pathways identified using BVEL mapping are in good agreement with those determined through computational modelling in the literature.

4.4 Ionic conductivity characterisation of the Bi-containing apatites

AC impedance spectroscopy was performed on pellets of six of the apatite-type materials (compositions 1, 5, 8, 9, 15, and 16). The pellets were pressed with 250 MPa of pressure and fired at their synthesis temperatures for 6 hours, producing pellets with the dimensions and densities given in Table 4.9.

Table 4.9: Pellet dimensions for the bismuth apatite samples used for impedance spectroscopy.

Composition	Mass (g)	Diameter (cm)	Height (cm)	Density (%)
$Bi_2La_8[(GeO_4)_6]O_3$	0.0634 ± 0.0001	0.491 ± 0.001	0.072 ± 0.001	73.26 ± 0.01
$Bi_4Ca_2La_4[(GeO_4)_6]O_2$	0.4877 ± 0.0001	0.943 ± 0.001	0.123 ± 0.001	89.26 ± 0.01
$Bi_4Ca_4La_2[(VO_4)_2(GeO_4)_4]O_2$	0.3545 ± 0.0001	0.960 ± 0.001	0.102 ± 0.001	83.44 ± 0.01
$Bi_2Ca_6La_2[(VO_4)_4(GeO_4)_2]O_2$	0.3124 ± 0.0001	0.980 ± 0.001	0.110 ± 0.001	79.49 ± 0.01
$Bi_2Ca_4La_4[(VO_4)_2(GeO_4)_4]O_2$	0.3333 ± 0.0001	1.001 ± 0.001	0.104 ± 0.001	76.03 ± 0.01
$Bi_2Ca_2La_6[(GeO_4)_6]O_2$	0.3333 ± 0.0001	1.003 ± 0.001	0.134 ± 0.001	52.86 ± 0.01

The complex impedance spectra for all six samples show a single large semi-circular arc attributed to bulk response at low temperatures, with Warburg-type electrode responses observed at frequencies below 10 Hz. A parallel resistor-capacitor model was used to treat the bulk responses, and the grain boundary and bulk responses could not be separated at high frequencies in the large impedance arc. The low-frequency intercepts of the semi-circular arcs arise from the bulk resistivities of the samples (marked in Figure 4.21a), with capacitances calculated using $\omega RC = 1$ at 300 °C ranging between 2.20 and 4.79 pFcm^{-1} for the six materials studied, which are consistent with bulk responses. Below 10 Hz, the calculated capacitances from the Warburg-type responses are between 10^{-7} and 10^{-5} Fcm^{-1}, indicating ionic conduction.[58] At high temperatures the bulk responses disappear, resulting in a single observable arc forming, and so the total resistivities of the materials are estimated from the high-frequency intercepts (marked in Figure 4.21b).

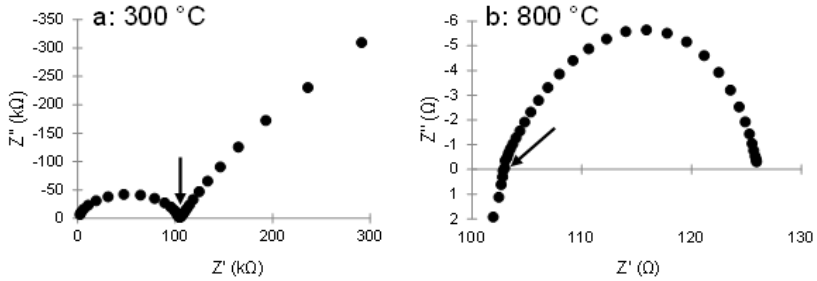

Figure 4.21: Nyquist plots showing the impedance curves for $Bi_4Ca_4La_2[(VO_4)_2(GeO_4)_4]O_2$ at: a) 300 °C; b) 800 °C.

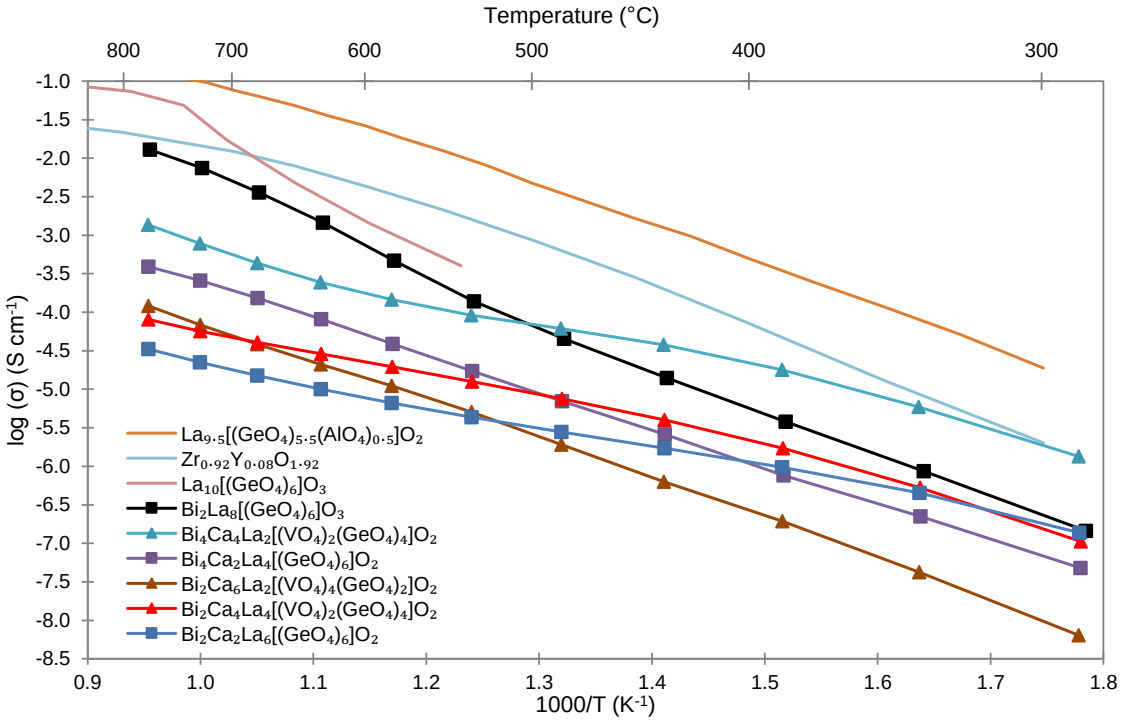

Figure 4.22: Arrhenius plots of total conductivity values as a function of temperature for the Bi(III)-containing apatite compounds studied, plus those for $La_{10}[(GeO_4)_6]O_3$,[59] $La_{9.5}[(GeO_4)_{5.5}(AlO_4)_{0.5}]O_2$, and $Zr_{0.92}Y_{0.08}O_{1.92}$.[25]

Table 4.10: Conductivity values and activation energies (E_{act}, 500 to 800 °C) for the Bi-containing apatite-type materials compared to that for $La_{10}[(GeO_4)_6]O_3$.[25] The crystal systems given are those exhibited by the materials in the temperature region studied during the impedance spectroscopy experiments.

Composition	Crystal system	$\sigma_{775\ °C}$ (Scm^{-1})	E_{act} (eV)
$La_{10}[(GeO_4)_6]O_3$	Triclinic	8×10^{-2} (800 °C)	1.70
$Bi_2La_8[(GeO_4)_6]O_3$	Triclinic/hexagonal	1.29×10^{-2}	1.46
$Bi_4Ca_4La_2[(VO_4)_2(GeO_4)_4]O_2$	Hexagonal	1.37×10^{-3}	0.90
$Bi_4Ca_2La_4[(GeO_4)_6]O_2$	Hexagonal	3.89×10^{-4}	1.03
$Bi_2Ca_6La_2[(VO_4)_4(GeO_4)_2]O_2$	Hexagonal	1.21×10^{-4}	1.03
$Bi_2Ca_4La_4[(VO_4)_2(GeO_4)_4]O_2$	Hexagonal	8.04×10^{-5}	0.63
$Bi_2Ca_2La_6[(GeO_4)_6]O_2$	Hexagonal	3.33×10^{-5}	0.69

The plots of the oxide-ion conductivities between 300 and 800 °C for the six compositions studied, in addition to those for the Al-doped apatite with the highest recorded oxide ion conductivity, $La_{9.5}[(GeO_4)_{5.5}(AlO_4)_{0.5}]O_2$,[25] the triclinic apatite with the highest reported conductivity, $La_{10}[(GeO_4)_6]O_3$,[59] and the commercially used yttria-stabilised zirconia electrolyte, $Zr_{0.92}Y_{0.08}O_{1.92}$,[25] are presented in Figure 4.22.

The conductivity of triclinic $Bi_2La_8[(GeO_4)_6]O_3$ above 500 °C is greater than for the hexagonal compounds and is ~0.01 Scm^{-1} at 775 °C. Defect trapping in the triclinic structure at low temperatures decreased the observed conductivity,[2] but this effect diminishes following the phase transition to the hexagonal form. Defect trapping could also account for the elevated activation energies for triclinic $Bi_2La_8[(GeO_4)_6]O_3$ and $La_{10}[(GeO_4)_6]O_3$ compared to those for the hexagonal apatites (Table 4.10), by inhibiting oxide-ion migration. In addition, the interstitial oxygen atoms provide additional oxide-ion conductivity pathways between the GeO_4 tetrahedra, both along the *z* axis and in the *xy* plane (*vide supra*). When these migration effects are combined with the intra-channel oxide-ion migration of the O4 oxygen atoms along the centre of the framework cavities, as for apatite-type compounds with 26 oxygen atoms, the net result is heightened conductivity values compared to the apatites containing no interstitial oxygen. Despite the diminished conductivity of $Bi_2La_8[(GeO_4)_6]O_3$ relative to that for $La_{10}[(GeO_4)_6]O_3$, the observed conductivity is similar to that for other $La_8M_2[(GeO_4)_6]O_3$ (M = Y, Yb, Gd) compounds.[2]

The conductivity levels of all the studied Bi-containing apatite-type materials are lower than for the $La_{10}[(GeO_4)_6]O_3$ triclinic apatite, potentially arising from the presence of Bi^{3+} cations in the former materials. These cations possess lone pairs of electrons which can partially occupy the framework cavities, thereby hindering the intra-channel conductivity of the mobile O4 oxygen atoms.[60]

The conductivities of the Ca-containing apatite-type materials (Table 4.10) are similar to those reported for other alkaline-earth-doped lanthanum germanium apatites,[1, 20, 61] such as $La_8Ca_2[(GeO_4)_6]O_2$ reported by Li *et al.* ($\sigma_{800\ °C}$ = 2.8×10^{-4} Scm^{-1}).[40] Li *et al.* also show Ca-doped apatites with increased conductivities when doped with V (e.g. $\sigma_{800\ °C}$ = 1.2×10^{-2} Scm^{-1} for $La_8Ca_2[(GeO_4)_{5.75}(VO_4)_{0.25}]O_{2.125}$), but those materials possess

additional interstitial oxygen atoms, which will improve the conductivity values as seen for $Bi_2La_8[(GeO_4)_6]O_3$ compared to apatites with only 26 oxygen atoms.

4.5 Conclusions

$Bi_2La_8[(GeO_4)_6]O_3$ is the first reported Bi-containing apatite-type material with a triclinic structure. This material undergoes a reversible triclinic-to-hexagonal phase transition on heating above 680 °C. The triclinic and hexagonal structure for $Bi_2La_8[(GeO_4)_6]O_3$ have been characterised through combined Rietveld refinements using synchrotron PXRD and PND data sets at room temperature and 830 °C. In conjunction with collaborators, ABF STEM imaging allowed interstitial oxygen to be imaged directly for the first time in triclinic $Bi_2La_8[(GeO_4)_6]O_3$. The interstitial oxygen atoms are located between some pairs of GeO_4 tetrahedra, forming GeO_5 trigonal bipyramidal structural units.

Hexagonal room-temperature structural models were characterised for $Bi_4Ca_4La_2[(VO_4)_2(GeO_4)_4]O_2$ and $Bi_4Ca_2La_4[(GeO_4)_6]O_2$, through the combined analysis of room-temperature synchrotron PXRD and PND data sets. $La_{9.5}[(GeO_4)_{5.5}(AlO_4)_{0.5}]O_2$ is reported as a triclinic phase for the first time, having been reported previously as a hexagonal phase.

Analysis of BVELs show that interstitial oxygen positions identified for $Bi_2La_8[(GeO_4)_6]O_3$ lie on low-energy oxide-ion migration pathways. Oxide-ion migration pathways are found to exist within the apatite frameworks (either parallel to the *z* axis, or in the *xy* plane) between TO_x polyhedra. These migration pathways through the frameworks are of lower energy than the migration pathway parallel to the *z* axis down the centre of the apatite cavities. These lower-energy framework pathways provide a reason for the elevated conductivities of $Bi_2La_8[(GeO_4)_6]O_3$ and $La_{10}[(GeO_4)_6]O_3$ compared to apatites containing 26 oxygen atoms.

For hexagonal $Bi_4Ca_4La_2[(VO_4)_2(GeO_4)_4]O_2$ and $Bi_4Ca_2La_4[(GeO_4)_6]O_2$, the conductivities observed were of the same magnitude as those reported for similar alkaline-earth-doped apatites in the literature. The conductivity of $Bi_2La_8[(GeO_4)_6]O_3$ was found to be the highest of all six apatites which underwent ionic-conductivity characterisation experiments, exhibiting a conductivity of ~0.01 Scm^{-1} at 800 °C, similar to that for the commercially-used SOFC electrolyte, yttria-stabilised zirconia.

4.6 References

1. P. R. Slater, J. E. H. Sansom and J. R. Tolchard, *Chemical Record*, 2004, **4**, 373-384.
2. A. Orera, T. Baikie, E. Kendrick, J. F. Shin, S. Pramana, R. Smith, T. J. White, M. L. Sanjuan and P. R. Slater, *Dalton Transactions*, 2011, **40**, 3903-3908.
3. L. Leon-Reina, J. M. Porras-Vazquez, E. R. Losilla and M. A. G. Aranda, *Solid State Ionics*, 2006, **177**, 1307-1315.
4. J. E. H. Sansom and P. R. Slater, *Solid State Ionics*, 2004, **167**, 23-27.
5. T. Funahashi, A. Mineshige, H. Yoshioka, K. Kobayashi, Y. Matsushita, Y. Katsuya, M. Tanaka, O. Sakata and T. Yazawa, *Solid State Ionics*, 2016, **289**, 106-112.
6. H. Zhang, F. Li, J. Jin, Q. Wang and Y. Sun, *Solid State Ionics*, 2008, **179**, 1024-1028.

7. J. McFarlane, S. Barth, M. Swaffer, J. E. H. Sansom and P. R. Slater, *Ionics*, 2002, **8**, 149-154.

8. S. P. Jiang, L. Zhang, H. Q. He, R. K. Yap and Y. Xiang, *Journal of Power Sources*, 2009, **189**, 972-981.

9. J. R. Tolchard and P. R. Slater, *Journal of Physics and Chemistry of Solids*, 2008, **69**, 2433-2439.

10. E. Kendrick, M. S. Islam and P. R. Slater, *Chemical Communications*, 2008, 715-717.

11. S. S. Pramana, W. T. Klooster and T. J. White, *Acta Crystallographica Section B*, 2007, **63**, 597-602.

12. E. Kendrick, A. Orera and P. R. Slater, *Journal of Materials Chemistry*, 2009, **19**, 7955-7958.

13. J. E. H. Sansom, D. Richings and P. R. Slater, *Solid State Ionics*, 2001, **139**, 205-210.

14. M. S. Islam, J. R. Tolchard and P. R. Slater, *Chemical Communications*, 2003, 1486-1487.

15. K. Imaizumi, K. Toyoura, A. Nakamura and K. Matsunaga, *Solid State Ionics*, 2014, **262**, 512-516.

16. K. Matsunaga and K. Toyoura, *Journal of Materials Chemistry*, 2012, **22**, 7265-7273.

17. T. An, T. Baikie, A. Orera, R. O. Piltz, M. Meven, P. R. Slater, J. Wei, M. L. Sanjuán and T. J. White, *Journal of the American Chemical Society*, 2016, **138**, 4468-4483.

18. Y. Nojiri, S. Tanase, M. Iwasa, H. Yoshioka, Y. Matsumura and T. Sakai, *Journal of Power Sources*, 2010, **195**, 4059-4064.

19. J. F. Huang and A. W. Sleight, *Journal of Solid State Chemistry*, 1993, **104**, 52-58.

20. J. R. Tolchard, J. E. H. Sansom, P. R. Slater and M. S. Islam, *Journal of Solid State Electrochemistry*, 2004, **8**, 668-673.

21. B. Hamdi, H. El Feki, A. Ben Salah, P. Salles, P. Baules and J. M. Savariault, *Solid State Ionics*, 2006, **177**, 1413-1420.

22. N. Lakshminarasimhan and U. V. Varadaraju, *Journal of Solid State Chemistry*, 2004, **177**, 3536-3544.

23. V. D. Zhuravlev, A. P. Tyutyunnik, V. G. Zubkov, L. A. Perelyaeva, I. V. Baklanova and A. L. Blinova, *Journal of Solid State Chemistry*, 2012, **194**, 32-36.

24. N. Lakshminarasimhan and U. V. Varadaraju, *Journal of Solid State Chemistry*, 2005, **178**, 3284-3292.

25. L. Leon-Reina, E. R. Losilla, M. Martinez-Lara, M. C. Martin-Sedeno, S. Bruque, P. Nunez, D. V. Sheptyakov and M. A. G. Aranda, *Chemistry of Materials*, 2005, **17**, 596-600.

26. L. Leon-Reina, M. C. Martin-Sedeno, E. R. Losilla, A. Cabeza, M. Martinez-Lara, S. Bruque, F. M. B. Marques, D. V. Sheptyakov and M. A. G. Aranda, *Chemistry of Materials*, 2003, **15**, 2099-2108.

27. K. M. Ok, E. O. Chi and P. S. Halasyamani, *Chemical Society Reviews*, 2006, **35**, 710-717.

28. L. Leon-Reina, J. M. Porras-Vazquez, E. R. Losilla and M. A. G. Aranda, *Journal of Solid State Chemistry*, 2007, **180**, 1250-1258.

29. E. J. Abram, C. A. Kirk, D. C. Sinclair and A. R. West, *Solid State Ionics*, 2005, **176**, 1941-1947.

30. R. Ali, M. Yashima, Y. Matsushita, H. Yoshioka, K. Ohoyama and F. Izumi, *Chemistry of Materials*, 2008, **20**, 5203-5208.

31. S. S. Pramana, W. T. Klooster and T. J. White, *Journal of Solid State Chemistry*, 2008, **181**, 1717-1722.

32. G. S. Pawley, *Journal of Applied Crystallography*, 1981, **14**, 357-361.

33. Y. Zhang, Z. Su, A. K. Azad, W. Zhou and J. T. S. Irvine, *Advanced Energy Materials*, 2012, **2**, 316-321.

34. J. Canales-Vázquez, M. J. Smith, J. T. S. Irvine and W. Zhou, *Advanced Functional Materials*, 2005, **15**, 1000-1008.

35. A. Jones, P. R. Slater and M. S. Islam, *Chemistry of Materials*, 2008, **20**, 5055-5060.

36. J. S. O. Evans, *multitopas, FORTRAN 77 routine*, University of Durham, 1999.

37. R. D. Shannon, *Acta Crystallographica Section A*, 1976, **32**, 751-767.

38. T. Baikie, P. H. J. Mercier, M. M. Elcombe, J. Y. Kim, Y. Le Page, L. D. Mitchell, T. J. White and P. S. Whitfield, *Acta Crystallographica Section B*, 2007, **63**, 251-256.

39. N. E. Brese and M. O'Keeffe, *Acta Crystallographica Section B*, 1991, **47**, 192-197.

40. H. Li, T. Baikie, S. S. Pramana, J. F. Shin, P. R. Slater, F. Brink, J. Hester, K. Wallwork and T. J. White, *Journal of Materials Chemistry*, 2012, **22**, 2658-2669.

41. T. An, T. Baikie, F. Wei, S. S. Pramana, M. K. Schreyer, R. O. Piltz, J. F. Shin, J. Wei, P. R. Slater and T. J. White, *Chemistry of Materials*, 2013, **25**, 1109-1120.

42. T. J. White and Z. L. Dong, *Acta Crystallographica Section B*, 2003, **59**, 1-16.

43. I. D. Brown, *Chemical Reviews*, 2009, **109**, 6858-6919.

44. M. Sale and M. Avdeev, *Journal of Applied Crystallography*, 2012, **45**, 1054-1056.

45. K. Tateishi, D. du Boulay, N. Ishizawa and K. Kawamura, *Journal of Solid State Chemistry*, 2003, **174**, 175-181.

46. J. O. Thomas, *Solid State Ionics*, 1992, **53**, 1311-1316.

47. M. Avdeev, M. Sale, S. Adams and R. P. Rao, *Solid State Ionics*, 2012, **225**, 43-46.

48. D.-H. Seo, Y.-U. Park, S.-W. Kim, I. Park, R. A. Shakoor and K. Kang, *Physical Review B*, 2011, **83**, 205127.

49. Y. Janssen, D. S. Middlemiss, S.-H. Bo, C. P. Grey and P. G. Khalifah, *Journal of the American Chemical Society*, 2012, **134**, 12516-12527.

50. C. A. J. Fisher, V. M. Hart Prieto and M. S. Islam, *Chemistry of Materials*, 2008, **20**, 5907-5915.

51. S. Adams and R. P. Rao, *physica status solidi (a)*, 2011, **208**, 1746-1753.

52. S. Adams, *Solid State Ionics*, 2000, **136–137**, 1351-1361.

53. Accelrys Software Inc, *Discovery Studio Modelling Environment, Release 6.0, San Diego: Accelrys Software Inc.*, 2011.

54. K. Momma and F. Izumi, *Journal of Applied Crystallography*, 2011, **44**, 1272-1276.

55. S. Adams, *Solid State Ionics*, 2006, **177**, 1625-1630.

56. M. Yashima, N. Kubo, K. Omoto, H. Fujimori, K. Fujii and K. Ohoyama, *The Journal of Physical Chemistry C*, 2014, **118**, 5180-5187.

57. J. R. Tolchard, M. S. Islam and P. R. Slater, *Journal of Materials Chemistry*, 2003, **13**, 1956-1961.

58. J. T. S. Irvine, D. C. Sinclair and A. R. West, *Advanced Materials*, 1990, **2**, 132-138.

59. H. Arikawa, H. Nishiguchi, T. Ishihara and Y. Takita, *Solid State Ionics*, 2000, **136**, 31-37.

60. E. Kendrick, M. S. Islam and P. R. Slater, *Journal of Materials Chemistry*, 2007, **17**, 3104-3111.

61. S. S. Pramana, T. Baikie, E. Kendrick, M. K. Schreyer, P. R. Slater and T. J. White, *Solid State Ionics*, 2010, **181**, 1189-1196.

5 Understanding variable Re coordination environments in $Bi_{28}Re_2O_{49}$

5.1 Background

The bismuth rhenate, $Bi_{28}Re_2O_{49}$, was first characterised by Crumpton *et al.* as having a tetragonal structure in space group I4/m (a = 8.7216(1) Å, c = 17.4177(2) Å) at room temperature based on time-of-flight powder neutron diffraction (PND) data.[1] This structure is a commensurate superstructure of the cubic fluorite-type δ-Bi_2O_3, with $a \sim(\sqrt{10}/2)a_F$ and $c \sim 3a_F$ (where a_F is the fluorite lattice parameter), and has been reported for a range of related $Bi_{14}MO_{24}$ compositions.[2-5] $Bi_{28}Re_2O_{49}$ is reported to exhibit higher levels of conductivity than yttria-stabilised zirconia (5.4×10^{-4} Scm^{-1} and $\sim 7.2 \times 10^{-5}$ Scm^{-1} at 400 °C, respectively),[1, 6] of a similar order to that for other doped bismuth oxide materials ($\sim 3.2 \times 10^{-4}$ Scm^{-1} for cubic $Bi_{0.88}Nb_{0.12}O_{1.62}$).[7] The heightened levels of conductivity can be attributed partially to oxide-ion exchange between the Bi-O and isolated Re-O sublattices, arising from the ability of Re to possess variable coordination environments.[8]

Using the starting model for the related material, $Bi_{14}CrO_{24}$,[5] Crumpton *et al.* were able to refine the atomic coordinates for the oxygen atoms on the Bi-O sublattice, but not for the oxygen atoms bonded to Re. These oxygen atoms could not be refined due to local-scale orientational disorder preventing their accurate location in the ReO_x groups. EXAFS and IR experimental results showed that ReO_x polyhedra are strictly 4- or 6-coordinate (in a 75 % to 25 % ratio, giving an average Re coordination number of 4.5). The reported structural model only corresponds to $Bi_{28}Re_2O_{48}$, with one oxygen atom missing from the structural formula. This material has been modified in recent years by doping M^{3+} cations to give compositions $Bi_{25}M_3Re_2O_{49}$. These materials are either cubic (M = Nd, Er, Y),[9] or the cubic phase undergoes cubic-to-tetragonal phase transitions between 600 and 800 °C, before reverting to the cubic phase above 800 °C (M = La, Pr).[10]

A model with the complete $Bi_{28}Re_2O_{49}$ formula was reported by Payne *et al.* in 2013 from the analysis of single-crystal data (Figure 5.1).[8] This model details large anisotropic displacement parameters for the oxygen atoms in the ReO_x polyhedra (Figure 5.1b), suggesting potential disorder. In the reported structure, oxygen atoms occupy five unique sites, with atoms on the O1, O2, and O3 sites bonding solely to bismuth atoms, whilst atoms on the O4 and O5 sites only bond to rhenium. Taking this into account with the 75 % occupancy of the O4 and O5 sites leads to the alternative formula of $(Bi_{28}O_{40})(Re_2O_9)$, which reflects a three-dimensional Bi-O sublattice containing isolated ReO_x polyhedra, with an average Re coordination number of 4.5.

The aim of the work presented in this chapter is to provide a detailed structural characterisation of $Bi_{28}Re_2O_{49}$ on a local scale by using Reverse Monte Carlo (RMC) analyses of neutron total-scattering (TS) data. This method was used to investigate whether Re atoms exist solely in 4- and 6-coordinate ReO_x polyhedra as reported from EXAFS and IR data, by

probing the ReO_x polyhedra on a local scale, and observing how the Re coordination numbers change during the RMC analyses. Also, an investigation was undertaken into whether variable Re^{7+} coordination environments play a role in the oxide-ion conductivity of this compound and related materials, as reported from *ab initio* molecular dynamics calculations for this material.[8] Analysis of high-temperature TS data allows for the investigation of potential oxygen atom migration between the Bi-O and Re-O sublattices. Molecular dynamics (MD) calculations undertaken at 1100 °C found this oxygen migration to occur, with an increase in the average Re coordination number from 4.5 to 5.67 over the course of the simulation.[8]

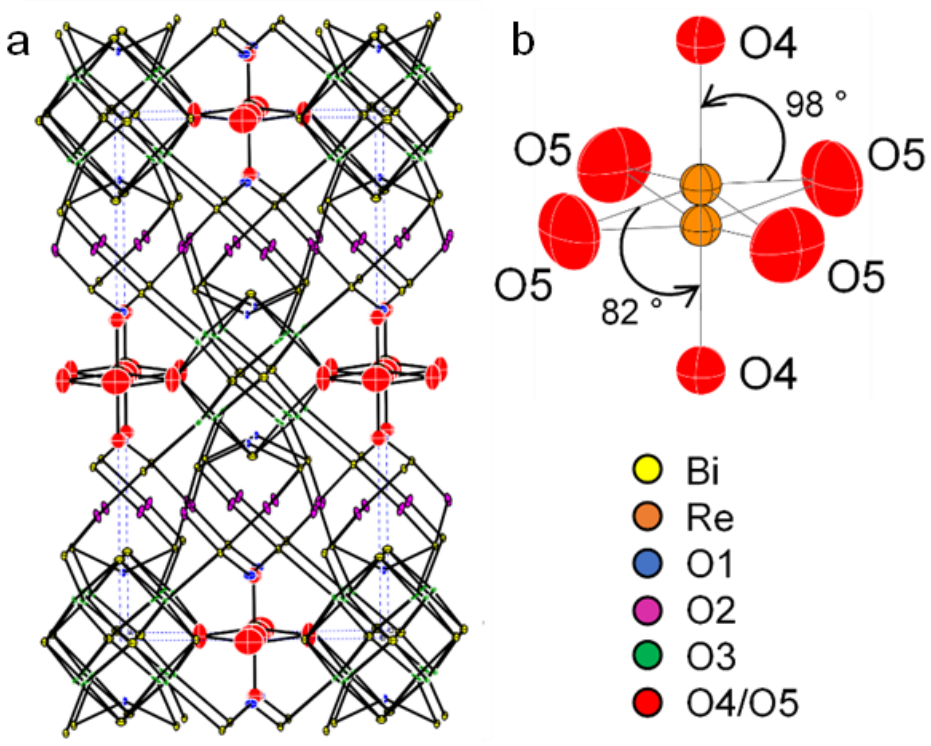

Figure 5.1: a) Projected view of the room-temperature $Bi_{28}Re_2O_{49}$ structure along the *y* axis including atomic displacement parameters plotted with 50 % probability; b) Projection of the Re coordination environment, based on the image from Payne *et al.*[8]

5.2 Synthesis of $Bi_{28}Re_2O_{49}$

10 g of powdered $Bi_{28}Re_2O_{49}$ was synthesised by solid-state synthesis. Stoichiometric amounts of powdered Bi_2O_3 (9.3088 g, 19.98 mmol, 99.99 %, Aldrich) and NH_4ReO_4 (0.7656 g, 2.86 mmol, 99 %, Aldrich) were ground together in an agate mortar using a pestle before being fired at 800 °C for 60 hours in an alumina crucible with a heating and cooling rate of 5 °C per minute, yielding a yellow powder.

5.3 Characterisation of $Bi_{28}Re_2O_{49}$

5.3.1 Laboratory powder X-ray diffraction

To investigate the purity of the synthesised $Bi_{28}Re_2O_{49}$ sample prior to central facility experiments, laboratory powder X-ray diffraction (PXRD) data were collected and a Rietveld refinement performed. The starting model for the refinement was that reported by Payne *et al.*

(Table 5.1),[8] with the following parameters refined: ten background parameters, two lattice parameters, zero-point error, peak-shape function parameters, one isotropic displacement parameter, and a scale factor. The recorded PXRD pattern and calculated model based on the refinement are shown in Figure 5.2. The refinement showed the sample to be single phase and so was used for subsequent total scattering analyses.

Table 5.1: Atomic fractional coordinates and site fractional occupancies for the initial $Bi_{28}Re_2O_{49}$ model.[8] *a* = 8.7216(1) Å, *c* = 17.4177(2) Å, space group I4/m.

Atom	Site	x	y	z	Occupancy
Bi1	16i	0.70058(9)	0.89430(8)	0.67043(4)	1
Bi2	8h	0.78806(12)	0.55405(12)	0.5	1
Bi3	4e	0.5	0.5	0.65539(8)	1
Re1	4e	0	0	0.48569(19)	0.5
O1	8g	0.5	0	0.6233(12)	1
O2	16i	0.5757(16)	0.7528(15)	0.74385(91)	1
O3	16i	0.6304(17)	0.6785(16)	0.57739(88)	1
O4	4e	0	0	0.6155(34)	0.75
O5	8h	0.0008(85)	0.2101(58)	0.5	0.75

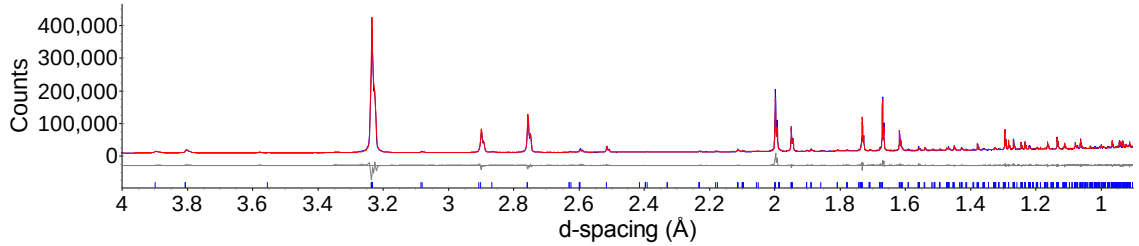

Figure 5.2: Rietveld refinement of $Bi_{28}Re_2O_{49}$ at room temperature, d7_05431, *a* = 8.7219(1) Å, *c* = 17.4056(1) Å, space group = I4/m, R_{wp} = 4.505 %.

5.3.2 Powder neutron diffraction

Powder neutron total-scattering data for $Bi_{28}Re_2O_{49}$ were collected at room temperature and 700 °C on the Polaris diffractometer at ISIS, with the TS data to be used in RMC analyses to deepen the understanding of the local structure of the material. Data were collected in runs of 150 μAh (~1 hour), with twelve runs collected at room temperature and nine runs collected at 700 °C. The Rietveld refinements for the room temperature and 700 °C data were undertaken in GSAS[11] using data collected from detector banks 3 and 5. These two banks were chosen as data from bank 5 has the highest resolution, whilst data from bank 3 has a wide Q range, a feature required for a comprehensive total-scattering experiment.

For both the room-temperature and 700 °C data sets, the following parameters were refined: ten background terms per data set, zero point displacement parameter, two lattice parameters, all atomic coordinates, one independent isotropic displacement parameter per atomic site, peak-shape function terms, and scale factors for each detector bank. The room-temperature data sets showed no presence of any impurities, but at 700 °C there is the presence of an impurity phase (Figure 5.3c), which was identified subsequently as Bi_3ReO_8.

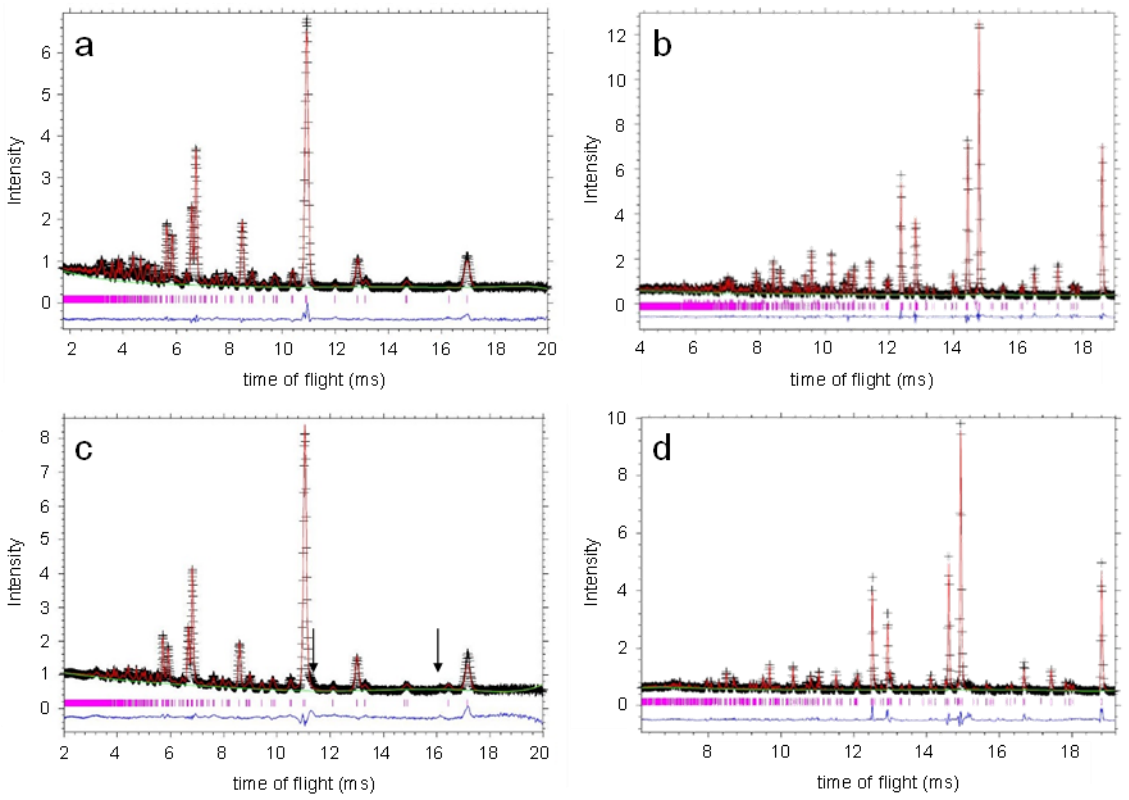

Figure 5.3: Rietveld refinements of $Bi_{28}Re_2O_{49}$ at room temperature collected on: a) Bank 3, POL66913_b3, R_{wp} = 1.850 %; b) Bank 5, POL66913_b5, R_{wp} = 2.190 %: *a* = 8.7157(1) Å, *c* = 17.3674(1) Å. Rietveld refinements of $Bi_{28}Re_2O_{49}$ at 700 °C collected on: c) Bank 3, POL66974_b3, R_{wp} = 2.570 %; d) Bank 5, POL66974_b5, R_{wp} = 2.510 %: *a* = 8.8142(1) Å, *c* = 17.5020(1) Å. The arrows in Figure 5.3c identify the peaks corresponding to the Bi_3ReO_8 impurity phase.

5.4 Room-temperature total-scattering data analysis

A previous report states that the ReO_x polyhedra in $Bi_{28}Re_2O_{49}$ are solely 4- and 6-coordinate in a 3:1 ratio, with an average Re coordination number of 4.5.[1] To investigate whether only these two coordination environments exist for Re, or if a range of coordination environments exist on a local scale, three model configurations were considered (Table 5.2).

Table 5.2: RMCProfile configurational models considered for analysis of the room-temperature data. .dw and .bvs pertain to distance-window constraints and bond-valence-sum restraints respectively.

Model	Average Re coordination	Atom swapping	Restraints and constraints
Model 1	4.5	Yes, O-Va on Re-O sublattice	.dw, .bvs
Model 2	4.5	No	.dw, .bvs
Model 3	4.5	No	Rigid body

5.4.1 Model 1

The first RMC model produced was designed to allow the Re atoms in the ReO_x polyhedra to possess any coordination number from x = 0 to 6 (Model 1). The maximum value for x in the ReO_x polyhedra is six as there are only six neighbouring O4 and O5 oxygen positions which can be occupied. A 5 × 5 × 4 supercell of tetragonal $Bi_{28}Re_2O_{49}$ was reduced to P1 symmetry and used to create the starting configurations for the RMCProfile refinements. Within the supercell, the atoms are grouped according to their element or coordination environment: Bi, Re, O1-O3

(O atoms in the Bi-O sublattice), O4-O5 (O atoms in the Re-O sublattice), and O45Va (vacancies on the O4 and O5 sites caused by the site occupancies of 0.75).

In the Crumpton *et al.* and Payne *et al.* models,[1, 8] atoms on the Re1 site lie on the 4e (0, 0, *z*) special position close to the inversion centre at (0, 0, 0.5), giving two sites with 0.5 occupancy, but for our initial model the Re atoms were placed onto the inversion centre on the 2b (0, 0, 0.5) special position. This is because RMC analyses perform translational atomic movements, allowing an investigation into whether the Re atoms displace onto positions around the inversion centre.

The starting configurations for Model 1 were created by taking the 200 Re atoms and randomly selecting 150 of these to start as 4-coordinate ReO_4 polyhedra. Once these atoms were chosen, two oxygen atoms from each of these 150 polyhedra were assigned as vacancies in the O45Va group, thereby generating the correct starting model of 75 % 4-coordinate and 25 % 6-coordinate ReO_x polyhedra. 6 of these starting configurations were created (C*X*, *X* = 1 to 6), with 6 RMC runs carried out on each configuration (R*Y*, *Y* = 1 to 6). Each of the RMC runs consisted of approximately 13 million moves, with this number of moves chosen as a good balance between processing time and quality of fit (*vide infra*). The RMCProfile refinements were carried out using the simultaneous refinement of Bragg, *F(Q)* (total-scattering structure factor), and *G(r)* (total radial distribution function) data sets, producing outputs of Bragg, *T(r)* (total correlation function), and *S(Q)* (normalised total-scattering structure function) data. The relationships between *S(Q)* and *F(Q)*, and *T(r)* and *G(r)* are explained in Chapter 2.

During the RMCProfile refinement runs, the 'atom-swap' function was used to swap oxygen atoms and oxygen vacancies between the O4-O5 and O45Va groups, potentially allowing for a range of Re coordination environments to be created. This atom swapping was performed with a 25 % swap frequency i.e. for every three RMC translational moves, one atom swap was attempted.

For the RMC runs, the command files included the use of distance-window (DW) constraints of 1.90 Å to 2.75 Å for the Bi to O1-O3 distances, and 1.58 Å to 2.50 Å for the Re to O distances. These values for the distance constraints were chosen to keep the distances between the atom groups at sensible values without being too restrictive and hindering the translational movements generated by the RMCProfile program. Additionally, bond-valence-sum (BVS) restraints were used to prevent the species from becoming under- or overbonded.

The final fits of the RMC models show good agreement to the Bragg, *T(r)*, and *S(Q)* data (Figure 5.4), with no major discrepancies seen across their entire ranges. The final fit to the Bragg data is the poorest of all three data sets, with lower calculated intensities than those observed experimentally, but this is attributed to RMCProfile sacrificing the fit to the average structure (Bragg) to improve the fit to the local structure (*T(r)* and *S(Q)*).

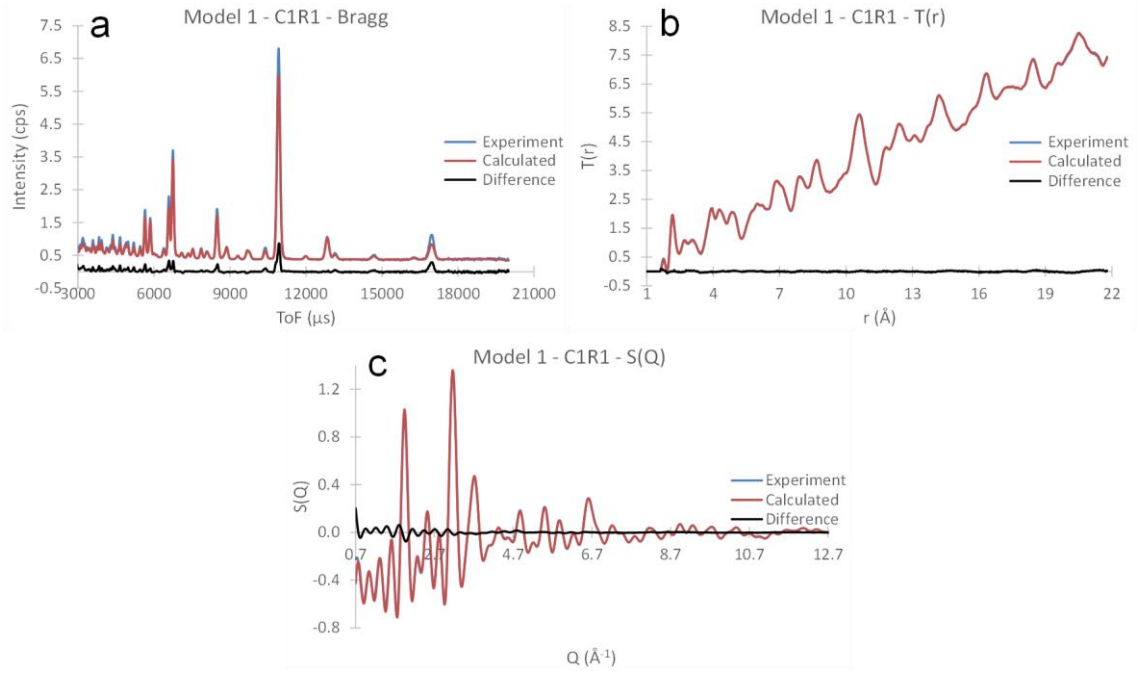

Figure 5.4: Experimental data, RMC calculated fits, and difference curves for Model 1 for $Bi_{28}Re_2O_{49}$ at room temperature for: a) Bragg data; b) *T(r)* data; c) *S(Q)* data.

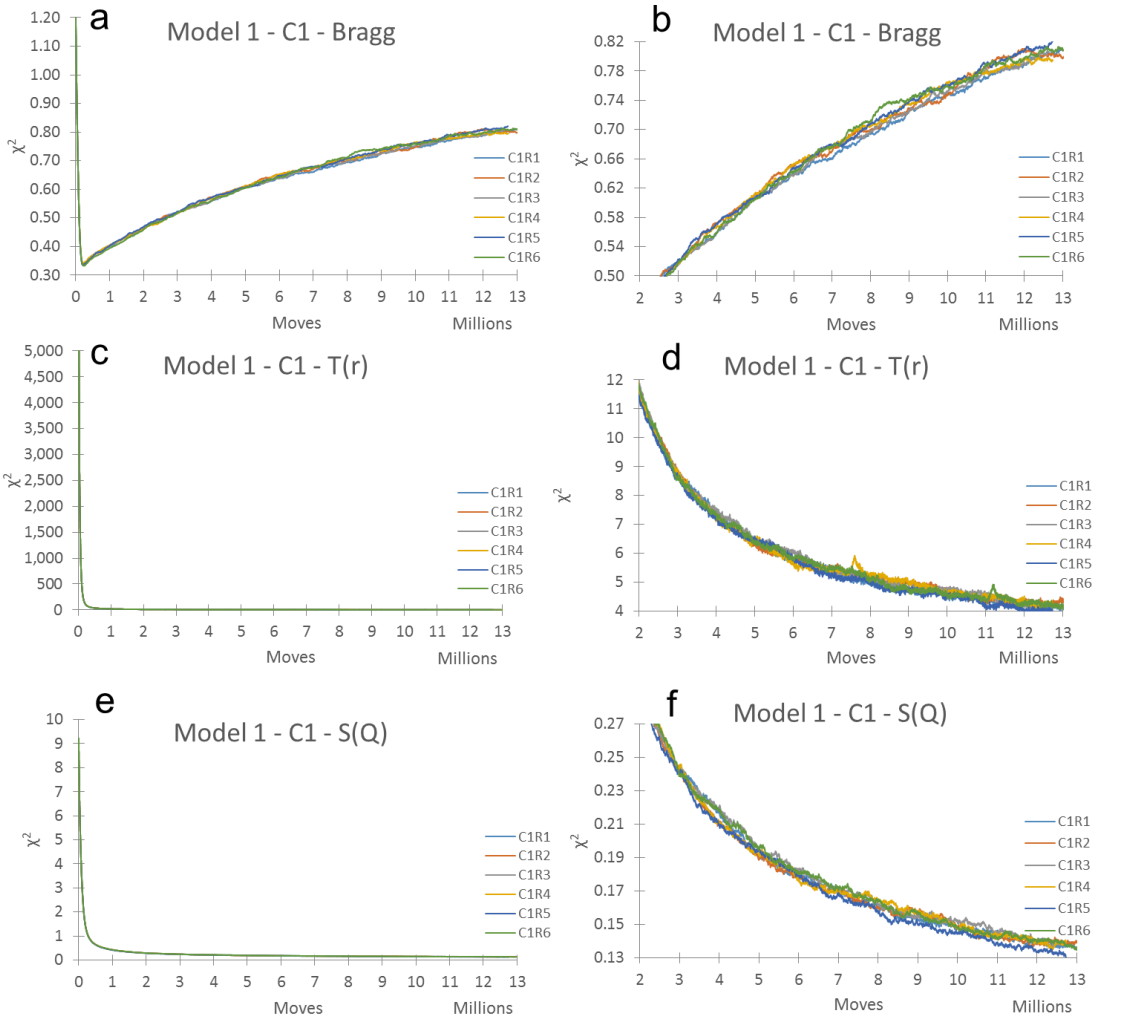

Figure 5.5: Plots showing the χ^2 values versus number of moves for the six runs of C1 of Model 1 using: a) and b) Bragg; c) and d) *T(r)*; e) and f) *S(Q)* data sets. The plots labelled b, d, and f are close-up versions of plots a, c,and e, detailing the region of 2 to 13 million moves. The curves for C2 to C6 have been omitted for clarity, but overlay with the curves for C1.

The χ^2 values for the RMC runs show high levels of agreement both intra- and inter-configuration (Figure 5.5), with only small deviations between the observed values (Bragg = 0.04, *T(r)* = 0.1, and *S(Q)* = 0.02). For each of the 36 runs, the Bragg χ^2 values decrease over the first ~200,000 moves before increasing again, whilst the *T(r)* and *S(Q)* χ^2 values continually decrease before plateauing. This indicates that the fit to the average and local structures both improve initially, but over time the fit quality to the average structure is reduced to improve the fit to the local structure.

Following the RMC runs, the final coordination number for each Re atom was determined using the *neighbour_list* program, with a maximum Re-O length of 2.5 Å. This cut-off distance was chosen as this is the value for the upper distance limit for a Re-O bond length using the distance window constraints.

Analysis of the Re coordination numbers generated from all 7200 ReO_x polyhedra for Model 1 show that Re atoms primarily adopt 4- and 5-coordinate polyhedra (46.28 % and 42.92 % of all ReO_x polyhedra respectively, Figure 5.6), with a small percentage of ReO_6 polyhedra (5.98 %). This local-structure model therefore shows greater variation in the ReO_x coordination polyhedra compared to the average structure case reported previously.[1] The RMC analysis also showed the presence of ReO_2 and ReO_3 polyhedra (0.03 % and 4.81 % respectively). However, as there is no reported evidence of these polyhedra in a review on the crystal chemistry of oxorhenates by Müller-Buschbaum,[12] and that the BVS values for 2- and 3-coordinate Re would be considerably lower than the expected value of 7, they are discounted as outliers arising from the random nature of the atom-swapping process.

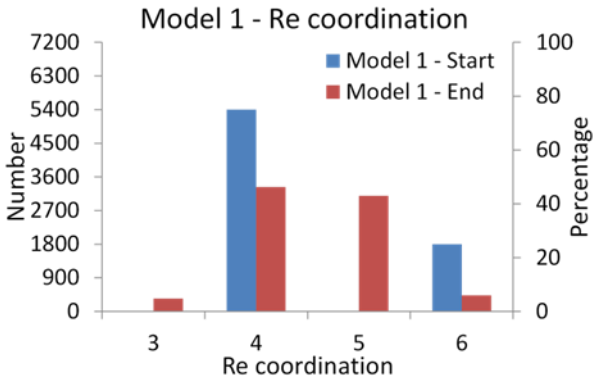

Figure 5.6: Coordination numbers for Re in ReO_x polyhedra for Model 1. The 2-coordinate polyhedra have been omitted from the figure for clarity.

To investigate whether the vacancies on the O4-O5 sites are randomly distributed following the RMC runs or if they accumulate in specific locations within the supercell, the supercell was collapsed back into a single unit cell (Figure 5.7b). From this image, it can be seen that the vacancies (black circles) do not preferentially occupy the axial or equatorial positions around the Re atoms, but rather remain randomly distributed. Additionally, this image reveals that the distance-window and bond-valence restraints allow for displacement of the atoms from their starting locations whilst not moving too far away, as shown by the comparison of Figure 5.7a and Figure 5.7b.

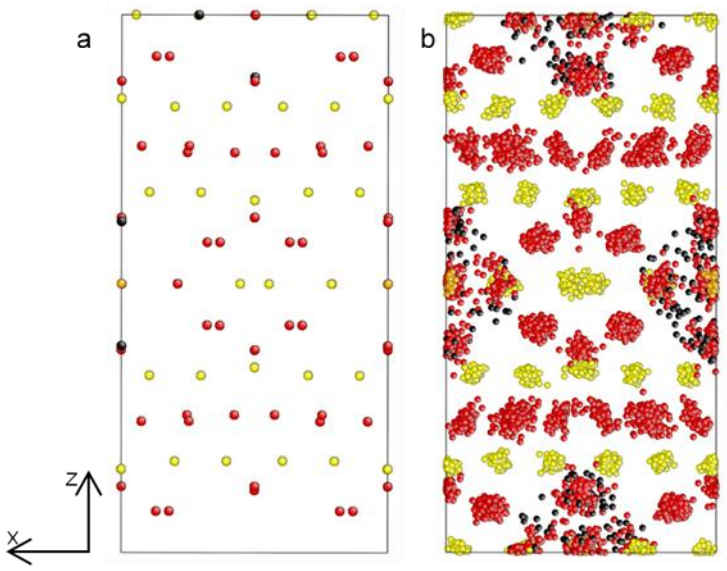

Figure 5.7: Views of the 5 × 5 × 4 supercell collapsed into a single unit cell for Model 1 viewed along the *y* axis at: a) C1 start; b) end of the C1R1 run. Bi = yellow, Re = orange, O = red, Vacancy = black.

How effective the BVS restraints are in restraining the bond valence sums for the various atom groups (Bi, Re, O1-O3, and O4-O5) towards their ideal values was discerned by plotting the BVS values for all atoms across the final configurations in the 36 runs (Figure 5.8), expressed as a percentage of the total number of atoms in that particular atom group.

These data show that the BVS values for the Bi, Re, and O1-O3 groups converge towards their expected values, with final average BVS values of 2.956(2), 7.060(8), and 2.038(2) for these three groups respectively. However, the O4-O5 atoms show deviations from this trend, with an average BVS value lower than expected at 1.710(7), with a wider range of values and a shoulder to the peak at low BVS. This could be attributed to the O4-O5 atoms swapping with vacancies and causing oxygen atoms to reside on positions with longer than ideal Re-O bond lengths.

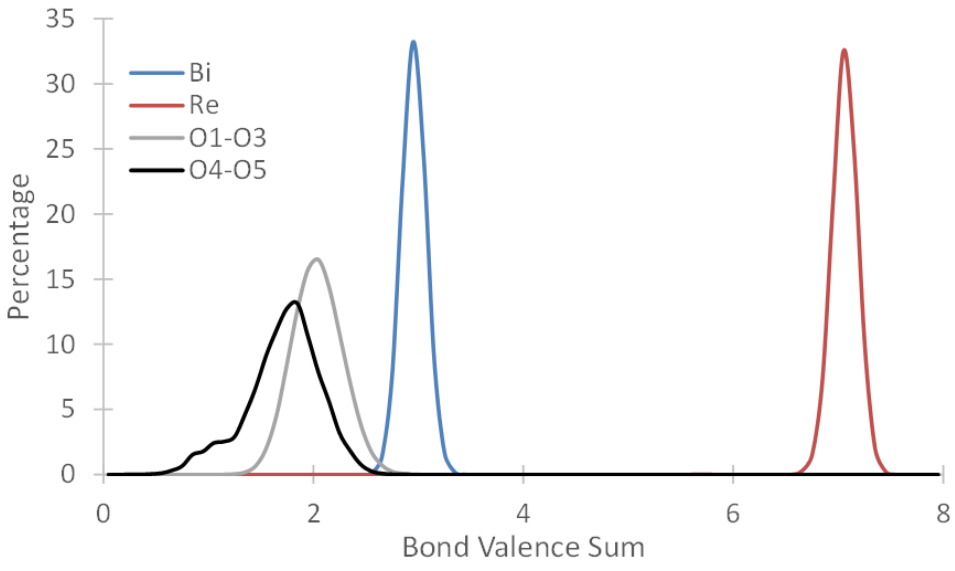

Figure 5.8: Plot of the BVS distributions for the Bi, Re, O1-O3, and O4-O5 atom groups in Model 1 of $Bi_{28}Re_2O_{49}$.

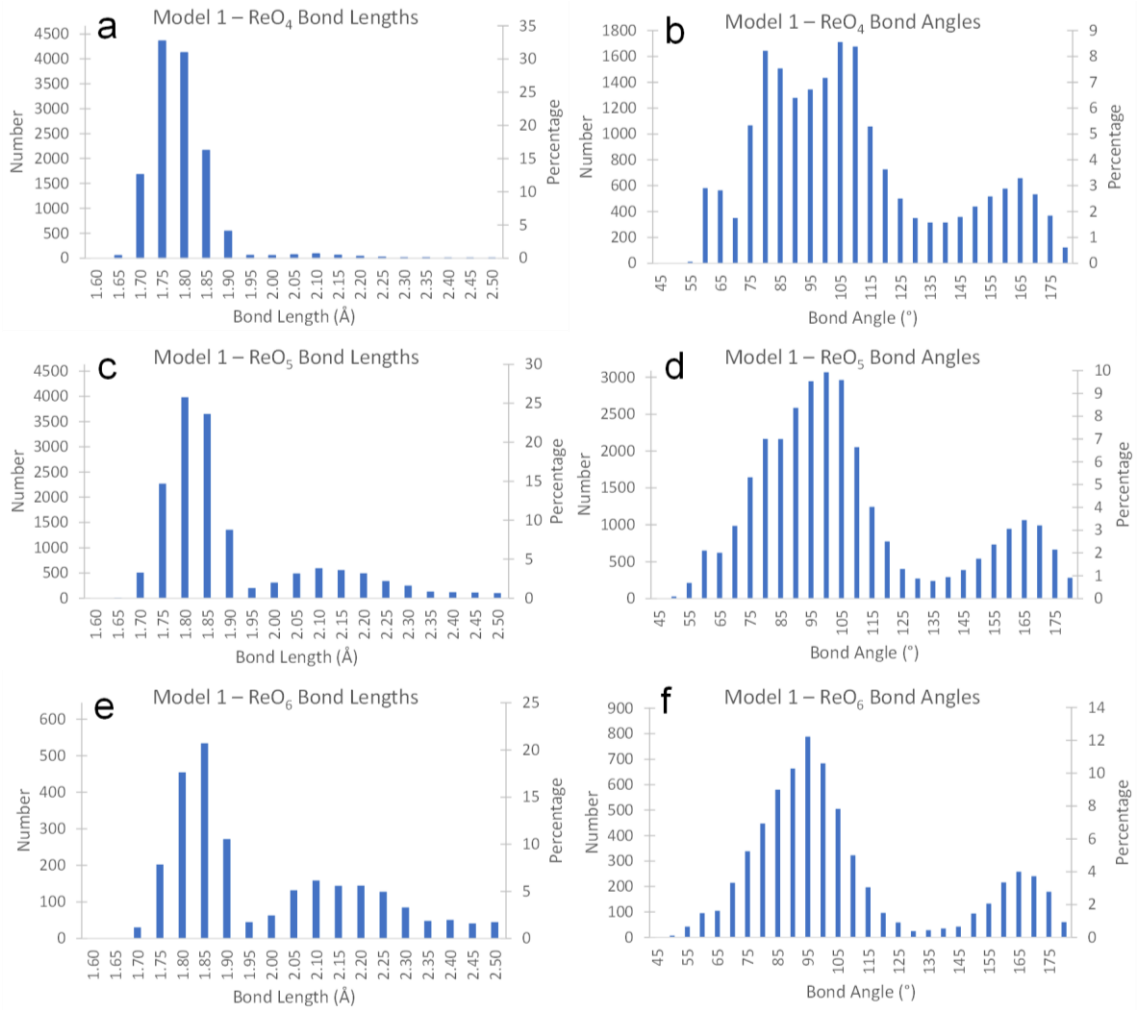

Figure 5.9: Plots comparing the ReO_x (x = 4 to 6): a), c), and e) Re-O bond lengths; b), d), and f) O-Re-O bond angles for Model 1 of $Bi_{28}Re_2O_{49}$.

To evaluate how distorted the ReO_x polyhedra are following an RMCProfile refinement, the Re-O bond lengths and O-Re-O bond angles for all runs of the Model 1 configuration were obtained and separated according to the ReO_x coordination environment. The plot of the Re-O bond lengths within the ReO_4 polyhedra (Figure 5.9a) clearly shows one peak centred around 1.75 Å. The ReO_5 and ReO_6 bond length distributions (Figure 5.9c and Figure 5.9e) show two maxima at ~1.80 Å and ~2.10 Å, although the former peak is considerably more intense than the latter. The peak centred at ~2.10 Å could be the cause of the low BVS shoulder of the O4-O5 curve in Figure 5.8. The O-Re-O angle peaks show evidence of bimodal distributions (Figure 5.9b, d, and f) arising from the O-Re-O bond angles starting centred on 90 ° and 180 °, as the initial ReO_x polyhedra are adapted from octahedra. Over the course of the RMC refinements these bond angles distort, but as there are no polyhedral restraints, there is nothing to restrain the bond angles to the ideal values for the given Re coordination environment.

5.4.2 Model 2

Whilst Model 1 allows Re coordination environments which are not solely 4- and 6-coordinate, a model where this is the case needed to be considered for comparison. This model, Model 2, investigates how the fit to the data differs between a model with a 25 %

6-coordinate and 75 % 4-coordinate distribution of ReO_x polyhedra, and one in which the Re coordination numbers are not fixed (Model 1).

As for Model 1, of the 200 Re atoms found in a 5 × 5 × 4 supercell of $Bi_{28}Re_2O_{49}$, two oxygen atoms on 150 of the 200 ReO_6 polyhedra were randomly assigned as vacancies instead, forming 4-coordinate polyhedra. This resulted in 300 of the 1200 O4-O5 sites in the six starting configurations for Model 2 being vacant, generating the average Re coordination number of 4.5 required.

Unlike Model 1, only translational movements were allowed, with no atom swapping between the atoms and vacancies in the O4-O5 and O45Va groups, thereby maintaining the 4- and 6-coordinate ReO_x polyhedra. Six configurations were produced, with each undergoing six different RMC runs for a total of 36 runs. Identical distance window and BVS restraints to those used for the Model 1 refinements were implemented.

As for all of the RMC runs presented in this chapter, the cut-off point for the runs was taken to be 13 million moves, since testing revealed that no significant improvement in the level of fit was observed past this point (Figure 5.10a-c). Therefore, this cut-off was chosen as a balance between the quality of fit and the amount of computing time required. Additionally, analysis shows that the visual fit of the model to the RMC data (Figure 5.10d) does not improve after RMC File 20 (~1.8 million moves). The initial fit to the PDF data (RMC File 01) is poor, as the model at this juncture is more representative of the average structure than the local structure. Over the course of the RMC refinement the fit improves as the translational movements of the atoms allow them to describe the local structure. Figure 5.11 shows that the fits to the data for Model 2 are comparable to those for Model 1, with very little intensity seen in the difference curve for these two models.

Analysis of the χ^2 curves in Figure 5.12a, c, and e appears to show a difference for Models 1 and 2. Further analysis reveals this not to be the case, with the two models having high levels of agreement in their χ^2 values (Figure 5.12b, d, and f). These initial differences in the χ^2 values arise from Model 1 having a 25 % atom-swap frequency, meaning that a quarter of the total moves are not translational. Therefore, multiplying the number of moves for the Model 1 curves by 0.75 generates χ^2 plots with the same number of translational moves as Model 2. When these curves are plotted together (Figure 5.12b, d, and f), they show a good degree of overlap for the two models.

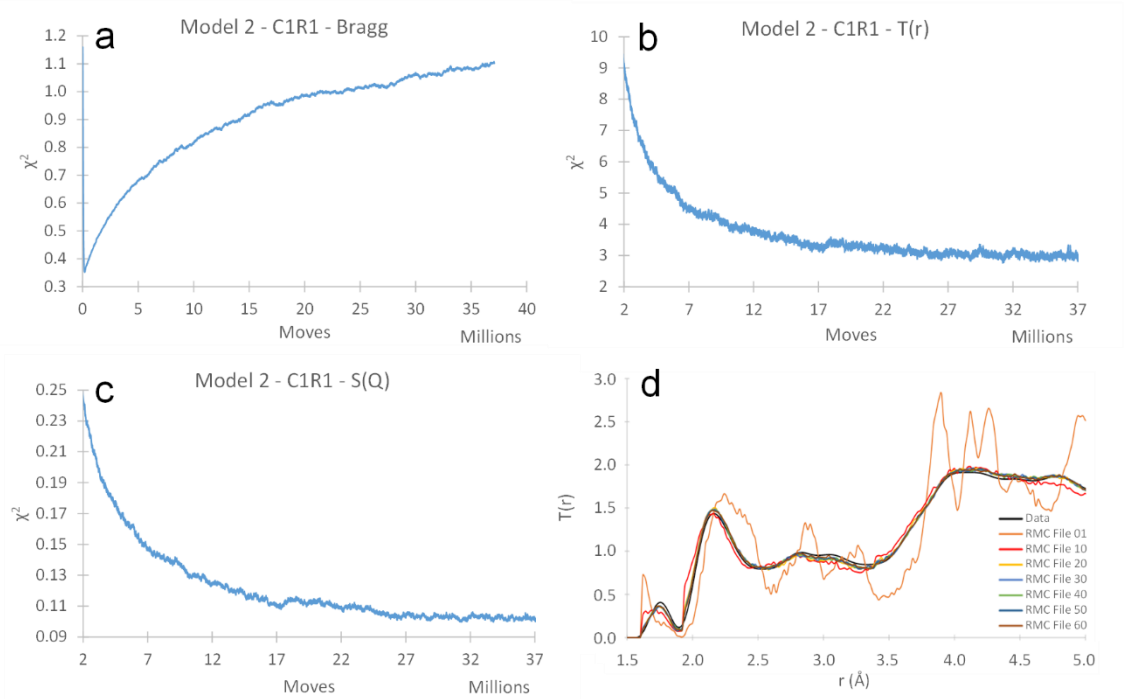

Figure 5.10: Longer RMCProfile refinements showing how the χ^2 values change over the course of the refinement for the: a) Bragg; b) *T(r)*; c) *S(Q)* data sets. d) *T(r)* plot showing that after RMC File 20 (~1.8 million moves), there is very little change in the fit to the data.

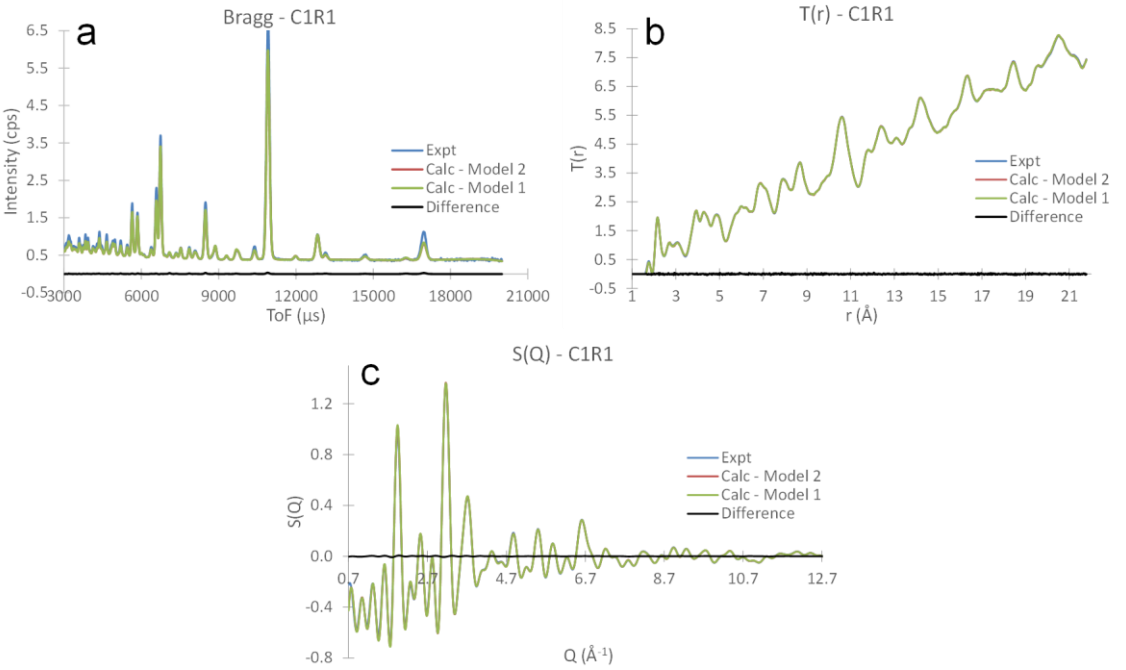

Figure 5.11: Comparison plots of Models 1 and 2 to the collected: a) Bragg; b) *T(r)*; c) *S(Q)* data. The 'Difference' curve is calculated from the difference between the calculated curves for Model 1 and Model 2 and shows the high level of agreement between the two calculated models.

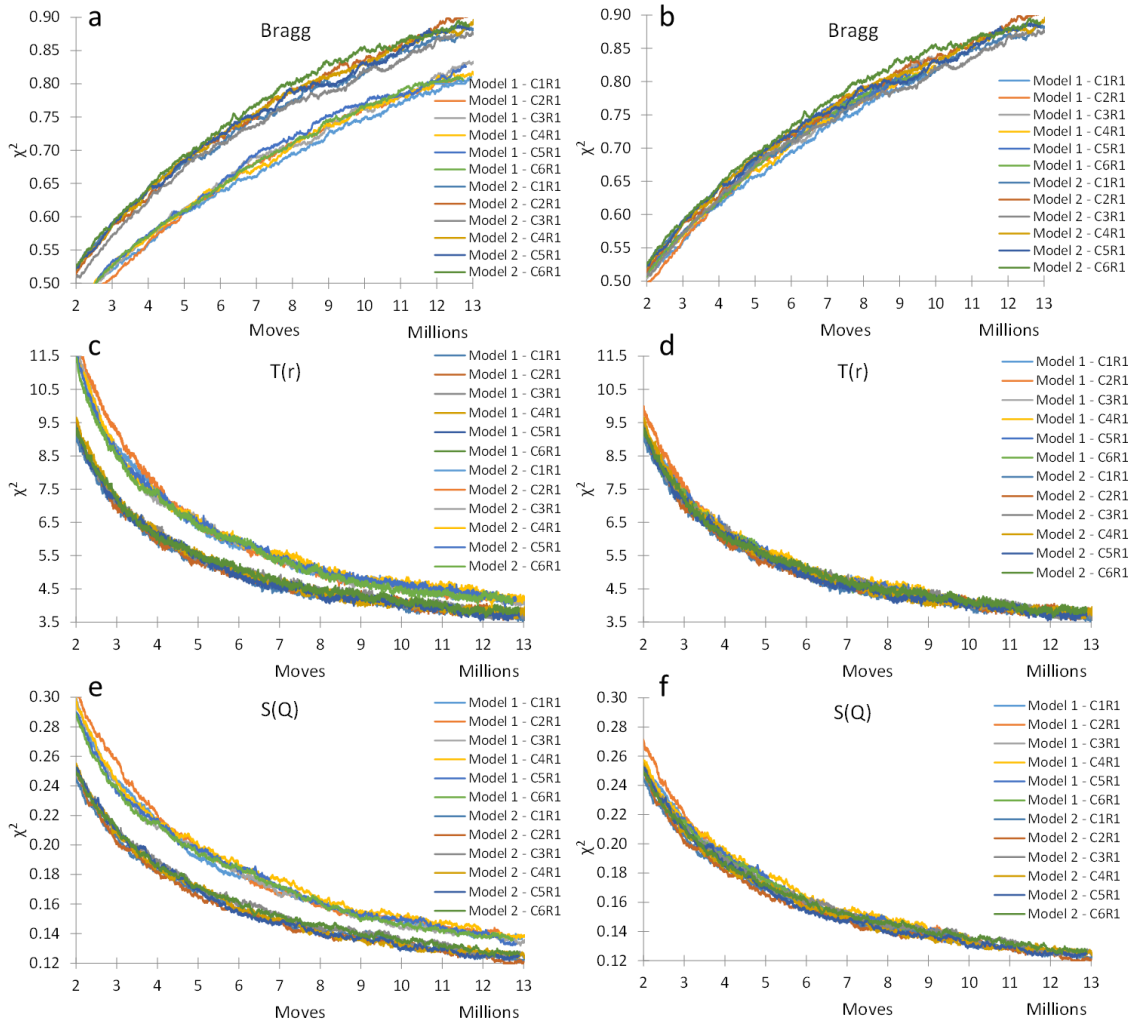

Figure 5.12: Plots illustrating that whilst the χ^2 curves for Model 1 and Model 2 look different initially, if only the translational movements are taken into account (due to 25 % atom-swap frequency in model 1) then the curves overlap with high levels of agreement.

Analysis of the ReO_x coordination polyhedra following the Model 2 RMC runs revealed that the ratio of 75 % ReO_4 and 25 % ReO_6 polyhedra were maintained throughout, with no evidence of ReO_3 or ReO_5 polyhedra observed. The ReO_4 and ReO_6 Re-O bond lengths and O-Re-O bond angles for Model 2 reveals differences in the distributions obtained through analysis of the TS data and those from previously reported MD simulations. The ReO_4 polyhedra are tetrahedra in the Crumpton *et al.* model, whilst the ReO_6 polyhedra are octahedra.[1] From this, it would be expected that the ReO_4 bond angles have a unimodal distribution tightly centred around 109 ° in Figure 5.13c. Instead, a broad range of bond angles are observed, with some ReO_4 polyhedra distorting into square-planar geometries. By contrast, for the ReO_6 bond angles (Figure 5.13d), a well-defined bimodal distribution with peaks centred around 90 ° and 180 ° is expected, in a 4:1 ratio of intensity due to the twelve 90 ° and three 180 ° O-Re-O bond angles in an octahedron. This distribution is observed, with the peak from 135 ° to 180 ° containing 19.9 % of the overall O-Re-O bond angles. This difference in bond length and angle distributions is due to the literature study fixing the ReO_x polyhedra into their coordination geometries, whereas in this RMC analysis, the Re and O atoms could displace freely, with no rigid-body restraints used to fix the geometries.

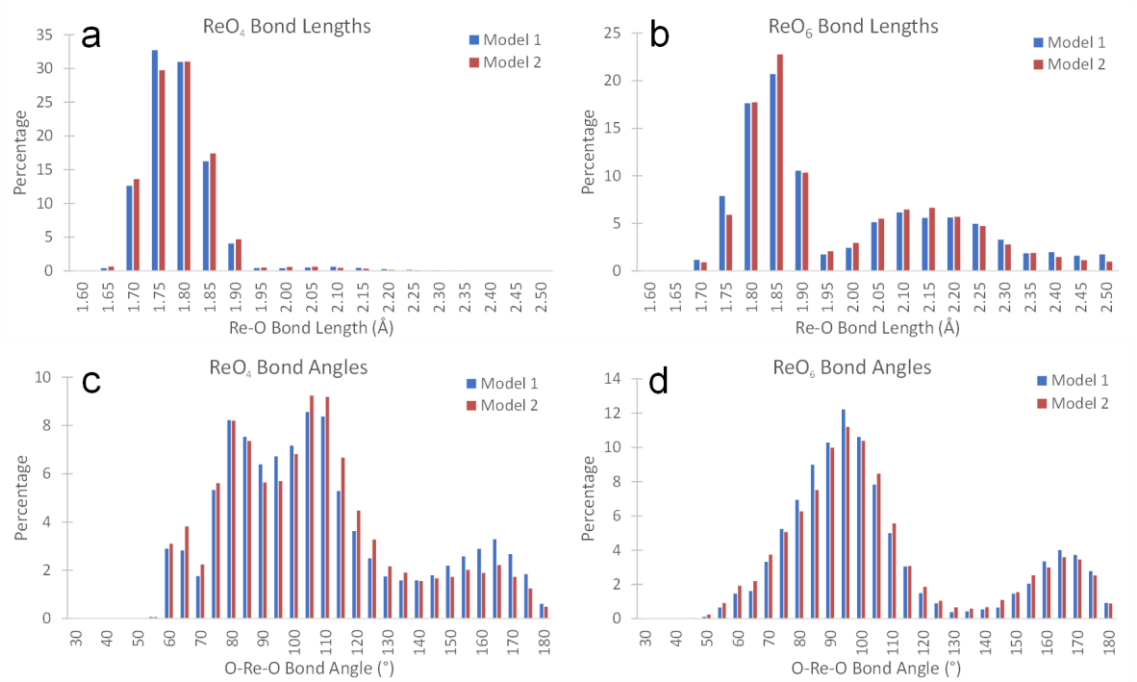

Figure 5.13: Plots comparing the ReO_x (x = 4 and 6): a)-b) Re-O bond lengths; c)-d) O-Re-O bond angles for Models 1 and 2.

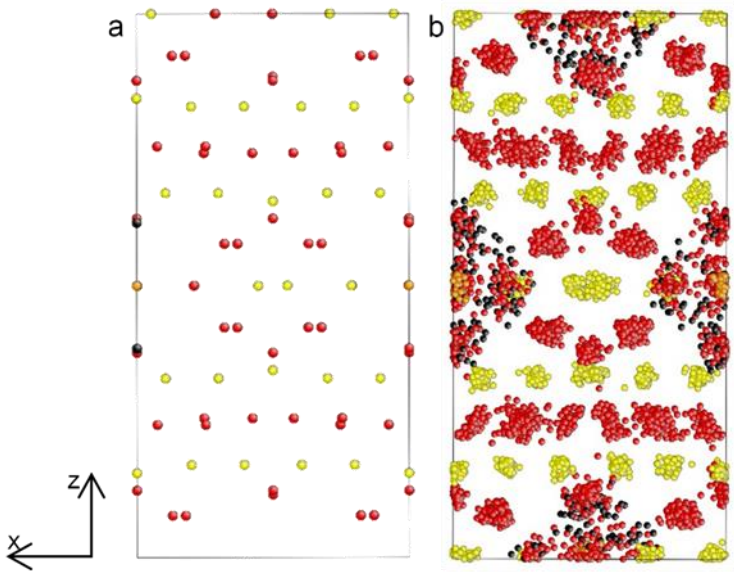

Figure 5.14: Views of the 5 × 5 × 4 supercell collapsed into a single unit cell for Model 2 viewed along the *y* axis at: a) C1 start; b) end of the C1R1 run. Bi = yellow, Re = orange, O = red, Vacancy = black.

From Figure 5.14b of the supercell collapsed into one unit cell, it can be shown that the vacant positions on the O4-O5 sites are randomly distributed, with no preference for axial or equatorial positions. Overall, a comparison of the initial and final atomic positions in the Model 2 structure (Figure 5.14) shows that the distance window and bond valence restraints allow for displacement of the atoms from their starting locations without allowing them to displace to unrealistic positions within the structure.

The similarity between the resulting configurations from Model 1 and Model 2 continues when comparing the bond valence sums for the four different atom groups across both models

(Figure 5.15). This plot shows that the BVS values for both models are virtually identical (e.g. the average BVS value is 2.906(2) and 2.961(2) for Bi in Model 1 and Model 2 respectively), with the same differences observed between the BVS values for O1-O3 and O4-O5.

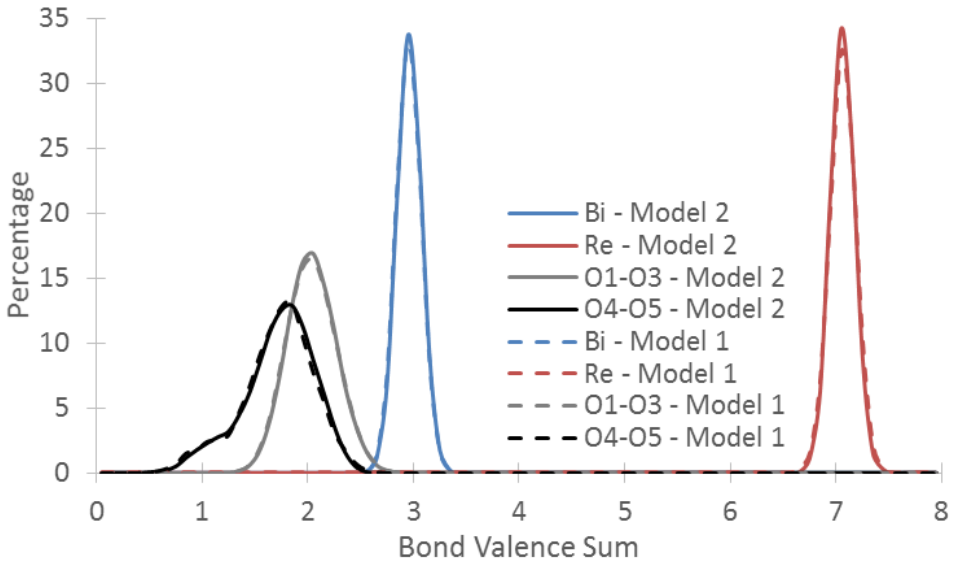

Figure 5.15: BVS distributions for the various atom groups in Model 1 and Model 2 for $Bi_{28}Re_2O_{49}$ at room temperature.

5.4.3 Model 3

A further RMC model (Model 3) was considered, utilising rigid-body polyhedral restraints to attempt to model the ReO_x polyhedra as ideal tetrahedra and octahedra and provide a direct comparison with the model of Crumpton *et al.*[1] A series of RMC runs were carried out using the Model 3 configuration, but the results show that the current RMCProfile software cannot model correctly our material with rigid-body restraints. This is because the rigid-body restraints used during the RMC runs are applicable only to the specific ratio of tetrahedra and octahedra found in ZrW_2O_8, the material for which the rigid-body restraints were designed. Therefore, these rigid-body restraints cannot be applied for $Bi_{28}Re_2O_{49}$, and further use of rigid bodies for local-structure modelling has been put on hold until the RMCProfile program is coded to include them for more generalised application, allowing the ratio of tetrahedra and octahedra present in $Bi_{28}Re_2O_{49}$ to be handled appropriately.

5.4.4 Distributions of Re atoms at room temperature

An investigation was undertaken to determine if the distribution of Re atoms is consistent with the split-site occupancy along the *z* axis as previously reported for the average structure of $Bi_{28}Re_2O_{49}$. For each RMC run, the maximum distances the Re atoms are displaced along the *x*, *y*, and *z* axes in both the positive and negative directions were summed to give the "atom spread" values in Ångströms. From these histograms for Models 1 and 2 (Figure 5.16), the Re atoms are found at distances further from their starting positions along the *z* axis compared to the *x* and *y* axes, indicated by the increased number of RMC runs at larger values of the "Atom Spread" for the *z* axis.

From Payne *et al.*, the Re fractional atomic coordinates are (0, 0, 0.4857) and (0, 0, 0.5143), hence the Re atoms are ± 0.249 Å from the special position (0, 0, 0.5) along the *z* axis, giving an Re atom-spread value of 0.498 Å, which is a smaller spread value than seen from the RMC analysis in Figure 5.16. This helps to support the previous assignment of Re atoms on a split site at (0, 0, *z*) in the average structure, close to the (0, 0, 0.5) special position.

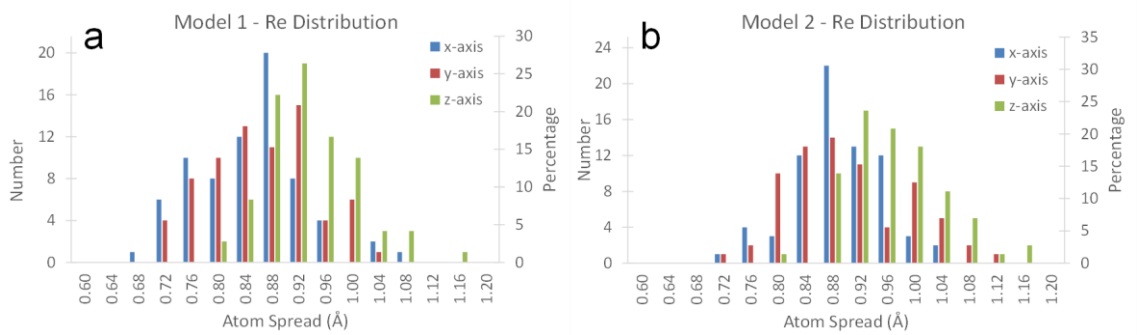

Figure 5.16: Plot of the spread of the Re atoms from their starting positions along the *x*/*y*/*z* axes for: a) Model 1; b) Model 2.

To study the spread of the Re atoms from their starting positions following the RMC runs more closely, plots were created (Figure 5.17) detailing the spherical coordinates for the Re atoms relative to the starting coordinates. A Python script was written to use the Cartesian coordinates of the atomic positions following the RMC runs - from the collapsed unit cell created by folding the supercell upon itself (Figure 5.7b) - to calculate the three spherical coordinate values (displacement distance, θ angle, and ϕ angle) for each Re atom relative to their starting coordinates. This was aided by splitting the atoms into two groups, determined by which of the two Re starting coordinates they originated from: (0.5, 0.5, 0) or (0, 0, 0.5). It was impossible to assign Re atoms against the wrong starting coordinates, as the parameters of the models prevent such large degrees of cation migration.

The spherical coordinates were plotted as histograms (Figure 5.17), with displacement distance referring to the length of the vector between the starting and final coordinates of a Re atom measured in Å. The θ angle is the angle between the *z* axis and the displacement vector, ranging between 0 and 180 °, whilst the ϕ angle is the angle measured from the positive *x* axis to the displacement vector rotating towards the positive *y* axis, ranging from 0 to 360 °.

There is a large degree of overlap between the histograms for Models 1 and 2, with a unimodal distribution seen for the Re displacement distances (Figure 5.17a). The average displacement distances for Models 1 and 2 are 0.343(1) Å and 0.355(1) Å respectively, showing that the utilised constraints and restraints are not preventing translational movement of the atoms from occurring. However, the Re θ angle distribution is bimodal (Figure 5.17b), whilst the number of Re atoms within each ϕ angle bin is relatively consistent across the entire angular range (Figure 5.17c). The bimodal distribution for the θ angle suggests that there are two clusters of Re atoms; one above the horizontal plane, and one below it. This is agreement with the findings of the distribution of Re atoms elongating preferentially along the *z* axis, as the pseudo-formation of a split site is observed.

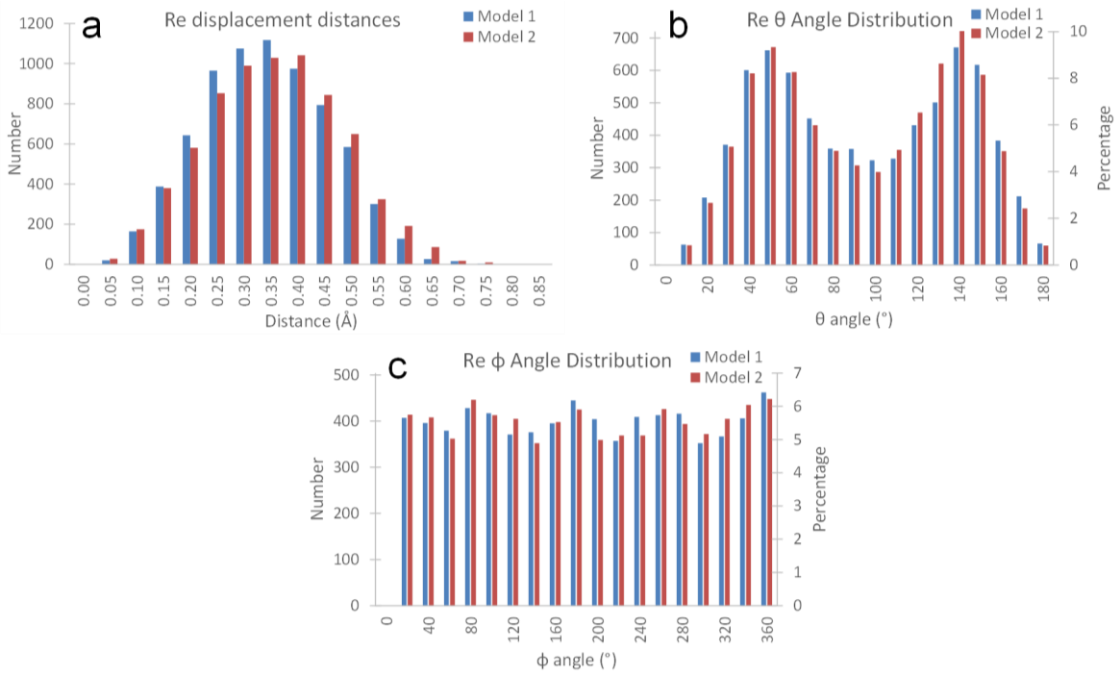

Figure 5.17: a) displacement vector lengths; b) θ angles; c) ϕ angles for Re atoms in Models 1 and 2 relative to their starting coordinates.

5.5 700 °C data total-scattering analysis

Ab initio molecular dynamics calculations performed on $Bi_{28}Re_2O_{49}$ at 1100 °C showed some transfer of oxygen atoms from the Bi-O to Re-O sublattice, resulting in an increase in the average Re coordination number from 4.5 to 5.67 over the course of the simulation.[8] To investigate if this effect is contained in the neutron total-scattering data, a pair of RMC models were created with different methods of atom swapping (Table 5.3). These two models, Model 4 and Model 5, used appropriate constraints and restraints, along with starting models which allow for a good level of comparison to the room temperature models, and so the results of these RMC runs will be described in the remainder of this chapter.

Table 5.3: RMCProfile configuration models created for analysis of the 700 °C data. .dw and .bvs pertain to distance-window constraints and bond-valence-sum restraints respectively.

Model	Average Re Coordination	Atom swapping	Restraints / Constraints
Model 4	Variable	Yes, O-Va both on and between Re-O and Bi-O sublattices	.dw, .bvs
Model 5	5.67	Yes, O-Va on Re-O and Bi-O Sublattices	.dw, .bvs

5.5.1 Model 4

RMC Model 4 for $Bi_{28}Re_2O_{49}$ has initially an average Re coordination number of 4.5 (75 % 4-coordinate and 25 % 6-coordinate), but over the course of the RMC run this value can change through oxygen atom migration between the Bi-O to Re-O sublattices, akin to what was reported previously using *ab* initio molecular dynamics (AIMD) simulations.[8] Three RMC configurations were produced for Model 4, using a 5 × 5 × 4 $Bi_{28}Re_2O_{49}$ supercell and starting average Re coordination number of 4.5. As for the creation of Models 1 and 2, this average

coordination number was generated by selecting randomly 150 of the 200 Re atoms to be 4-coordinate and then selecting randomly two of the six oxygen sites around these Re atoms to be vacancies, thereby generating a supercell where 75 % of the Re atoms are 4-coordinate and 25 % are 6-coordinate.

For each of these three configurations, three RMC runs were performed for approximately 13 million moves each. Within each configuration, the atoms were separated into five groups: Bi, Re, O1-O3 (O atoms initially on the Bi-O sublattice), O4-O5 (O atoms initially on the Re-O sublattice), and OVa (vacant oxygen positions). The RMC refinements were automated using a batch process, where the use of two command files allowed for atom swapping to be carried out in an alternating manner between the O4-O5 and OVa sites, or the O1-O3 and OVa sites, using a 25 % swap frequency. This alternating batch file process was used as RMCProfile cannot perform currently two sets of atom swapping within one command file, which is required to swap atoms between sublattices. The O atoms were kept in two separate groups (O1-O3 and O4-O5) to allow the distance window constraints and bond valence sum restraints to prevent unrealistic bond distances whilst allowing for migration of oxygen atoms between sublattices. The atom-swapping frequency was set at 25 %, the same frequency as used for the room temperature Model 1 RMC runs.

The final fits of the Model 4 RMC runs to the Bragg, *T(r)*, and *S(Q)* data sets show high levels of agreement, with no significant differences observed between the experimental and calculated data sets (Figure 5.18). The fit to the Bragg data shows evidence of weak peaks not modelled by Model 4 (denoted by arrows in Figure 5.18a), but as noted previously, these peaks are attributed to a small degree of partial decomposition of $Bi_{28}Re_2O_{49}$ to Bi_3ReO_8.

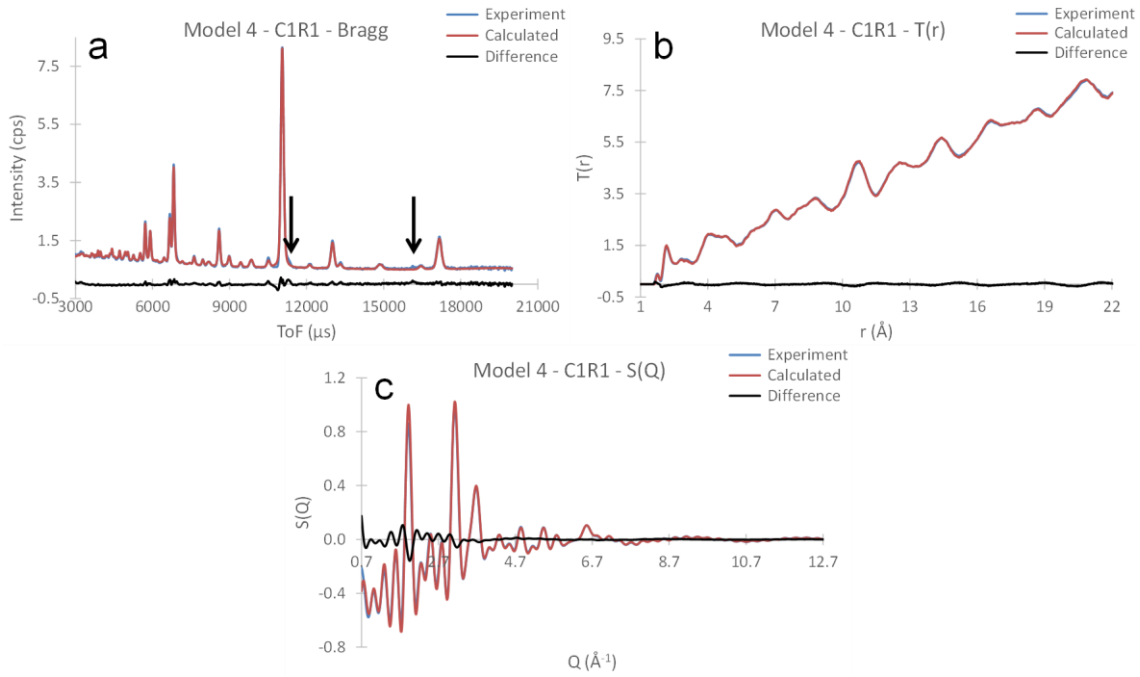

Figure 5.18: Experimental data, RMC calculated fits, and difference curves for $Bi_{28}Re_2O_{49}$ Model 4 at 700 °C for: a) Bragg data; b) *T(r)* data; c) *S(Q)* data.

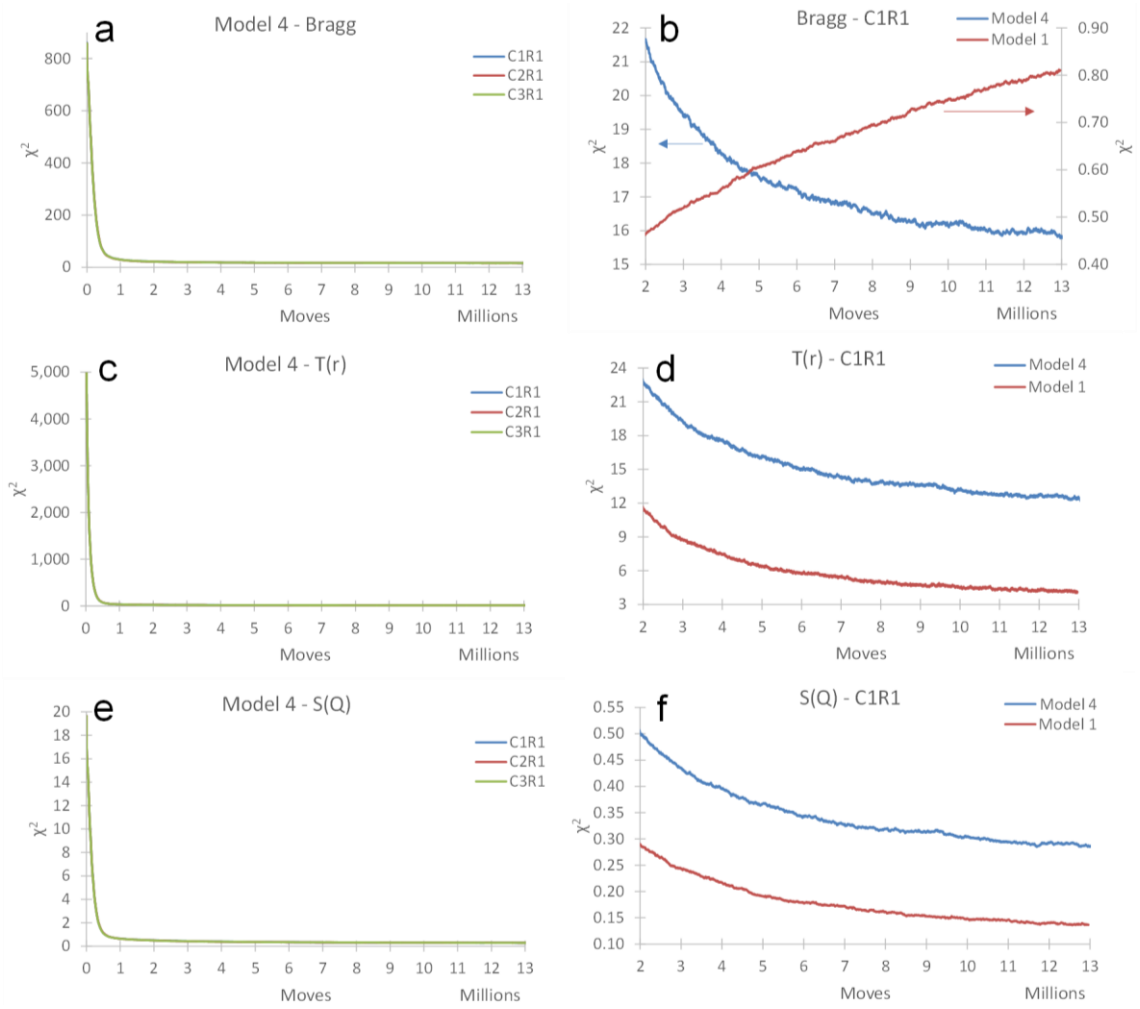

Figure 5.19: Plots showing the χ^2 values versus the number of moves for Model 4 using: a) Bragg; c) *T(r)*; e) *S(Q)* data sets. b), d), and f) Comparison plots detailing the χ^2 curves for Models 1 and 4.

The RMC runs show high levels of agreement both inter- and intra-configuration in terms of their χ^2 values (Figure 5.19a, c, and e). The fits of the RMC models to the collected data are worse at 700 °C than at room temperature, as shown by the larger χ^2 values for Model 4 compared to those for Model 1 (Figure 5.19b, d, and f). The *T(r)* and *S(Q)* χ^2 values are approximately twice as large as for Model 1, whilst the χ^2 values for the Bragg data are around an order of magnitude greater for Model 4. The higher χ^2 values on the Bragg curve could be due to the presence of the Bi_3ReO_8 impurity phase.

Following the RMC runs, the final Re coordination numbers were determined using the *neighbour_list* program, with cut-off distance for Re-O bond lengths set to 2.5 Å (Figure 5.20a). The average Re coordination number for the nine runs was found to be 4.63(2), showing that some transfer of oxygen atoms from the Bi-O to Re-O sublattice has occurred. Model 4 has a higher percentage of 5- and 6-coordinate ReO_x polyhedra compared to Model 1 (49.00 % and 8.00 % versus 42.92 % and 5.97 % for 5- and 6-coordinate polyhedra respectively), thereby raising the average Re coordination number. Additionally Model 4 has a smaller percentage of ReO_3 polyhedra (Figure 5.20b).

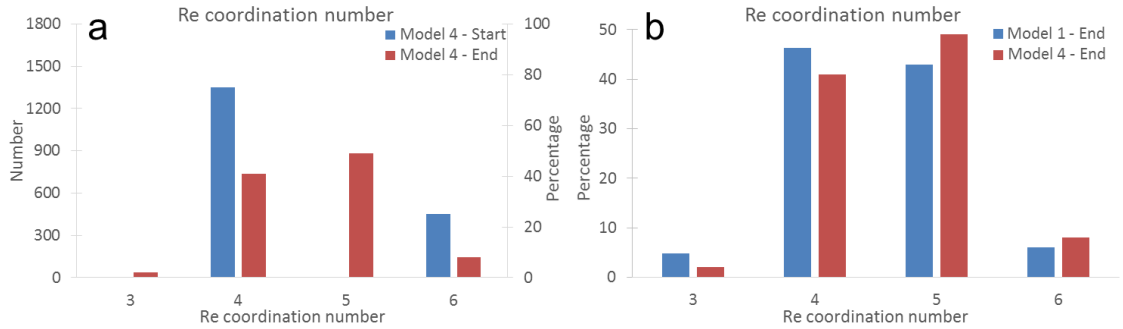

Figure 5.20: a) Number and percentage of Re atoms with specific coordination numbers for ReO_x (x = 3 to 6) polyhedra in Model 4. b) Comparison of the final Re coordination numbers for ReO_x (x = 3 to 6) polyhedra in Models 1 and 4.

However, whilst there is an overall increase in the average Re coordination number relative to the starting configurations and to that seen at room temperature, the value obtained is lower than that observed from the MD calculations. There are a few reasons for this difference, with the principle reason being that the MD simulations were carried out at 1100 °C, and not 700 °C as per this experiment. Payne *et al.* note that the mean-square displacements of the oxygen atoms are greater at 1100 °C compared to 700 °C,[8] which is expected due to increased thermal mobility at higher temperatures. Additional reasons include: the modelling processes for the RMC and MD techniques differ, with RMC able to access every possible configuration compatible with the *G(r)*, whilst MD only explores the potential energy surface that is compatible with the kinetic energy;[13] the use of different constraints, with RMC using distance and bond-valence restraints to prevent unreasonable bond distances, whilst MD is focussed on potential-energy constraints. However, whilst the RMC and MD techniques differ in their quantitative results, qualitatively they agree, with oxide ion transfer from the Bi-O to the Re-O sublattice observed at high temperatures. These conclusions of quantitative differences yet qualitative agreements are reported in the literature for a variety of oxide-ion materials.[14-17]

By collapsing the 5 × 5 × 4 supercell into a single unit cell (Figure 5.21b), it can be seen that the vacant sites are distributed across both axial and equatorial positions in the ReO_x polyhedra, and the oxygen vacancies on the Bi-O sublattice are dispersed throughout the structure and not accumulating in one region. Both observations indicate that the randomised atom swapping between the Bi-O and Re-O sublattices was successful.

The BVS values for all four atom types converge towards their expected values at 700 °C (Figure 5.22a), with average values of 2.980(2), 7.097(10), 2.009(2), and 1.919(8) for Bi, Re, O1-O3, and O4-O5 groups respectively. The average BVS value for the O4-O5 sites is closer to the expected value of 2 than it is with Model 1 (1.710(7)), with the large shoulder in the peak at low BVS values observed at room temperature virtually eliminated in Model 4 (Figure 5.22b).

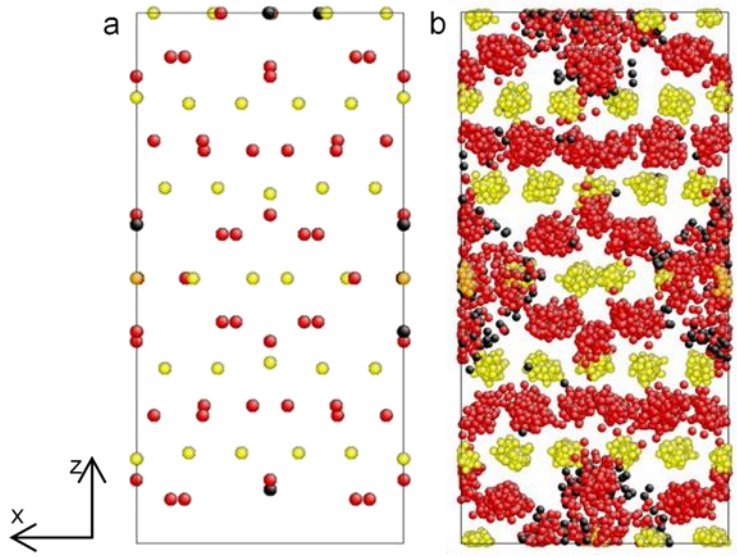

Figure 5.21: Views of the collapsed 5 × 5 × 4 supercell into a single unit cell for Model 4 viewed along the *y* axis at: a) C1 start; b) end of the C1R1 run. Bi = yellow, Re = orange, O = red, Vacancy = black.

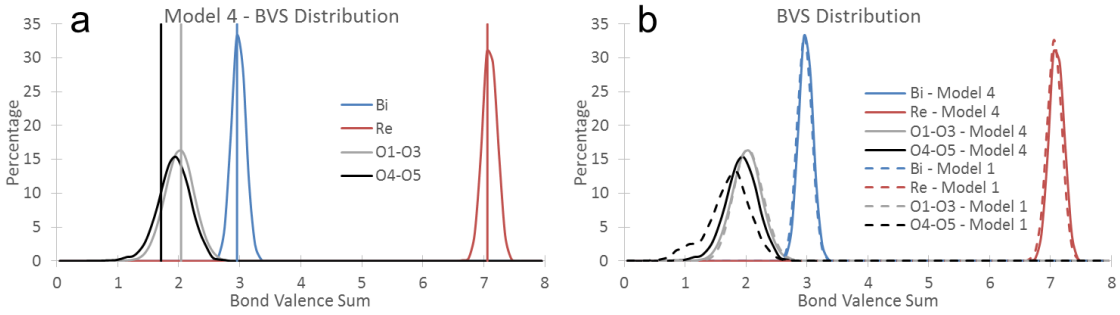

Figure 5.22: a) Plot of the BVS values for the Bi, Re, O1-O3, and O4-O5 atom groups in the Model 4 configurations of $Bi_{28}Re_2O_{49}$. b) Plot comparing the BVS values for atom groups in Model 1 and Model 4.

Plotting the Re-O bond lengths and O-Re-O bond angles in the ReO_x (x = 4 to 6) polyhedra in Model 4 (Figure 5.23a, c, and e and b, d, and f respectively) shows structural relaxation occurs through distortion of the polyhedra, given by the broad O-Re-O bond angle and Re-O bond length ranges. The figures show that the ReO_x bond angles range from 65 to 180 °. In comparison to the ReO_4 bond angles for Model 1, Model 4 shows an increased percentage of bond angles between 80 and 90 °. Additionally, the bond angle distributions are less bimodal than for Model 1, with the angles from 90 ° to 180 ° more akin to a shoulder on the low angle peak as opposed to a true bimodal distribution. This is potentially due to the atoms displacing further from their starting positions at high temperatures, hence the O-Re-O bond angles are not as rigid as they are at room temperature, and can adopt a wider range of angles. In terms of the ReO_x bond lengths (Figure 5.23b, d, and f), there is no real difference between those observed for Model 4 and Model 1.

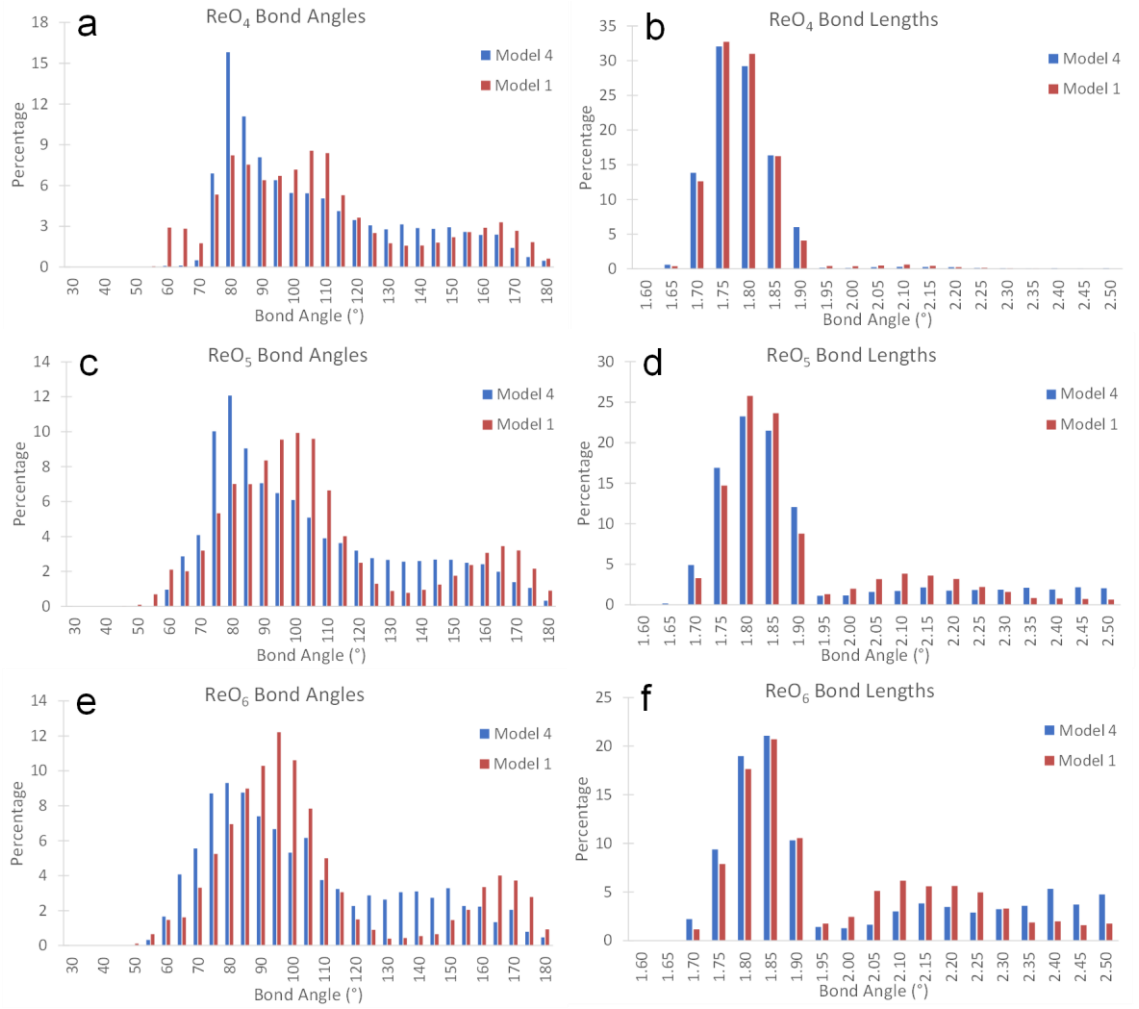

Figure 5.23: Plots comparing the ReO_x (x = 4 to 6): a), c), and e) O-Re-O bond angles; b), d), and f) Re-O bond lengths for Models 1 and 4.

Analysis of the spherical coordinates for the Re atoms in Model 4 shows that the displacement vectors follow the same unimodal trend as for Model 1, with average displacement distances of 0.343(1) Å and 0.338(3) Å for Models 1 and 4 respectively (Figure 5.24a). Whilst the average displacement values are virtually identical, there is a decrease in the percentage of Re atoms in the 0-0.25 Å region of the plot, indicating that whilst the average may not have changed, there is an increase in the number of Re atoms which have displaced to positions further from their starting coordinates (seen by the ~5 % difference in the heights of the histogram bars for Models 1 and 4 at 0.40 Å).

The Re θ angles (Figure 5.24b) for Model 4 tend to plateau between 60 and 150 ° unlike the bimodal distribution seen for Model 1, whilst the ϕ angles shows the same approximately equal distribution across the entire angular range as Model 1 (Figure 5.24c). This indicates that the Re atoms have less preference for occupying positions above or below the horizontal plane, with the increased thermal motion more evenly distributing the Re atoms.

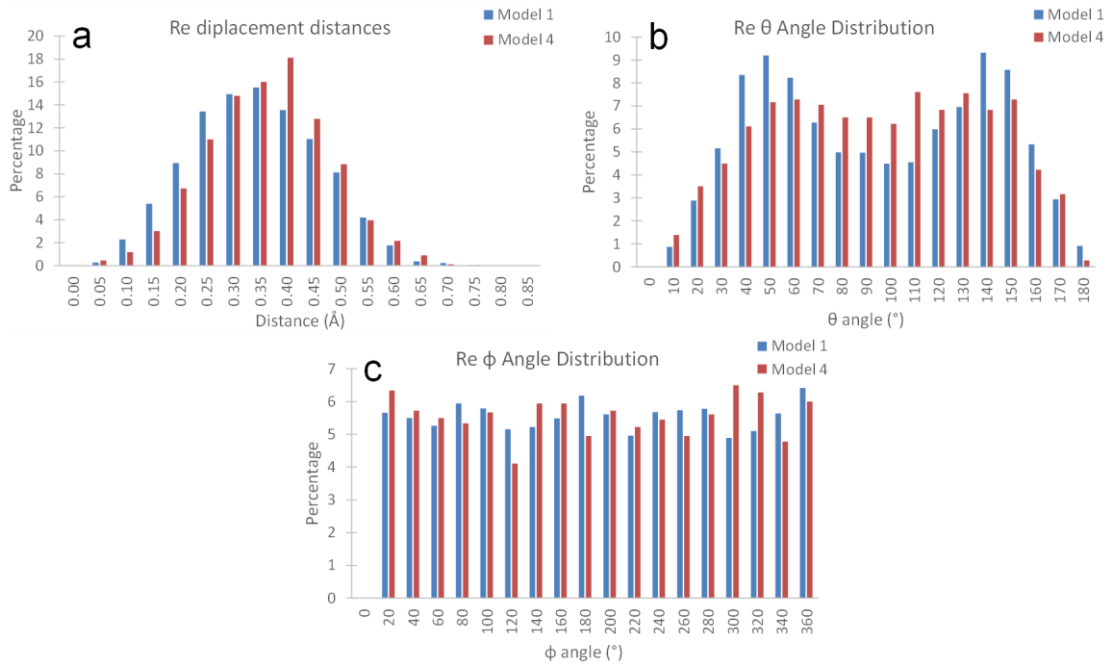

Figure 5.24: Plots of: a) displacement vector lengths; b) *θ* angles; c) *ϕ* angles for Re atoms in Models 1 and 4 relative to their starting coordinates.

The Re atom spreads for the Model 4 runs (Figure 5.25) show that the cluster of Re atoms are elongated along the *z* axis as for Models 1 and 2, consistent with Re atoms in the average structure occupying a split site along the *z* axis on the (0, 0, *z*) special position close to (0, 0, 0.5) at 700 °C. All three distributions (for the *x*, *y*, and *z* axes) show an increase in the average atom spread values in Model 4 (0.868(10) Å, 0.875(10) Å, and 0.962(11) Å for the *x*/*y*/*z* axis atom spreads respectively) compared to Model 1 (0.830(9) Å, 0.845(9) Å, and 0.914(8) Å for the *x*/*y*/*z* axes respectively), which is expected due to the increased thermal energy allowing for greater displacement of the atoms from their starting coordinates.

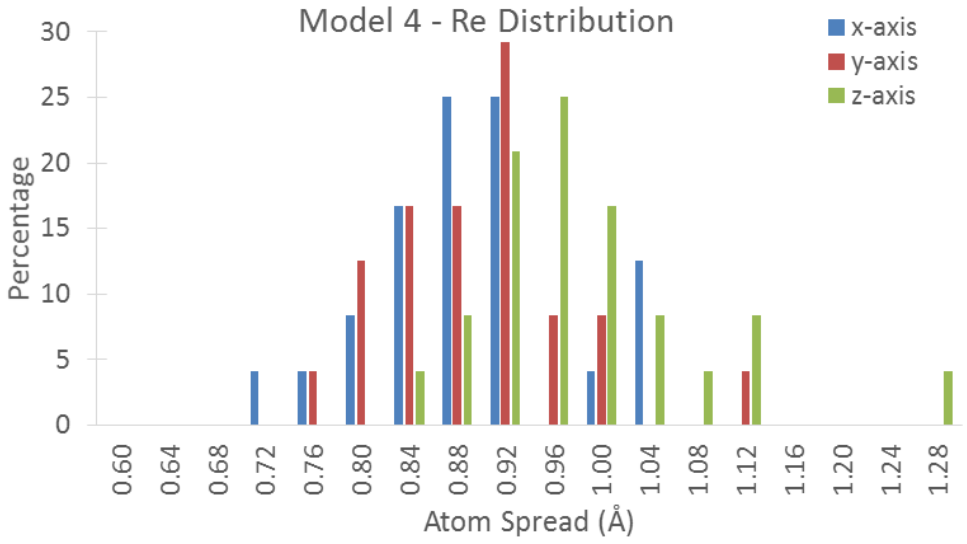

Figure 5.25: The spread of the Re atoms from their starting positions along the *x*, *y*, and *z* axes for Model 4.

5.5.2 Investigating oxygen migration between sublattices at room temperature

Model 4 shows that oxygen migration can occur between the Bi-O and Re-O sublattices, but it is unclear if the migration is caused by information in the measured data or whether it is simply due to the RMCProfile command files allowing migration between sublattices to occur. To investigate this, an RMC run was carried out against the room-temperature data using a starting configuration for Model 1 and command files for Model 4, to allow for atom swapping between sublattices at room temperature. By analysing the data following the RMC run, we can gain insight into whether the data supports atom swapping, and what effect this has on the level of fit. This model is henceforth referred to as Model 1/4.

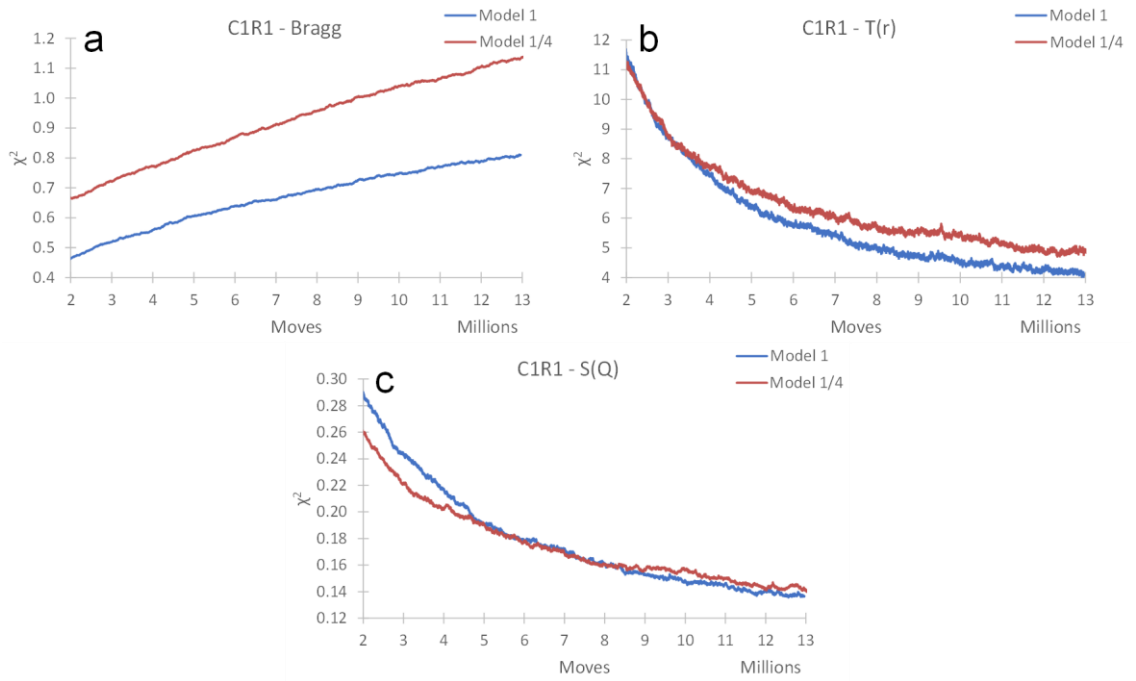

Figure 5.26: χ^2 values versus number of moves for Models 1 and 1/4 using: a) Bragg; b) *T(r)*; c) *S(Q)* data sets.

Analysis of the data following the Model 1/4 run found the average Re coordination number increased from 4.5 to 5.455, demonstrating that the transfer of oxygen atoms from the Bi-O to the Re-O sublattice has occurred during modelling of the room temperature data. However, analysis of the χ^2 Bragg, *T(r)*, and *S(Q)* curves for Model 1/4 showed higher values than those for Model 1 (Figure 5.26), suggesting that whilst atom swapping occurs during RMC modelling (as it is allowed to), it appears to be less consistent with the experimental data at room temperature than at high temperature.

The same conclusion can be reached by comparing the outputs of the Model 1 and Model 1/4 configurations with the experimental data (Figure 5.27). The fit is worse for Model 1/4 across all three data sets, and is noticeable especially across the length of the Bragg data and the region around *r* ~1.9 Å in the *T(r)* plot, as shown by the greater discrepancy between the calculated and experimental data.

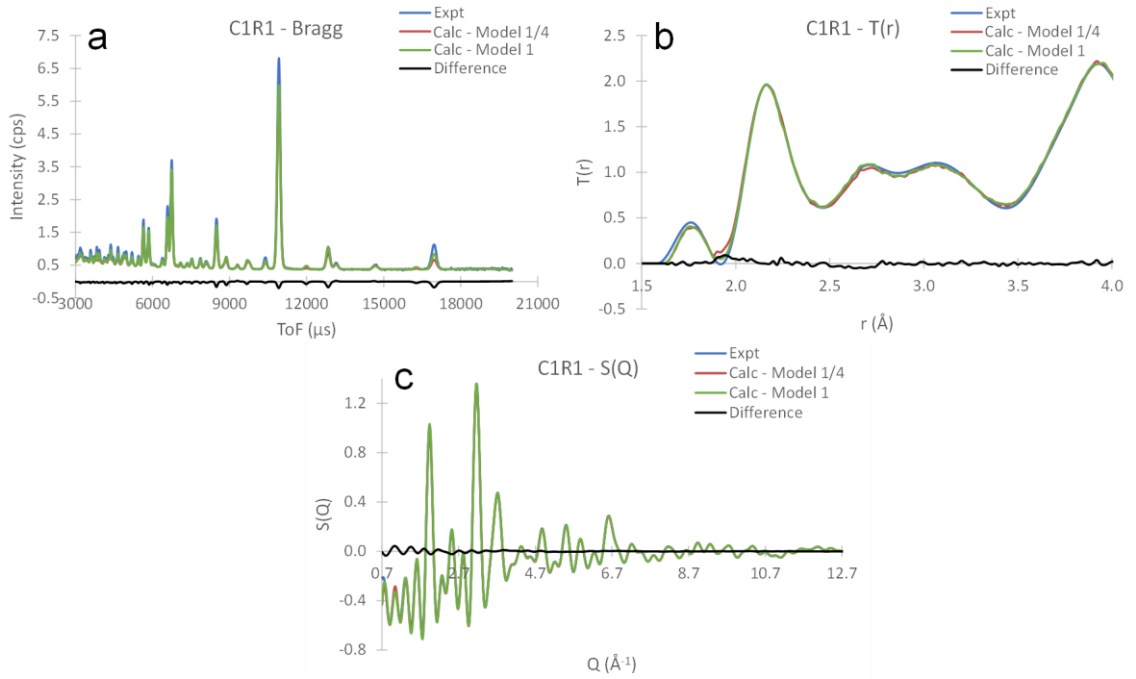

Figure 5.27: a) Bragg; b) *T(r)*; and c) *S(Q)* plots for Model 1 and Model 1/4 highlighting the difference in fit quality between the two configurations. The difference curve is calculated from the Model 1/4 fit minus the Model 1 curve, i.e. negative values indicate Model 1/4 is smaller than model 1 at that point. There is a high level of agreement between the calculated fits for Model 1/4 and Model 1. Note the poor fits for the Bragg and *T(r)* (in particular the peak at *r* ~1.90 Å) curves for Model 1/4.

5.5.3 Model 5

Following the use of Model 4 to investigate the migration of oxygen atoms from the Bi-O to Re-O sublattice in $Bi_{28}Re_2O_{49}$ at 700 °C, the data were analysed using a model in which the average Re coordination number was fixed at 5.67, called Model 5. This was to see how the fit to the experimental data compares between Model 4 and that for a configuration based on the findings of the AIMD calculations. For this analysis, three starting RMC configurations for Model 5 were created using 5 × 5 × 4 supercells of $Bi_{28}Re_2O_{49}$. The average Re coordination numbers were fixed at 5.67 by randomly selecting 66 of the 200 Re atoms and randomly assigning one of the six oxygen atoms in the coordination sphere around it to be a vacant site instead, forming a 5-coordinate ReO_5 polyhedron. This resulted in 66 ReO_5 and 134 ReO_6 polyhedra, giving the average Re coordination number desired. This combination of starting polyhedra were selected as the report by Payne *et al.* stated that their MD calculations showed that the "Re atoms remain essentially 5- or 6-coordinate".[8] The remaining vacancies required to match the stoichiometry were randomly distributed across the Bi-O sublattice on the O1-O3 positions.

In creating the starting configurations, six different atom groups were defined: Bi, Re, O1-O3 (oxygen atoms on the Bi-O sublattice), O4-O5 (oxygen atoms on the Re-O sublattice), O13Va (vacancies on oxygen positions in the Bi-O sublattice), and O45Va (vacancies on oxygen positions in the Re-O sublattice). During the RMC run, two sets of command files were created which ran in an alternating fashion. The first command file allows for atom swapping between the O1-O3 and O13Va groups, whilst the second allows for atom swapping between O4-O5 and

O45Va. This allows vacancies to be randomised within the two sublattices without swapping between them, thereby preventing the alteration of the average Re coordination number, keeping it fixed at 5.67 throughout the RMCProfile runs. For the three configurations, three runs of 13 million moves each were carried out, for a total of nine RMC runs for Model 5.

From the results of the Re coordination numbers following the RMC runs, the final average coordination number remained 5.67, and it was found that the total number of ReO_5 polyhedra decreased to facilitate the inclusion of a small number of ReO_4 polyhedra (Figure 5.28, 56 of 1800 total ReO_x polyhedra, 3.11 %). This small number of ReO_4 polyhedra supports the statement by Payne *et al.* that at elevated temperatures, the ReO_x polyhedra are mainly 5- and 6-coordinate.

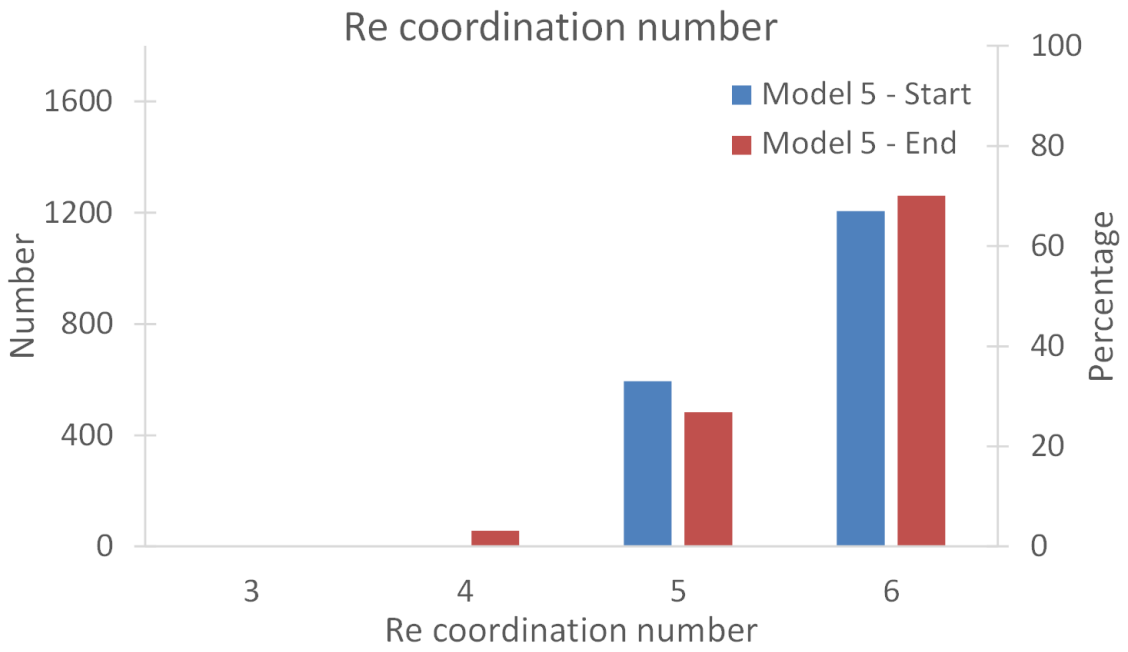

Figure 5.28: Number and percentage of total Re atoms of specific coordination numbers in ReO_x (x = 3 to 6) polyhedra in Model 5.

The final fits of the RMC runs to the Bragg and *S(Q)* data sets show similar levels of agreement with those for Model 4 (Figure 5.29a and c) with only slight discrepancies, as denoted by the oscillations in the difference curves. The fit to the *T(r)* data is poorer for Model 5 (Figure 5.29b and d), particularly for the Re-O peak (r ~1.74 Å, Figure 5.29d). This peak could be fitting badly due to the larger average Re coordination number for Model 5 than Model 4, combined with the use of BVS restraints leading to a distribution of Re-O bond lengths which is too narrow.

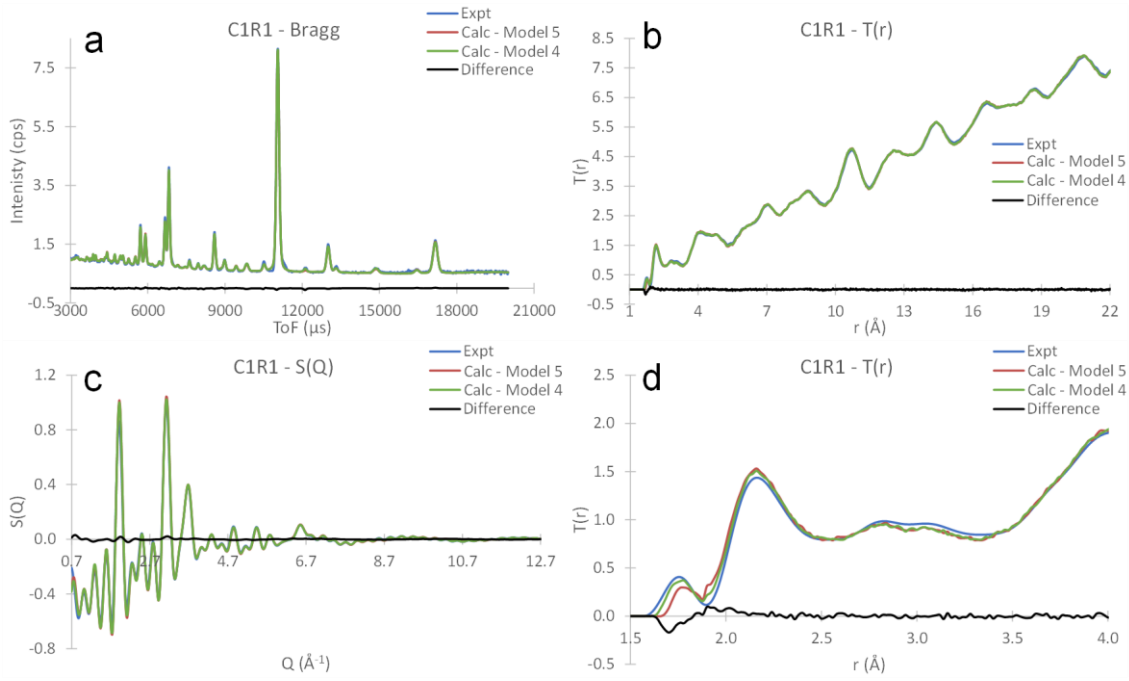

Figure 5.29: Calculated versus experimental curves for Model 4 and Model 5, including the difference curve between the two models.

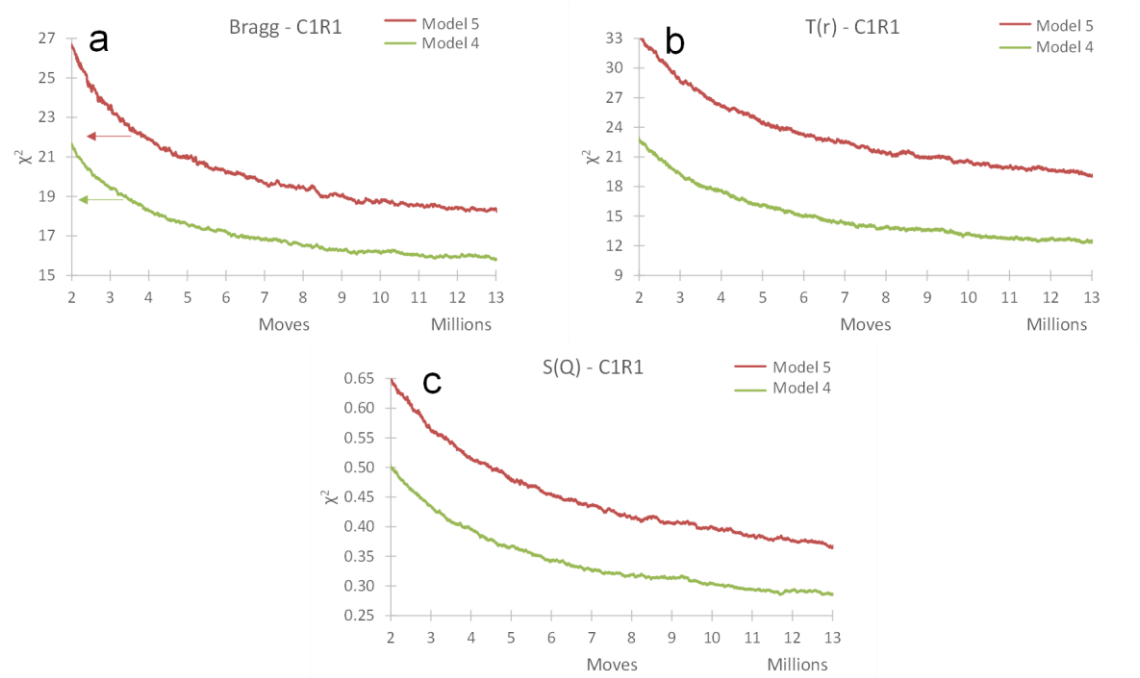

Figure 5.30: Plots showing the χ^2 values versus number of moves for Models 4 and 5 using: a) Bragg; b) *T(r)*; c) *S(Q)* data sets.

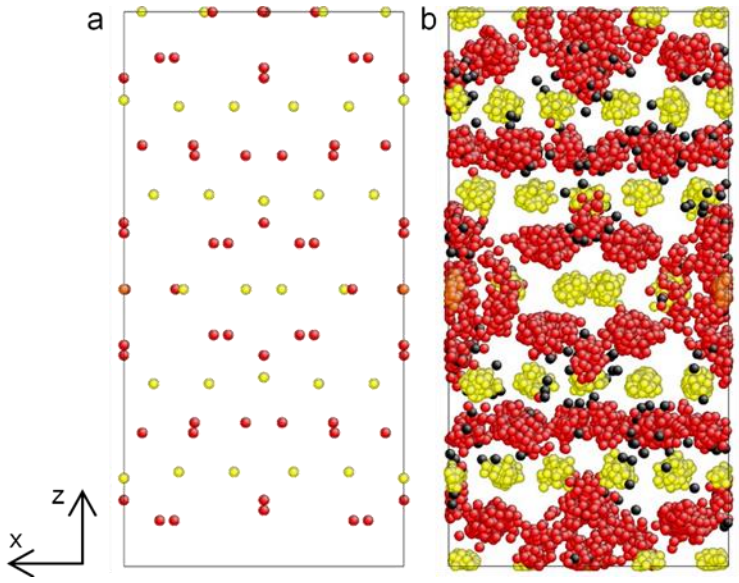

Figure 5.31: Views along the *y* axis of the collapsed 5 × 5 × 4 supercell into a single unit cell for Model 5 at: a) C1 start; b) end of the C1R1 run. Bi = yellow, Re = orange, O = red, Vacancy = black.

The RMC runs for Model 5 show high levels of inter- and intra-configuration agreement in their χ^2 values, with the data converging to a satisfactory level after 13 million moves. However, the χ^2 values for Model 5 are higher than those for Model 4 (Figure 5.30), showing that the fit to the data is worse when the RMC model is fixed with an average Re coordination number of 5.67.

Collapsing the 5 × 5 × 4 supercell into a single unit cell shows the vacant atom sites to be distributed randomly throughout the Bi-O and Re-O sublattices (Figure 5.31b), indicating that the randomised atom swapping in Model 5 was working successfully and that there are no preferences for vacancy positioning within the structure.

The average BVS values for Model 5 are also worse than for Model 4, particularly for the Re (average BVS value of 7.244(10)) and O4-O5 (average value of 1.603(2)) atom groups. The average value for O4-O5 is very low due to the bimodal distribution of the BVS values (Figure 5.32), which could also be contributing to the poor fit of the Re-O peak in the *T(r)* plot (*r* ~1.75 Å in Figure 5.29d).

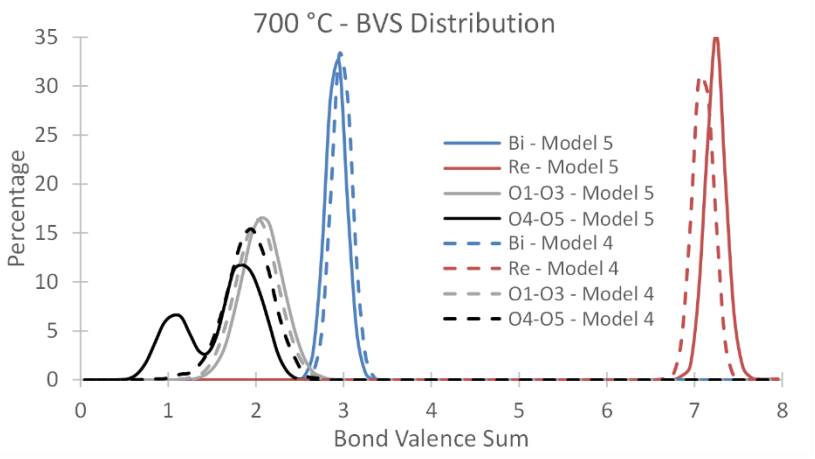

Figure 5.32: Comparison of BVS values for the Bi, Re, O1-O3, and O4-O5 atom groups in Models 4 and 5.

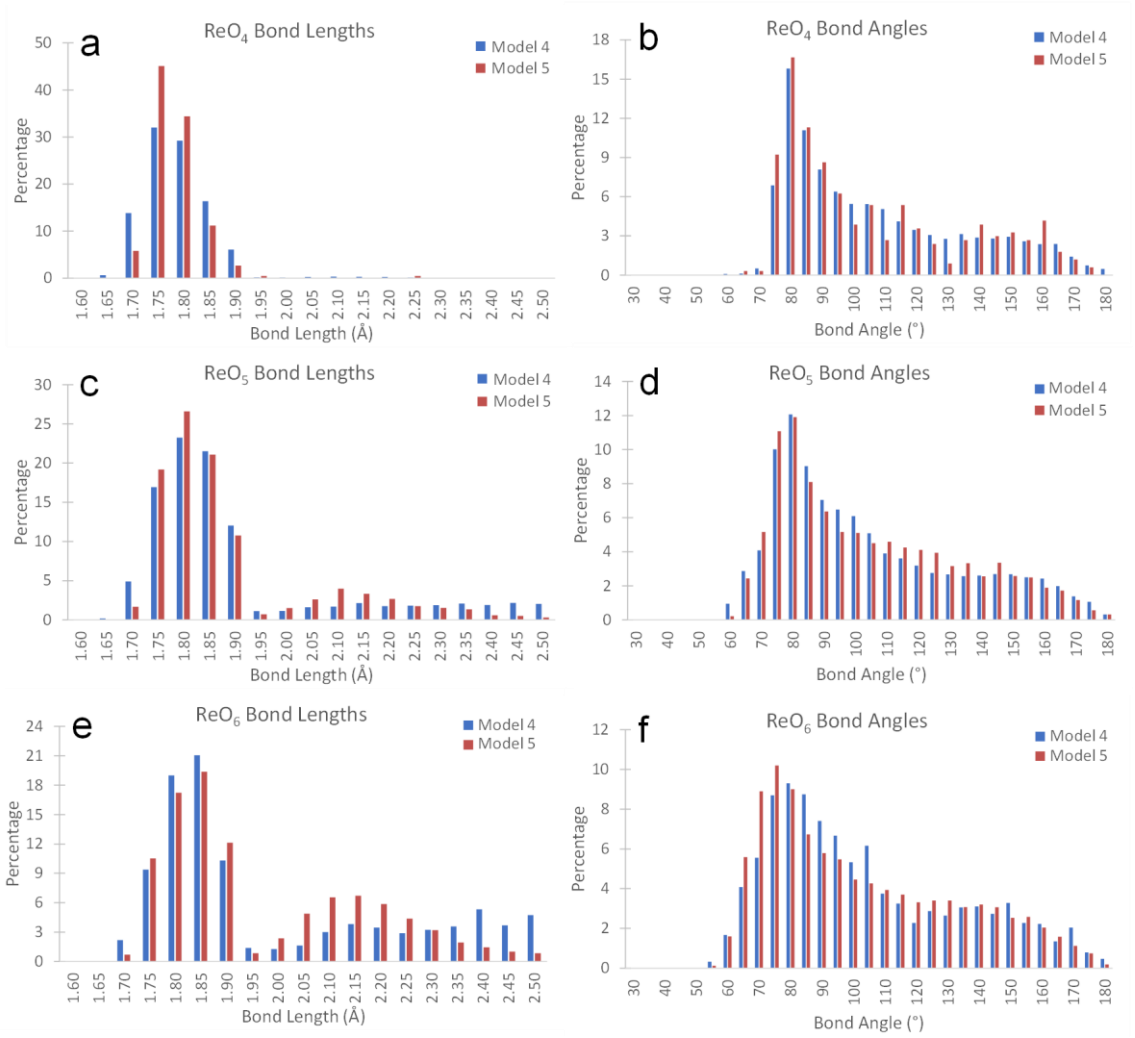

Figure 5.33: ReO_x (x = 4 to 6) polyhedra: a), c), e) O-Re-O bond angles; b), d), and f) Re-O bond lengths for Models 4 and 5.

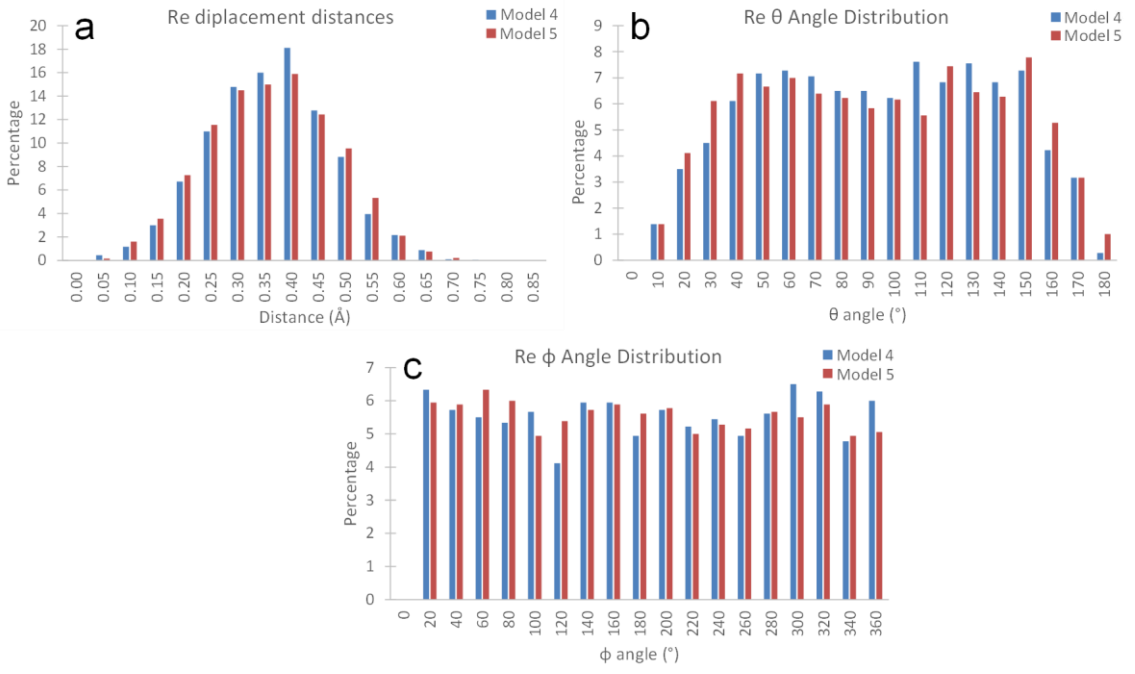

Figure 5.34: a) Displacement vector lengths; b) θ angles; c) ϕ angles for Re atoms in Models 4 and 5 relative to their starting coordinates.

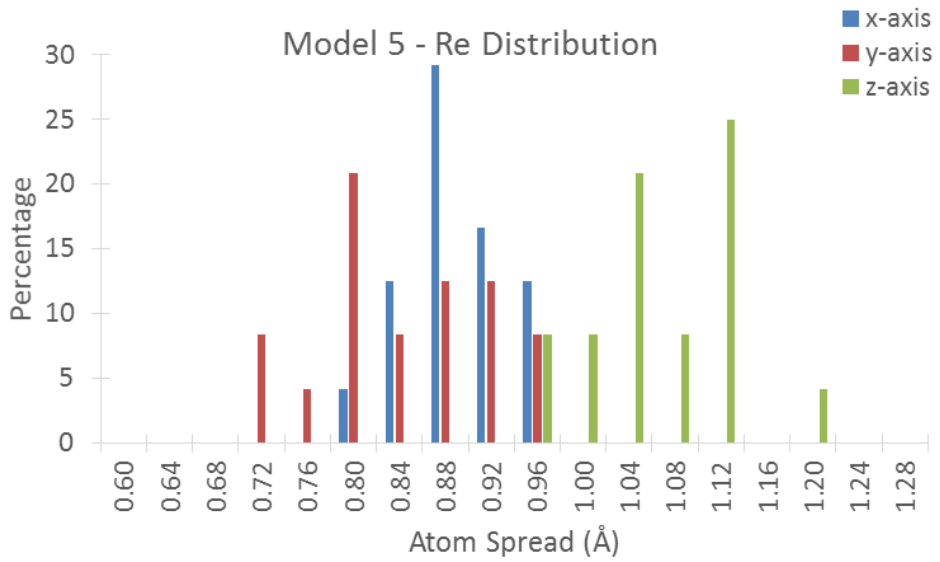

Figure 5.35: Plot of the spread of the Re atoms from their starting positions along the *x*/*y*/*z* axes for Model 5.

As for Model 4, the lack of polyhedral restraints in the Model 5 configurations allows for a high degree of structural relaxation through distortion of the polyhedra. The similarity in the O-Re-O bond angles and Re-O bond lengths for Models 4 and 5 in Figure 5.33 is expected as both models use the same values for the BVS and distance window restraints. Likewise, the Re spherical coordinate analysis shows very similar ranges of displacement vector lengths, θ, and ϕ angles for the Re atoms in Model 5 compared to Model 4 (Figure 5.34).

The spreads for the Re atomic coordinates for Model 5 show that the Re atoms have a larger average displacement along the *z* axis compared to the *x* and *y* axes, as seen for Model 4 (Figure 5.35). However, in Model 5 there is virtually no overlap between the *z* axis plot and those for the *x* and *y* axes. This configuration is again consistent with the average structure in which the Re atoms exist on a split-site at (0, 0, *z*) close to the (0, 0, 0.5) special position at elevated temperatures.

5.6 Conclusions

The ReO_x polyhedra in $Bi_{28}Re_2O_{49}$ have previously been reported to exist solely as regular ReO_4 tetrahedra and ReO_6 octahedra in the average structure at room temperature. In this work, variable temperature neutron total-scattering data, analysed by RMC modelling, were used to investigate in full detail the local structure around Re centres in this material.

Room-temperature RMC analyses using Model 1 and Model 2 show a high level of similarity following RMCProfile refinements, despite one model using atom swapping to exchange oxygen atoms and vacancies on the Re-O sublattice, and alter the individual Re coordination numbers. However, this could be due to translational movements distorting the polyhedra. A rigid-body model is likely to give a poorer fit to the data, but due to a lack of general functionality in the RMCProfile software, experimental evidence to support this cannot be produced. Despite this, there are strong indications that the true room-temperature structure for $Bi_{28}Re_2O_{49}$ is more complex than that reported by Crumpton *et al.*, and likely to contain ReO_x polyhedra which are

4-, 5-, or 6-coordinate. Additionally, there is evidence of the distribution of Re atoms from their starting positions elongating along the *z* axis to a greater extent than along the *x* and *y* axes following the RMC runs, supporting reports of Re atoms occupying a split site along the *z* axis close to (0, 0, 0.5) in the average structure.

From RMC analyses performed at 700 °C, an increase in the average Re coordination number from 4.5 to 4.63(2) is observed, suggesting that migration of oxygen atoms from the Bi-O to Re-O sublattice does occur at elevated temperatures. However, whilst fewer oxygen atoms migrate than suggested previously from MD simulations, the reasons for these differences are twofold: Firstly, the temperature that the experiments were carried out were different, with the AIMD simulations performed at 1100 °C and not 700 °C as for the TS analyses, giving the atoms increased thermal energy with which to migrate between the Bi-O and Re-O sublattices. Secondly, RMC and MD simulations use different constraints and methods of refinement, and so quantitative differences in the fits to the data are expected despite qualitative agreement between the results of the two techniques. If a fixed average Re coordination number of 5.67 is used, this yields a poorer fit to the data than for a model with freely refining Re coordination polyhedra. This is supported with evidence of discrepancies in the *T(r)* data, poor BVS distributions (particularly for the Re and O4-O5 atom groups), and higher χ^2 values for Model 5 than those for Model 4.

The use of RMC gives the most disordered or distorted final configuration (for any given set of computational instructions), thereby making it difficult to distinguish between different models in structurally complex systems.

5.7 References

1. T. E. Crumpton, J. F. W. Mosselmans and C. Greaves, *Journal of Materials Chemistry*, 2005, **15**, 164-167.
2. M. G. Francesconi, A. L. Kirbyshire, C. Greaves, O. Richard and G. Van Tendeloo, *Chemistry of Materials*, 1998, **10**, 626-632.
3. C. D. Ling, *Journal of Solid State Chemistry*, 1999, **148**, 380-405.
4. S. A. Warda, W. Pietzuch, W. Massa, U. Kesper and D. Reinen, *Journal of Solid State Chemistry*, 2000, **149**, 209-217.
5. T. E. Crumpton, M. G. Francesconi and C. Greaves, *Journal of Solid State Chemistry*, 2003, **175**, 197-206.
6. L. Leon-Reina, E. R. Losilla, M. Martinez-Lara, M. C. Martin-Sedeno, S. Bruque, P. Nunez, D. V. Sheptyakov and M. A. G. Aranda, *Chemistry of Materials*, 2005, **17**, 596-600.
7. M. L. Tate, J. Hack, X. Kuang, G. J. McIntyre, R. L. Withers, M. R. Johnson and I. Radosavljevic Evans, *Journal of Solid State Chemistry*, 2015, **225**, 383-390.
8. J. L. Payne, J. D. Farrell, A. M. Linsell, M. R. Johnson and I. R. Evans, *Solid State Ionics*, 2013, **244**, 35-39.
9. R. Punn, A. M. Feteira, D. C. Sinclair and C. Greaves, *Journal of the American Chemical Society*, 2006, **128**, 15386-15387.
10. C. H. Hervoches and C. Greaves, *Journal of Materials Chemistry*, 2010, **20**, 6759-6763.
11. A. C. Larson and R. B. Von Dreele, *The General Structure Analysis System (GSAS)*, Los Alamos National Laboratory: Los Alamos, 2004.

12. H. Müller-Buschbaum, *Zeitschrift Fur Anorganische Und Allgemeine Chemie*, 2007, **633**, 2491-2522.

13. Y. Wang, M. Klenk, K. Page and W. Lai, *Chemistry of Materials*, 2014, **26**, 5613-5624.

14. M. J. Noordhoek, V. Krayzman, A. Chernatynskiy, S. R. Phillpot and I. Levin, *Applied Physics Letters*, 2013, **103**, 022909.

15. M. Burbano, S. T. Norberg, S. Hull, S. G. Eriksson, D. Marrocchelli, P. A. Madden and G. W. Watson, *Chemistry of Materials*, 2012, **24**, 222-229.

16. S. T. Norberg, S. Hull, I. Ahmed, S. G. Eriksson, D. Marrocchelli, P. A. Madden, P. Li and J. T. S. Irvine, *Chemistry of Materials*, 2011, **23**, 1356-1364.

17. L. Pusztai, I. Harsányi, H. Dominguez and O. Pizio, *Chemical Physics Letters*, 2008, **457**, 96-102.

6 Structure-property relationships of bismuth molybdate compositions, $Bi_{38-x}Mo_{7+x}O_{78+3x/2}$ (x = 0, 0.5)

6.1 Background

$Bi_{38}Mo_7O_{78}$ was first reported by Buttrey *et al.* with a unit cell obtained from electron diffraction as an orthorhombic 3 × 5 × 3 fluorite-type δ-Bi_2O_3 superlattice in space group Pccn.[1] Early single-crystal X-ray diffraction led to a report of monoclinic unit-cell distortion for this material, but this was interpreted as crystal twinning and not representative of the unit cell of the material.[2] Later, single-crystal X-ray diffraction performed on crystals grown in a floating-zone furnace identified the true space group as Pbcn, a 5 × 3 × 3 δ-Bi_2O_3-like structure containing both MoO_4 tetrahedra and MoO_6 octahedra.[3] However, whilst this work successfully used difference Fourier maps to locate the O positions, restraints on the Mo-O bond lengths were required for refinement, and the O atomic coordinates in the MoO_6 octahedra could not be determined accurately. Instead, fixed values obtained from density-functional theory (DFT) calculations were used for the MoO_6 O atomic coordinates, which gave extremely large equated isotropic displacement values for these O sites (B_{iso} up to 44 Å^2), attributed to long-range disorder. This B_{iso} value corresponds to a root-mean-square displacement of up to 0.75(7) Å from the stated atomic coordinates, a value which places into question whether the O atoms are actually located on these positions.

To add further complexity, this material was reported subsequently as a more complicated 5 × 3 × 6 δ-Bi_2O_3 superstructure with a monoclinic distortion in space group Pn11, which undergoes a phase transition at ~90 °C to an orthorhombic structure.[4] A complete crystal structure for this monoclinic phase has not been reported. The same work identified the closely related $Bi_{37.5}Mo_{7.5}O_{78.75}$ composition,[4] thereby expanding the range of compositions in the Bi_2O_3-MoO_3 phase diagram around the Bi:Mo ratio of 38:7 (Figure 6.1). This material was reported to have an orthorhombic 5 × 3 × 3 fluorite-type superstructure, with space group Pbcn, but a complete structural model was not presented. In light of these findings, the $Bi_{38}Mo_7O_{78}$ material identified previously by Sharma *et al.* may in fact not have the stated composition,[3] but could have been a single crystal of orthorhombic $Bi_{37.5}Mo_{7.5}O_{78.75}$.

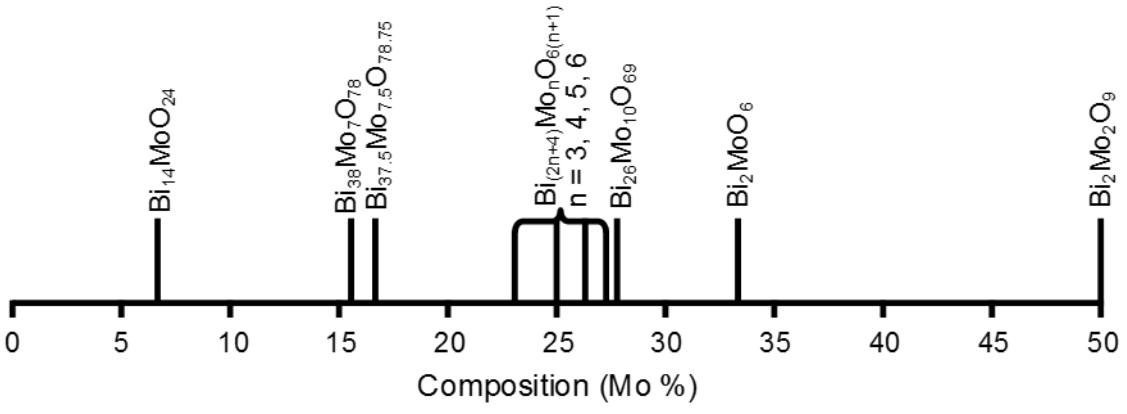

Figure 6.1: The Bi-rich end of the Bi_2O_3-Mo_2O_6 phase diagram detailing the bismuth molybdates containing up to 50 % Mo_2O_6.

All materials in the Bi_2O_3-Mo_2O_6 phase diagram have complicated structures, consisting of three-dimensional Bi-O lattices containing MoO_x polyhedra. The exception to this is Bi_2MoO_6, a layered material containing planes of corner-connected MoO_6 octahedra.[5] The majority of the bismuth molybdates contain isolated MoO_4 tetrahedra ($Bi_{14}MoO_{24}$, $Bi_{(2n+4)}Mo_nO_{6(n+1)}$ (n = 3, 4, 5, and 6), and $Bi_2Mo_2O_9$).[6-8] Initially, the MoO_x polyhedra in $Bi_{26}Mo_{10}O_{19}$ were reported only as MoO_4 tetrahedra,[9] but subsequent work found the structure to contain a mixture of MoO_4 tetrahedra and pairs of corner-connected trigonal bipyramidal MoO_5 polyhedra, which form Mo_2O_9 units.[10] Like $Bi_{26}Mo_{10}O_{19}$, $Bi_{38}Mo_7O_{78}$ contains a mixture of MoO_x polyhedra, isolated MoO_4 tetrahedra, and groups of three corner-connected MoO_6 octahedra which form (Mo_3O_{16}) units.[3] This is surprising, given that all of the surrounding bismuth molybdates materials in the phase diagram only contain MoO_4 tetrahedra.

$Bi_{38}Mo_7O_{78}$ and $Bi_{37.5}Mo_{7.5}O_{78.75}$ are both excellent oxide-ion conductors (σ ~1 × 10^{-3} and 1.5 × 10^{-4} Scm^{-1} at 500 °C),[4] with $Bi_{37.5}Mo_{7.5}O_{78.75}$ showing comparable conductivity to that for $Bi_{26}Mo_{10}O_{19}$.[11] All three of these materials exhibit elevated conductivities compared to other bismuth molybdates, with conductivity values reported to range from ~1 to 4 orders of magnitude lower for Bi_2MoO_6 (σ ~7.8 × 10^{-5} Scm^{-1} at 500 °C)[12] and the $Bi_{(2n+4)}Mo_nO_{6(n+1)}$ (n = 3, 4, 5, and 6) compositions (σ ~8.5 × 10^{-7} to 6.3 × 10^{-6} Scm^{-1} at 500 °C).[7]

This chapter reports the characterisation of the $Bi_{38}Mo_7O_{78}$ orthorhombic phase through a combined refinement using variable-temperature (VT) powder neutron diffraction (PND) and synchrotron powder X-ray diffraction (PXRD) data collected at 200 °C. The VT-PXRD data are also used to show the reversible monoclinic-to-orthorhombic phase transition on heating and cooling between room temperature and 680 °C, along with discontinuities in the temperature dependencies of the lattice parameters at ~530 °C. The orthorhombic structure has also been transformed to the room-temperature monoclinic phase to attempt structure determination by distortion-mode analysis.

6.2 Synthesis of bismuth molybdate materials, $Bi_{38-x}Mo_{7+x}O_{78+3x/2}$ (x = 0, 0.5)

Solid-state synthesis was undertaken to prepare powdered samples of $Bi_{38}Mo_7O_{78}$ and $Bi_{37.5}Mo_{7.5}O_{78.75}$. For $Bi_{38}Mo_7O_{78}$, 4.4891 g of Bi_2O_3 (9.63 mmol, Sigma-Aldrich, 99.9 %) and 0.5109 g of MoO_3 (3.55 mmol, Sigma-Aldrich, 99.5 %) were ground together and fired in a closed alumina crucible at 600, 700, and 840 °C for 12 hours at each temperature with intermediate grinding, using heating and cooling rates of 5 °C per minute to yield a pale-yellow powder. A 30 g powdered sample was also prepared for floating-zone-furnace crystal growth (Section 7.5). 26.9346 g (57.78 mmol) of Bi_2O_3 and 3.0654 g (21.30 mmol) of MoO_3 were ground together in a planetary ball mill for 12 hours, then fired at 840 °C for 12 hours in an alumina crucible, producing a pale-yellow powder. For $Bi_{37.5}Mo_{7.5}O_{78.75}$, 11.5703 g of Bi_2O_3 (24.83 mmol, Sigma-Aldrich, 99.9 %) and 1.4297 g of MoO_3 (9.93 mmol, Sigma-Aldrich, 99.5 %) were ground together and fired in a closed alumina crucible for 12 hours at 600, 700, and

840 °C with intermediate grinding. Heating and cooling rates of 5 °C per minute were used, producing a pale-yellow powder.

6.3 Characterisation of $Bi_{38}Mo_7O_{78}$

6.3.1 Structural analysis of the high-temperature orthorhombic phase

At the Australian Synchrotron, variable-temperature (VT) synchrotron PXRD data for $Bi_{38}Mo_7O_{78}$ were collected on the Powder Diffraction beamline using a wavelength of 0.6359 Å (refined using LaB_6, NIST Standard SRM660b). A 0.3 mm quartz capillary was loaded with material, and data were collected from 30 to 680 °C on heating and from 675 to 35 °C on cooling in 10 °C intervals, with a count time of 210 seconds per detector position (2.0 and 2.5 °) per temperature.

VT PND data for $Bi_{38}Mo_7O_{78}$ were collected on ECHIDNA at OPAL, ANSTO. 3.535 g of sample was loaded into a 6 mm diameter V can, and data were collected at room temperature and from 100 to 500 °C in 100 °C increments for 480 minutes per temperature (563 seconds per step), then at 600 and 700 °C for 360 minutes (419 seconds per step) on heating. On cooling, data were collected from 600 to 100 °C in 100 °C intervals for 60 minutes each (59 seconds per step). The furnace temperature deviated by less than ± 5 °C over the course of the data collections between room temperature and 500 °C, but by less than 1 °C at 600 and 700 °C. For refinement of the orthorhombic structure, the 200 °C data sets were chosen to ensure that the monoclinic phase had transformed fully into the orthorhombic phase, whilst using a temperature sufficiently low to prevent the atomic sites from having extremely large displacement parameters due to heightened thermal atomic motion.

The starting orthorhombic structural model used for the refinement was reported by Sharma *et al.* with space group Pbcn.[3] Whilst this material has the standard space group setting of Pbcn, ISODISTORT[13] was used to transform the orthorhombic structure to the non-standard Pnca space group to provide a compatible parent-child relationship for the distortion-mode analysis of the monoclinic structure (*vide infra*). The reorganisation of the lattice parameters and atomic coordinates in the Pbcn structure to the new Pnca structure involved a transformation with the basis [{0,0,-1},{1,0,0},{0,-1,0}], and no change in origin position. This means that the Pbcn lattice parameters *a*, *b*, and *c*, and atomic coordinates *x*, *y*, and *z* become Pnca lattice parameters *c*, *a*, and *b*, and atomic coordinates *–z*, *x*, and *–y* respectively.

Following the transformation of the model, a combined Rietveld refinement was undertaken using the 200 °C synchrotron PXRD and PND data sets to refine the orthorhombic structure of $Bi_{38}Mo_7O_{78}$, in space group Pnca. The following parameters were refined against the synchrotron PXRD data: 15 background parameters, zero-point error, scale factor, cylindrical-sample intensity correction,[14] and size-strain terms to account for the sample contribution to peak broadening. For the PND analysis, 13 background terms, zero-point error, scale factor, peak shape terms, and 1 lattice parameter for Nb modelled using Pawley[15] fitting (contribution from the elements in the furnace) were refined. 3 lattice parameters, 183 atomic coordinates, and 4 isotropic displacement parameters (one each for all Bi sites, all Mo sites, all O sites on

the Bi-O sublattice, and all O sites on the Mo-O sublattice) were refined. Equated isotropic displacement parameters were used as attempts to refine these for each site independently resulted in some values becoming either negative or large ($B_{iso} \geq 20$).

A number of restraints were applied to the structural model during the Rietveld refinements, to attempt to obtain the best fit to the data whilst maintaining sensible bond lengths and angles between the atoms. Anti-bumping restraints were introduced for the Bi-O and O-O distances of 2.05 Å and 2.30 Å. If the Bi-O or O-O distances were smaller than these values, penalties would be applied equal to $\Sigma(R\text{-}2.05)^2$ or $\Sigma(R\text{-}2.30)^2$ for the Bi-O and O-O anti-bumping restraints respectively (where R is the Bi-O or O-O distance), which the refinements would attempt to minimise. An overall penalty weighting of 2 was applied for these restraints, which is a multiplicative weighting term applied to the sums of the penalty and restraint functions during the least-squares minimisation routine. To maintain the MoO_4 and MoO_6 polyhedra as tetrahedra and octahedra respectively, Mo-O distance restraints and O-Mo-O angle restraints were introduced. For the Mo-O distance restraints in the MoO_4 polyhedra, the bond lengths were restrained to 1.74 Å (tolerance = 0.1 Å), whilst the O-Mo-O angles were restrained to 109.47 ° (tolerance = 3 °). This distance was chosen as the Mo-O bond lengths reported in the literature for MoO_4 tetrahedra range between 1.58(2) and 1.88(1) Å.[2, 6, 7, 10] For the MoO_6 octahedra, Mo-O bond lengths were restrained to 1.8 Å and 2.3 Å for the non-bridging and bridging Mo-O bonds respectively (tolerances = 0.1 Å). These bond-length restraints are larger than those for the MoO_4 polyhedra, as longer bond lengths are reported for MoO_6, with bridging Mo-O bonds longer than the non-bridging bonds.[5, 16] For the MoO_6 polyhedra at the ends of the (Mo_3O_{16}) unit (i.e. Mo23), O-Mo-O bond angle restraints of 90 ° and 180 ° (tolerance = 3 °) were used. Angle restraints of 90 ° (tolerance = 10 °) were only used between the Mo24, O62, and O63 sites, to allow the central MoO_6 polyhedron (Mo24) potentially to distort, as corner-connected MoO_6-containing structures in the literature show bond angles for the Mo-O-Mo bridges ranging from 143.0(4) to 169.5(2) °.[5, 16] The relative weighting of the Mo-O distance restraints and O-Mo-O angle restraints were set to 1.0 and 0.0004 respectively. All the restraints presented here were kept throughout the refinements and for production of the final structural model. The use of bond-distance and bond-angle restraints for the MoO_x polyhedra resulted in a decrease in R_{wp} from 5.430 % to 5.204 %. The use of Bi-O and O-O box interaction restraints helped to prevent unreasonably short bond distances, with the shortest Bi-O bonds of 2.11(4) Å (Bi09-O40, Bi15-O37, and Bi17-O45) and O-O bond of 2.36(5) Å (O30-O43) being longer than the restraint values by more than one estimated standard deviation (esd).

The orthorhombic structural model from the combined refinement of synchrotron PXRD and PND data (Figure 6.2) is presented as the final structural model for $Bi_{38}Mo_7O_{78}$ at 200 °C (Table 6.1 and Figure 6.3). The model from the combined refinement is presented due to the increased precision of the obtained values relative to those determined using only PND data, which gives errors on the lattice parameters and atomic coordinates for the Bi- and Mo-containing sites that are two orders and one order of magnitude greater respectively.

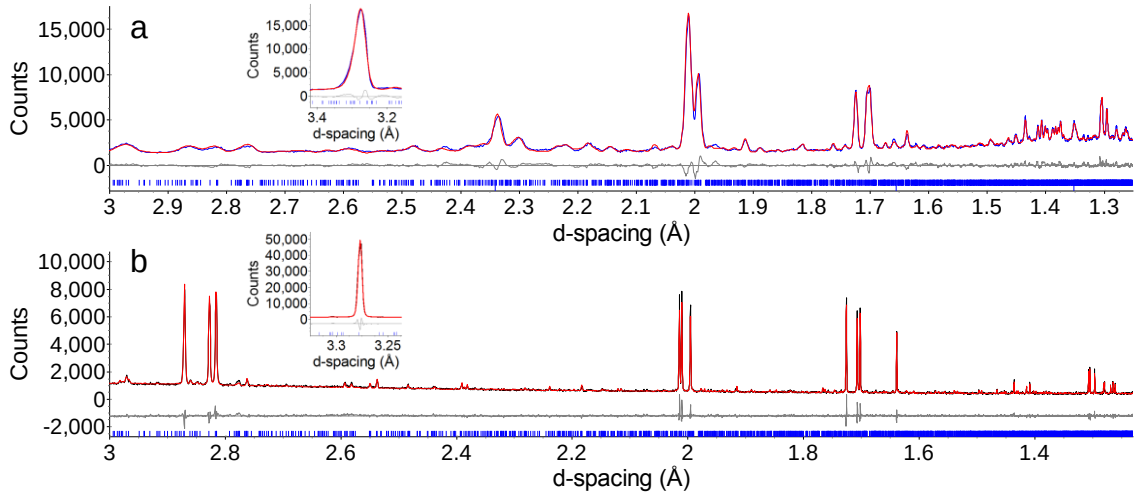

Figure 6.2: Rietveld fits for $Bi_{38}Mo_7O_{78}$ (*a* = 16.97177(7) Å, *b* = 28.71762(11) Å, *c* = 16.90225(6) Å, *V* = 8237.97(5) Å^3, space group = Pnca) at 200 °C to: a) PND data, ECH0012532_Bi38Mo7O78 (pattern filename), R_{wp} = 5.387 %; b) synchrotron PXRD data, VT_M_p12_ns_017 (pattern filename), R_{wp} = 5.043 %, total R_{wp} = 5.204 %. The peak positions for the Nb Pawley phase are denoted by the lower of the two sets of tick marks in Figure 6.2a.

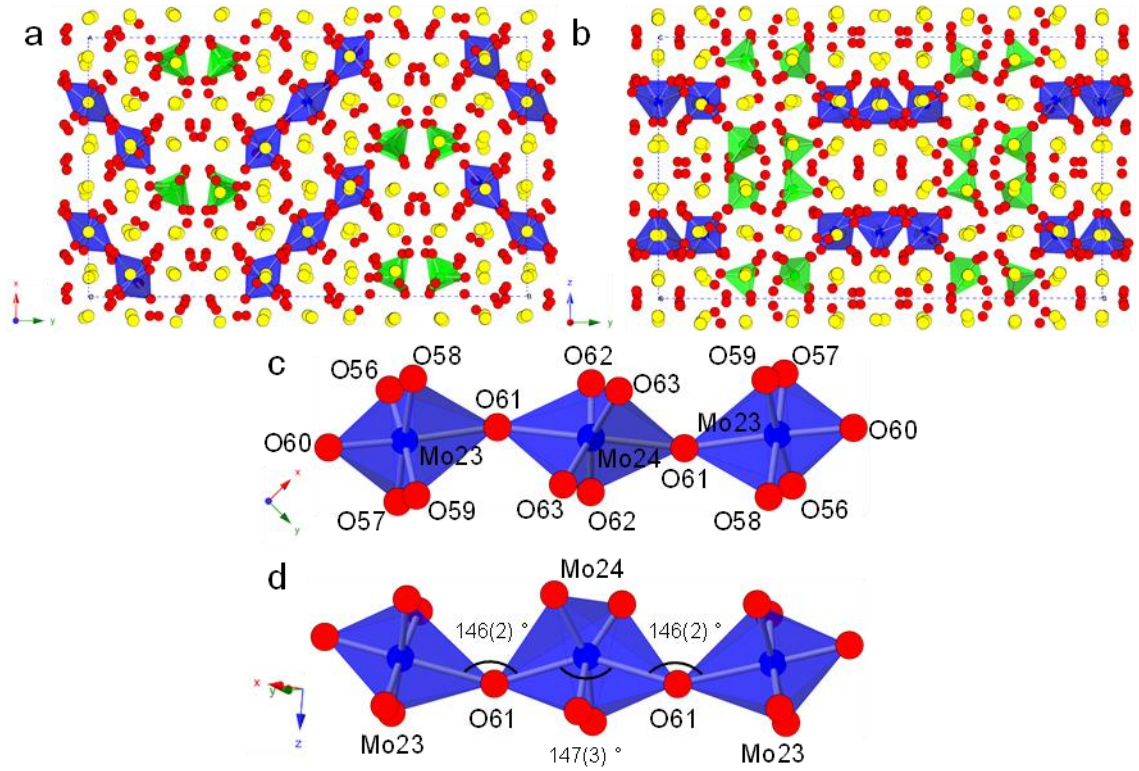

Figure 6.3: Orthorhombic structure for $Bi_{38}Mo_7O_{78}$ viewed along the: a) *z* axis; b) *x* axis. Bi = yellow, O = red, tetrahedral Mo21/Mo22 = green, octahedral Mo23/Mo24 = blue. Three corner-connected MoO_6 octahedra in a (Mo_3O_{16}) unit with: c) all Mo and O sites labelled; d) Mo-O-Mo bridge angles and O-Mo24-O angle labelled, showing the distortion of the Mo24-O_6 polyhedron and the (Mo_3O_{16}) unit.

The structural model in Figure 6.3 shows similarities to and improvements over that presented in the literature.[3] The orthorhombic structure is a Bi-O fluorite-like sublattice containing isolated MoO_4 (Mo21 and Mo22) tetrahedra and chains of three corner-connected MoO_6 octahedra (Mo23 and Mo24). The bond-distance and bond-angle restraints help to prevent distortion of the MoO_x polyhedra. The O-Mo-O bond angles in the MoO_4 tetrahedra

range from 108(2) to 112(2) °, with the Mo-O bond lengths ranging between 1.66(5) and 1.70(5) Å. For the MoO_6 octahedra, the non-bridging Mo-O bonds are 1.66(5) to 1.88(5) Å in length, which corresponds to an increased range of up to 3 esds from the restraint value of 1.80 Å. The bridging Mo-O bonds are 2.22(4) Å and 2.24(4) Å for Mo23-O61 and Mo24-O61 respectively, placing them within 2 esds of the 2.30 Å distance restraint. The distortion of the Mo-O bridges between the Mo23 and Mo24 octahedra are observed clearly, with values for the Mo23-O61-Mo24 and O61-Mo24-O61 bond angles of 146(2) ° and 147(3) ° (Figure 6.3c), within the range of Mo-O-Mo bridging bond angles reported in the literature.[5, 16]

The orthorhombic model for $Bi_{38}Mo_7O_{78}$ reported by Sharma *et al.* was obtained only through refinement using synchrotron single crystal XRD and DFT calculations.[3] These will not give accurate refinement of the atomic coordinates for the oxygen sites, due to contribution to an X-ray diffraction pattern scaling with the atomic number, *Z*, so the oxygen atoms contribute significantly less than the heavier Bi and Mo atoms. The neutron scattering lengths for the atoms Bi, Mo, and O are all similar (8.532, 6.715, and 5.803 fm for Bi, Mo, and O, respectively), so all atoms in the structure contribute to similar degrees. Secondly, the atomic coordinates for the O atomic sites within the MoO_6 octahedra in the Sharma model were not refined, but fixed at coordinates determined by DFT. Finally, whilst Sharma *et al.* were able to refine independent isotropic displacement parameters for most atomic sites, they equate the values for the O sites in the MoO_6 octahedra, with exceptionally large values reported. These are up to 30 times larger than the B_{iso} value for the same sites in this report (B_{iso} = 44(6) Å^2 for O37 to O39 compared to 1.4(2) Å^2 over the same sites (O61 to O63) in Table 6.1), with associated root-mean-square (rms) displacements nearly six times the size (0.75(7) Å and 0.13(1) Å for the models reported by Sharma *et al.* and in Table 6.1 respectively). These differences in the B_{iso} values and rms displacements arise potentially due to the atomic coordinates being derived from DFT calculations and not refined against the data, hence the distortion of the central MoO_6 octahedron (Mo24) is not taken into account unlike the structure presented in Table 6.1. Therefore, the orthorhombic structure presented in Table 6.1 should be used as the starting model for all future refinements.

Table 6.1: Crystallographic data for orthorhombic $Bi_{38}Mo_7O_{78}$ at 200 °C. Space group Pnca, *a* = 16.97177(7) Å, *b* = 28.71762(11) Å, *c* = 16.90225(6) Å, *V* = 8237.97(5) Å^3.

Site	Atom	x	y	z	occ	B_{iso} (Å^2)
Bi01	Bi	0.1149(8)	0.5975(6)	0.4123(9)	1	0.96(8)
Bi02	Bi	0.2577(9)	0.6062(6)	0.5698(9)	1	0.96(8)
Bi03	Bi	0.2512(9)	0.6974(6)	0.4053(10)	1	0.96(8)
Bi04	Bi	0.3949(8)	0.5057(5)	0.2578(10)	1	0.96(8)
Bi05	Bi	0.0975(8)	0.6999(5)	0.2428(11)	1	0.96(8)
Bi06	Bi	0.7558(8)	0.7051(5)	0.2553(9)	1	0.96(8)
Bi07	Bi	0.4149(9)	0.6983(6)	–0.0878(11)	1	0.96(8)
Bi08	Bi	0.2623(9)	0.5951(6)	–0.0751(9)	1	0.96(8)
Bi09	Bi	0.7425(8)	0.5896(4)	0.7550(10)	1	0.96(8)
Bi10	Bi	0.0693(8)	0.5974(5)	0.7572(11)	1	0.96(8)
Bi11	Bi	0.0805(9)	0.4907(5)	–0.0817(10)	1	0.96(8)

Site	Atom	x	y	z	occ	B_{iso} (Å^2)
Bi12	Bi	0.4063(8)	0.6911(5)	0.2448(11)	1	0.96(8)
Bi13	Bi	0.0917(9)	0.6023(6)	0.0875(11)	1	0.96(8)
Bi14	Bi	0.0738(9)	0.4993(6)	0.5686(9)	1	0.96(8)
Bi15	Bi	–0.0732(8)	0.5965(6)	–0.0945(11)	1	0.96(8)
Bi16	Bi	0.4137(9)	0.8037(6)	0.4026(10)	1	0.96(8)
Bi17	Bi	0.4151(9)	0.8037(6)	0.0870(11)	1	0.96(8)
Bi18	Bi	0.2588(9)	0.6960(5)	0.0663(9)	1	0.96(8)
Bi19	Bi	1/4	0	0.6043(12)	1	0.96(8)
Bi20	Bi	1/4	0	–0.0856(13)	1	0.96(8)
Mo21	Mo	0.0732(15)	0.6979(10)	0.5822(17)	1	0.1(2)
Mo22	Mo	0.0943(14)	0.6927(9)	–0.0872(18)	1	0.1(2)
Mo23	Mo	–0.0696(12)	0.6033(10)	0.2575(18)	1	0.1(2)
Mo24	Mo	1/4	0	0.2479(25)	1	0.1(2)
O25	O	0.4895(20)	0.5491(13)	0.4707(20)	1	0.3(1)
O26	O	0.2275(20)	0.674(12)	0.4483(19)	1	0.3(1)
O27	O	0.3129(20)	0.5478(11)	0.5147(21)	1	0.3(1)
O28	O	0.3302(22)	0.6507(12)	0.3351(21)	1	0.3(1)
O29	O	0.8456(22)	0.7323(13)	0.3296(20)	1	0.3(1)
O30	O	0.1424(21)	0.5448(12)	–0.0227(21)	1	0.3(1)
O31	O	0.3350(22)	0.6572(12)	0.1587(20)	1	0.3(1)
O32	O	0.1607(23)	0.5521(12)	0.1572(22)	1	0.3(1)
O33	O	0.3095(20)	0.6605(13)	–0.0402(19)	1	0.3(1)
O34	O	0.3325(20)	0.5506(13)	0.3419(19)	1	0.3(1)
O35	O	0.3391(20)	0.5617(11)	0.0221(21)	1	0.3(1)
O36	O	0.1433(21)	0.6497(13)	0.3222(20)	1	0.3(1)
O37	O	0.8569(20)	0.5536(14)	0.8322(22)	1	0.3(1)
O38	O	0.0369(20)	0.5470(13)	0.6712(24)	1	0.3(1)
O39	O	0.3304(20)	0.7315(13)	0.8394(22)	1	0.3(1)
O40	O	0.1651(20)	0.5549(13)	0.3232(23)	1	0.3(1)
O41	O	–0.0525(18)	0.6162(11)	0.7736(19)	1	0.3(1)
O42	O	0.0223(23)	0.5532(12)	0.8556(20)	1	0.3(1)
O43	O	0.2083(19)	0.6079(12)	0.0380(21)	1	0.3(1)
O44	O	0.3829(19)	0.7411(12)	0.0279(22)	1	0.3(1)
O45	O	0.3442(20)	0.8465(13)	0.0149(20)	1	0.3(1)
O46	O	0.7159(17)	0.7747(12)	0.2236(22)	1	0.3(1)
O47	O	0.1495(21)	0.6550(13)	0.1581(20)	1	0.3(1)
O48	O	0.0086(22)	0.7221(14)	0.6432(20)	1	1.4(2)
O49	O	0.1651(24)	0.7159(13)	0.6607(22)	1	1.4(2)
O50	O	0.0514(22)	0.7086(14)	0.4876(21)	1	1.4(2)
O51	O	0.0733(21)	0.6403(12)	0.5947(24)	1	1.4(2)
O52	O	0.1223(22)	0.6574(15)	0.8403(24)	1	1.4(2)
O53	O	0.0287(22)	0.7186(13)	0.8508(22)	1	1.4(2)
O54	O	0.1669(20)	0.7309(14)	–0.0687(25)	1	1.4(2)
O55	O	0.0746(19)	0.6600(15)	–0.0062(23)	1	1.4(2)
O56	O	0.8964(24)	0.6401(13)	0.3248(24)	1	1.4(2)
O57	O	–0.0047(25)	0.5727(16)	0.3299(23)	1	1.4(2)
O58	O	0.8629(21)	0.6332(14)	0.1857(23)	1	1.4(2)

Site	Atom	x	y	z	occ	B_{iso} (Å^2)
O59	O	–0.0294(21)	0.5657(15)	0.1846(25)	1	1.4(2)
O60	O	0.0088(20)	0.6421(14)	0.2306(21)	1	1.4(2)
O61	O	0.8286(23)	0.5585(13)	0.2895(20)	1	1.4(2)
O62	O	0.8022(22)	0.0304(13)	0.8334(24)	1	1.4(2)
O63	O	0.8209(22)	0.0106(12)	0.6754(23)	1	1.4(2)

6.3.2 Phase transition in $Bi_{38}Mo_7O_{78}$

To investigate fully the cause of the non-linear trends of the cell parameters with respect to temperature around 530 °C for $Bi_{38}Mo_7O_{78}$, and the temperature at which the monoclinic-to-orthorhombic phase transition occurs, sequential Rietveld refinements were undertaken using the *in situ* VT synchrotron PXRD data sets collected between 30 and 680 °C and the *multitopas* in-house software.[17]

For each synchrotron PXRD data set collected, the zero-point error and 10 background parameters were refined. 3 lattice parameters and 1 isotropic displacement parameter were also refined for the orthorhombic Pnca phase, whilst 4 lattice parameters and 1 isotropic displacement parameter were refined for the monoclinic P1c1 phase along with individual scale factors and peak-shape terms. From this analysis, the variation in the lattice parameters and cell volume of the orthorhombic phase with temperature were plotted (Figure 6.5a to Figure 6.5d) along with the weight percentages of the monoclinic and orthorhombic phases in the sample (Figure 6.5e).

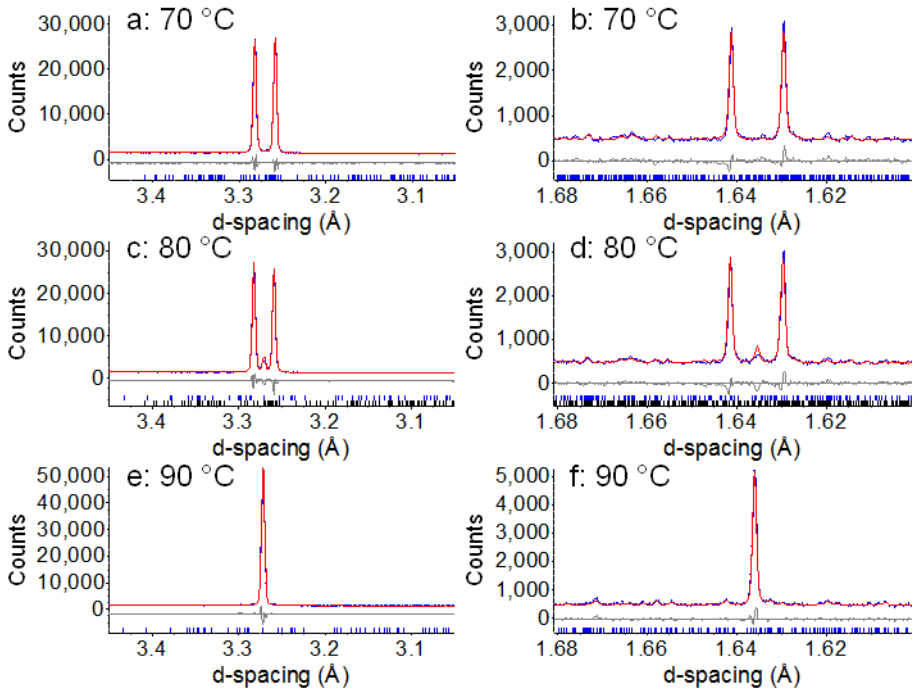

Figure 6.4: Rietveld refinements to the synchrotron PXRD data collected on heating at: a,b) 70 °C, showing only peaks from the monoclinic phase; c,d) 80 °C, showing peaks from the monoclinic and orthorhombic phases; e,f) 90 °C, showing peaks only from the orthorhombic phase.

As the temperature is increased from 30 to 680 °C, there is a monoclinic-to-orthorhombic phase transition between 70 and 90 °C (Figure 6.5c). This can also be seen in Figure 6.4, where the pairs of peaks at d ~ 3.27 Å and 1.64 Å (Figure 6.4a and Figure 6.4b) seen in the 30

to 70 °C data sets merge together to form a single peak above the phase-transition temperature (Figure 6.4e and Figure 6.4f). There is evidence of phase coexistence of the monoclinic and orthorhombic phases at 80 °C, indicative of a first-order phase transition (Figure 6.4c and Figure 6.4d). On cooling, the orthorhombic phase reverts to the monoclinic phase below 85 °C (monoclinic weight percent = 4.4(1) % at 75 °C). The lattice parameters and cell volume for the orthorhombic structure are not plotted between 30 and 80 °C in Figure 6.5a and Figure 6.5c, due to the negligible weight percentage of this phase present in the sample.

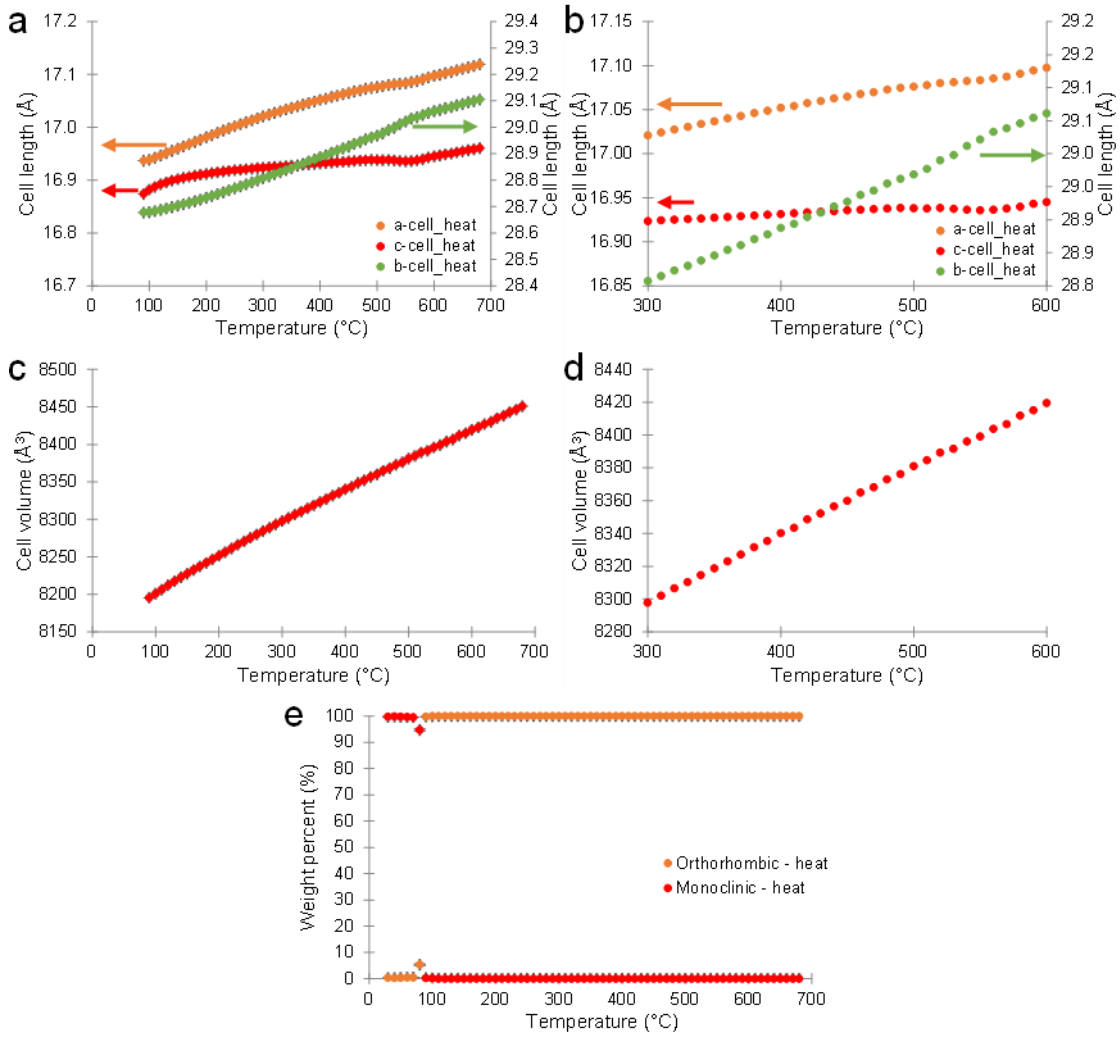

Figure 6.5: Variation of *a*, *b*, and *c* cell parameters for orthorhombic $Bi_{38}Mo_7O_{78}$ with temperature from VT synchrotron PXRD between: a) 90 and 680 °C; b) 300 and 600 °C. Variation of cell volume for orthorhombic $Bi_{38}Mo_7O_{78}$ with temperature from VT synchrotron PXRD data between: c) 90 and 680 °C; d) 300 and 600 °C. Changes in the trends of lattice-parameter and cell-volume expansion with temperature are observed at ~530 °C. e) Variation of weight percentages of the monoclinic and orthorhombic $Bi_{38}Mo_7O_{78}$ phases with temperature, showing the reversible transformation between the monoclinic and orthorhombic phases between 80 and 100 °C. Error bars are included in a), c), and e), but have been omitted from b) and d) for clarity.

Figure 6.5a and Figure 6.5b show changes in the rates of lattice parameter expansion with temperature for the orthorhombic cell parameters at ~530 °C, close to the temperature previously reported.[4] The *c* cell parameter decreases slightly on heating between 520 and 550 °C (16.93816(7) to 16.9357(1) Å), before increasing again with temperature above 550 °C. Between 520 to 550 °C the rate of *a* cell-parameter expansion decreases slightly, as shown by the decreased gradient of the plot in this temperature range compared to the surrounding

temperatures. At ~550 °C, there is a change in the linear thermal expansion coefficients, α_l, for the *a*, *b*, and *c* cell parameters: the *a* cell α_l decreases from 17.4 × 10^{-6} K^{-1} (250 to 500 °C) to 16.4 × 10^{-6} K^{-1} (560 to 680 °C), the *b* cell α_l decreases from 27.8 × 10^{-6} K^{-1} (250 to 500 °C) to 20.7 × 10^{-6} K^{-1} (560 to 680 °C), whilst the *c* cell α_l increases from 4.6 × 10^{-6} K^{-1} (250 to 500 °C) to 11.9 × 10^{-6} K^{-1} (560 to 680 °C). To coincide with these changes in rate of lattice expansion, the plot of cell volume against temperature shows evidence of non-linearity at 530 °C (Figure 6.5d).

From synchrotron PXRD data collected previously (ID31 data),[4] weak peaks present at room temperature disappeared at 600 °C. Slight relaxation of the structural model was required to produce zero intensity for the calculated peaks at these *d*-spacings. In the VT synchrotron PXRD data collected at the Australian Synchrotron, the ratio of peak-to-background intensities are smaller relative to the ID31 data, hence these weak peaks could not be observed, so the fine structural change occurring at ~550 °C could not be investigated.

6.3.3 Structural analysis of monoclinic $Bi_{38}Mo_7O_{78}$

At room temperature, $Bi_{38}Mo_7O_{78}$ is reported to have a 5 × 3 × 6 superstructure with a monoclinic distortion in space group Pn11.[4] To investigate whether the 5 × 3 × 6 superstructure is observable using the synchrotron PXRD and PND data, Pawley fitting was performed (Figure 6.6) using lattice parameters corresponding to both of the 5 × 3 × 3 and 5 × 3 × 6 superstructures (*a* ~28.8 Å, *b* ~16.7 Å, *c* ~16.8 or 33.6 Å, α ~90.5 °).

For the Pawley fits to the PND data, 10 background parameters, 4 lattice parameters, peak-shape terms, and a zero-point error were refined, whilst 20 background parameters, 4 lattice parameters, and a zero-point error were refined for the synchrotron PXRD data analysis. The resulting Pawley fits to the PND data show that the 5 × 3 × 3 superstructure (Figure 6.6a and Figure 6.6b) is sufficient to account for the observed peaks in the diffraction data, and this was used for the subsequent structural analysis.

When a material undergoes a phase transition which lowers the symmetry, a number of the symmetry elements of the higher-symmetry (parent) structure are lost, whilst others persist in the lower-symmetry (child) structure. The elements which remain define the isotropy subgroup of the higher-symmetry structure. For a pair of structures which have a group-subgroup relationship, it is possible to represent the child structure as a series of distortion modes of the parent structure. Multiple stages to this relationship may be involved if the child is not a maximal subgroup of the parent, which is denoted in the *International Tables of Crystallography*. Refinement of the amplitudes of the distortion modes and not the individual atomic coordinates for each atomic site provides an alternative method to refine the child structure, and means a phase transition can be presented as a series of active distortion modes. Though structures can have a large number of displacive modes, only a few active modes may be required to describe the structural differences between the parent and child. This has been reported previously for WO_3, where only 5 of the 24 possible displacive modes were required to describe the distortion of the monoclinic child in relation to the parent structure,[18] and for $Bi_2Sn_2O_7$, where only a small

number of displacive modes were shown to have large amplitudes to describe the α-to-β phase transition.[19]

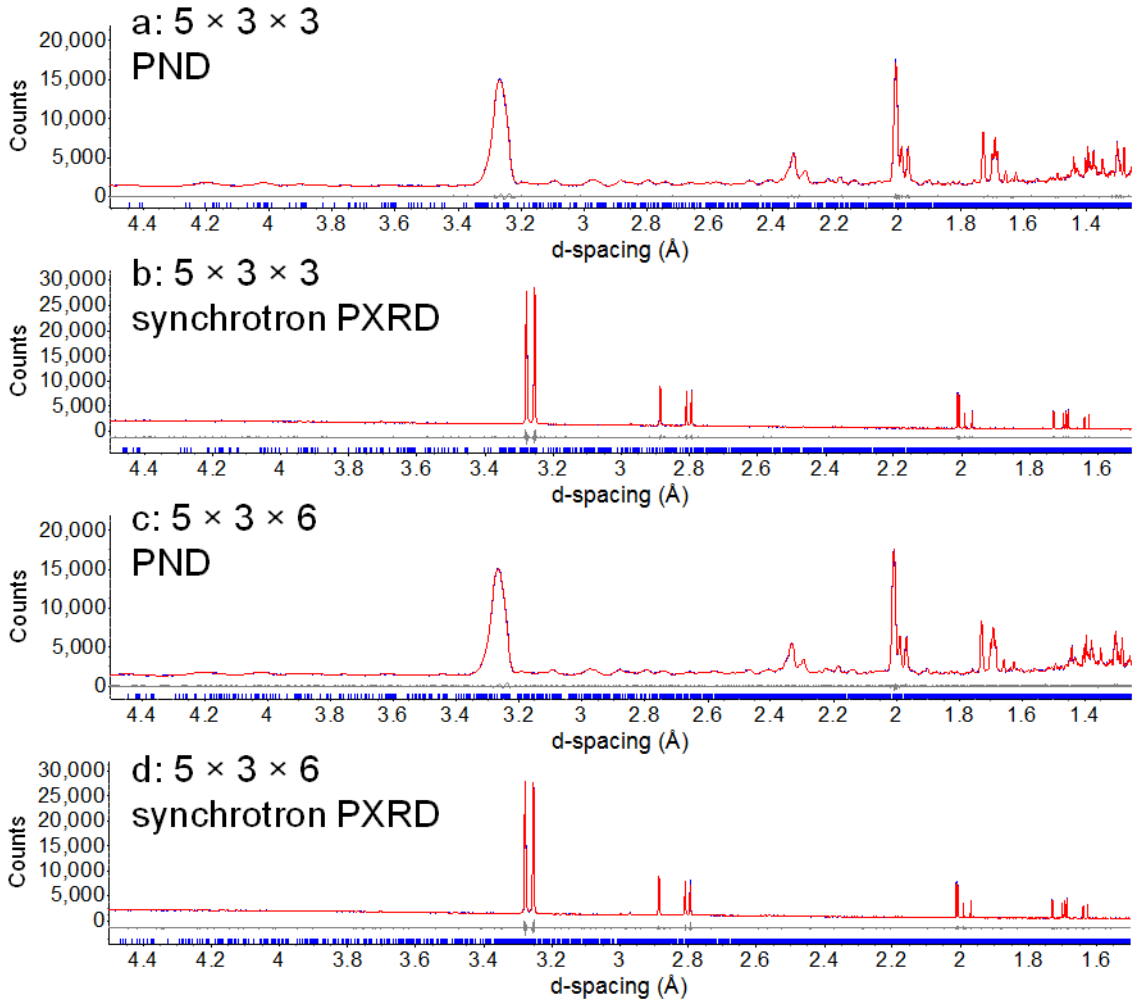

Figure 6.6: Pawley fits to the: a) PND data with a 5 × 3 × 3 superstructure, R_{wp} = 1.876 %; b) synchrotron PXRD data with a 5 × 3 × 3 superstructure, R_{wp} = 2.837 %; c) PND data with a 5 × 3 × 6 superstructure, R_{wp} = 1.867 %; d) synchrotron PXRD data with a 5 × 3 × 6 superstructure, R_{wp} = 3.277 %.

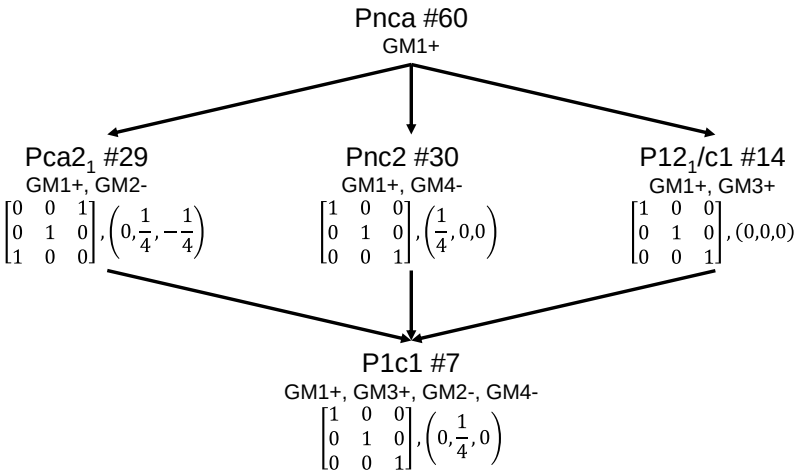

Figure 6.7: Parent-child subgroup tree for the transformation from Pnca to P1c1. For each subgroup, the transformation basis and origin shift are given relative to the Pnca structure. The terms GM1+ etc. denote the irreducible representations corresponding to the distortion modes involved in the parent-child relationship.

Monoclinic $Bi_{38}Mo_7O_{78}$ is currently reported in the literature with the non-standard space group Pn11, and unique *a* axis and α angle.[4] To have a standard space group setting, the structure would need be described in the space group P1c1, with a unique *b* axis and β angle. A subgroup tree can then be generated for the parent-child relationship between the Pnca parent structure and the P1c1 child structure which only requires an identity transformation matrix and an origin shift (Figure 6.7).[13]

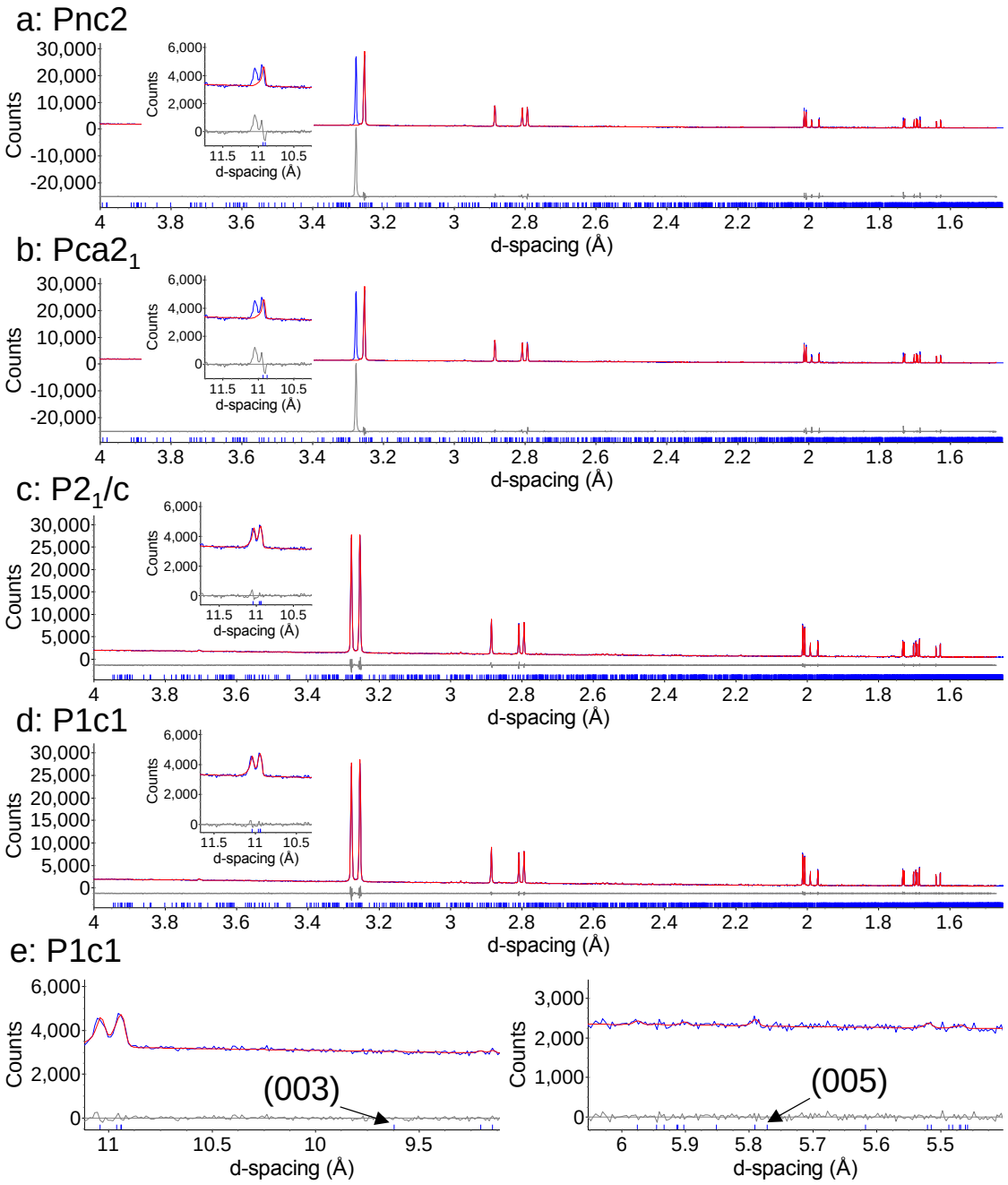

Figure 6.8: Pawley analyses for the four subgroups of the orthorhombic Pnca supergroup and the fit to the collected synchrotron PXRD data: a) Pnc2, R_{wp} = 11.347 %; b) $Pca2_1$, R_{wp} = 11.475 %; c) $P2_1/c$, R_{wp} = 3.022 %; d) P1c1, R_{wp} = 2.869 %. a) and b) show that peaks at *d* ~3.2 Å and 11 Å are not fitted by the orthorhombic space group. e) Zoomed-in regions of d) showing that the additional reflections disallowed by the $P2_1/c$ systematic absences correspond to peaks of negligible intensity.

The subgroup tree in Figure 6.7 shows the indirect parent-child relationship between Pnca and P1c1, undergoing a two-generation process which passes through three intermediate subgroups before reaching the P1c1 child. To confirm that the P1c1 space group is the correct choice of these four subgroups, Pawley fits were performed on for all four choices using the 30 °C synchrotron PXRD data, with 15 background parameters, zero-point error, and 3 or 4 (for monoclinic and orthorhombic space groups respectively) lattice parameters refined. The fits are shown in Figure 6.8, with the Pawley fits to the data for the orthorhombic space groups Pnc2 and $Pca2_1$ being the poorest, with only one of the two peaks at *d* ~3.3 Å and 11 Å fitted (Figure 6.8a and Figure 6.8b).

Use of the monoclinic space groups $P2_1/c$ and P1c1 do manage to fit these peaks, showing that these peaks arise from splitting of the single peak when transitioning from the orthorhombic to monoclinic phase (*vide supra*). The Pawley fits for the two monoclinic space groups are virtually identical (Figure 6.8c and Figure 6.8d), with only a small difference in R_{wp} for the $P2_1/c$ (R_{wp} = 3.022 %) and P1c1 (R_{wp} = 2.869 %) space groups. The systematic absences for $P2_1/c$ only allow 0*k*0 peaks when *k* = 2n, whilst space group P1c1 has no such constraints. In the Pawley fit for space group P1c1, the predicted (030) and (050) reflections correspond to regions with no observable peaks in the data, and so the synchrotron PXRD data cannot show conclusively which of the two monoclinic space groups is correct. However, second-harmonic-generation (SHG) measurements performed on this monoclinic phase are reported to show a lack of centrosymmetry,[4] confirming that P1c1 is the correct space group to use, as opposed to centrosymmetric $P2_1/c$.

To generate the starting monoclinic structure, the orthorhombic Pnca structural model (Table 6.1) was imported into ISODISTORT to attempt to identify the best child subgroup of the Pnca parent supergroup. Monoclinic axes *a*(*b*)*c* and cell choice "1" were selected, corresponding to the unique *b* axis expected for the P1c1 structure given in the *International Tables for Crystallography*. Three choices of distortion were generated (Table 6.2). Distortion mode 3 was rejected as the basis shows a reorganisation of the axes and elongation of the *c* axis, whilst mode 2 reorganised the axes making the *a* axis unique (and therefore expecting α to be the unique angle). Distortion mode 1 was chosen as no reorganisation of the axes is required between the parent and child, only an origin shift of +1/4*y*.

Table 6.2: The three choices of distortion available for the Pnca-to-P1c1 transformation in ISODISTORT, all with different transformation matrices and origin shifts, but identical unit-cell sizes relative to the parent cell (s), and isotropy subgroup indices (i).

Mode	Space Group	Basis	Origin	s	i
1	7 Pc	[{1,0,0},{0,1,0},{0,0,1}]	(0, 1/4, 0)	1	4
2	7 Pc	[{0,1,0},{0,0,1},{1,0,0}]	(0, 0, 0)	1	4
3	7 Pc	[{0,0,-1},{-1,0,0},{0,1,1}]	(-1/4, 0, 0)	1	4

Combined distortion-mode refinements were undertaken using the room-temperature synchrotron PXRD and PND data to refine the monoclinic structural model for $Bi_{38}Mo_7O_{78}$. The following parameters were refined against the synchrotron PXRD data: 12 background terms,

zero-point error, scale factor, cylindrical-sample intensity correction, and size-strain terms. 10 background terms, zero-point error, scale factor, peak-shape terms, and 1 lattice parameter for Nb modelled as a Pawley phase were refined against the PND data. 4 lattice parameters (*a*, *b*, *c*, and β), 738 distortion mode parameters, and 4 isotropic displacement parameters (Bi, Mo, O on Bi-O sublattice, and O on Mo-O sublattice) were refined for the $Bi_{38}Mo_7O_{78}$ phase. However, the amplitudes refined to values which were within 2 esds of zero. Therefore, it can be concluded that the quality of the data collected is insufficient for refinement of these distortion-mode amplitudes, and so only the lattice parameters can be determined accurately from the data. Therefore, to aid with the refinement of the monoclinic structure, single-crystal Laue neutron diffraction data were collected on floating-zone-furnace grown crystals of $Bi_{38}Mo_7O_{78}$ (Section 7.5). These data have not yet been fully analysed, and will be the subject of future work.

6.4 Phase transition in $Bi_{37.5}Mo_{7.5}O_{78.75}$

Variable-temperature synchrotron PXRD data for $Bi_{37.5}Mo_{7.5}O_{78.75}$ loaded into a 0.2 mm diameter quartz capillary were collected from 30 to 700 °C on heating in 10 °C intervals, with a count time of 240 seconds at two positions (2.0 and 2.5 °) per temperature, at a wavelength of 0.6359 Å. At 30 and 700 °C, 7 data sets were collected per temperature. PND data for $Bi_{37.5}Mo_{7.5}O_{78.75}$ were collected on ECHIDNA at OPAL, ANSTO. 10.075 g of $Bi_{37.5}Mo_{7.5}O_{78.75}$ was loaded into a 9 mm diameter V can and placed into a vacuum furnace before data were collected at room temperature for 270 minutes (311 seconds per step), then for 240 minutes (275 seconds per step) from 100 to 700 °C in 100 °C intervals, and on cooling from 600 to 100 °C in 100 °C intervals for 60 minutes per temperature (59 seconds per step). Temperature tolerances ranged from ± 5 °C from room temperature to 500 °C over the data collections, but by less than 1 °C for the 600 and 700 °C data collections.

To extract the unit-cell parameter behaviours with temperature, sequential Rietveld refinements were undertaken using the variable-temperature synchrotron PXRD data between 30 and 700 °C and the orthorhombic structure for $Bi_{38}Mo_7O_{78}$ (Table 6.1, as no structural model has been reported for $Bi_{37.5}Mo_{7.5}O_{78.75}$). The following parameters were refined: 10 background parameters, zero-point error, scale factor, peak-shape terms, and 3 lattice parameters and 1 isotropic displacement parameter to describe the orthorhombic structure.

The change in lattice parameters with temperature for $Bi_{37.5}Mo_{7.5}O_{78.75}$ (Figure 6.9) show similar features to those for orthorhombic $Bi_{38}Mo_7O_{78}$, with the rates of lattice-parameter expansion changing at elevated temperatures. A small discontinuity in the linear trend of unit-cell volume with temperature is seen at 550 °C (Figure 6.9d). This is the same temperature reported in the literature, where discontinuities in cell volume and rates of lattice-parameter expansion are all reported to occur at ~550 °C.[4] Whilst small deviations from linearity in the trends of the cell parameters with temperature are observed at 550 °C for $Bi_{37.5}Mo_{7.5}O_{78.75}$ (Figure 6.9b), more significant changes in the rates of lattice-parameter expansion are found at 450 °C (Figure 6.9a and Figure 6.9b).

Therefore, whilst structural changes reported at 550 °C in the literature could be the cause of the observations seen here at the same temperature, the cause of the abrupt changes from linearity at 450 °C is currently unknown. As for $Bi_{38}Mo_7O_{78}$, the synchrotron PXRD data is of too low intensity to probe the weak peaks found in the ID31 data to investigate if they hold information pertaining to the cause of these observations.

To fully characterise the orthorhombic $Bi_{37.5}Mo_{7.5}O_{78.75}$ structure, the interstitial oxygen atoms will need to be located. However, locating the interstitial oxygen atoms using difference Fourier maps will be virtually impossible due to the low level of interstitial oxygen content (6 out of 4057.5 electrons per formula unit). This level of interstitial oxygen is smaller than that located for $Bi_2La_8[(GeO_4)_6]O_3$ (Section 4.3.1), which was at the limits of detectability using data collected on the same instrument.

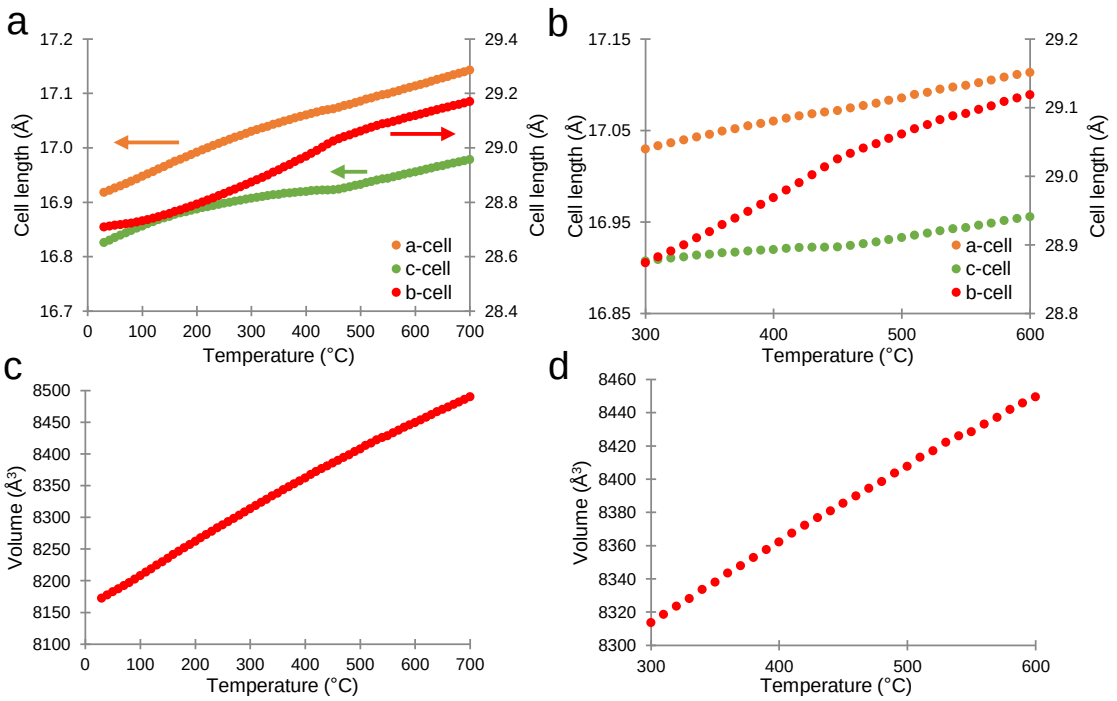

Figure 6.9: Variation of *a*, *b*, and *c* cell parameters for orthorhombic $Bi_{37.5}Mo_{7.5}O_{78.75}$ with temperature from VT synchrotron PXRD data between: a) 30 to 680 °C; b) 300 to 600 °C. Variation of cell volume for orthorhombic $Bi_{37.5}Mo_{7.5}O_{78.75}$ with temperature from VT synchrotron PXRD data between: c) 30 and 680 °C; d) 300 and 600 °C. Changes in the trends of lattice-parameter and cell-volume expansion with temperature are observed at ~450 °C and 550 °C. Error bars are smaller than the data points and omitted for clarity.

6.5 Conclusions

In summary, $Bi_{38}Mo_7O_{78}$ is found to exhibit a reversible monoclinic-to-orthorhombic phase transition between 70 and 90 °C, with the temperature dependencies of the orthorhombic unit-cell parameters changing between 530 and 560 °C. These are accompanied by changes in the linear thermal-expansion coefficients for the *a*, *b*, and *c* cell parameters above this temperature range, the cause of which is unknown. This is also seen for $Bi_{37.5}Mo_{7.5}O_{78.75}$, along with non-linearity in the trend of unit-cell volume with temperature, although larger changes in the rates of lattice-parameter expansion are observed at ~450 °C, with unknown causes. The orthorhombic structural model with space group Pnca was refined using 200 °C synchrotron

PXRD and PND data, and found to consist of a fluorite-like Bi-O superlattice containing isolated MoO_4 tetrahedra and chains of MoO_6 octahedra. This structural model provides a more accurate description of the orthorhombic structure of $Bi_{38}Mo_7O_{78}$ compared to the structural model with space group Pbcn reported previously, in which the atomic coordinates of the O sites in the MoO_6 octahedra have been refined.

Structure determination by distortion-mode analysis was attempted following transformation of the orthorhombic structure to the room-temperature monoclinic phase. This lower-symmetry monoclinic phase was found to be a 3 × 5 × 3 fluorite-based δ-Bi_2O_3-based superstructure. The structural refinement for this phase is ongoing, with single-crystal Laue neutron-diffraction data collected to aid with refinement of the displacive distortion modes, to attempt to understand if the cause for the monoclinic-to-orthorhombic phase transition is due to a decrease in the distortion of the MoO_x polyhedra.

6.6 References

1. D. J. Buttrey, D. A. Jefferson and J. M. Thomas, *Materials Research Bulletin*, 1986, **21**, 739-744.
2. C. D. Ling, *Journal of Solid State Chemistry*, 1999, **148**, 380-405.
3. N. Sharma, R. B. Macquart, M. Christensen, M. Avdeev, Y.-S. Chen and C. D. Ling, *Journal of Solid State Chemistry*, 2009, **182**, 1312-1318.
4. X. Kuang, Y. Li, C. D. Ling, R. L. Withers and I. R. Evans, *Chemistry of Materials*, 2010, **22**, 4484-4494.
5. F. Theobald, A. Laarif and A. W. Hewat, *Ferroelectrics*, 1984, **56**, 219-237.
6. T. E. Crumpton, M. G. Francesconi and C. Greaves, *Journal of Solid State Chemistry*, 2003, **175**, 197-206.
7. P. J. Bereciartua, F. J. Zuniga, J. M. Perez-Mato, V. Petricek, E. Vila, A. Castro, J. Rodriguez-Carvajal and S. Doyle, *Acta Crystallographica Section B*, 2012, **68**, 323-340.
8. H.-Y. Chen and A. W. Sleight, *Journal of Solid State Chemistry*, 1986, **63**, 70-75.
9. D. J. Buttrey, T. Vogt, G. P. A. Yap and A. L. Rheingold, *Materials Research Bulletin*, 1997, **32**, 947-962.
10. C. D. Ling, W. Miiller, M. R. Johnson, D. Richard, S. Rols, J. Madge and I. R. Evans, *Chemistry of Materials*, 2012, **24**, 4607-4614.
11. R. N. Vannier, G. Mairesse, F. Abraham and G. Nowogrocki, *Journal of Solid State Chemistry*, 1996, **122**, 394-406.
12. L. T. Sim, C. K. Lee and A. R. West, *Journal of Materials Chemistry*, 2002, **12**, 17-19.
13. B. J. Campbell, H. T. Stokes, D. E. Tanner and D. M. Hatch, *Journal of Applied Crystallography*, 2006, **39**, 607-614.
14. T. M. Sabine, B. A. Hunter, W. R. Sabine and C. J. Ball, *Journal of Applied Crystallography*, 1998, **31**, 47-51.
15. G. S. Pawley, *Journal of Applied Crystallography*, 1981, **14**, 357-361.
16. H. Sitepu, *Powder Diffraction*, 2009, **24**, 315-326.
17. J. S. O. Evans, *multitopas, FORTRAN 77 routine*, University of Durham, 1999.
18. B. Campbell, J. Evans, F. Perselli and H. Stokes, *Compcomm Newsletter*, 2007, **8**, 81-95.
19. J. W. Lewis, J. L. Payne, I. R. Evans, H. T. Stokes, B. J. Campbell and J. S. O. Evans, *Journal of the American Chemical Society*, 2016, **138**, 8031-8042.

7 Floating-zone-furnace crystal growth of fluorite- and apatite-type oxide-ion conductors

7.1 Introduction to crystal growth using a floating-zone furnace

Crystal growth using a floating-zone furnace (FZF) is based on the principle of zone melting, where a molten zone is translated along a polycrystalline rod and the molten material solidifies into a single crystal. Pfann in 1951 used zone melting for metal purification by passing horizontally a tube of Ge through a set of heating coils.[1] The impurities remained in the molten phase allowing them to be translated to the ends of the tube where they could be removed. This method was adapted by Theuerer in 1952 for float-zone refining of Si,[2] a process by which a molten zone is trapped between two vertically-aligned solid rods by surface tension, and then translated through a circular heating coil to produce Si of very-high purity. The heating coil applies a steep temperature gradient to a narrow section of the rods, producing a small molten zone within the “hot zone” (region of high temperature). As the upper (feed) rod is translated downwards through the static hot zone, the molten material leaving the zone cools and crystallises at the hot zone boundary, whilst the incoming feed rod melts into the molten zone at the same rate, assuming identical translation rates of the upper and lower rods.

A seed is required to initiate crystallisation from the molten phase, which in the floating-zone method is the upper surface of the lower sintered polycrystalline powder rod (seed rod), comprised of a large number of crystallites oriented randomly, each of which can act as a seed grain for the crystal growth. As the molten zone travels out of the hot zone, the material crystallises onto these grains at the solid-liquid interface along the translation direction (Figure 7.1).

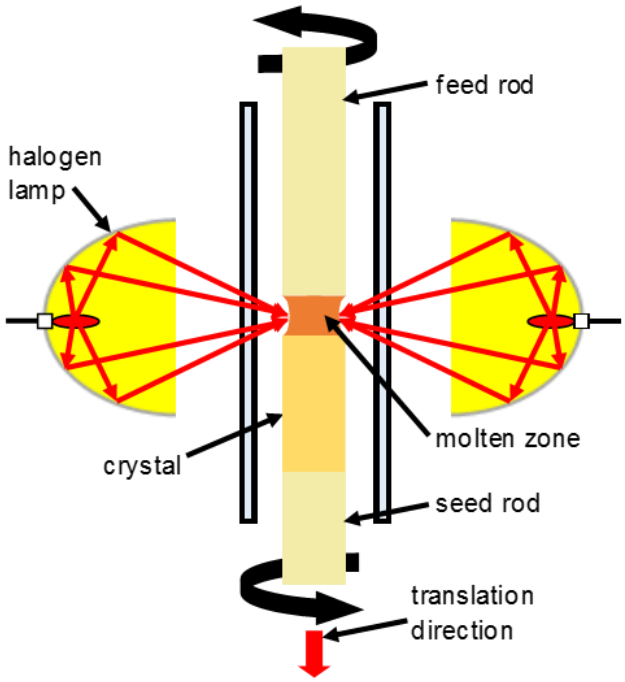

Figure 7.1: Schematic of FZF operation showing downwards translation of the rods through the hot zone and growth of a crystal.

Single crystals have been reported to grow quicker in certain directions.[3-5] Therefore, grains which are oriented with the fastest growth directions parallel to the direction of travel will grow preferentially compared to grains which are oriented otherwise. Over the course of the crystal growth, and providing that the angles of the grain boundaries of these unfavourable grains tilt inwards, these slower-growing crystal domains are covered over, and a single domain forms from the crystallite oriented in the fastest-growing direction across the entirety of the cross-section of the crystal. Once this occurs, the crystal rod will continue to grow in this same direction and orientation, resulting in a single crystal forming. Therefore, the initial region of crystal growth should not be used for diffraction experiments, as it will be comprised of multiple crystallites before the less-favoured domains have been eliminated. Multiple domains can persist throughout the crystal growth if a number of seed grains with different orientations but similar growth rates exist on the polycrystalline surface of the seed rod, with grain boundary angles almost parallel to the translation direction.

Early floating-zone furnaces used heating coils of graphite, but over the following decades the methods of heating were refined, leading to a range of FZFs in operation today, all of which have different methods for forming the molten zone. The primary methods of heating are laser, radio-frequency (RF) induction, and optical, with optical FZFs the most widely used. An optical FZF functions by having a number (1, 2, or 4) of high-powered lamps which emit visible or IR radiation focussed onto the central hot zone by half-ellipsoid mirrors. Lamps of different power can be placed in the FZF according to the expected melting point of the material undergoing crystallisation, meaning the hot zone can reach temperatures in excess of 2000 °C.

Crystal growth using a FZF has a large advantage over the Czochralski and Bridgman methods.[6, 7] In those latter cases, the molten material is in contact with a crucible, which presents a risk of crystal contamination. This does not occur in floating-zone growth, where the molten zone is contained by surface tension alone by material of identical composition. On the other hand this can be problematic if the molten material has a low viscosity, as the reduced surface tension could lead to zone collapse.

Crystal growth using a floating-zone furnace has been reported for a wide range of materials, with the works by Dabkowska and Gaulin,[8] and Koopayeh *et al.* tabulating a large number of these.[9] However, crystal growth using a FZF of doped bismuth-oxide-based materials are rare and challenging (due to bismuth volatilisation), with crystal growths reported only for $Bi_{0.76}Nb_{0.24}O_{1.74}$,[10] $BiVO_4$,[11] and $Bi_{38}Mo_7O_{78}$.[12] This chapter will present the attempts at crystal growth of a number of materials in the bismuth vanadate, bismuth molybdate, and apatite families, detailing issues identified during the crystal growths and methods employed to resolve them.

7.2 Introduction to bismuth vanadate materials, $Bi_{1-x}V_xO_{1.5+x}$ (x = 0.087, 0.2)

Compounds with the formula $Bi_{1-x}V_xO_{1.5+x}$ (x = 0.05 to 0.20) were first prepared by Takahashi *et al.*[13] Samples of the compositions studied were synthesised at 800 or 850 °C then

either quenched to room temperature, or annealed subsequently at 500 °C for in excess of 15 hours, before cooling slowly to room temperature. When x = 0.05 to 0.09, the annealed samples were found to contain a mixture of δ-Bi_2O_3-based fluorite-type and body-centered cubic phases, whilst the quenched samples were single-phase δ-Bi_2O_3-based materials. The presence of the body-centered-cubic phase on annealing is attributed to decomposition of the fluorite-type cubic phase to a V-doped γ-Bi_2O_3-based phase, as reported subsequently.[14] For x = 0.10 to 0.20, the annealed samples contained a mixture of the δ-Bi_2O_3-based phase and an unidentified phase, whilst the quenched samples contained an unidentified phase. For all of these analyses, Takahashi *et al.* collected only laboratory powder X-ray diffraction data, presenting no fits to the collected patterns using the structure types noted in their report, so the quality of the fits cannot be established. The identification of the δ-Bi_2O_3-based phases may point to the authors only observing peaks in the diffraction patterns corresponding to the fluorite-type subcell and not peaks corresponding to the superstructures reported in later works. However, without the presentation of diffraction data, this cannot be ascertained for certain. Zhou *et al.* in 1988 reported six compositions (x = 0.10, 0.11, 0.14, 0.20, 0.22, 0.33), and their structure types classified further.[15] The x = 0.10 composition was described as a pseudocubic (3 × 3 × 3) fluorite-based supercell (Type I) of δ-Bi_2O_3 (a ~16.5 Å), based on electron diffraction and X-ray studies. The structures of the x = 0.14, 0.20, and 0.22 compositions were classified as Type II, a triclinic superstructure with a fluorite-based subcell. For none of the six compositions were structural models presented. In 1994, Kashida *et al.* reported a rhombohedral structural model for the x = 0.10 composition (a = 11.76(1) Å, α = 59.78(9) °, space group = R3m).[16] However, there are multiple problems with the structural model, with the structural formula reported as $Bi_{0.9}V_{0.1}O_{1.566}$ instead of the stoichiometric $Bi_{0.9}V_{0.1}O_{1.6}$, and containing several very short Bi-O bond lengths of ~1.0 Å.

Subsequent work reported two related compositions (x = 0.087, 0.095) with the Type I structure.[14] Both $Bi_{0.913}V_{0.087}O_{1.587}$ and $Bi_{0.905}V_{0.095}O_{1.595}$ are excellent oxide-ion conductors, with the x = 0.087 composition exhibiting the highest conductivity of any singly-substituted δ-Bi_2O_3-based material (σ = 3.9 × 10^{-2} Scm^{-1} at 500 °C), approximately one-to-two orders of magnitude greater than for the commercially-used yttria-stabilised zirconia.[17] Whilst the conductivities of doubly-substituted δ -Bi_2O_3-based compounds on the first heating are comparable to that for $Bi_{0.913}V_{0.087}O_{1.587}$ (e.g. $Bi_{0.85}Pr_{0.105}V_{0.045}O_{1.545}$ σ ~8 × 10^{-2} Scm^{-1} at 500 °C),[18] they convert into stable tetragonal phases on thermal cycling, resulting in their conductivities decreasing by around two orders of magnitude. To contrast this, $Bi_{0.913}V_{0.087}O_{1.587}$ crystallises as a stable ordered superstructure, showing no evidence of conversion to a lower-symmetry structure with reduced conductivity.

In 2006, Wrobel *et al.* reported a rhombohedral structural model for $Bi_{0.8}V_{0.2}O_{1.7}$ (x = 0.2, a = 3.815(4) Å, c = 9.990(8) Å, space group = $R\bar{3}m$) from single-crystal data.[19] The rhombohedral substructure can be described either as a series of partially-occupied edge- and corner-sharing OM_4 tetrahedra, or as a series of MO_8 distorted cubic polyhedra where the coordination number of the M cation varies statistically due to the fractional occupancy of the O

site (85 %). The rhombohedral model does not predict a number of reflections present in collected powder diffraction patterns, suggesting the true structure is more complex.

This chapter will focus on two $Bi_{1-x}V_xO_{1.5+x}$ (x = 0.087, 0.2) compositions, detailing the single-crystal growth attempts using a floating-zone furnace and neutron diffraction studies of these materials. The x = 0.087 composition is shown to form a rhombohedral structure with space group R3m, though combined refinement with synchrotron X-ray data is required to characterise fully the structure and refine the atomic positions of the V sites. The x = 0.2 composition proved very difficult to grow, due to a very narrow power tolerance to maintain a stable molten zone during crystal growth. However, the process is detailed and the techniques are highlighted which attempted to aid the growth process and produce crystals, which could be applicable to other difficult crystal growths. Finally, work is presented showing the range of superstructures tested in attempts to index the x = 0.2 composition and identify the supercell.

7.3 Synthesis of bismuth vanadate materials, $Bi_{1-x}V_xO_{1.5+x}$ (x = 0.087, 0.2)

7.3.1 Solid-state synthesis

Solid-state synthesis was undertaken to prepare large (30 g) powdered samples of compositions $Bi_{0.913}V_{0.087}O_{1.587}$ and $Bi_{0.8}V_{0.2}O_{1.7}$ for subsequent single-crystal growth. For $Bi_{0.913}V_{0.087}O_{1.587}$, 28.9242 g of Bi_2O_3 (62.07 mmol, Sigma-Aldrich, 99.9 %) and 1.0758 g of V_2O_5 (5.92 mmol, Sigma-Aldrich, 99.99 %) were ground together with a mortar and pestle, then fired in an alumina crucible at 700 °C, 750 °C, 800 °C, and 825 °C for 12 hours each, with intermediate grindings and heating and cooling rates of 5 °C per minute between successive firings, to yield a pale-yellow powder.

For $Bi_{0.8}V_{0.2}O_{1.7}$, 27.3327 g of Bi_2O_3 (58.66 mmol) and 2.6673 g of V_2O_5 (14.67 mmol) were ground together in a mortar using a pestle, then fired in an alumina crucible at 650 °C for 12 hours with a heating and cooling rate of 5 °C per minute, then 840 °C for 10 hours with a heating rate of 5 °C per minute and a cooling rate of ~1 °C per minute, producing a pale-yellow powder.

7.3.2 Single-crystal growth of $Bi_{0.913}V_{0.087}O_{1.587}$

Growth of a large single crystal of $Bi_{0.913}V_{0.087}O_{1.587}$ was attempted using the floating-zone-furnace (FZF) technique at the University of Sydney. Roughly 30 g of starting material was divided into two batches, and cylindrical feed and seed rods prepared using a hydrostatic press with 40 MPa of pressure. The pressed rods were then sintered at 825 °C for 12 hours prior to mounting in the FZF. As the melting point of this material is below 1000 °C, the FZF was equipped with 4 × 150 W lamps.

The initial programmed ramp in FZF lamp power was from 0 to 50 % power in 0.4 hours. At 47.5 % power, the tips of the feed and seed rods began to melt, so the programme was paused. Whilst the sintered rods are pale yellow in colour, the melt is dark orange. This caused the melt to have greater heat absorption, hence a lower lamp power was required to sustain the stable molten zone. To prevent the melt from becoming too hot – which would cause an elongation of

the melt attached to the feed rod tip and potential dripping onto the seed rod due to loss of surface tension for the molten droplet – the lamp power was decreased manually to 42.5 % power.

This lower lamp power kept just the tips of the rods molten, and so the tips were joined together and both rods programmed to translate downwards at a rate of 3 mm per hour, starting the crystal growth process. After approximately one hour, a small bubble was seen within the molten zone, in addition to an erratic rotation of the rods. This erratic rotation was caused by the bubble partially cooling the molten zone due to reduced heat absorption of the bubble relative to the molten $Bi_{0.913}V_{0.087}O_{1.587}$. This meant that the temperature was hot enough to melt completely the outer edges of the feed and seed rods, but not enough to allow the bulk of the tip to melt. This left pieces of solid material within the melt which could rotate against each other and cause the erratic rotations observed (Figure 7.2). This problem was remedied by increasing the lamp power to 43.1 %, which was sufficient to melt the rod tips fully.

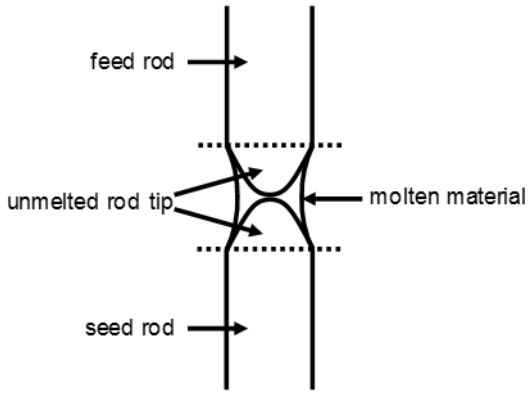

Figure 7.2: Image showing how erratic rotation of the feed and seed rods can be caused by partial melting of the rod tips. Compare the geometry around the molten region to that in Figure 7.1.

After 4.5 mm of growth, an increased quantity of bubbles were observed within the melt, which coalesced to form a single large bubble. To prevent an unstable collapse of the molten zone later in the growth, a stable collapse was performed by translating the feed rod upwards, elongating and separating the molten zone and removing the bubble. The feed rod was translated back to its previous position and the two molten tips joined, continuing the growth.

No further problems were observed during the remainder of the growth process, with the power increased to 46.3 % and subsequently to 46.5 % in the last couple of hours of the growth to mitigate the cooling effect caused by the formation of a small number of bubbles within the melt. After a total growth time of 14 hours, the growth was ended and the rods separated in conjunction with reducing the FZF lamp power from 46.5 to 0 % in 0.2 hours.

During the process of removing the seed rod and grown crystal from the furnace cavity, the crystal broke into two pieces (Figure 7.3b). Together, the two pieces form a crystalline rod 42.5 mm in length (Figure 7.3a). Of note, 1.5 mm on the tip of the rod has a partial silver colouration to it, distinct from the deep-orange colour of the remainder of the crystal. The tip of the crystal rod was ground up and characterised by powder X-ray diffraction, but the cause of

the silvering could not be identified, with only Bragg peaks originating from the primary bismuth vanadate phase present in the diffraction pattern.

Figure 7.3: a) Image showing the entire length of the grown 42.5 mm $Bi_{0.913}V_{0.087}O_{1.587}$ crystal rod; b) The fractured $Bi_{0.913}V_{0.087}O_{1.587}$ crystal rod, showing the ~30 mm of crystalline material of the longest fragment.

7.3.3 Single-crystal growth of $Bi_{0.8}V_{0.2}O_{1.7}$

As for $Bi_{0.913}V_{0.087}O_{1.587}$, the FZF technique was used to try and grow single crystals of $Bi_{0.8}V_{0.2}O_{1.7}$. Unlike for the x = 0.087 composition however, multiple crystal growths using fresh sintered rods were required for the x = 0.2 composition due to difficulties in maintaining a stable molten zone. During each growth, multiple attempts were required to form a stable zone, due to the zone collapsing repeatedly.

150 W lamps were used for the first $Bi_{0.8}V_{0.2}O_{1.7}$ growth, as a similar melting point to $Bi_{0.913}V_{0.087}O_{1.587}$ was expected. However, a lamp power of 95 % was unable to melt the sample rods. Therefore 4 × 300 W lamps were used, which provided sufficient heat to melt the tips of the feed and seed rods. Unfortunately, a large disparity in power was observed between that required to melt the material in the feed rod initially, and that at which the melt was stable for crystal growth. Multiple attempts were taken to form a stable molten zone, but each resulted in material dripping from the feed rod onto the seed rod and drip catcher mounted within the FZF (~14.5 g in total). The cause of this large power disparity is the same as seen for $Bi_{0.913}V_{0.087}O_{1.587}$. The sintered rods are pale yellow whilst the molten material is dark orange. This means that as the sintered powder melts, the melt has increased heat absorption compared to the powdered material, thereby melting the rod more rapidly, resulting in a 'runaway' heating process.

In light of the problems with the first crystal growth, another 30 g of $Bi_{0.8}V_{0.2}O_{1.7}$ was prepared for a second growth. Owing to the difficulties in obtaining a stable molten zone following the initial melt during the first growth, the decision was made to decrease rapidly the power to the FZF lamps once the rods started to melt, so the molten material would not become too hot and drip from the feed rod.

To try and simplify the growth process, it was decided to melt only the tip of the feed rod and leave the tip of the seed rod just below the lower hot-zone boundary, so that only one potential runaway melt would have to be mitigated, instead of two. Additionally, the tip of the seed rod

was removed carefully with a diamond wheel saw to create a flat surface onto which the molten feed rod tip could be joined. If this was not done, then the molten seed rod would have to be joined to the hemispherical tip of the seed rod, making any attempts at joining the two rods more difficult.

For the initial heating stage, the furnace lamps were programmed to ramp from 0 to 60 % power in 0.5 hours, with rod rotation speeds of 24.9 rpm (feed) and 24.6 rpm (seed). The feed rod did not melt at this power, so the furnace was programmed to ramp from 60 to 65 % power. At 60.1 % power the tip of the feed rod began to show signs of melting, so the ramp was paused and the lamp power decreased manually to 53.6 % within several seconds. Unfortunately, even a decrease in power on this timescale was unable to prevent the molten feed-rod material from dripping down the side of the seed rod (Figure 7.4a). This process was repeated several times but remained unsuccessful, with molten material dripping from the feed rod onto the seed rod. The sheer lack of consistency in the power levels required to melt the feed rod and collapse of the molten zone (Figure 7.5) hampered attempts to grow a single crystal. Over the course of the growth, 11 attempts to form a molten zone resulted in zone collapse, but only three periods of molten zone stability were achieved, which will be described in more detail.

The first stable molten zone occurred after 11.1 mm of feed rod had been lost to runaway melting during the first five attempts at zone formation. This stable zone was formed after the tip of the feed rod melted at 39.5 % power, with the rods joined at 38.8 % power. This zone collapsed at 39.5 % power after 5 minutes.

The second stable molten zone was maintained for 30 minutes with a translation rate of 3 mm per hour. The feed rod melted at 43.1 % power, and the rods were joined at 43.2 % power with the power range fluctuated by ~7 % to maintain zone stability. The stable zone is shown in Figure 7.4b, prior to its collapse at 38.9 % power. The final stable zone formed following a melt at 41.3 % power and subsequently joined at 40.4 % power. The zone collapsed at 38.6 % power after roughly one hour of stable growth. A graph showing the different power settings required to melt the rods and collapse the molten zone are given in Figure 7.5 as red and blue points respectively. The periods during which the molten zone was stable and crystal growth could be performed are denoted with black lines, which connect the different power levels required to maintain zone stability (black points).

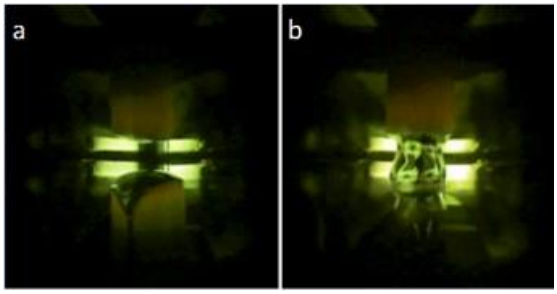

Figure 7.4: a) Collapsed zone following runaway heating after the initial melt, causing the molten material to drip from the feed rod (upper rod) down the side of the seed rod. b) The stable molten zone at 38.6 % power, prior to zone collapse.

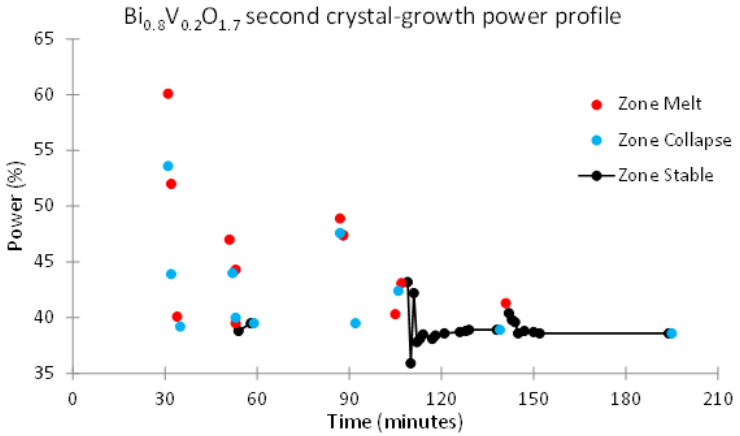

Figure 7.5: The ranges of power levels required for the feed rod tip to melt, the molten zone to collapse, or the molten zone to be stable, during the second crystal growth for $Bi_{0.8}V_{0.2}O_{1.7}$.

Due to the large amount of feed rod material used, and difficulties associated with attempts to obtain and maintain a stable molten zone, crystal growth with this pair of rods was aborted after 195 minutes. Of the crystal grown, the material was of poor quality, with very little force required to break the crystalline rod apart. On breaking the rod, a small number of crystal fragments were obtained along with a large amount of fine powder, though none of the fragments were of use for single-crystal neutron diffraction experiments.

The third crystal growth of $Bi_{0.8}V_{0.2}O_{1.7}$ used the material remaining from the sintered feed and seed rods of the two previous growths. As for the second growth, the tip of the seed rod was cut with a diamond wheel saw and mounted so that the tip was just at the bottom of the hot zone of the furnace. Additionally, to attempt to melt the feed rod at a lower initial power than for the first two growths, the tip of the feed rod was darkened with a graphite pencil (Figure 7.6). This would minimise the difference in colour between the sintered rod tip and the melt, thereby maintaining a consistent level of heat absorption between the solid and the melt. To avoid any potential contamination of the crystal through incorporation of the graphite, the first several millimetres of crystal grown should not be used for diffraction experiments. This could be disregarded in the third growth due to the loss of the potentially contaminated material during the initial attempts to form a molten zone (*vide infra*).

Figure 7.6: Tip of feed rod darkened with a graphite pencil to minimise the disparity in levels of heat absorption of sintered and molten $Bi_{0.8}V_{0.2}O_{1.7}$.

The initial heating of the rods was provided by a programmed ramp of the furnace from 0 to 50 % power in 0.4 hours, but paused at 44.2 % after the feed rod tip began to show evidence of melting (Figure 7.7a). This power level is ~15 to 20 % lower than the power levels required for the initial melting during the first two growths. The power was ramped down quickly to 39.3 %, by which time the molten region had elongated to touch the seed rod (Figure 7.7b). Due to the high viscosity of the molten zone, the power was increased to 39.9 % to widen the diameter of the zone to the full width of the feed rod. However, this caused a loss in surface tension within the melt, and the liquid material was lost down the side of the seed rod (Figure 7.7c and Figure 7.7d).

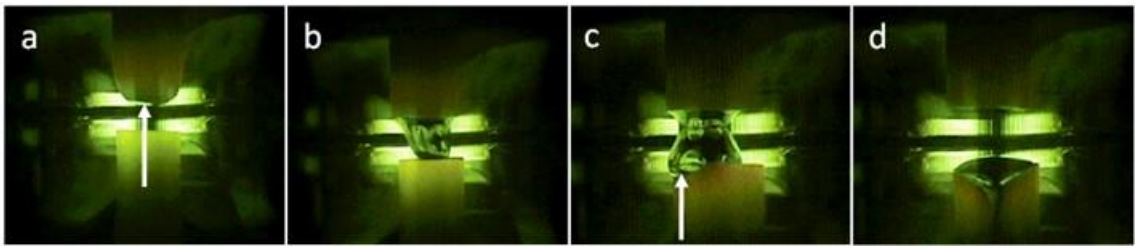

Figure 7.7: a) Initial melt of $Bi_{0.8}V_{0.2}O_{1.7}$ at 44.2 % power. b) Rapid decrease of power to 39.3 % unable to prevent elongation of molten feed-rod tip. c) Attempt to widen the base of molten zone led to loss of surface tension. d) Molten zone collapse down side of seed rod.

Over the next ~60 minutes, several further attempts were made at forming a molten zone across a narrow range in lamp power, with no success (Figure 7.9). On the tenth attempt, a stable zone was formed lasting for around 40 minutes, with a translation rate of 3 mm per hour. Despite increasing the lamp power from 37.2 to 39.3 %, the zone froze and collapsed.

On the thirteenth attempt, a stable zone was maintained for 108 minutes, and the power increased from 38.1 to 39.4 % to prevent the molten zone freezing due to the formation of bubbles within the melt (Figure 7.8a and Figure 7.8b). The bubbles can be observed by the different colouration and reflective properties they exhibit compared to the melt. Over the course of 25 minutes, these bubbles accumulated to form a single large bubble which extended across the width of the molten zone (Figure 7.8c). Removal of this bubble was attempted by moving the feed rod upwards and away from the seed rod to break the molten zone. On bursting the bubble, molten material ran down the side of the grown crystalline material due to loss of surface tension of the melt on the seed rod (Figure 7.8d).

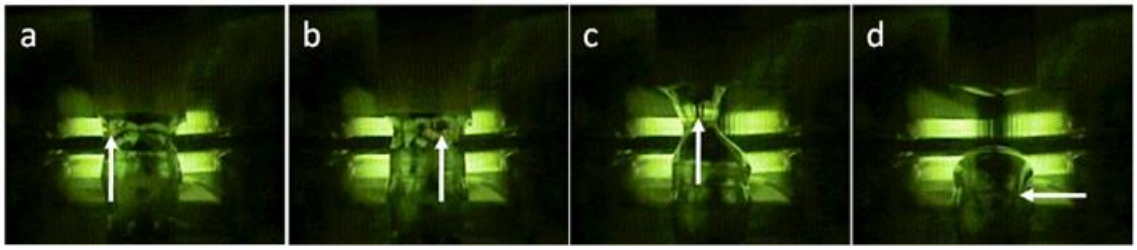

Figure 7.8: a) and b) Bubbles trapped in the molten zone. c) Small bubbles coalesced to form a single large bubble which extended across the width of the molten zone. d) Removal of the bubble caused loss of molten material down the side of the grown crystal.

One final stable zone was created on the fourteenth attempt, lasting for ~40 minutes. A number of bubbles were observed in the molten zone during this time, leading to zone collapse. No further crystal growth was carried out as only 5 mm of material remained in the feed rod. As with the second $Bi_{0.8}V_{0.2}O_{1.7}$ growth, the range of power settings required for the melting and collapsing points of the molten zone during the third crystal growth are given in Figure 7.9 as red and blue points, with the power settings needed to maintain the three stable molten zones (black points) connected by black lines. Roughly 30 mm of crystalline material were formed during the third growth, with the rod predominantly pale yellow in colour (Figure 7.10). Visual inspection showed that the rod is not a single crystal, containing multiple smaller crystallites.

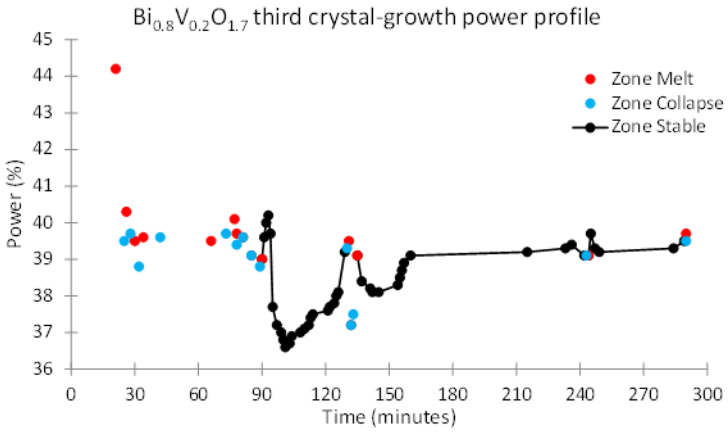

Figure 7.9: The range of power levels required for: the feed rod tip to melt, the molten zone to collapse, or the molten zone to be stable during the third crystal growth for $Bi_{0.8}V_{0.2}O_{1.7}$.

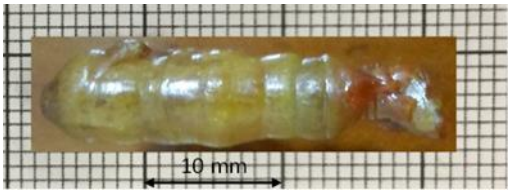

Figure 7.10: $Bi_{0.8}V_{0.2}O_{1.7}$ crystal grown during the third growth.

7.4 Characterisation of bismuth vanadate materials, $Bi_{1-x}V_xO_{1.5+x}$ (x = 0.087, 0.2)

7.4.1 Laue diffraction of $Bi_{0.913}V_{0.087}O_{1.587}$

Laue diffraction patterns for $Bi_{0.913}V_{0.087}O_{1.587}$ were collected at room temperature on the KOALA Laue diffractometer at OPAL, ANSTO. Throughout these measurements, a 3 mm aperture was placed in the incident neutron beam 49 cm before the sample. Initially, the length of the crystal rod was screened by wrapping the rod in aluminium foil and affixing it to a sample pin. Data were then collected at two positions along the crystal: near the tip of the rod, and halfway along the rod length across a region 3 mm in diameter. The collected Laue patterns (Figure 7.11) show a large number of peaks with no clear arcs of Laue spots, indicating that the crystal rod is not comprised of one large single crystal, but rather a number of overlapping crystallites. Due to these findings, a small section was cleaved from the rod and broken into smaller crystal fragments, which could be screened independently for quality.

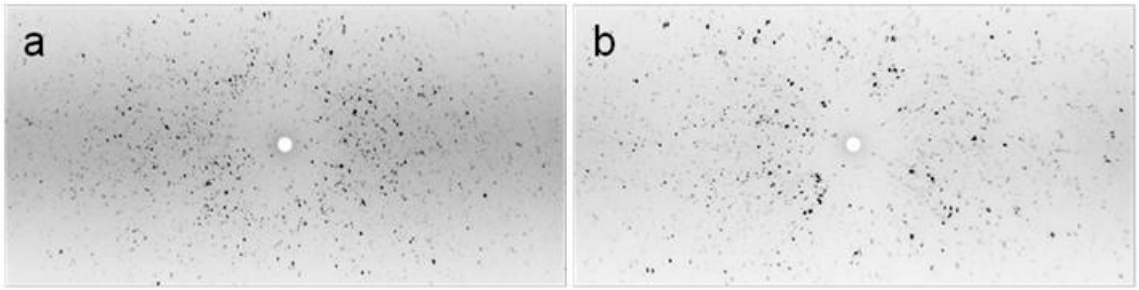

Figure 7.11: Laue patterns for $Bi_{0.913}V_{0.087}O_{1.587}$ collected from the: a) tip of the crystal rod, BiVO_1.tif (filename); b) centre of the crystal rod, BiVO_hor_1.tif (filename).

26 different $Bi_{0.913}V_{0.087}O_{1.587}$ crystal fragments ranging in size from 0.7 to 24 mm^3 underwent 5 to 10 minute data collections. The three best fragments (2, 5, and 16) were used for longer data collections, with the details given in Table 7.1. Prior to the long data collection for fragment 2, this sample was cleaved to attempt to remove the crystallite responsible for the additional streaked reflections observed in the collected pattern, albeit unsuccessfully. From the long data collections performed on crystals of this composition, it was found that the data of highest quality came from fragment 5 (crystal size ~0.7 mm^3) and not fragment 16 (crystal size ~5.6 mm^3), as fragment 16 shows evidence of a large number of spots from additional crystallites in close proximity to those for the primary crystal.

Table 7.1: Parameters for the long data collections for fragments 2, 5, and 16 for $Bi_{0.913}V_{0.087}O_{1.587}$.

Fragment	Orientation	ϕ start (°)	ϕ end (°)	Step size (°)	Exposure time per pattern (minutes)	Number of patterns
2	1	0	189	9	40	22
5	1	–90	90	10	70	19
5	2	–100	100	10	70	21
16	1	–90	90	10	15	19
16	2	–100	100	10	15	21
16	2	–95	105	10	15	21
16	2	–97.5	102.5	5	15	41

7.4.2 Structural analysis of $Bi_{0.913}V_{0.087}O_{1.587}$

Pawley analyses were undertaken against time-of-flight neutron powder and synchrotron X-ray powder diffraction data to identify the space group and lattice parameters which best describe the structure of $Bi_{0.913}V_{0.087}O_{1.587}$. Lattice parameters were chosen which relate to the 3 × 3 × 3 fluorite-type superstructure (a ~16.5 Å), which was detected by electron diffraction performed by Prof. Ray Withers (Australian National University, Canberra) (Figure 7.12a and Figure 7.12b). These images also show streaking when the grains are viewed off-axis (Figure 7.12c), suggesting a degree of local-scale ordering within the material.

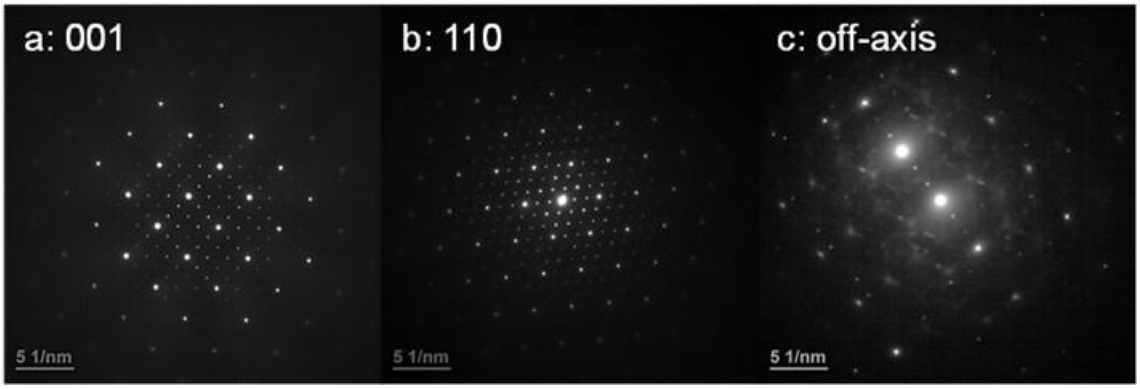

Figure 7.12: Electron microscopy images for $Bi_{0.913}V_{0.087}O_{1.587}$ viewed along: a) 001; b) 110 showing the fluorite-type subcell reflections (most-intense spots) and 3 × 3 × 3 supercell reflections (weaker spots). c) View off-axis showing diffuse streaking suggesting a local-scale ordering in the structure.

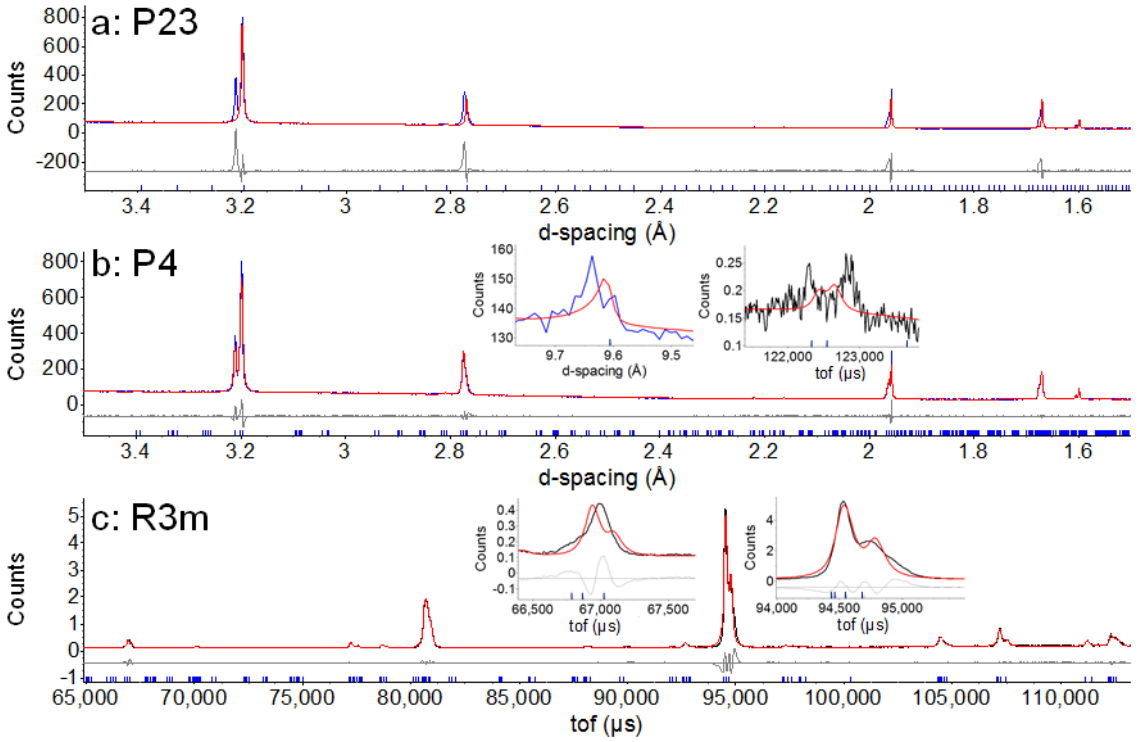

Figure 7.13: Pawley fits to the collected synchrotron PXRD data (blue) and PND data (black) using: a) cubic P23 unit cell, *a* = 16.627 Å; b) tetragonal P4 unit cell, *a* = 16.624 Å, *c* = 16.703 Å. Inset of Pawley fit to synchrotron PXRD with a P4 unit cell (blue) showing only one predicted reflection compared to two observed peaks at *d* ~9.65 Å. Inset of Pawley fit to time-of-flight PND data with a P4 unit cell (black) showing the two predicted reflections have incorrect *d*-spacings compared to the observed peaks; c) trigonal (rhombohedral) R3m unit cell, *a* = 11.806 Å, *α* = 59.676 °. Insets of Pawley fit to time-of-flight PND data with a R3m unit cell showing insufficient numbers of predicted reflections and poorly fitted peaks.

Pawley fits were undertaken testing the lowest-symmetry space group of each crystal system, and the space group R3m, identified previously by Kashida *et al.* based on single-crystal diffraction experiments.[16] The results showed that the lowest-symmetry cubic (P23), hexagonal (P6), and trigonal (P3) space groups predicted insufficient peaks compared to the observed data (Figure 7.13a for P23). Whilst the lowest-symmetry space groups for the tetragonal (P4), orthorhombic (P222), and monoclinic (P2) crystal systems all predicted reflections corresponding to the majority of the observed peaks (Figure 7.13b for P4), issues

were found when comparing the predicted reflection positions to the observed peaks at high *d*-spacing in the synchrotron XRD data set or at long time-of-flight in the PND data, with either only one peak predicted when two are observed, or the predicted peak positions being inaccurate (insets of Figure 7.13b).

For space group R3m, incorrect numbers of predicted reflections compared to the number of observed peaks were observed when using the PND data (Figure 7.13c). Whilst these data indicate that the symmetry is lower than rhombohedral, no evidence of this could be observed in the single-crystal data collected, where all of the observed Laue spots could be indexed using the rhombohedral cell. Therefore R3m was chosen as the space group to use for analysis of the single-crystal Laue neutron data, with lattice parameters a = 11.806 Å and α = 59.676 °. The rhombohedral cell is related to the 3 × 3 × 3 fluorite-like supercell (black and blue in Figure 7.14 respectively), with both cells having identical body-diagonal lengths, and the rhombohedral a cell length (a_R) equal to $3a_F/\sqrt{2}$ (where a_F is the cell length of the fluorite subcell). The rhombohedral cell volume (1157 Å^3) is approximately a quarter of that for the 3 × 3 × 3 supercell (~4584 Å ^{3}).

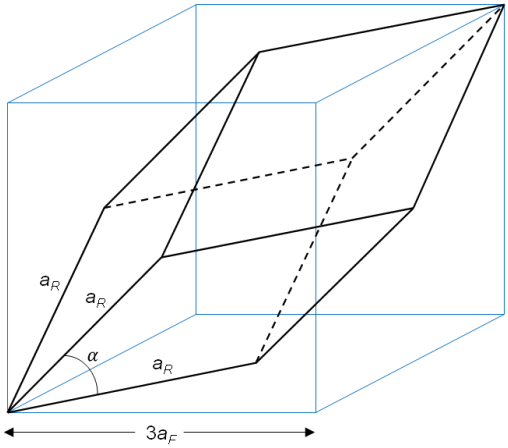

Figure 7.14: Relationship between fluorite-type 3 × 3 × 3 supercell (blue, $3a_F$ ~16.5 Å) and rhombohedral supercell (black, a_R ~11.8 Å, α ~59.7 °).

The *Laue2* program within the *LaueG* software package was used to index the observed spots in the collected patterns to the rhombohedral cell. The indexing was performed sequentially for each orientation, with all reflections from the primary crystallite predicted by the trigonal (rhombohedral) cell (Figure 7.15a). A number of unindexed spots were observed in the collected patterns, arising due to diffraction from the secondary crystallite in the fragment. Once the spots in the patterns were indexed, the *argonne boxes* and *Laue4* programs[20, 21] (other components of *LaueG*) were used to integrate and normalise the data, with the multi-wavelength peak intensities across all collected patterns corrected and merged. This is because the Laue diffraction experiment uses a white neutron beam, so reflections with identical (*hkl*) indices are observed with different wavelengths, with the intensities of these reflections needing to be normalised. Figure 7.15b shows the wavelength normalisation profile for the KOALA instrument for a typical experiment in blue ("old"), whilst the normalisation profile based on the diffraction experiment for $Bi_{0.913}V_{0.087}O_{1.587}$ is given in red ("new"). This shows that the trends of

the two normalisation scaling profiles are similar, with the profile for $Bi_{0.913}V_{0.087}O_{1.587}$ having some minor deviations from the expected profile.

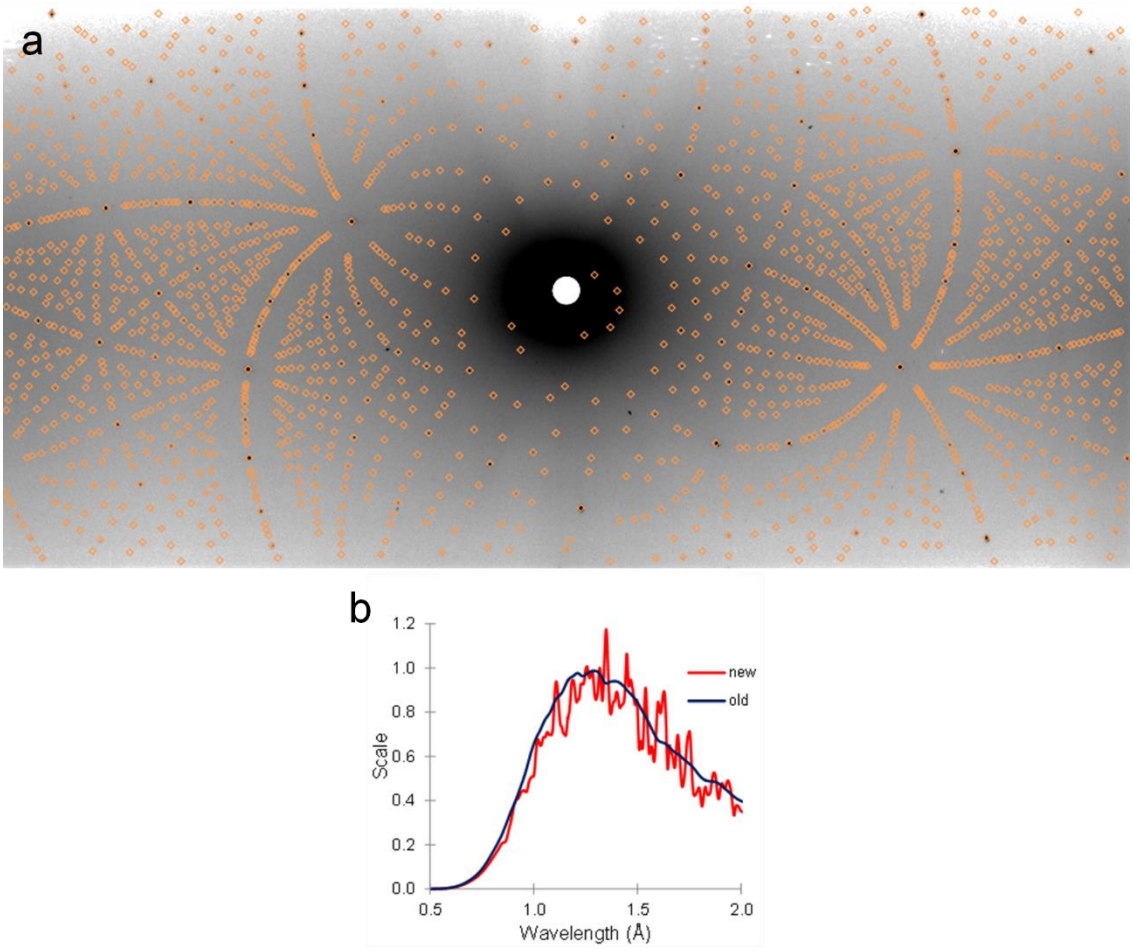

Figure 7.15: a) Indexing fragment 5 pattern, using a trigonal (rhombohedral) cell, *a* = 11.763 Å, α = 60.12 °. Observed spots are black, whilst predicted spots are shown in orange; b) Wavelength normalisation profile for fragment 5 (new) compared to that for the original KOALA wavelength profile (old).

The *SHELXS* software[22] was used to obtain the initial set of atomic coordinates for the metal sites by direct methods, before the O atoms were introduced using difference Fourier maps generated in the *ShelXle* software program (a graphical user interface version for *SHELXL*).[23] O atoms were placed onto sites of high nuclear density and the atomic coordinates refined to check if the selected site has sensible M-O and O-O bond distances and angles. After 14 fully-occupied oxygen sites had been identified, the structural formula was $Bi_{0.913}V_{0.087}O_{1.556}$, hence the remaining 0.031 oxygen atoms to generate the $Bi_{0.913}V_{0.087}O_{1.587}$ formula needed to be located. Difference Fourier maps identified a position (O15) close to the V(3)O_4 tetrahedra (V3-O15 bond length = 1.70(4) Å), resulting in the formation of a VO_5 trigonal bipyramid. Additional positions close to the other V-containing sites were also tested for oxygen content, but these were found to be unoccupied. Therefore, the O15 site occupancy was fixed to reflect the stoichiometry of the material.

Attempts to refine the atomic coordinates for the V-containing sites proved difficult, due to V having a small neutron scattering length of -0.38 fm (compared to 8.53 fm and 5.80 fm for Bi

and O respectively). This means that it is difficult to locate accurately V sites from neutron data alone. Therefore, the starting atomic coordinates for the three V-containing sites were taken from the model by Kashida *et al.*,[16] with the Bi and V content refined to attempt to obtain the correct ratio of the two metals on these sites. An overall restraint was applied to the total Bi and V content to match the stoichiometric value, with the total occupancy for the three sites each restrained to 1. It was found that the V2 and V3 sites contain Bi, whilst the V1 site only contains V. These Bi and V site occupancies were then fixed for subsequent refinements. For a more accurate analysis of the metal content across these sites and to obtain accurately the atomic coordinates for the V1 site, combined refinements using neutron and X-ray data must be carried out, as X-rays allow V to contribute more strongly to the data, due to the scattering factor scaling with atomic number.

The atomic coordinates of all Bi, O, and Bi-containing V sites (V2 and V3) were refined. To aid with the refinement, anti-bump restraints were applied to the V-O and O-O distances in the VO_x polyhedra, with minimum distances of 1.700(5) Å and 2.300(5) Å imposed for the V-O and O-O bonds respectively. Additional anti-bump restraints were applied for several O-Bi bonds in the $O10Bi_4$ and $O14Bi_4$ tetrahedra plus Bi6-O6, Bi4-O8, and Bi10-O9 (all minimum distances of 2.100(5) Å), along with the O4-O6 bond (2.300(5) Å), as these distances were found to refine initially to unrealistically short values. These restraints were kept throughout the refinements, and were all weighted equally with a WGHT *a* parameter value of 0.1.

At the beginning of the structural refinement, three atomic-displacement parameters were refined (V2 and V3 together, Bi4 to Bi10 together, and all O atoms together, with V1 fixed at U_{iso} = 0.05 Å^2) before independent refinement of the U_{iso} values was undertaken. The U_{iso} values for V2 and V3 were constrained to the same value, as the low Bi content on the V3 site made the U_{iso} refine to a non-positive definite (NPD) value if refined independently. Attempts were made to refine anisotropically the displacement parameters, but this led to unrealistic thermal ellipsoids and so isotropic displacement parameters were kept. The current R3m structural model is presented in Table 7.3 and Figure 7.16, with details of the analysis given in Table 7.2.

R-factors obtained from Laue neutron data tend to be higher than those obtained by single-crystal X-ray diffraction. This can be seen in the report by Miiller *et al.*,[24] who performed single-crystal diffraction experiments on $YCa_3(VO)_3(BO_3)_4$ and obtained R-factors of 2.97 % and 13.46 % based on analysis of X-ray and Laue neutron data respectively. Likewise, refinements using single-crystal Laue neutron data collected by Sharma *et al.* for $BiRe_2O_6$ obtained an R-factor of 7.82 %,[25] whilst Rae-Smith and Cheetham obtained an R-factor of 2.61 % based on single-crystal X-ray diffraction data.[26] Whilst this can explain partially the high R_1 value (0.2961) for the obtained $Bi_{0.913}V_{0.087}O_{1.587}$ structural model, the magnitude of this value indicates that there are some problems with the current model. Additionally, the large R_{int} value (0.1738) highlights that there are some problems with the merged intensities for equivalent reflections within the data used in the analysis, potentially due to the low intensities of the superstructure reflections.

Table 7.2: Crystallographic information for the refinement of the $Bi_{0.913}V_{0.087}O_{1.587}$ trigonal (rhombohedral) R3m structure.

Space Group	R3m
Lattice parameters	a = 11.7630(5) Å, α = 59.78 °
Volume	1145.2(2) Å^3
Crystal size	1 mm^3
Temperature	Room temperature
Range of *hkl* values	–6 ≤ *hkl* ≤ 13
Number of reflections collected	48944
Number of unique reflections	1089
Number of parameters refined	69
R_{int}	0.1738
R_1	0.2961 (522 $F_o > 4\sigma(F_o)$)
	0.3358 (all 621 data)

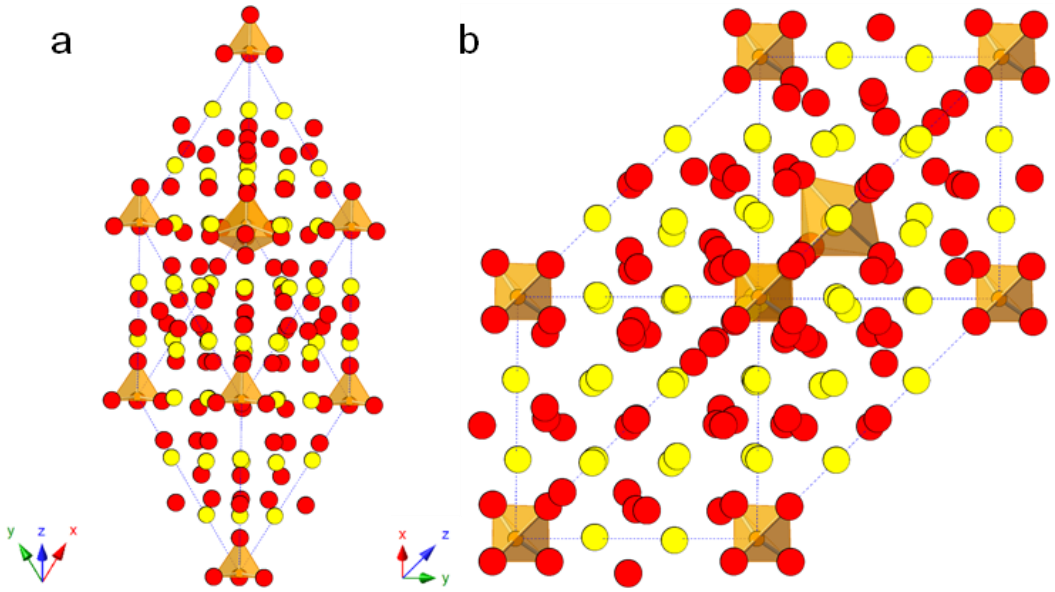

Figure 7.16: Room-temperature rhombohedral structure of $Bi_{0.913}V_{0.087}O_{1.587}$: a) viewed perpendicular to the [111] axis; b) showing the fluorite-like structure of this material. Sites Bi4 to Bi10 = yellow, V1 to V3 = orange, and all O sites are red.

Table 7.3: Current crystallographic data for rhombohedral $Bi_{0.913}V_{0.087}O_{1.587}$. Space group = R3m, a = 11.7630(5) Å, α = 59.78 °, V = 1145.2(2) Å^3.

Site	Atom	x	y	z	occ	U_{iso} (Å^2)
V1	V	0	0	0	1	0.05
V2	V	0.352(2)	0.352(2)	0.352(2)	0.48(4)	0.09(7)
Bi2	Bi	0.352(2)	0.352(2)	0.352(2)	0.52(4)	0.09(7)
V3	V	0.667(2)	0.667(2)	0.667(2)	0.87(4)	0.09(7)
Bi3	Bi	0.667(2)	0.667(2)	0.667(2)	0.13(4)	0.09(7)
Bi4	Bi	0.326(2)	0.326(2)	0.667(3)	1	0.027(6)
Bi5	Bi	0.686(4)	0.268(6)	0.686(4)	1	0.10(1)
Bi6	Bi	0.325(3)	0.003(2)	0.003(2)	1	0.007(4)
Bi7	Bi	0.662(2)	0.997(2)	0.997(2)	1	0.008(4)
Bi8	Bi	0.323(4)	–0.008(6)	0.323(4)	1	0.08(1)
Bi9	Bi	0.634(3)	0.004(5)	0.634(3)	1	0.08(1)
Bi10	Bi	0.009(2)	0.332(2)	0.657(2)	1	0.004(3)

Site	Atom	x	y	z	occ	U_{iso} (Å^2)
O1	O	0.067(6)	0.067(6)	0.067(6)	1	0.09(6)
O2	O	0.411(2)	0.411(2)	0.411(2)	1	0.04(1)
O3	O	0.607(7)	0.607(7)	0.607(7)	1	0.08(8)
O4	O	0.061(3)	0.061(3)	0.438(4)	1	0.04(8)
O5	O	0.071(6)	0.071(6)	0.834(7)	1	0.11(3)
O6	O	0.928(8)	0.928(8)	0.540(8)	1	0.12(5)
O7	O	0.452(4)	0.452(4)	0.042(6)	1	0.06(1)
O8	O	0.416(7)	0.416(7)	0.779(9)	1	0.13(4)
O9	O	0.755(7)	0.755(7)	0.420(9)	1	0.12(3)
O10	O	0.615(6)	0.615(6)	0.194(8)	1	0.11(3)
O11	O	0.231(3)	0.231(3)	0.961(6)	1	0.06(1)
O12	O	0.762(4)	0.762(4)	–0.031(6)	1	0.08(2)
O13	O	0.097(5)	0.378(6)	0.733(5)	1	0.09(1)
O14	O	0.638(7)	0.904(6)	0.212(7)	1	0.11(2)
O15	O	0.726(2)	0.726(2)	0.726(2)	0.858	0.07(3)

The $Bi_{0.913}V_{0.087}O_{1.587}$ structure (Table 7.3) can be described as a rhombohedral fluorite-type superstructure, formed of a Bi-O fluorite-type sublattice containing isolated VO_4 and VO_5 polyhedra (orange polyhedra in Figure 7.16). This model shows a number of similarities and enhancements over the literature model presented by Kashida *et al.*,[16] whilst simultaneously showing areas in which future improvements will need to be made. The literature model is based on X-ray diffraction data only and Kashida *et al.* reported difficulty in refining the positions of the oxygen atoms, as shown by large standard uncertainties associated with the O atomic coordinates. The use of neutron diffraction data has allowed for the refinement of the oxygen coordinates with errors reduced by up to an order of magnitude.

To obtain the correct Bi and V content in the structural formula, Kashida *et al.* placed Bi equally onto all three V sites instead of refining the occupancy across all sites to determine whether Bi occupies preferentially certain V sites. The refinements carried out using the neutron diffraction data shows that Bi does exhibit a preference for the V2 and V3 sites, though analysis of synchrotron single-crystal diffraction data will be required to determine accurately the site occupancies, and whether a small percentage of Bi occupies the V1 site. The literature model also shows a number of unrealistically short Bi-O bond lengths (Bi10-O14 = 1.1(3) Å and Bi9-O9 = 1.2(4) Å). Short bonds are also observed in the model derived from neutron data, with a number of restrained Bi-O and V-O bonds at the restraint values (e.g. Bi9-O10 = 2.0(1) Å, Bi6-O6 = 2.06(8) Å, and V2-O2 = 1.70(3) Å). Whilst subsequent removal of the bond-distance restraints does not result in the Bi-O bond lengths refining to shorter values, the V2-O2 bond length does decrease to 1.50(5) Å.

Finally, Kashida *et al.* were unable to identify the locations of all of the oxygen atoms, locating 14 fully-occupied oxygen sites, corresponding to a structural formula of $Bi_{0.9}V_{0.1}O_{1.556}$, and not $Bi_{0.9}V_{0.1}O_{1.6}$. The oxygen site, O15, was located successfully from Laue neutron diffraction data, but as this oxygen resides 1.70(4) Å from the V3 site, it has reached the anti-bump restraints. Removal of the V3-O15 bond-distance restraint did not cause the bond

length to refine to a shorter value, though this may change with the refinement of the atomic coordinates of the V-containing sites from combined refinements using neutron and X-ray data. The inclusion of the O15 atom into the VO_4 polyhedron forms a distorted VO_5 trigonal bipyramidal unit, with O_{eq}-V-O_{ax} bond angles of 73(5) ° and 107(5) ° for O9-V3-O3 and O9-V3-O15 respectively. This form of V-containing polyhedron is uncommon, with 5-coordinate V adopting typically a square-pyramidal geometry (e.g. V_2O_5 and $Bi_4V_2O_{10}$),[27, 28] though VO_5 trigonal bipyramids have been reported in LiV_3O_8 and $H_2V_3O_8$.[29, 30]

Diffuse streaking observed in the off-axis electron diffraction pattern (*vide supra*) implies a degree of local-scale ordering of the Bi^{3+} and V^{5+} cations disordered over the same crystallographic sites in the average structure. This could be attributed potentially to structured diffuse scattering due to the differing bonding requirements of Bi and V, with Bi preferring to have longer Bi-O bonds compared to those for V-O. This has been reported previously for $Bi_{0.9375}Nb_{0.0625}O_{1.5625}$,[31] where streaks in the electron diffraction patterns were related to differences in the pair-distribution functions for Bi-O and Nb-O from *ab initio* molecular dynamics calculations.

In the structural model presented here, the bond lengths on the V-only site V1 are 1.62(6) to 1.9(1) Å. A similar range of bond lengths, with three short and one long bond has been reported previously for $M_3V_2O_8$ (M = Co, Ni, Mg), with bond lengths ranging from 1.695(1) Å to 1.810(5) Å.[32] The bond lengths on the two mixed-occupancy Bi/V sites range from 1.69(4) to 2.97(6) Å for site V2/Bi2 and 1.70(4) to 2.37(7) Å for site V3/Bi3. The mixed Bi/V sites exhibit longer bond lengths than the V-only site by up to 1 Å, and the Bi/V site with the highest Bi concentration has the largest bond length range.

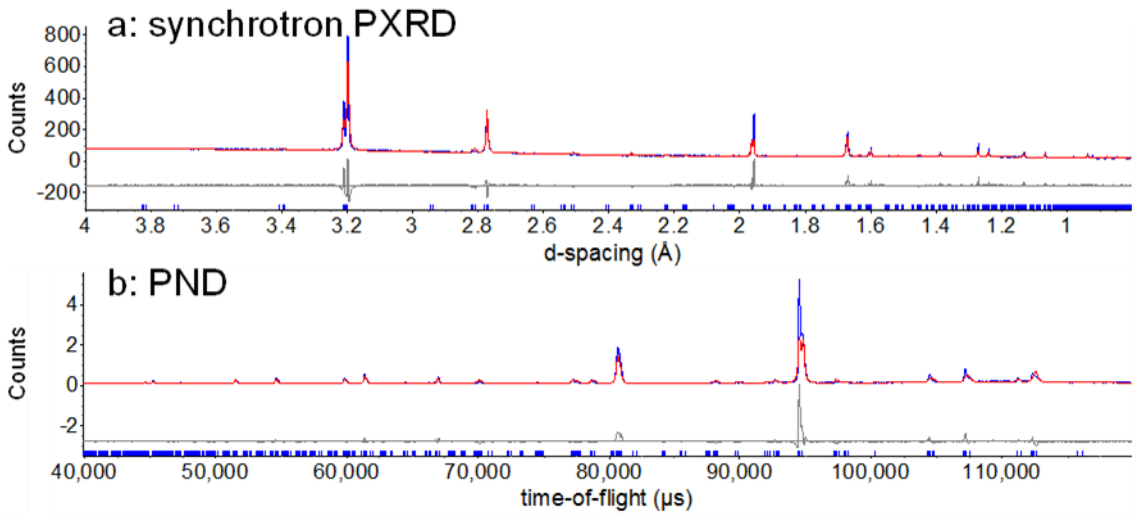

Figure 7.17: Rietveld refinements using the structural model in Table 7.3 for $Bi_{0.913}V_{0.087}O_{1.587}$ against a) synchrotron PXRD data and b) PND data, showing discrepancies between the calculated structural model and the collected data.

The poor fit to the collected data can also be shown when Rietveld refinements of this model are undertaken against PND and synchrotron PXRD data collected for $Bi_{0.913}V_{0.087}O_{1.587}$ (Figure 7.17), with discrepancies observed between the intensities of the calculated and observed peaks. In the Rietveld refinements 2 lattice parameters, 10 and 15 background

parameters (PND and synchrotron PXRD respectively), scale factors, peak-shape terms (PND), independent isotropic displacement parameters, and size-strain terms and zero-point error (synchrotron PXRD) were refined, whilst the atomic coordinates were fixed at the values given in Table 7.3. In light of these issues, the structural model presented should be treated as approximate, and a combined refinement using single-crystal neutron and X-ray diffraction data will need to be performed to attempt to obtain an accurate structural model for $Bi_{0.913}V_{0.087}O_{1.587}$, with potential pair-distribution-function analysis to investigate the differences in Bi-O and V-O bonding environments on the V-containing sites.

7.4.3 Laue diffraction of $Bi_{0.8}V_{0.2}O_{1.7}$

The as-grown crystal rod of $Bi_{0.8}V_{0.2}O_{1.7}$ (Figure 7.10) was wrapped in aluminium foil before a sample pin was affixed at both ends. This choice of mounting was due to the *z* axis translation stage on KOALA having a maximum travel distance of ± 10 mm, thereby necessitating that the sample be removed and mounted on the opposite end in order to scan the entire length of the crystal in 2 mm intervals. Data were collected at room temperature at 15 positions along the length of the crystal rod, using a 3 mm aperture and an exposure time of 5 minutes per position. Whilst some regions of the rod generated very few spots in the Laue diffraction patterns (Figure 7.18a), other regions contained large numbers of spots arising from multiple crystallites (Figure 7.18b). The patterns containing the most numbers of spots originated from collections on the central portion of the crystal rod, and so the central 15 mm of the rod were broken into smaller crystal fragments for screening.

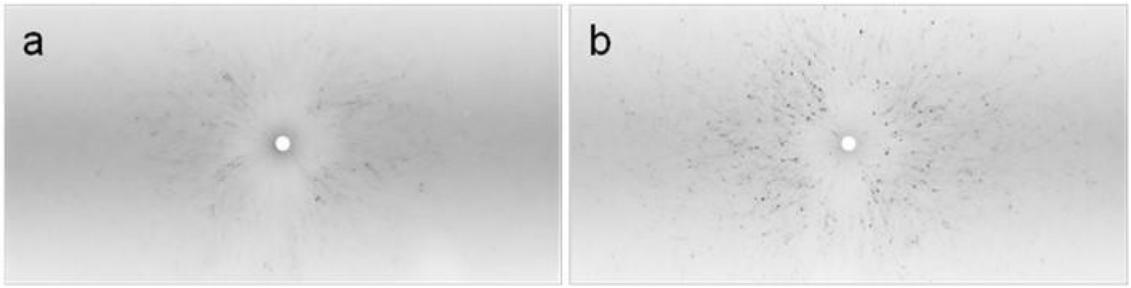

Figure 7.18: Laue patterns for $Bi_{0.8}V_{0.2}O_{1.7}$ collected from the crystal rod: a) near base of rod, BiVO_rod_pos01_2.tif; b) near centre of rod, BiVO_rod_pos13_1.

Table 7.4: Parameters for the long data collections for fragments 1 and 2 of $Bi_{0.8}V_{0.2}O_{1.7}$.

Fragment	Orientation	ϕ start (°)	ϕ end (°)	Step size (°)	Exposure time per pattern (minutes)	Number of patterns
1	1	0	180	15	60	13
2	1	0	195	15	60	14
2	2	0	195	5	60	40
2	2	0	120	60	270	3

28 crystal fragments of $Bi_{0.8}V_{0.2}O_{1.7}$ ranging in volume from 0.6 to 7.5 mm^3 were screened, using a 3mm aperture and an exposure time of 15 minutes. Of the fragments screened, the two of highest data quality (fragments 1 and 2) underwent multiple long data collections (Table 7.4). Following the first data collection from ϕ = 0 to 195 °, fragment 2 (0.84 mm^3 in size) was removed from the sample pin and mounted in a second orientation by rotating the crystal 90 °

about the incident beam direction prior to additional data collections, to obtain as complete unique data as possible.

Analysis of the Laue patterns for fragment 2 shows the presence of an additional crystallite causing additional arcs and streaked spots in the patterns. However, these spots are sufficiently separated from the arcs of Laue spots of the primary crystallite that they do not cause a problem in indexing the Laue pattern for this crystal, and so structural analysis can be performed for $Bi_{0.8}V_{0.2}O_{1.7}$ with these data sets.

7.4.4 Structural analysis of $Bi_{0.8}V_{0.2}O_{1.7}$

The structure for $Bi_{0.8}V_{0.2}O_{1.7}$ is an as-yet unidentified superstructure of the trigonal (a = 3.815(4) Å, c = 9.990(8) Å, space group = $R\bar{3}m$) subcell reported by Wrobel *et al*.[19] Initially, the subcell lattice parameters were used to index the patterns from the long data collections on $Bi_{0.8}V_{0.2}O_{1.7}$ fragment 2, and the predicted positions of the spots overlap with some of those observed. Figure 7.19a shows predicted spots for the $Bi_{0.8}V_{0.2}O_{1.7}$ subcell in orange, which, whilst predicting correctly a number of the observed spots, a large number of observed spots (black spots) are unpredicted, meaning that the choice of unit cell is incorrect.

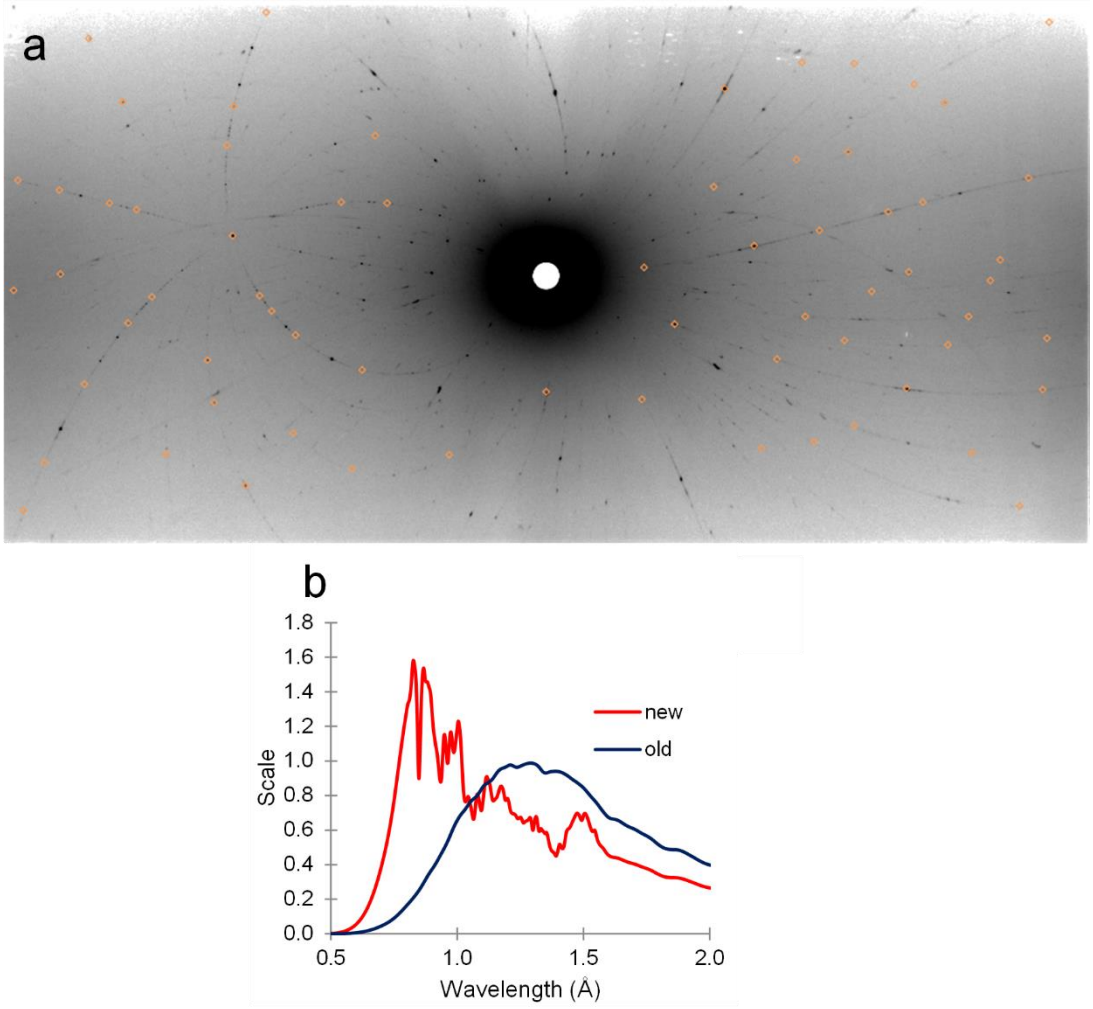

Figure 7.19: a) Indexing to Bi8V2O17_frag02_10.tif using the trigonal (hexagonal) subcell, a = 3.823 Å, c = 9.980 Å. Orange squares correspond to predicted spots. b) Wavelength normalisation profile where 'old' = KOALA normalisation profile, 'new' = normalisation profile based on the data collected for $Bi_{0.8}V_{0.2}O_{1.7}$, using wavelength cut-offs of 0.8 and 2.0 Å.

The indexed data were integrated, but attempts to normalise the wavelength resulted in an unexpected peak in the wavelength profile between 0.8 and 1.0 Å (new, Figure 7.19b), far in excess of that expected for the KOALA instrument (old, Figure 7.19b). This means that the normalisation profile is scaling the intensities of the spots observed between 0.8 and 1.0 Å to considerably higher values than would be expected for the instrument, whilst it is scaling down the intensities between 1.0 and 2.0 Å. This unexpected scaling is thought to arise from the small number of predicted subcell reflections compared to the number of observed reflections preventing accurate normalisation of the relative intensities of the spots across the Laue diffraction patterns.

Following this, an attempt was made to index the supercell, which would improve the normalisation of the wavelength profile. To achieve this, indexing attempts were performed for the 16 different lattice parameter combinations from $a = a_s$ and $c = c_s$ to $a = 4a_s$ and $c = 4c_s$ (a_s and c_s are the subcell lattice parameters) in integer steps for both R-centered and P-centered trigonal (hexagonal) supercells. Of these 32 different indexing attempts, none were found to match the data exactly, with a number of spots remaining unindexed. In light of this, further work on a better sample will need to be undertaken in the future to identify the correct supercell for $Bi_{0.8}V_{0.2}O_{1.7}$ and characterise the structural model.

7.5 Single-crystal growth of $Bi_{38}Mo_7O_{78}$

Using PND and synchrotron PXRD data, a distortion-mode analysis was attempted for the monoclinic P1c1 phase of $Bi_{38}Mo_7O_{78}$, but was unable to obtain a complete structural model (*vide supra*, Chapter 7). Therefore, the use of Laue neutron diffraction may aid with the structural characterisation of this material. FZF crystal growth of bismuth molybdates has been reported previously for $Bi_{38}Mo_7O_{78}$ only,[12] though only synchrotron single-crystal XRD data were collected on a very small crystal, ~1.25×10^{-7} mm^3 in size.

A 30 g powdered sample of $Bi_{38}Mo_7O_{78}$ was prepared for FZF crystal growth. 26.9346 g (57.78 mmol) of Bi_2O_3 and 3.0654 g (21.30 mmol) of MoO_3 were ground together in a planetary ball mill for 12 hours, then fired in an alumina crucible at 840 °C for 12 hours, yielding a pale-yellow powder. This powder was then portioned equally into two balloons, and the cylindrical feed and seed rods pressed with 40 MPa of pressure using a hydrostatic press. The rods were sintered at 840 °C for 6 hours then mounted into a FZF equipped with 4 × 300 W lamps.

The lamp power of the FZF was ramped initially from 0 to 30 % power in 0.3 hours, with the rods counter-rotated at 24.2 rpm (feed rod) and 24.9 rpm (seed rod). This is in accordance with the crystal growth carried out by Sharma *et al.* on the same composition, who reported that the rods melted between 32 and 35 % lamp power using 300 W lamps and a rod rotation speed of 10 to 30 rpm.[12] Following the initial programmed ramp, the lamp power was increased manually up to 50 % power, with no indication of the rods beginning to melt. The reason for the rods not melting in the power range reported could be due to multiple factors: age of the lamps causing reduced light output at identical power settings; particulate build-up on the surface of the FZF

mirrors resulting in reduced reflectivity and poorer focussing of the lamp light; inaccurate alignment of the lamps causing reduced focussing of the light onto the hot zone.

Following the manual increase to 50 % power, the FZF was programmed to ramp from 50 to 65 % power in 0.3 hours. During this time, the colour of the rods darkened, indicating that the material was close to melting (Figure 7.20a and Figure 7.20b), before melting at 60.1 % power (Figure 7.20c). The programmed ramp was paused once the rod started to melt, and the furnace power decreased quickly. This is because the molten material is much darker in colour than the solid material (as for the bismuth vanadates grown), meaning the melt can absorb heat more efficiently, thereby requiring a lower power setting to maintain a stable molten zone. Unfortunately, the rate of the lamp power decreasing was too slow, causing the molten tip of the feed rod to elongate and contact the seed rod (Figure 7.21a), before reduced surface tension resulted in elongation at the base of the molten zone (Figure 7.21b) and zone collapse at 59.4 % power (Figure 7.21c).

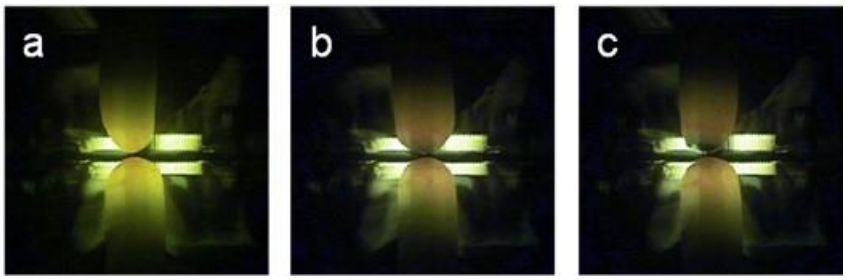

Figure 7.20: a) and b) $Bi_{38}Mo_7O_{78}$ rod tips darkening prior to reaching melting point; c) initial melting of feed-rod tip at 60.1 % lamp power.

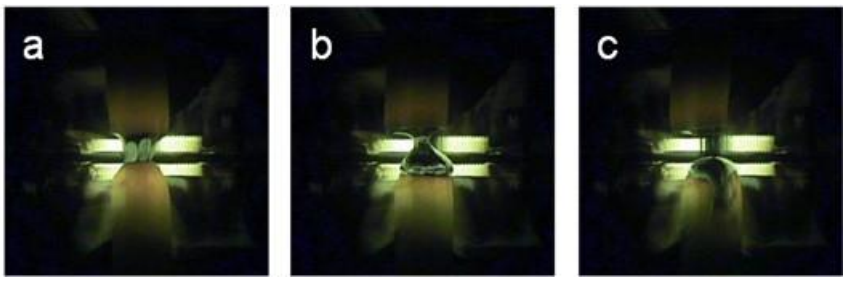

Figure 7.21: a) Initial contact of molten feed-rod tip with unmelted surface of seed rod; b) reduced surface tension of the molten zone causing widening of the base of the molten zone, leading to; c) collapse of the molten zone due to increased thermal absorption of melt.

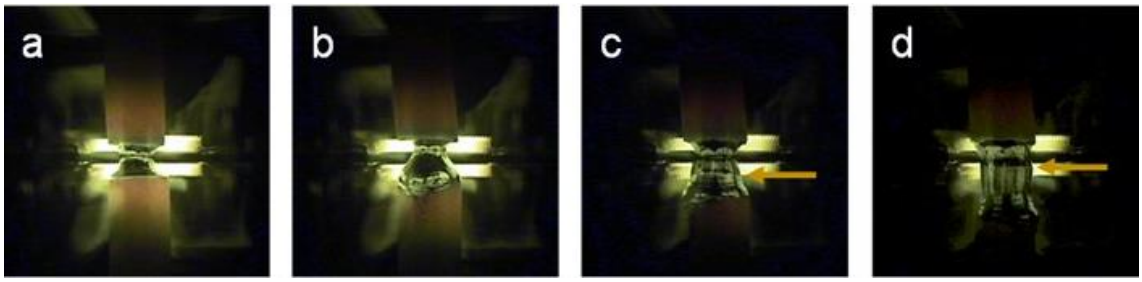

Figure 7.22: a) Initial formation of first stable molten zone at 40.9 % power; b) widening of the base of molten zone due to temperature being too high; c) and d) boundary of molten zone translates upwards vertically through the hot zone due to power of lamps set too low.

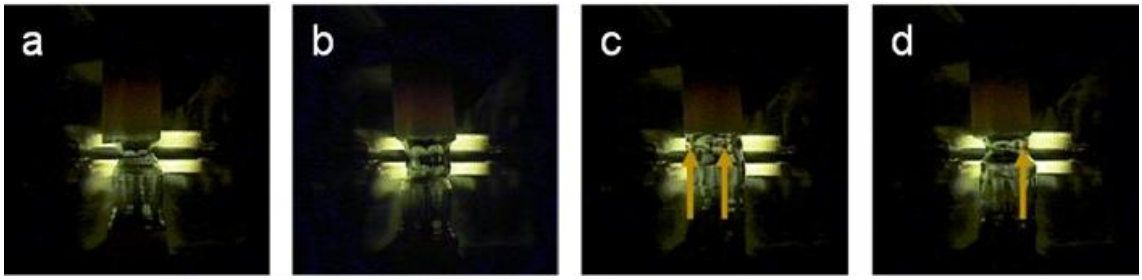

Figure 7.23: a) Formation of second stable molten zone at 40.3 % power; b) both feed and seed rods translated vertically down to increase size of molten zone without melting crystal grown during first stable zone; c) and d) bubbles observed in molten zone (marked with orange arrows) leading to the size of molten zone decreasing.

The power to the lamps was decreased further to 40.9 % power, during which time several drops of molten material fell from the tip of the feed rod onto the seed rod. At 40.9 % power, the tips of the two rods were joined (Figure 7.22a), and the power decreased to 39.8 % to prevent the observed widening of the molten zone base (Figure 7.22b) leading to a zone collapse. This molten zone remained stable, and so the rods were programmed to translate downwards vertically through the hot zone at a rate of 3 mm per hour. Over the next 90 minutes the molten zone decreased gradually in size, as seen by the upward migration of the molten-zone boundary through the hot zone (Figure 7.22c and Figure 7.22d) prior to collapse.

The lamp power was increased to 40.3 % to reform the molten zone and join the tips of the rods (Figure 7.23a). Once the second stable molten zone was formed, both the feed and seed rods were translated manually downwards, to increase the size of the molten zone without melting any of the crystal grown previously (Figure 7.23b). This zone remained stable for ~6 hours, at which time bubbles were observed within the melt which over 30 minutes caused the size of the molten zone to decrease (Figure 7.23c and Figure 7.23d). Therefore, the growth experiment was halted, as attempts to remove the bubbles from the molten zone manually could cause molten material to flow down the already grown crystal and damage it, whilst leaving the bubbles in would cool the molten zone and lead to zone collapse, either through the zone freezing or the bubbles bursting. The lamp power profile for the $Bi_{38}Mo_7O_{78}$ crystal growth experiment is given in Figure 7.24, with power levels for zone melting and zone collapse given in red and blue respectively, whilst periods of zone stability are denoted by black points and lines. Unlike for the crystal growths for the bismuth vanadate materials, the power settings did not have to be changed numerous times to maintain a stable molten zone.

When removing the seed rod and grown crystal from the FZF cavity, the crystal rod sheared into two pieces where the first stable molten zone collapsed (marked in Figure 7.25a). The small piece of crystal attached to the seed rod was removed with a diamond wheel saw, giving two pieces of crystalline material, 6 and 23 mm in length (Figure 7.25b). Of note, the final 2 to 3 mm of crystal growth are an orange colour compared to the pale yellow of the rest of the grown rods. This difference in colour is attributed to the faster cooling rate applied to that section of the molten zone whilst the furnace was ramped down, compared to the slow cooling rate applied to the rest of the crystal rod.

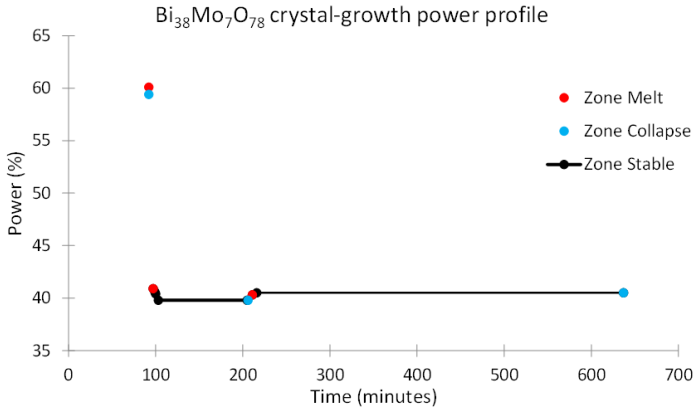

Figure 7.24: The range of power levels required for the feed and seed rod to melt, the molten zone to collapse, or the molten zone to be stable during the crystal growth of $Bi_{38}Mo_7O_{78}$.

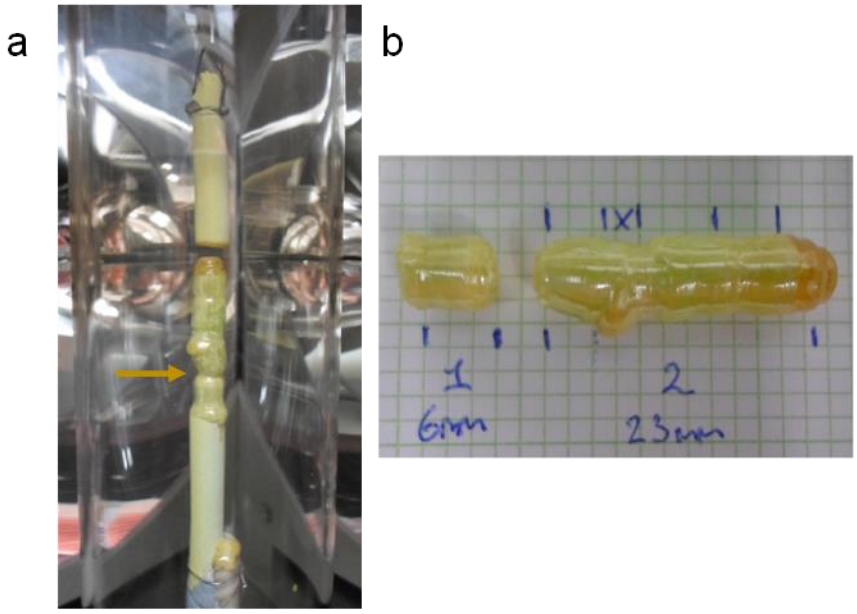

Figure 7.25: a) $Bi_{38}Mo_7O_{78}$ crystal rod mounted in the FZF cavity. The arrow marks the point where the first stable zone collapsed. b) Crystalline pieces of the $Bi_{38}Mo_7O_{78}$ rod. The grown crystal broke along the line of the first zone collapse.

7.5.1 Room-temperature single-crystal analysis of $Bi_{38}Mo_7O_{78}$

Single-crystal Laue diffraction data were collected on the KOALA Laue diffractometer at OPAL, ANSTO, with a 3 mm aperture placed in the incident neutron beam 49 cm before the sample for the duration of the data collections. The two pieces of crystal rod grown in the FZF (Figure 7.25b) were wrapped in aluminium foil and affixed vertically to sample pins so their entire lengths could be scanned, to locate regions within the rod which are single crystals. 8 positions along the 23 mm crystal rod were scanned in 2 mm steps at ϕ = 0 and 90 °, for a total of 16 patterns collected with 30 minutes per pattern. For the 6 mm rod, 5 positions were scanned in 2 mm steps at one phi angle, for 30 minutes per pattern.

Following the data collections, it was found that the rods were comprised of a number of crystallites, with Laue spots from multiple crystallites in close proximity to one another. Therefore, the rods were broken into smaller fragments and screened individually to try to locate a single crystal fragment which could be used for data collection at multiple ϕ angles.

16 fragments were screened, with exposure times ranging from 5 to 25 minutes. The fragment which produced the cleanest pattern (fragment 1), was cleaved three times with intermediate data collections to attempt to isolate a single crystal. The final attempt (fragment 4, frag04), produced a Laue diffraction pattern with the least additional spots of the screened fragments and so underwent long data collections, the details of which are given in Table 7.5. Orientations 1 and 2 differ in that the fragment is removed from the sample pin and rotated 90 ° with respect to the incident beam direction before being remounted in the second orientation for subsequent data collections.

Table 7.5: Details of long data collections on the KOALA Laue diffractometer for $Bi_{38}Mo_7O_{78}$ crystal fragment 4.

Fragment	Orientation	ϕ start (°)	ϕ end (°)	Step size (°)	Exposure time per pattern (minutes)	Number of patterns
4	1	0	180	15	60	13
4	2	0	180	15	60	13
4	2	7.5	172.5	15	60	12

Despite the arcs of Laue spots originating from the primary crystallite being visible clearly and well distinguished in the collected patterns, there are multiple arcs of Laue spots observed along a number of the arc directions, indicating clear evidence of a second crystallite in the fragment (Figure 7.26). This will need to be taken into account during the indexing and integration process, which is the subject of future work and will need to be undertaken prior to refinement of the monoclinic crystal structure for $Bi_{38}Mo_7O_{78}$.

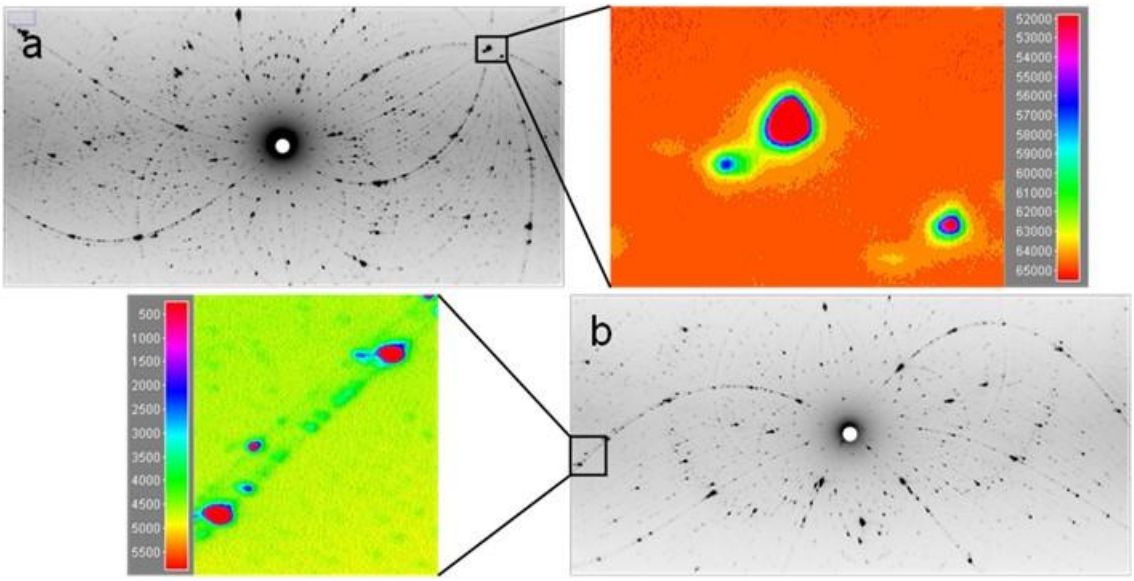

Figure 7.26: Room-temperature Laue diffraction patterns collected for $Bi_{38}Mo_7O_{78}$: a) ϕ = 150 °, Bi38Mo7O78_frag4_o1_11.tif; b) ϕ = 0 °, Bi38Mo7O78_frag4_o1_1.tif. The insets show the evidence of spots from multiple crystallites in close proximity.

7.6 Single-crystal growth of apatite-type materials: $Bi_2La_8[(GeO_4)_6]O_3$ and $La_{9.5}[(GeO_4)_{5.5}(AlO_4)_{0.5}]O_2$

Crystal growth with a FZF has been reported in the literature for a number of apatites, though exclusively for silicate apatites. The majority of these silicate apatites grown have Nd,

Pr, or Sm on the large A-cation sites,[33-37] with only one example reported of a lanthanum silicate apatite growth attempt.[38] This crystal growth of $La_{9.33}[(SiO_4)_6]O_2$ was reported as problematic, as the white material absorbs heat poorly, resulting in a polycrystalline rod being grown. The use of germanium in FZF crystal growth attempts is rare, due to the volatility of GeO_2 above 1250 °C.[39] Growth of crystalline rods of $GeNi_2O_4$ and $GeCo_2O_4$ is reported, though these were comprised of multiple crystallites.[40] To minimise the loss of Ge from the melt due to volatilisation, fast translation speeds (30 to 40 mm/hr) and additional Ge in the starting feed rod (1.65-1.75:2 for Ge:Ni and 1.05:2 for Ge:Co instead of 1:2 in both cases) had to be used. Single crystals were grown of the sillenite-type $Bi_{12}GeO_{20}$ material by the FZF method, though this was due to the low melting point of the material,[41] below the volatilisation temperature of Ge.

Section 4.2 reports the synthesis of the $Bi_2La_8[(GeO_4)_6]O_3$ and $La_{9.5}[(GeO_4)_{5.5}(AlO_4)_{0.5}]O_2$ materials by solid-state synthesis. FZF crystal growths for crystals of these two compositions for Laue neutron diffraction experiments were attempted, which would allow for improvements in the existing structural models.

For $Bi_2La_8[(GeO_4)_6]O_3$, 4.86 g of Bi_2O_3 (10.43 mmol, Sigma-Aldrich, 99.9 %), 13.5930 g of La_2O_3 (41.72 mmol, Sigma-Aldrich, 99.9 %, precalcined at 1000 °C for 2 hours), and 6.5466 g of GeO_2 (62.58 mmol, Sigma-Aldrich, 99.99 %) were ground together in a mortar using a pestle and fired for 30 hours at 1050 °C, with intermediate grindings and heating and cooling rates of 5 °C per minute. For $La_{9.5}[(GeO_4)_{5.5}(AlO_4)_{0.5}]O_2$, 21.6086 g of La_2O_3 (66.32 mmol, Sigma-Aldrich, 99.9 %, precalcined at 1000 °C for 2 hours), 1.6071 g of GeO_2 (76.79 mmol, Sigma-Aldrich, 99.99 %), and 0.3559 g of Al_2O_3 (3.49 mmol, Sigma-Aldrich, 99.0 %) were ground together and fired at 1100 °C for 6 hours, then at 1250 °C for 12 hours, with intermediate grindings and heating and cooling rates of 10 °C per minute. For each sample, the powders were divided into two roughly equal batches and pressed in a hydrostatic press with a pressure of 40 MPa, which were fired at 1050 °C for 15 hours ($Bi_2La_8[(GeO_4)_6]O_3$) and 1250 °C for 12 hours ($La_{9.5}[(GeO_4)_{5.5}(AlO_4)_{0.5}]O_2$).

Due to the unknown melting points of both of these materials in addition to the white colour of the sintered rods, the crystal growths were attempted using 4 × 1500 W lamps. The growth of $Bi_2La_8[(GeO_4)_6]O_3$ crystals was unsuccessful, as heating the rods lead to sublimation of material from the tip of the feed and seed rods instead of formation of a molten zone. This resulted in a build-up of powder on the inner wall of the quartz tube used to contain the rods. Following the crystal-growth attempt, the tip of the feed rod and the deposit on the quartz tube were analysed by Rietveld refinements using laboratory PXRD data, to identify the phases which evolved from the rod during the heating process. Analysis of the feed rod material showed the presence of a small percentage (~7 %) of the $La_2Ge_2O_7$ impurity phase (Figure 7.27a), whilst the FZF deposit was comprised of a mixture of the Bi_2GeO_5 and cubic δ-Bi_2O_3 phases (Figure 7.27b).

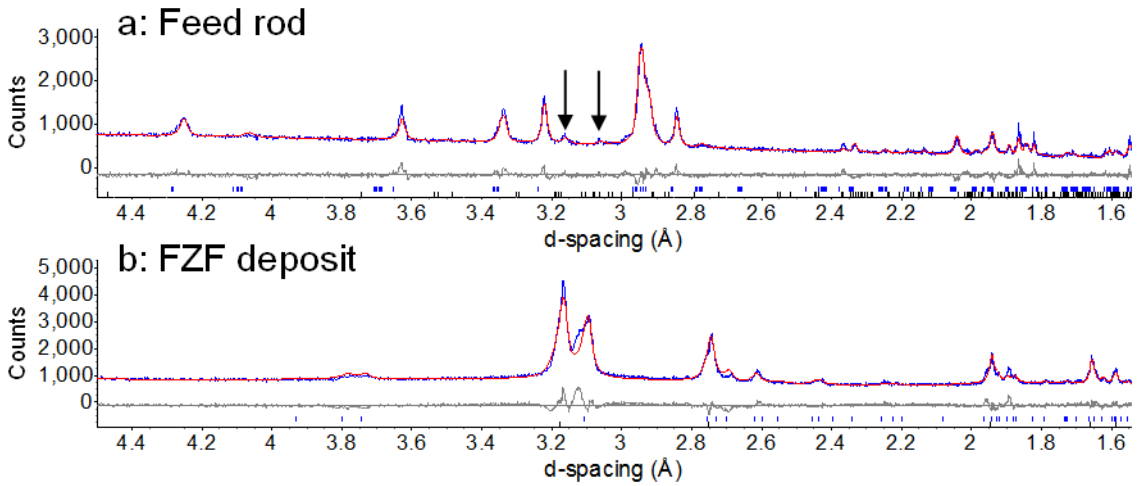

Figure 7.27: a) Rietveld refinement for material from tip of feed rod following FZF crystal growth, showing peaks from the $La_2Ge_2O_7$ impurity phase (black arrows). b) Rietveld refinement for material collected from the walls of the quartz tube surrounding the feed and seed rod, with peaks from the Bi_2GeO_5 and δ-Bi_2O_3 phases.

As the $La_{9.5}[(GeO_4)_{5.5}(AlO_4)_{0.5}]O_2$ rods are also white, the tip of the feed rod was darkened with a pencil to try and improve the heat absorption properties of the rod (as for the third growth of $Bi_{0.8}V_{0.2}O_{1.7}$), meaning that it would melt at a lower lamp power than that for $Bi_2La_8[(GeO_4)_6]O_3$, and avoid potentially temperatures which cause volatilisation. This was unsuccessful, with the melting point remaining above the volatilisation temperature and sublimation of the rods observed. Therefore, further crystal-growth attempts for the germanium-containing apatite-type materials should not be attempted unless the melting temperature of the material is below the Ge volatilisation temperature.

7.7 Conclusions

Two large crystal growths were carried out for the $Bi_{1-x}V_xO_{1.5+x}$ (x = 0.087, 0.2) compositions in an attempt to grow single crystals for use in Laue neutron diffraction. Whilst crystals were grown, analysis of the rods showed evidence of multiple crystals. When broken apart, additional reflections were observed in the collected Laue patterns for the fragments screened, indicating that the crystals obtained were not single crystals.

The molten bismuth vanadate material is significantly darker than the solid powder phase. This means that an initial high lamp power is required to start melting the sintered rods, before they darken in colour and the power needs to be reduced significantly and on a short time scale to prevent loss of molten material. The crystal growth process for $Bi_{0.913}V_{0.087}O_{1.587}$ was carried out in one attempt, but multiple attempts were required for $Bi_{0.8}V_{0.2}O_{1.7}$ due to difficulties in maintaining a stable molten zone without collapsing the zone.

Analysis of the x = 0.087 Laue diffraction data revealed a fluorite-based rhombohedral superstructure (a ~ 11.7630(5) Å, α = 59.78 °, space group = R3m), whilst a range of trigonal supercells were tested to attempt to identify the supercell for the x = 0.2 composition. Work on the analysis of the diffraction data will continue into the future, with a combined refinement of neutron and synchrotron X-ray single crystal data required to refine atomic coordinates and

displacement parameters for the V-containing sites in $Bi_{0.913}V_{0.087}O_{1.587}$. The lattice parameters and symmetry of the $Bi_{0.8}V_{0.2}O_{1.7}$ supercell will need to be identified before a complete structural model can be refined.

Crystal growth attempts of $Bi_{38}Mo_7O_{78}$ were successful, with Laue neutron diffraction data collected, though this will need to be analysed in more detail in future to aid with the refinement of the monoclinic room-temperature crystal structure.

Attempts at crystal growth for lanthanum germanium apatite-type materials were unsuccessful, with volatilisation of Bi and Ge at elevated temperatures instead of molten zone formation.

7.8 References

1. W. G. Pfann, *Transactions of the American Institute of Mining and Metallurgical Engineers*, 1952, **194**, 747-753.
2. H. C. Theuerer, *United States Pat.,* 3060123, 1962.
3. S. Hayashi and H. Komatsu, *Kristall und Technik*, 1979, **14**, 761-764.
4. J. E. Auckett, A. J. Studer and C. D. Ling, *Australian Journal of Chemistry*, 2014, **67**, 1824-1828.
5. S. Kimura and I. Shindo, *Journal of Crystal Growth*, 1977, **41**, 192-198.
6. P. W. Bridgman, *Proceedings of the American Academy of Arts and Sciences*, 1925, **60**, 305-383.
7. J. Czochralski, *Zeitschrift für Physikalische Chemie*, 1918, **92**, 219-221.
8. H. A. Dabkowska and B. D. Gaulin, in *International School on Crystal growth of technologically important electronic materials*, eds. K. Bryrappa, T. Ohachi, H. Klapper and R. Fornari, Allied Publishers Pvt. Ltd., 2003, pp. 341-354.
9. S. M. Koohpayeh, D. Fort and J. S. Abell, *Progress in Crystal Growth and Characterization of Materials*, 2008, **54**, 121-137.
10. C. D. Ling, S. Schmid, P. E. R. Blanchard, V. Petricek, G. J. McIntyre, N. Sharma, A. Maljuk, A. A. Yaremchenko, V. V. Kharton, M. Gutmann and R. L. Withers, *Journal of the American Chemical Society*, 2013, **135**, 6477-6484.
11. A. J. E. Rettie, H. C. Lee, L. G. Marshall, J.-F. Lin, C. Capan, J. Lindemuth, J. S. McCloy, J. Zhou, A. J. Bard and C. B. Mullins, *Journal of the American Chemical Society*, 2013, **135**, 11389-11396.
12. N. Sharma, R. B. Macquart, M. Christensen, M. Avdeev, Y.-S. Chen and C. D. Ling, *Journal of Solid State Chemistry*, 2009, **182**, 1312-1318.
13. T. Takahashi, H. Iwahara and T. Esaka, *Journal of the Electrochemical Society*, 1977, **124**, 1563-1569.
14. X. Kuang, J. L. Payne, M. R. Johnson and I. R. Evans, *Angewandte Chemie-International Edition*, 2012, **51**, 690-694.
15. W. Zhou, *Journal of Solid State Chemistry*, 1988, **76**, 290-300.
16. S. Kashida, T. Hori and K. Nakamura, *Journal of the Physical Society of Japan*, 1994, **63**, 4422-4426.
17. V. V. Kharton, F. M. B. Marques and A. Atkinson, *Solid State Ionics*, 2004, **174**, 135-149.
18. M. Benkaddour, S. Obbade, P. Conflant and M. Drache, *Journal of Solid State Chemistry*, 2002, **163**, 300-307.

19. W. Wrobel, F. Krok, I. Abrahams, A. Kozanecka-Szmigiel, M. Malys, S. C. M. Chan and J. R. Dygas, *Materials Science-Poland*, 2006, **24**, 23-30.

20. R. Piltz, *Acta Crystallographica Section A*, 2011, **67**, C155.

21. C. Wilkinson, H. W. Khamis, R. F. D. Stansfield and G. J. McIntyre, *Journal of Applied Crystallography*, 1988, **21**, 471-478.

22. G. Sheldrick, *Acta Crystallographica Section A*, 2008, **64**, 112-122.

23. C. B. Hübschle, G. M. Sheldrick and B. Dittrich, *Journal of Applied Crystallography*, 2011, **44**, 1281-1284.

24. W. Miiller, M. Christensen, A. Khan, N. Sharma, R. B. Macquart, M. Avdeev, G. J. McIntyre, R. O. Piltz and C. D. Ling, *Chemistry of Materials*, 2011, **23**, 1315-1322.

25. N. Sharma, T. Söhnel, G. J. McIntyre, R. Piltz and C. D. Ling, *Journal of Physics: Conference Series*, 2010, **251**, 012028.

26. A. R. Rae-Smith and A. K. Cheetham, *Journal of Solid State Chemistry*, 1979, **30**, 345-352.

27. R. Enjalbert and J. Galy, *Acta Crystallographica Section C*, 1986, **42**, 1467-1469.

28. S. Sorokina, R. Enjalbert, P. Baules, A. Castro and J. Galy, *Journal of Solid State Chemistry*, 1996, **125**, 54-62.

29. L. A. de Picciotto, K. T. Adendorff, D. C. Liles and M. M. Thackeray, *Solid State Ionics*, 1993, **62**, 297-307.

30. Y. Mettan, R. Caputo and T. Chatterji, *RSC Advances*, 2015, **5**, 106543-106550.

31. M. L. Tate, J. Hack, X. Kuang, G. J. McIntyre, R. L. Withers, M. R. Johnson and I. Radosavljevic Evans, *Journal of Solid State Chemistry*, 2015, **225**, 383-390.

32. E. E. Sauerbrei, R. Faggiani and C. Calvo, *Acta Crystallographica Section B*, 1973, **29**, 2304-2306.

33. M. Higuchi, K. Kodaira and S. Nakayama, *Journal of Crystal Growth*, 1999, **207**, 298-302.

34. S. Nakayama, M. Sakamoto, M. Higuchi, K. Kodaira, M. Sato, S. Kakita, T. Suzuki and K. Itoh, *Journal of the European Ceramic Society*, 1999, **19**, 507-510.

35. T. An, T. Baikie, F. Wei, H. Li, F. Brink, J. Wei, S. L. Ngoh, T. J. White and C. Kloc, *Journal of Crystal Growth*, 2011, **333**, 70-73.

36. T. An, A. Orera, T. Baikie, J. S. Herrin, R. O. Piltz, P. R. Slater, T. J. White and M. L. Sanjuán, *Inorganic Chemistry*, 2014, **53**, 9416-9423.

37. M. Higuchi, H. Katase, K. Kodaira and S. Nakayama, *Journal of Crystal Growth*, 2000, **218**, 282-286.

38. H. Okudera, Y. Masubuchi, S. Kikkawa and A. Yoshiasa, *Solid State Ionics*, 2005, **176**, 1473-1478.

39. E. J. Abram, C. A. Kirk, D. C. Sinclair and A. R. West, *Solid State Ionics*, 2005, **176**, 1941-1947.

40. S. Hara, Y. Yoshida, S.-I. Ikeda, N. Shirakawa, M. K. Crawford, K. Takase, Y. Takano and K. Sekizawa, *Journal of Crystal Growth*, 2005, **283**, 185-192.

41. D. H. H. Quon, S. Chehab, J. Aota, A. K. Kuriakose, S. S. B. Wang, M. Z. Saghir and H. L. Chen, *Journal of Crystal Growth*, 1993, **134**, 266-274.

8 Synthesis, characterisation, and properties of the $La_xSr_{10-x}Ga_6O_{19+x/2}$ family (x = 0, 0.2, and 0.4)

8.1 Background

Within the melilite family of compounds, $La_{1+x}Sr_{1-x}Ga_3O_{7+x/2}$ ($0 \leq x \leq 0.64$), it has been reported that interstitial oxide ions are introduced into the structure, thereby increasing the oxide-ion conductivities.[1] Kuang *et al.* report that $La_{1.54}Sr_{0.46}Ga_3O_{7.27}$ exhibits a conductivity increase of 4 orders of magnitude relative to $LaSrGa_3O_7$ at 800 °C (σ ~7 × 10^{-2} Scm^{-1} and 8 × 10^{-6} Scm^{-1} respectively).[2] The inclusion of interstitial oxide ions enables the formation of GaO_5 polyhedra through incorporation of an interstitial oxygen atom into some existing GaO_4 tetrahedra. As these features of variable coordination cations and inclusion of interstitial oxide ions lead to significant increase in oxide ion conductivities for the melilite family, novel strontium gallate compositions are investigated to determine if high conductivity levels can be attained in similar systems.

The parent compound of the $La_xSr_{10-x}Ga_6O_{19+x/2}$ family, $Sr_{10}Ga_6O_{19}$, was first reported by Kahlenberg in 2001.[3] This room-temperature monoclinic structure of α-$Sr_{10}Ga_6O_{19}$ (space group C2/c) contains unbranched puckered chains of six corner-sharing GaO_4 tetrahedra (inset, Figure 8.1) running approximately parallel to the (20-1) plane, with Sr^{2+} cations located amongst the GaO_4 tetrahedra and in planes parallel to (100) at $x = \frac{1}{8}, \frac{1}{4}, \frac{3}{8}$, etc. (Figure 8.1).

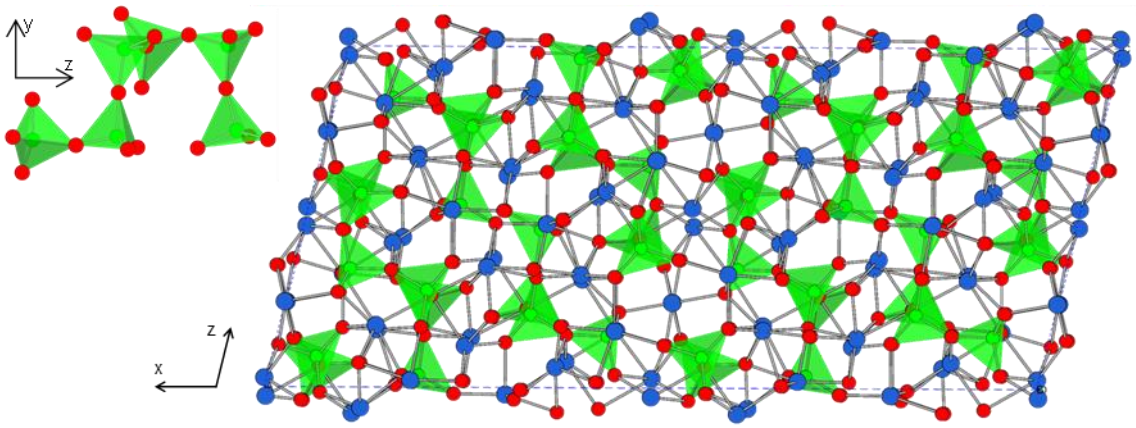

Figure 8.1: Room-temperature structure of α-$Sr_{10}Ga_6O_{19}$ viewed along the *y* axis showing the chains of GaO_4 tetrahedra; Sr = blue, Ga = green, O = red, unit cell = dashed blue line. The inset shows an unbranched chain of six corner-sharing GaO_4 tetrahedra when viewed down the *x* axis.

The GaO_4 tetrahedra in α-$Sr_{10}Ga_6O_{19}$ are distorted, with O-Ga-O bond angles ranging from 99.7 to 130.2 °, and the Ga-O bond lengths ranging from 1.78 to 1.90 Å, a similar distribution to that reported for other strontium gallates ($SrGa_4O_7$ and $Sr_3Ga_2O_6$).[3, 4] The Sr-O bond lengths range from 2.34 to 3.35 Å, with the SrO_x polyhedra defined as distorted octahedra (Sr3 and Sr5) or irregular 7- or 8-coordinate polyhedra, where the Sr in the octahedral coordination polyhedra show evidence of overbonding (bond-valence values greater than 2) whilst the other strontium atoms underbond (bond-valence-sum values = 1.25 to 1.90 valence units).

The GaO_4 tetrahedra in the chain contain one or two bridging oxygen atoms (depending if the polyhedron in question is at the end of the polyhedra chain or not), meaning that the tetrahedra possess the potential to incorporate interstitial oxygen atoms, forming GaO_5 polyhedra through the repositioning of non-bridging oxygen atoms and inclusion of an interstitial oxygen atom. The high Sr content in the parent compound should allow for a wide lanthanum dopant range, with compositions from $Sr_{10}Ga_6O_{19}$ (x = 0) to $La_{10}Ge_6O_{24}$ (x = 10) accessible potentially.

Krueger *et al.* reported the presence of additional satellite peaks in single-crystal X-ray diffraction data collected on $Sr_{10}Ga_6O_{19}$, in addition to the peaks arising from the α-$Sr_{10}Ga_6O_{19}$ structure reported previously by Kahlenberg. They described $Sr_{10}Ga_6O_{19}$ at room temperature as an incommensurately modulated monoclinic structure (modulation wave located along the *y* axis) which undergoes a phase transition before transforming into the unmodulated monoclinic structure (α-$Sr_{10}Ga_6O_{19}$) on heating at 400 °C (Figure 8.2).[5]

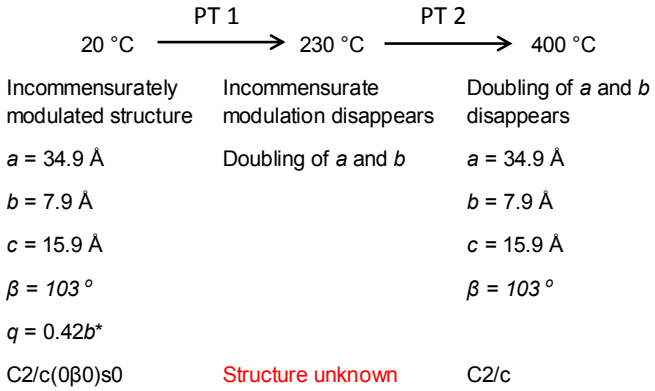

Figure 8.2: Details of the phase transitions (PT) reported on heating for the incommensurately modulated structure of $Sr_{10}Ga_6O_{19}$ reported by Krueger *et al.*[5]

In addition, Kahlenberg identified an orthorhombic room temperature form, β-$Sr_{10}Ga_6O_{19}$ (a = 34.3 Å, b = 7.9 Å, c = 15.9 Å, space group = Pbcn) from single crystal data.[6] There are many similarities between the structures of α-$Sr_{10}Ga_6O_{19}$ and β-$Sr_{10}Ga_6O_{19}$, with the principal difference being the arrangement of the unbranched chain of six GaO_4 corner-sharing tetrahedra. In β-$Sr_{10}Ga_6O_{19}$, the fifth GaO_4 tetrahedron has been rotated with respect to the fourth tetrahedron about the Ga-O-Ga bridge (Figure 8.3), resulting in the $(Ga_6O_{19})^{20-}$ unit forming a ~6.5 Å wide slab, with the Sr^{2+} cations residing between and within these gallium oxide units.

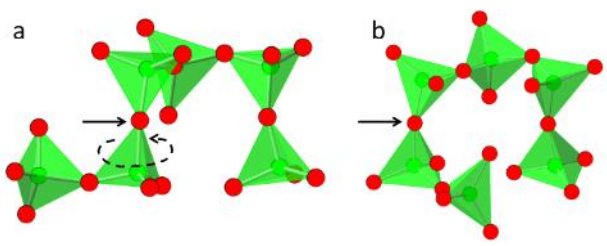

Figure 8.3: Differences between the unbranched chains of six corner-sharing GaO_4 tetrahedra in: a) α-$Sr_{10}Ga_6O_{19}$, and b) β-$Sr_{10}Ga_6O_{19}$, showing how the rotation of the fifth tetrahedron with respect to the fourth produces the different $(Ga_6O_{19})^{20-}$ units in the two structures.

This chapter will focus on work performed on three $La_xSr_{10-x}Ga_6O_{19+x/2}$ compositions (x = 0, 0.2, and 0.4). The main aim was to prepare these excess-oxygen materials by replacing some Sr^{2+} with La^{3+}, and to investigate how the change in composition affects their structures and properties relative to $Sr_{10}Ga_6O_{19}$. In addition, the aim was to investigate the phase transitions in this material suggested by Krueger *et al*.,[5] and determine the structures of any new forms identified.

8.2 Synthesis of $La_xSr_{10-x}Ga_6O_{19+x/2}$ (x = 0, 0.2, and 0.4) materials

Solid-state synthesis was carried out to prepare samples of nominal compositions $Sr_{10}Ga_6O_{19}$, $La_{0.2}Sr_{9.8}Ga_6O_{19.1}$, and $La_{0.4}Sr_{9.6}Ga_6O_{19.2}$. For $Sr_{10}Ga_6O_{19}$, $SrCO_3$ (4.6177 g, 31.28 mmol, Aldrich, 99.9 %) and Ga_2O_3 (1.7589 g, 9.38 mmol, Aldrich, 99.99 %) were ground together in a mortar using a pestle, then fired in a Pt crucible at 1200 °C for 108 hours with intermediate grindings, yielding an off-white powder.

La_2O_3 was initially fired at 1000 °C for 2 hours, before 0.1012 g (0.31 mmol, Aldrich, 99.9 %) was combined with $SrCO_3$ (4.4920 g, 30.43 mmol, Aldrich, 99.9 %) and Ga_2O_3 (1.7459 g, 9.32 mmol, Aldrich, 99.99 %) and ground in a mortar using a pestle to form the precursor powder for $La_{0.2}Sr_{9.8}Ga_6O_{19.1}$. This precursor was fired in a Pt crucible at 1200 °C for 144 hours with intermediate grindings to yield a pale-purple powder. For $La_{0.4}Sr_{9.6}Ga_6O_{19.2}$, 0.0803 g of pre-fired La_2O_3 (0.25 mmol, Aldrich, 99.9 %), 0.6933 g of Ga_2O_3 (3.70 mmol, Aldrich, 99.99 %), and 1.2164 g of SrO (11.84 mmol, Aldrich, 99.99 %) were ground together then fired in a Pt crucible at 1200 °C for 132 hours to yield a pale-purple powder.

8.3 Characterisation of $La_xSr_{10-x}Ga_6O_{19+x/2}$ (x = 0, 0.2, and 0.4) materials

8.3.1 Laboratory powder X-ray diffraction

Figure 8.4 shows the recorded PXRD patterns and subsequent Rietveld refinements for $Sr_{10}Ga_6O_{19}$, $La_{0.2}Sr_{9.8}Ga_6O_{19.1}$, and $La_{0.4}Sr_{9.6}Ga_6O_{19.2}$. The structural model reported for α-$Sr_{10}Ga_6O_{19}$ by Kahlenberg was used as a starting model for the refinements,[3] and for each composition the following parameters were refined: 10 background terms, sample-height displacement, 4 lattice parameters, 1 isotropic displacement parameter, peak-shape terms, and a scale factor. The calculated fit to the collected data for $Sr_{10}Ga_6O_{19}$ based on the orthorhombic β-$Sr_{10}Ga_6O_{19}$ structural model was poor (Figure 8.4d) compared to the almost perfect fit using the monoclinic α-$Sr_{10}Ga_6O_{19}$ structural model (Figure 8.4a), indicating that the monoclinic phase had been synthesised.

For $La_{0.4}Sr_{9.6}Ga_6O_{19.2}$, there was evidence of the $Sr_3Ga_2O_6$ and $LaSrGa_3O_7$ impurity phases (black and green tick marks respectively in Figure 8.4c, in conjunction with arrows) which were not observed in the diffraction patterns for the x = 0 and 0.2 compositions, and so the x = 0.4 composition was not used in any subsequent analyses.

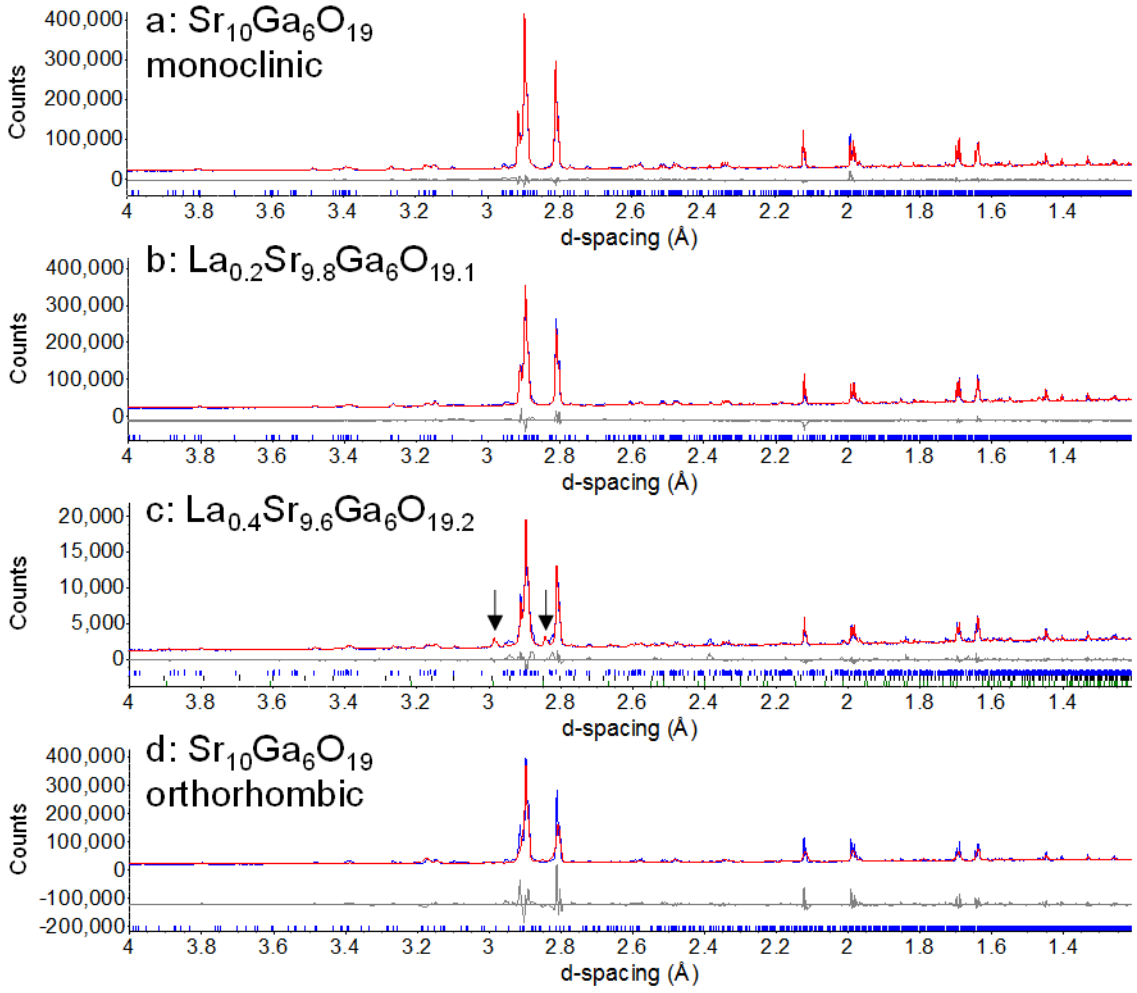

Figure 8.4: Rietveld refinements using the monoclinic α-$Sr_{10}Ga_6O_{19}$ structural model (without the incommensurate modulation) of: a) $Sr_{10}Ga_6O_{19}$, d7_05665, *a* = 34.9632(2) Å, *b* = 7.9377(1) Å, *c* = 15.9452(1) Å, β = 103.556(1) °, R_{wp} = 2.621 %. b) $La_{0.2}Sr_{9.8}Ga_6O_{19.1}$, d7_05702, *a* = 34.9401(3) Å, *b* = 7.9393(1) Å, *c* = 15.9417(2) Å, β = 103.510(1) °, R_{wp} = 2.980 %. c) $La_{0.4}Sr_{9.6}Ga_6O_{19.2}$, d7_05158, *a* = 34.938(1) Å, *b* = 7.9389(3) Å, *c* = 15.9424(6) Å, β = 103.512(2) °, R_{wp} = 4.715 %, impurity peaks denoted with arrows. d) Rietveld refinement with the orthorhombic β-$Sr_{10}Ga_6O_{19}$ structural model for $Sr_{10}Ga_6O_{19}$, d7_05665, *a* = 33.969(3), *b* = 7.955(1) Å, *c* = 15.926(3) Å, R_{wp} = 8.402 %.

8.3.2 Powder neutron diffraction

Powder neutron diffraction data were collected at room temperature, and on heating at 230, 400, 500, and 680 °C for 190 μAh (~5 hours) per collection using the HRPD diffractometer at ISIS for $Sr_{10}Ga_6O_{19}$ and $La_{0.2}Sr_{9.8}Ga_6O_{19.1}$. Data were also collected for the latter composition in 60 °C increments on cooling from 620 °C to 160 °C for 75 μAh per collection (~2 hours). For all data collections, data were not recorded until the temperature of the furnace stabilised within a temperature tolerance. The initial room-temperature refinements of the two samples showed weak unidentified peaks which were not observed in the laboratory PXRD data (Figure 8.5, weak peaks marked with triangles), with the pattern for $Sr_{10}Ga_6O_{19}$ also containing evidence (~0.5 %) of SrO, which was included as a second phase in the refinement. A search-match analysis performed using the EVA software package following the conversion of the time-of-flight data to 2θ data (with a Cu K_α wavelength of 1.5406 Å) revealed no conclusive matches for the unidentified peaks. Both samples were tested for impurities seen in samples of $La_{0.4}Sr_{9.6}Ga_6O_{19.2}$ ($Sr_3Ga_2O_6$ and $LaSrGa_3O_7$) and $La_{0.6}Sr_{9.4}Ga_6O_{19.3}$ (La_2O_3 and $LaSrGaO_4$),[7]

but none of these impurities corresponded to the unidentified peaks observed in our data. The peaks at ~104,000 μs correspond to the signals from the V cans which held the samples during the data collections.

10 background parameters, sample peak-shape terms, and a scale factor were used for each refinement. 4 lattice parameters, all atomic coordinates, and one isotropic displacement parameter per crystallographic site were refined for $Sr_{10}Ga_6O_{19}$ and $La_{0.2}Sr_{9.8}Ga_6O_{19.1}$, in addition to one cell parameter and one isotropic displacement parameter for the SrO impurity phase.

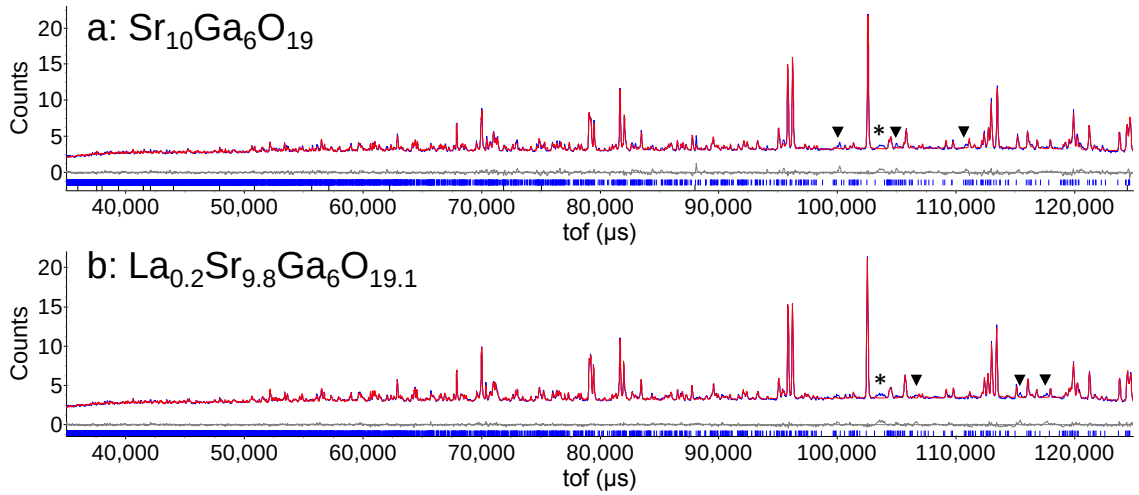

Figure 8.5: PND data and Rietveld refinements using the monoclinic structural model for: a) $Sr_{10}Ga_6O_{19}$, hrp58770_b1, *a* = 34.9930(1) Å, *b* = 7.9436(1) Å, *c* = 15.9566(1) Å, *β* = 103.571(1) °, R_{wp} = 3.080 %, black ticks marks = SrO reflections. b) $La_{0.2}Sr_{9.8}Ga_6O_{19.1}$, hrp58776_b1, *a* = 34.970(1) Å, *b* = 7.9456(2) Å, *c* = 15.9547(5) Å, *β* = 103.512(1) °, R_{wp} = 2.688 %. For both patterns, * = V can peak, and ▼ = impurity peaks.

As Krueger *et al.* report an incommensurately modulated structure for $Sr_{10}Ga_6O_{19}$,[5] it would be expected that the fit to the peaks containing reflections with *k* contributions in the indices (e.g. 0*k*0) would be poorer than those which do not possess a *k* contribution (e.g. *h*0*l*). However, this cannot be shown conclusively with the collected powder diffraction data as the quality of fit to the PND data suggests that the modulation does not exist, or is so small that it can be ignored.

Difference Fourier maps were created to attempt to locate the interstitial oxygen atoms in $La_{0.2}Sr_{9.8}Ga_6O_{19.1}$, as the structural model used for the refinement was that of α-$Sr_{10}Ga_6O_{19}$ and did not contain the correct atomic stoichiometry. However, no interstitial oxygen content was identified, with the residual nuclear density peaks located at unrealistic distances or angles relative to existing atomic positions. The inability to locate the interstitial oxygen positions can be attributed to the low levels of additional oxygen content present within the sample (approximately 0.5 %, corresponding to occupancy of a general position in this space group of 10 %); alternatively this could be due to the absence of the interstitial oxygen atoms.

8.3.3 Ionic conductivities of $Sr_{10}Ga_6O_{19}$ and $La_{0.2}Sr_{9.8}Ga_6O_{19.1}$

Impedance spectroscopy measurements were carried out on the $La_xSr_{10-x}Ga_6O_{19+x/2}$ compositions for x = 0 and 0.2. Data were not collected for the x = 0.4 composition due to the high percentage of impurity phases present in the sample. Pellets were pressed with 250 MPa of pressure, then fired at 1200 °C for 6 hours to produce pellets with the dimensions and masses given in Table 8.1. For both pellets, the temperature was increased from 300 °C to 800 °C in 50 °C increments with a 30 minute equilibration time before the data were collected.

Table 8.1: Pellet dimensions for the $Sr_{10}Ga_6O_{19}$ and $La_{0.2}Sr_{9.8}Ga_6O_{19.1}$ compounds used for impedance spectroscopy.

Composition	Mass (g)	Diameter (cm)	Height (cm)	Density (%)
$Sr_{10}Ga_6O_{19}$	0.5621 ± 0.0001	0.965 ± 0.001	0.200 ± 0.001	77.90 ± 0.01
$La_{0.2}Sr_{9.8}Ga_6O_{19.1}$	0.4708 ± 0.0001	0.931 ± 0.001	0.163 ± 0.001	86.00 ± 0.01

The conductivity data for the two materials are presented in Figure 8.6 along with those for the known impurity phases, $Sr_3Ga_2O_6$ and $LaSrGa_3O_7$.[2, 8] The conductivities of these potential impurities are lower than the compositions studied, and so their presence would not lead to erroneously high conductivity values.

Both the x = 0 and x = 0.2 compositions exhibit two changes in their conductivity gradients at approximately 420 °C and 630 °C. In the literature, the primary cause of changes in activation energy are crystallographic phase transitions.[9, 10] Whilst the change in gradient at 420 °C occurs at a temperature close to a previously reported phase transition, no clear structural phase transitions were observed in the PND or laboratory PXRD patterns at these two temperatures for $Sr_{10}Ga_6O_{19}$ and $La_{0.2}sr_{9.8}Ga_6O_{19.1}$. Vacancy trapping can also increase the activation energy without a phase transition occurring by forming metal-vacancy clusters at low temperatures, as reported for Mg- and Sr-doped $LaGaO_3$.[11] However, there are no vacancies available to form these clusters as the O sites in $Sr_{10}Ga_6O_{19}$ are fully-occupied, thereby rejecting this as the cause of the elevated activation energy.

The obtained conductivity values for $La_{0.2}Sr_{9.8}Ga_6O_{19.1}$ are slightly higher than those for $Sr_{10}Ga_6O_{19}$, which could be due to multiple factors: the unknown La-containing phase seen in the SEM images (*vide infra*) and accounting potentially for the unidentified peaks in the PND patterns, or the greater percentage density for the x = 0.2 composition compared to that for $Sr_{10}Ga_6O_{19}$. The activation energies for the x = 0 and x = 0.2 samples across three temperature ranges are shown in Table 8.2. The activation energies for oxide-ion migration are similar for both compounds at low temperatures (≤ 420 °C), with $La_{0.2}Sr_{9.8}Ga_6O_{19.1}$ showing increased activation energies relative to $Sr_{10}Ga_6O_{19}$ above 420 °C, arising potentially from the La-containing phase.

Table 8.2: Activation energies for $Sr_{10}Ga_6O_{19}$ and $La_{0.2}Sr_{9.8}Ga_6O_{19.1}$ in the three distinct regions of the conductivity curves.

	Activation energy (eV)		
Compound	280-420 °C	420-630 °C	630-780 °C
$Sr_{10}Ga_6O_{19}$	1.07(5)	0.47(3)	1.39(9)
$La_{0.2}Sr_{9.8}Ga_6O_{19.1}$	1.018(1)	0.60(1)	1.63(1)

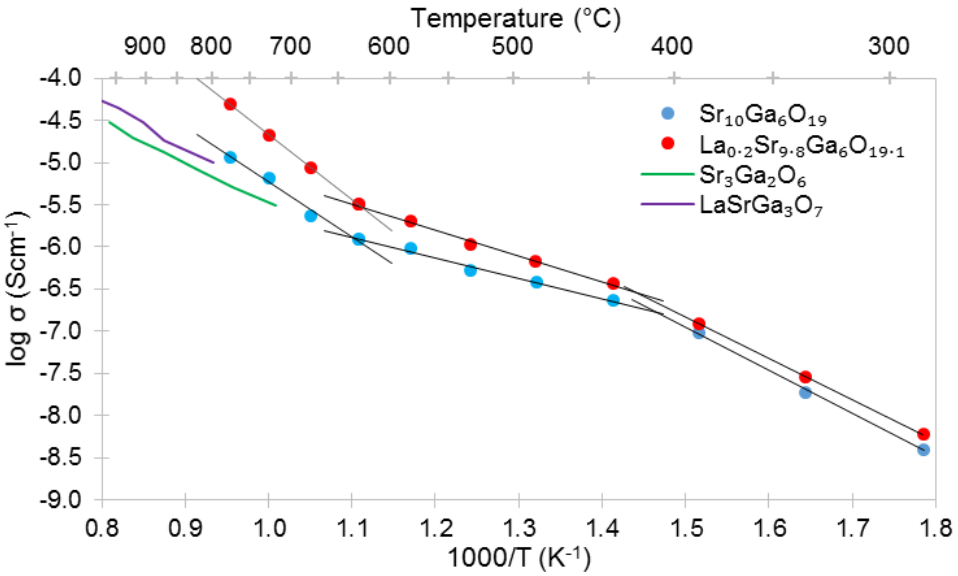

Figure 8.6: Arrhenius plot of log conductivity as a function of temperature for $Sr_{10}Ga_6O_{19}$, $La_{0.2}Sr_{9.8}Ga_6O_{19.1}$, and the phases $Sr_3Ga_2O_6$ and $LaSrGa_3O_7$.[2, 8] The changes in activation energy are shown by the changes in gradient on the plot.

8.3.4 *In situ* variable-temperature powder X-ray and neutron diffraction

Krueger *et al.* report that $Sr_{10}Ga_6O_{19}$ undergoes phase transitions on heating based on single-crystal diffraction data. Variable-temperature powder diffraction data were collected to investigate if these phase transitions could be observed using a powdered sample, and if they are also seen in the La-doped $La_{0.2}Sr_{9.8}Ga_6O_{19.1}$ material.

A laboratory VT-PXRD experiment was carried out on $Sr_{10}Ga_6O_{19}$, with data collected from 40 to 860 °C on heating, and then from 850 to 30 °C on cooling, both in 20 °C increments. The resulting diffraction film plot is shown in Figure 8.7. $Sr_{10}Ga_6O_{19}$ does not appear to undergo any phase transitions on heating or cooling, other than partial decomposition to $Sr_3Ga_2O_6$ above 720 °C. This is shown by the presence of additional peaks (2θ ~32 ° and ~45 °) above this temperature on heating, which then remain on cooling to room temperature. Therefore, heating the sample above 720 °C was avoided in subsequent variable-temperature experiments, to prevent sample decomposition.

Figure 8.8 illustrates the changes in lattice parameters and cell volume with temperature for $Sr_{10}Ga_6O_{19}$ and $La_{0.2}Sr_{9.8}Ga_6O_{19.1}$, obtained from Rietveld refinements using the *in situ* laboratory PXRD and PND data. From these plots, changes in the rates of thermal expansion are seen at approximately 230 °C and 400 °C for the *a* and *b* cell, and β angle parameters (Figure 8.8a-d,g,h) which coincide with the temperatures for the previously reported phase

transitions. However, no clear evidence of phase transitions are observed in the collected diffraction patterns, so it cannot be shown conclusively that these compositions pass through phase transitions at these temperatures. The thermal-expansion coefficient calculated for $Sr_{10}Ga_6O_{19}$ (α_l = 1.30 × 10^{-5} K^{-1}) is similar to the reported value for $Zr_{0.92}Y_{0.08}O_{1.92}$ (α_l = 1.05 × 10^{-5} K^{-1}).[12]

From the data, there is significant agreement in the lattice parameters obtained for the two compositions (especially for temperatures above 400 °C). Together with the inability to locate interstitial oxygen positions in the structure, this means potentially that the $La_{0.2}Sr_{9.8}Ga_6O_{19.1}$ sample is a mixture of $Sr_{10}Ga_6O_{19}$ and an unknown La-containing phase (presumably corresponding to the unidentified weak peaks observed in the PND data, marked with triangles in Figure 8.5).

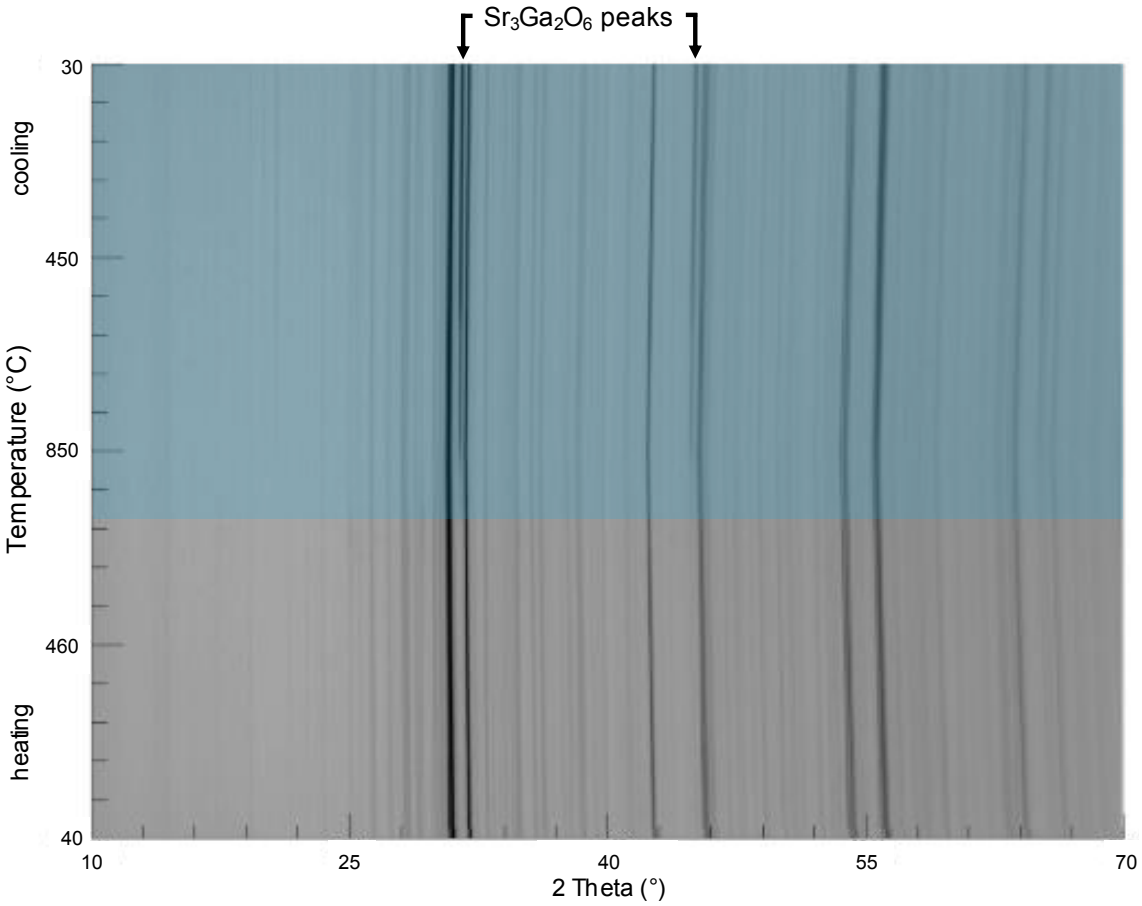

Figure 8.7: VT PXRD film plot for $Sr_{10}Ga_6O_{19}$ on heating and cooling. The blue region shows the partial decomposition to the $Sr_3Ga_2O_6$ phase (main peaks denoted by arrows).

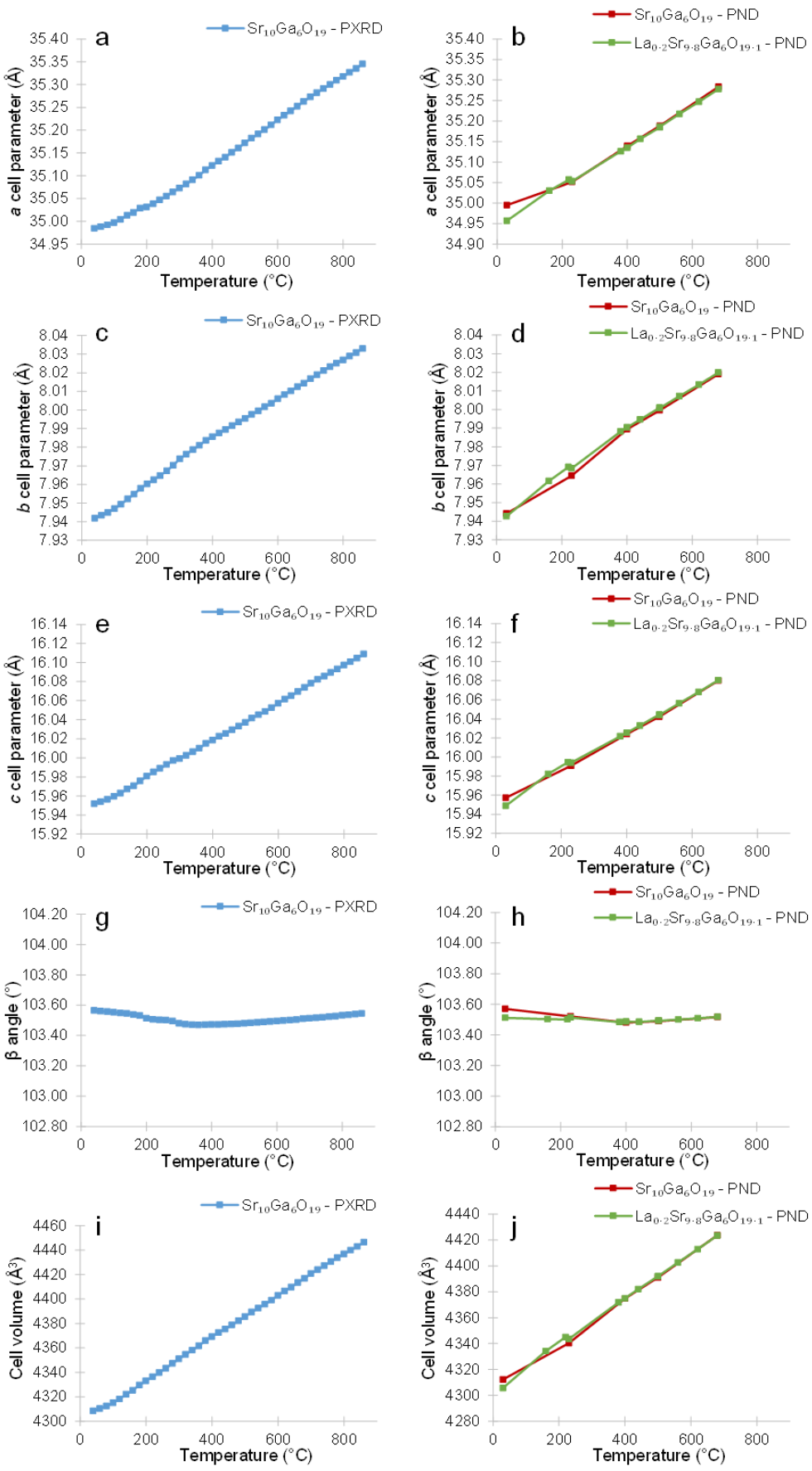

Figure 8.8: Variation with temperature of: a) and b) *a* cell parameter; c) and d) *b* cell parameter; e) and f) *c* cell parameter; g) and h) *β* angle; i) and j) cell volume for $Sr_{10}Ga_6O_{19}$ and $La_{0.2}Sr_{9.8}Ga_6O_{19.1}$ based on laboratory PXRD and neutron powder diffraction data showing evidence of changes in the rates of thermal expansion. Error bars are smaller than the data points and have been omitted for clarity.

8.3.5 Phase identification

To investigate whether $La_{0.2}Sr_{9.8}Ga_6O_{19.1}$ forms as a single phase or a mixture of $Sr_{10}Ga_6O_{19}$ and a La-containing phase, scanning electron microscopy was carried out on pelletised samples of $Sr_{10}Ga_6O_{19}$ and $La_{0.2}Sr_{9.8}Ga_6O_{19.1}$. Analysis of the SEM images revealed that $Sr_{10}Ga_6O_{19}$ is a single-phase material (Figure 8.9a), whilst $La_{0.2}Sr_{9.8}Ga_6O_{19.1}$ is inhomogeneous chemically, containing a mixture of $Sr_{10}Ga_6O_{19}$ (grey, Figure 8.9b) and a La-containing phase (white, Figure 8.9c). This is observed in the EDX plots, with lanthanum peaks only appearing during analysis of the white areas of the SEM images. This leads to the conclusion that the $La_{0.2}Sr_{9.8}Ga_6O_{19.1}$ composition has not been synthesised as a single-phase product.

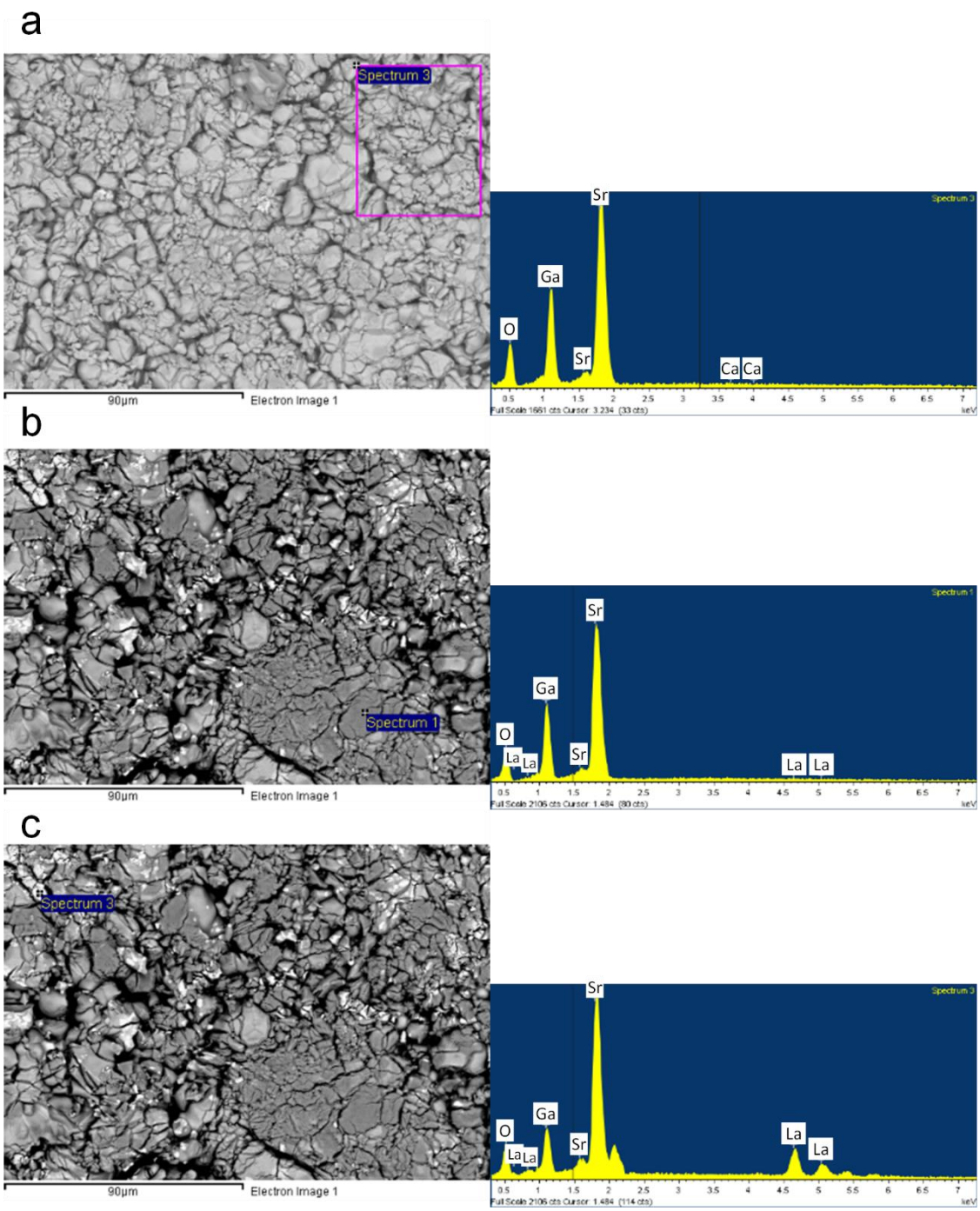

Figure 8.9: SEM images for: a) $Sr_{10}Ga_6O_{19}$; b) and c) $La_{0.2}Sr_{9.8}Ga_6O_{19.1}$, analysing different areas of the sample surfaces.

8.3.6 Bond-valence-sum (BVS) analysis and refined structure of $Sr_{10}Ga_6O_{19}$

Krueger *et al.*[5] report bond valence sums for the metal sites in $Sr_{10}Ga_6O_{19}$ at room temperature and 400 °C showing significant deviation from the expected values for Sr and Ga (red squares and dashed black lines, respectively, in Figure 8.10a and Figure 8.10c). Kahlenberg also reported underbonding (BVS values lower than expected) for the majority of Sr atoms in α-$Sr_{10}Ga_6O_{19}$.[3] To improve the structural model and reduce the underbonding and overbonding of the cations observed, bond-valence-sum restraints were introduced for each metal crystallographic site during the Rietveld refinements using the PND data.

The following parameters were refined at each temperature range: 10 background parameters, 4 lattice parameters, all atomic coordinates, scale factors, peak-shape terms, independent isotropic displacement parameters, and BVS restraints for each Sr and Ga crystallographic site. A penalty weighting of 2 was applied to attempt to minimise the differences between the calculated and expected bond valence sums. The respective Sr-O and Ga-O bond length cut-offs of 3.1 Å and 2.2 Å were used to calculate bond valence sums. Ga-O bonds in strontium gallates typically range between ~1.8 and 1.9 Å, with Sr-O bond lengths ranging around 2.5 Å,[3, 4, 13, 14] so these cut-off values allow for a distribution of bond lengths whilst keeping the bond lengths sensible.

The final BVS values for each crystallographic site for the five temperatures are presented in Figure 8.10 (blue diamonds), showing that in contrast to previous reports, the bond valence values for the atoms on the different crystallographic sites in the structural models obtained in this chapter are within error of their ideal values. It is difficult to determine exactly how Krueger *et al.* and Kahlenberg arrived at their BVS values, as they do not detail the distance cut-offs that they use for the Sr-O and Ga-O bond lengths in their refinements, but the models presented in this chapter show improvement over their reported values through the use of restraints.

The 30 °C structural model arising from the inclusion of the bond valence sum restraints is presented in Table 8.3. The structural model obtained shows the same key structural building blocks and connectivity as that reported previously, with the primary feature of the unbranched chain of six corner-sharing GaO_4 tetrahedra and the Sr^{2+} cations occupying sites amongst the GaO_4 polyhedra and running in planes parallel to the (100) plane remaining intact (Figure 8.11). Whilst the Sr-O bond lengths in the 30 °C structural model have approximately the same bond-distance range as the Kahlenberg model (0.95(4) Å and 1.01(1) Å respectively), the minimum and maximum bond lengths are shorter (2.15(3) to 3.10(2) Å compared to 2.34(1) to 3.35(1) Å for this model and the model by Kahlenberg respectively).[3] The O-Ga-O bond angles for the model presented in Table 8.3 (94(1) to 124(2) °) are shifted to lower angles compared to those reported by Kahlenberg for α -$Sr_{10}Ga_6O_{19}$ (99.7(6) to 130.2(6) °), whilst maintaining approximately the same angular range (30.0(6) ° to 30.5(2) °), whereas the 0.28(4) Å range (1.74(3) to 2.02(2) Å) of the Ga-O bond lengths is greater than the 0.12(1) Å range (1.78(1) to 1.90(1) Å) reported by Kahlenberg.[3] The conclusion is that the BVS restraints have allowed a structural model to be generated with reduced under- and overbonding of the atoms on the

metal crystallographic sites whilst maintaining the general description of the monoclinic $Sr_{10}Ga_6O_{19}$ structure.

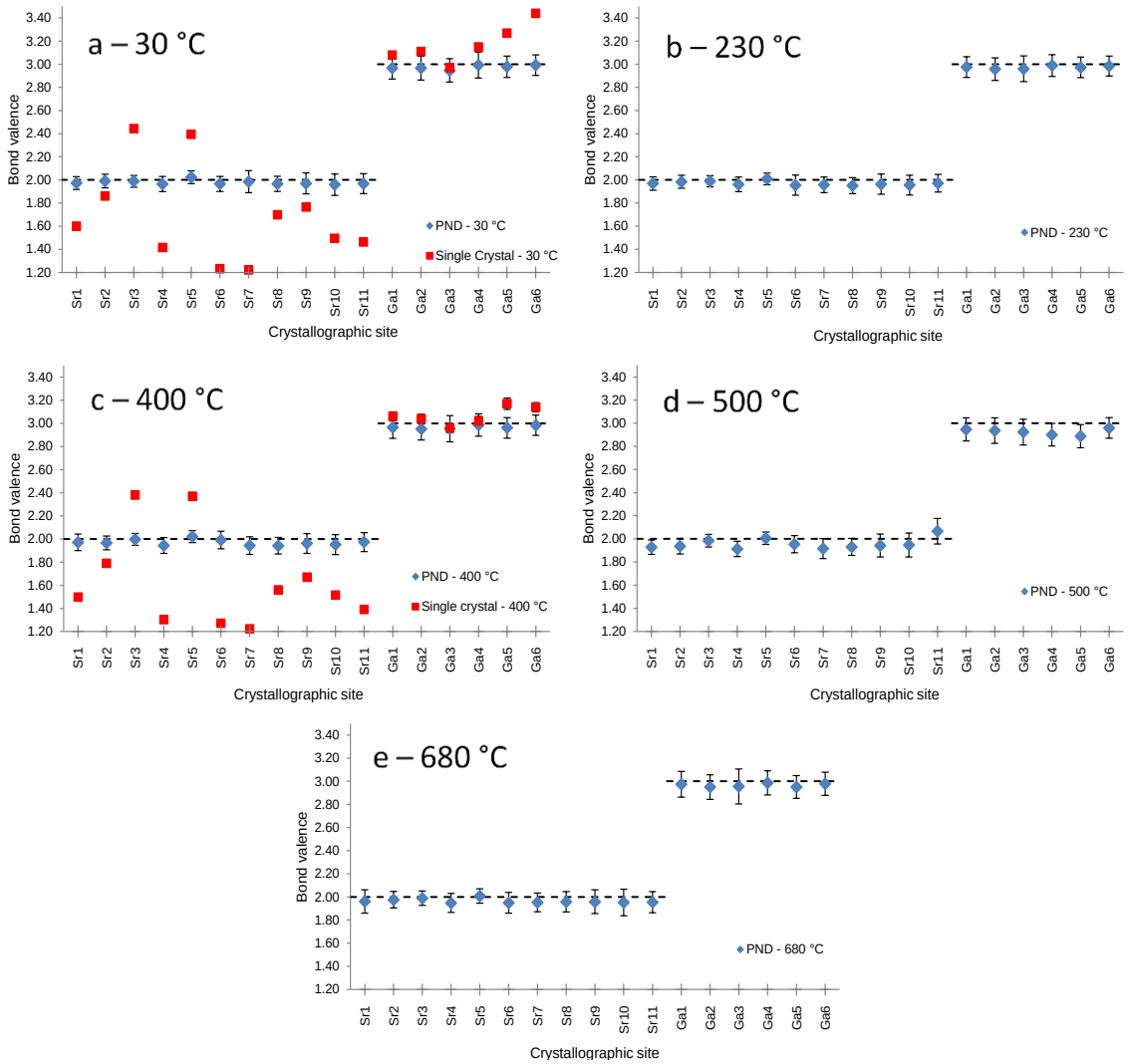

Figure 8.10: BVS values for the Sr and Ga crystallographic sites in $Sr_{10}Ga_6O_{19}$ at: a) 30 °C; b) 230 °C; c) 400 °C; d) 500 °C; e) 680 °C are denoted with blue diamonds. Figures a) and c) show the BVS values reported by Krueger *et al.* (red squares).[5] The dashed lines denote the ideal Sr and Ga BVS values of 2 and 3 respectively.

Table 8.3: Refined 30 °C structural model for $Sr_{10}Ga_6O_{19}$: *a* = 34.9929(1) Å, *b* = 7.94367(3) Å, *c* = 15.95648(7) Å, *β* = 103.5708(6) °, *V* = 4311.62(3) Å^3, space group = C2/c.

Atom	Site	x	y	z	Occupancy	Biso (Å^2)
Sr1	8f	0.1240(4)	0.261(2)	0.327(1)	1.0	1.3(3)
Sr2	8f	0.1218(5)	0.711(2)	0.079(1)	1.0	1.3(3)
Sr3	8f	0.0645(6)	0.445(2)	0.165(1)	1.0	3.1(4)
Sr4	8f	–0.0035(5)	0.769(2)	0.023(1)	1.0	3.3(5)
Sr5	8f	0.1859(6)	0.021(2)	0.481(1)	1.0	2.5(4)
Sr6	8f	0.1301(5)	0.755(2)	0.323(1)	1.0	3.1(4)
Sr7	8f	0.2460(5)	0.210(2)	0.345(1)	1.0	3.5(5)
Sr8	8f	0.1344(5)	0.272(2)	0.064(1)	1.0	2.0(4)
Sr9	4e	0	0.712(2)	0.25	1.0	0.1(3)
Sr10	4e	0	0.140(3)	0.25	1.0	4.8(8)

Atom	Site	x	y	z	Occupancy	Biso (Å^2)
Sr11	8f	0.2520(5)	0.254(2)	0.125(1)	1.0	1.1(3)
Ga1	8f	0.0577(5)	0.536(2)	–0.090(1)	1.0	1.0(3)
Ga2	8f	0.0634(4)	0.989(2)	–0.0738(9)	1.0	0.9(3)
Ga3	8f	0.0751(5)	0.985(2)	0.154(1)	1.0	3.3(4)
Ga4	8f	0.1810(5)	0.964(2)	0.218(1)	1.0	1.6(3)
Ga5	8f	0.1839(4)	0.510(2)	0.2348(9)	1.0	0.6(3)
Ga6	8f	0.1956(4)	0.490(2)	0.465(1)	1.0	1.1(3)
O1	8f	0.1898(8)	0.086(3)	0.321(2)	1.0	5.0(6)
O2	8f	0.1641(6)	0.324(3)	0.492(1)	1.0	3.3(5)
O3	8f	0.0212(7)	0.082(3)	0.855(2)	1.0	4.7(6)
O4	8f	0.0661(6)	0.770(2)	0.164(1)	1.0	2.4(4)
O5	8f	0.2329(8)	0.446(4)	0.201(2)	1.0	6.0(7)
O6	8f	0.0487(5)	0.054(2)	0.037(1)	1.0	0.8(3)
O7	8f	0.1866(6)	0.466(2)	0.347(1)	1.0	2.0(4)
O8	8f	0.1367(6)	0.430(2)	0.177(1)	1.0	1.9(4)
O9	8f	0.0652(6)	0.146(3)	0.236(1)	1.0	2.8(5)
O10	8f	0.0892(7)	0.487(3)	0.829(1)	1.0	3.3(5)
O11	8f	0.0664(6)	0.763(3)	–0.064(1)	1.0	2.9(5)
O12	8f	0.1267(9)	0.982(4)	0.164(2)	1.0	6.9(8)
O13	8f	0.2447(6)	0.511(2)	0.522(1)	1.0	2.3(4)
O14	8f	0.0717(6)	0.452(2)	0.014(1)	1.0	3.1(5)
O15	8f	0.1128(7)	0.036(3)	–0.077(2)	1.0	4.2(6)
O16	8f	0.1824(8)	0.737(3)	0.233(2)	1.0	5.0(6)
O17	8f	0.0046(7)	0.487(3)	0.875(1)	1.0	3.3(5)
O18	8f	0.1713(7)	0.709(3)	0.458(1)	1.0	4.1(6)
O19	8f	0.2033(7)	0.033(3)	0.135(1)	1.0	3.8(5)

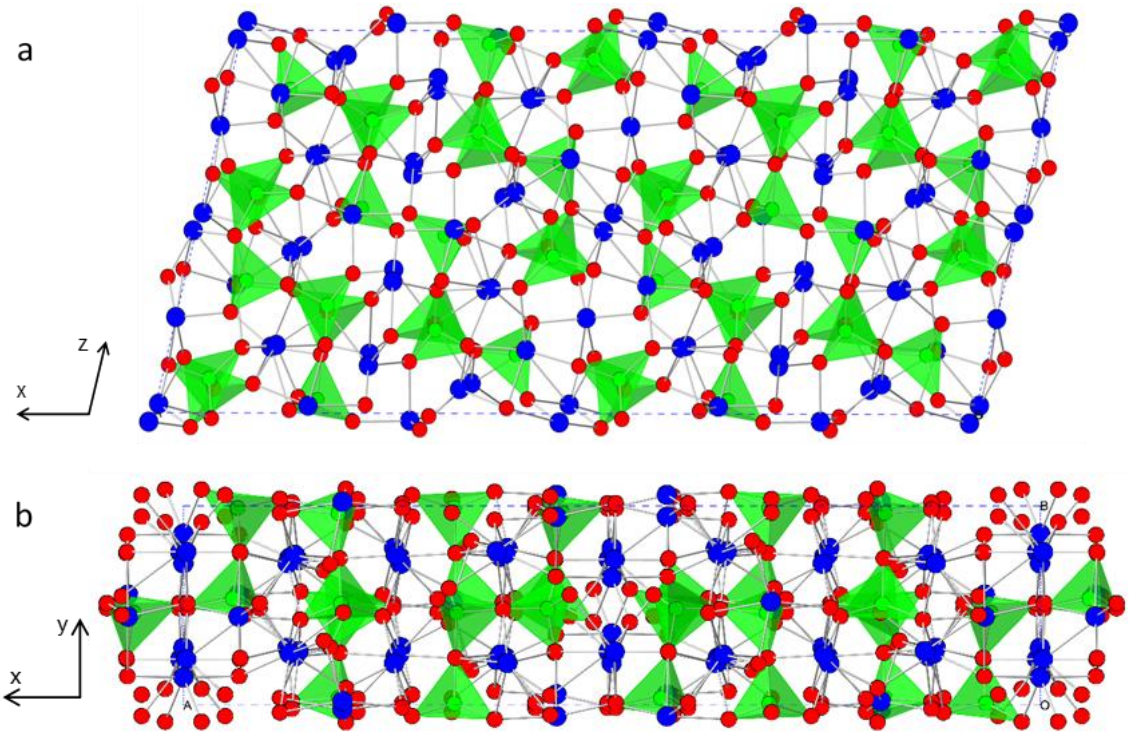

Figure 8.11: Refined structural model using BVS restraints for monoclinic $Sr_{10}Ga_6O_{19}$ when viewed: a) along the *y* axis, b) along the *z* axis. Sr = blue, Ga = green, O = red.

8.4 Conclusions

The analysis of powder diffraction data revealed no clear evidence of structural phase transitions for compositions $La_xSr_{10-x}Ga_6O_{19+x/2}$ (x = 0, 0.2), which were suggested previously by other workers based on single-crystal diffraction. From the powder neutron diffraction data, it cannot be shown conclusively that $La_{0.2}Sr_{9.8}Ga_6O_{19.1}$ contains any interstitial oxygen content, with SEM images showing that the synthesised sample contains a mixture of $Sr_{10}Ga_6O_{19}$ and a La-containing phase. An improved room-temperature structural model for $Sr_{10}Ga_6O_{19}$ was identified, through Rietveld refinements using powder neutron diffraction data and bond valence sum restraints.

Overall, the combination of: low oxide ion conductivity values of $Sr_{10}Ga_6O_{19}$, its irreversible decomposition to $Sr_3Ga_2O_6$ above 720 °C, and the inability to modify the material and its properties through aliovalent doping and introduction of excess oxide ions leads to the conclusion that $La_xSr_{10-x}Ga_6O_{19+x/2}$ materials are unsuitable for development as oxide-ion conductors.

8.5 References

1. C. I. Thomas, X. Kuang, Z. Deng, H. Niu, J. B. Claridge and M. J. Rosseinsky, *Chemistry of Materials*, 2010, **22**, 2510-2516.
2. X. Kuang, M. A. Green, H. Niu, P. Zajdel, C. Dickinson, J. B. Claridge, L. Jantsky and M. J. Rosseinsky, *Nature Materials*, 2008, **7**, 498-504.
3. V. Kahlenberg, *Journal of Solid State Chemistry*, 2001, **160**, 421-429.
4. H. J. Deiseroth and H. Müller-Buschbaum, *Zeitschrift Fur Anorganische Und Allgemeine Chemie*, 1972, **387**, 154-160.
5. H. Krueger, B. Lazic, E. Arroyabe and V. Kahlenberg, *Acta Crystallographica Section B*, 2009, **65**, 587-592.
6. V. Kahlenberg, *Solid State Sciences*, 2002, **4**, 183-189.
7. M. L. Tate, *MChem Thesis*, University of Durham, 2013.
8. T. Ishihara, H. Matsuda, M. A. B. Bustam and Y. Takita, *Solid State Ionics*, 1996, **86-8**, 197-201.
9. I. Abrahams, F. Krok, M. Malys and W. Wrobel, *Solid State Ionics*, 2005, **176**, 2053-2058.
10. L. Malavasi, C. A. J. Fisher and M. S. Islam, *Chemical Society Reviews*, 2010, **39**, 4370-4387.
11. J. Cheng and A. Navrotsky, *Journal of Solid State Chemistry*, 2004, **177**, 126-133.
12. I. Yasuda and M. Hishinuma, *Electrochemistry*, 2000, **68**, 526-530.
13. K. Kimura, M. Ohgaki, K. Tanaka, H. Morikawa and F. Marumo, *Journal of Solid State Chemistry*, 1990, **87**, 186-194.
14. V. Kahlenberg, B. Lazić and S. V. Krivovichev, *Journal of Solid State Chemistry*, 2005, **178**, 1429-1439.

9 Conclusions and future work

Utilisation of a range of complementary advanced techniques throughout this project, including: variable-temperature powder neutron diffraction (PND, constant wavelength and time-of-flight) and synchrotron powder X-ray diffraction (PXRD), single-crystal Laue neutron diffraction, floating-zone-furnace crystal growth, neutron total-scattering, Reverse Monte Carlo (RMC) analysis, annular bright-field scanning-transmission electron microscopy (ABF STEM), electron diffraction, scanning electron microscopy, impedance spectroscopy, second-harmonic generation, bond-valence energy landscape and bond-valence-sum mapping, and distortion-mode analysis, have provided new insight into the structure-property relationships of a range of solid electrolytes.

Three fluorite-type materials of general formula $Bi_{1-x}Nb_xO_{1.5+x}$ (x = 0.0625, 0.11, and 0.12) have been prepared and characterised. Cubic $Bi_{0.88}Nb_{0.12}O_{1.62}$ and $Bi_{0.89}Nb_{0.11}O_{1.61}$ have metastable fluorite-type cubic structures, with thermal annealing resulting in partial cubic-to-tetragonal phase transitions, with associated decreases in oxide-ion conductivity. These decreases are due to partial ordering of the oxygen atoms in the tetragonal phase, whereas they are disordered completely in the cubic phase. $Bi_{0.9375}Nb_{0.0625}O_{1.5625}$ was characterised at room temperature as having a tetragonal ($\sqrt{2} \times \sqrt{2} \times 1$) fluorite-type superstructure, with Bi^{3+} and Nb^{5+} cations disordered across mixed-occupancy cation sites. At elevated temperatures, *ab initio* molecular dynamics simulations found the average Nb coordination number in $Bi_{0.9375}Nb_{0.0625}O_{1.5625}$ to increase, owing to increased oxygen content in the NbO_x polyhedra. For $Bi_{0.9375}Nb_{0.0625}O_{1.5625}$, the collection and analysis of total-scattering (TS) data using RMC modelling could probe the local-scale ordering of Bi^{3+} and Nb^{5+} cations in the tetragonal superstructure. The analysis of high-temperature TS data could also investigate the increase in the average Nb coordination number, to identify the range of NbO_x groups present in the material.

The first triclinic Bi-containing apatite-type material, $Bi_2La_8[(GeO_4)_6]O_3$, was characterised using synchrotron PXRD, PND, and ABF STEM to identify a number of interstitial oxygen positions, with a level of interstitial oxygen atoms detected of 8 out of 1030 electrons per formula unit. The locations of the interstitial oxygen atoms result in the formation of GeO_5 trigonal bipyramids due to the ability of Ge to support variable coordination environments. The use of bond valence energy landscape modelling found these interstitial oxygen atoms to lie on oxide-ion migration pathways within the apatite framework, which are of lower energy than the pathways found within the apatite cavities. This means that apatite-type materials containing interstitial oxygen atoms within the apatite framework are expected to exhibit elevated conductivities compared to apatites without them. This was supported by ionic conductivity studies, which found the conductivity of $Bi_2La_8[(GeO_4)_6]O_3$ to be higher than the other Bi-containing apatites studied which only contain 26 oxygen atoms, showing that the presence of the interstitial oxygen content within the apatite framework promotes oxide-ion conduction. To increase the understanding of $Bi_2La_8[(GeO_4)_6]O_3$, total-scattering analyses of the local-scale structure would allow the interstitial oxygen locations to be probed further, investigating whether

the additional oxygen atoms are confined to the interstitial oxygen sites identified from ABF STEM and diffraction studies, or if they are found at multiple locations throughout the structure. This work would also probe the local-scale deviations from centrosymmetry observed using ABF STEM for a number of cation and anion sites, which are on a length scale too short for second-harmonic-generation experiments. For $La_{9.5}[(GeO_4)_{5.5}(AlO_4)_{0.5}]O_2$, reported previously as hexagonal but identified as triclinic in this work, the collection of and subsequent combined refinements using variable-temperature synchrotron PXRD and PND data will allow the triclinic structure to be characterised fully. This work would include refinement of the A- and T-site occupancies, to identify which A sites contain vacancies, and the distribution of Ge^{4+} and Al^{3+} cations disordered on the mixed-occupancy T sites. $La_{9.5}[(GeO_4)_{5.5}(AlO_4)_{0.5}]O_2$ may potentially undergo a reversible triclinic-to-hexagonal phase transition, as shown for $Bi_2La_8[(GeO_4)_6]O_3$, and so sequential refinements using variable-temperature diffraction data should be performed to investigate this possibility.

RMC analyses of $Bi_{28}Re_2O_{49}$ at 30 and 700 °C using neutron total-scattering data found the local-scale structure to contain isolated ReO_4, ReO_5, and ReO_6 polyhedra within a Bi-O sublattice. At 700 °C, oxygen atoms migrate from the Bi-O to Re-O sublattice, leading to an increase in the average Re coordination number from 4.5 to 4.63(2), as seen for $Bi_{0.9375}Nb_{0.0625}O_{1.5625}$ from molecular dynamics simulations. Additional total-scattering analyses for $Bi_{28}Re_2O_{49}$ need to be performed using a starting model which includes polyhedral restraints to fix the ReO_x polyhedra as rigid ReO_4 tetrahedra and ReO_6 octahedra, as reported in the literature. This will investigate if the model containing a range of ReO_x polyhedra (including ReO_5) provides a more accurate representation of the local-scale structure for $Bi_{28}Re_2O_{49}$ relative to the model containing solely ReO_4 tetrahedra and ReO_6 octahedra.

$Bi_{38}Mo_7O_{78}$ forms a fluorite-related superstructure and exhibits a reversible monoclinic-to-orthorhombic phase transition between 70 and 90 °C. The orthorhombic structure was characterised as a (3 × 5 × 3) superstructure, containing a three-dimensional Bi-O fluorite-like sublattice and two types of MoO_x polyhedra, isolated MoO_4 tetrahedra and chains of three corner-connected distorted MoO_6 octahedra forming (Mo_3O_{16}) units. Attempts to characterise the room-temperature monoclinic structure through a distortion-mode analysis were unsuccessful. Therefore, single-crystal Laue neutron diffraction data collected for this material need to be used to aid in the characterisation of the monoclinic room-temperature structure. Once completed, this will provide insight as to the causes of the monoclinic-to-orthorhombic phase transition, including potential distortion of the MoO_x polyhedra. For $Bi_{37.5}Mo_{7.5}O_{78.75}$, combined Rietveld refinements using collected PND and synchrotron PXRD data are required for the room-temperature orthorhombic structure to be characterised fully. Locating the positions of the interstitial oxygen atoms within the structure of this material using difference Fourier maps is virtually impossible due to the low level of interstitial oxygen content (6 out of 4057.5 electrons per formula unit), a level ~20 % of that identified for $Bi_2La_8[(GeO_4)_6]O_3$ (8 out of 1030 electrons per formula unit), which was at the limits of detectability using data collected on the same instrument. Once the $Bi_{37.5}Mo_{7.5}O_{78.75}$ structure has been characterised, it can be compared to the orthorhombic structure for $Bi_{38}Mo_7O_{78}$ to determine the cause of the elevated

oxide-ion conductivity reported for the former case, and whether this is due to a greater range of MoO_x coordination environments.

Crystals of $Bi_{0.913}V_{0.087}O_{1.587}$ and $Bi_{0.8}V_{0.2}O_{1.7}$ were grown using a floating-zone furnace. The complex structure of $Bi_{0.913}V_{0.087}O_{1.587}$ was characterised using single-crystal Laue neutron diffraction data as a rhombohedral fluorite-type superstructure. This superstructure is comprised of a Bi-O fluorite-type lattice containing isolated VO_4 tetrahedra and VO_5 trigonal bipyramids. This range of VO_x polyhedra provide additional migration pathways to facilitate the excellent oxide-ion conductivities reported for this material. A combined refinement of the $Bi_{0.913}V_{0.087}O_{1.587}$ structure using synchrotron XRD data in conjunction with Laue neutron diffraction data will allow the atomic coordinates and occupancies of the V-containing sites to be refined with increased accuracy. For $Bi_{0.8}V_{0.2}O_{1.7}$, the lattice parameters and symmetry of the superstructure need to be identified from single-crystal Laue neutron diffraction data, before the room-temperature structural model can be characterised fully, to identify the VO_x polyhedra present, whether they are a single type or a range of VO_x groups.

Analysis of the $La_xSr_{10-x}Ga_6O_{19+x/2}$ (x = 0, 0.2, and 0.4) materials found no conclusive evidence of incorporation of interstitial oxygen atoms into the structure when $x > 0$, with a sample of $La_{0.2}Sr_{9.8}Ga_6O_{19.1}$ found to contain $Sr_{10}Ga_6O_{19}$ and a secondary La-containing phase. Therefore, the inability to modify the $La_xSr_{10-x}Ga_6O_{19+x/2}$ materials and their associated properties through the introduction of interstitial oxygen results in them being unsuitable for use as oxide-ion conductors.

For any solid-oxide fuel cell electrolyte, two key aspects are the oxide-ion conductivity and cyclability. Nonetheless, multipronged characterisation, as illustrated in this thesis, plays a vital role in understanding the structure-property relationships of the materials studied. This need will only increase as the complexity of the next generation of solid-oxide fuel cells grows.

9.1 Publications

- M. L. Tate, D. A. Blom, M. Avdeev, H. E. A. Brand, G. J. McIntyre, T. Vogt and I. R. Evans, *Advanced Functional Materials*, 2017, **27**, 1605625.
- M. L. Tate, J. Hack, X. Kuang, G. J. McIntyre, R. L. Withers, M. R. Johnson and I. R. Evans, *Journal of Solid State Chemistry*, 2015, **225**, 383-390.
- I. R. Evans, J. S. O. Evans, H. G. Davies, A. R. Haworth and M. L. Tate, *Chemistry of Materials*, 2014, **26**, 5187-5189. (This is a collaborative work on a project unrelated to this thesis.)
- M. L. Tate, M. Avdeev, H. E. A. Brand, G. J. McIntyre and I. R. Evans, “Structure-property relationships of several new apatite-type oxide-ion conductors, including bond-valence energy landscape modelling of the oxide-ion migration pathways”, *in preparation*.